Development of Perovskite-Gallium Arsenide double-junction photovoltaic devices

Emmanouil G. Manidakis

PhD Thesis

«The implementation of the doctoral thesis was co-financed by Greece and the European Union (European Social Fund-ESF) through the Operational Programme «Human Resources Development, Education and Lifelong Learning» in the context of the Act "Enhancing Human Resources Research Potential by undertaking a Doctoral Research" Sub-action 2: IKY Scholarship Programme for PhD candidates in the Greek Universities».

Ευρωπαϊκή Ένωση
European Social Fund

Operational Programme
Human Resources Development,
Education and Lifelong Learning
Co-financed by Greece and the European Union

ΕΣΠΑ 2014-2020
ανάπτυξη - εργασία - αλληλεγγύη

ΠΑΝΕΠΙΣΤΗΜΙΟ ΚΡΗΤΗΣ
UNIVERSITY OF CRETE

October 2023
Heraklion, Greece

Acknowledgments

First and foremost, I want to express my deepest gratitude to my family. Their love, encouragement, guidance, and most important their belief in me, were the main source of energy and inspiration during my academic journey. Without them, nothing of what I have done would have been possible.

I also want to acknowledge my supervisor, professor Nikolaos Pelekanos. His expertise, mentorship, and dedication to my research field have been invaluable. He has consistently pushed me to do the best possible I can, challenged me to think critically, provided invaluable guidance that has enriched my work, and gave me plenty of supplies for the future.

Furthermore, I want to extend my appreciation to my co-supervisor, professor Costantinos Stoumpos. His collaboration and support have been essential, leading me in the correct direction of my research and ensuring its success. His insights and guidance on my research field have significantly contributed to the quality of my work.

Abstract

The perovskite solar cells represent today the most rapidly developed photovoltaic (PV) technology, as they combine low fabrication costs, high conversion efficiencies and the possibility to deposit on flexible substrates, while great progress has been accomplished recently on the stability issues of these materials under typical atmospheric conditions. On the other hand, the solar cells based on III-V semiconductors, such as GaAs, are still regarded as the reference technology in the PV industry, exhibiting the highest in the whole field PV efficiencies of 29.1% for single-junction devices and 46% for a four-junction solar cell with concentrated light.

In this thesis, we attempt to combine the benefits of the above two material systems to provide a high-efficiency perovskite/GaAs tandem solar cell with enhanced characteristics. Our main findings are:

- We have produced GaAs-based solar cell devices with PV efficiencies reaching ~15% values, comparing well with reported values for GaAs solar cells of similar design. Furthermore, these PV efficiencies are more than enough for the main purpose of this work, which is to demonstrate the benefits of tandem perovskite/GaAs devices.
- We have developed optimized recipes, adapted to our laboratory, for the deposition of every single layer of a full perovskite PV device, including the perovskite active layer, the electron and hole transporting layers, and the metal contacts.
- We have experimented with several deposition techniques such as hot-casting, antisolvent method and gas-quenching technique, to obtain high-quality perovskite films in "out-of-the-glovebox" conditions.
- We have synthesized high-bandgap "red" perovskites with a gap around 650nm for the needs of the tandem perovskite/GaAs structures and examined ways to limit their phase-separation phenomena under photoexcitation.
- We have fabricated "red" perovskite solar devices with the modest PV efficiency of ~6.5%, most likely attributed to the "out-of-the-glovebox" conditions.
- We have realized that the rf-sputtering deposition of Indium-Tin-Oxide, as transparent electrode on top of Spiro-OMeTAD/perovskite layers, degrades severely the PV characteristics of the underneath device,

suggesting that we need either to employ a milder ITO deposition method or find a protection scheme of the underneath layers during the ITO deposition.

- Combining a 1.77 eV perovskite solar cell with transparent contacts, provided to us from a collaborating lab, and a GaAs solar cell developed by our group, we have managed to demonstrate a tandem 4-terminal device with a PV efficiency close to 23%.
- Finally, we have demonstrated that the deposition of $MAPbI_3$ on native nominally-undoped (100) GaAs substrates generates a giant passivation effect. X-ray photoelectron spectroscopy on ultrathin $MAPbI_3$/GaAs and PbI_2/GaAs samples suggest that some Pb-related de-oxygenation of the GaAs surface occurs and is likely at the origin of the passivation effect. Interestingly, the whole process is fully reversible, in the sense that the $MAPbI_3$ layer can be easily removed, and the PL intensity and spectral features of the GaAs substrate are fully restored to their pristine condition.

Table of Contents

Chapter 1

Brief History

Photovoltaics

Photovoltaics (PV) is a type of technology that converts sunlight directly into electricity. The history of PV systems dates back to the 19th century, with the discovery of the photovoltaic effect by French physicist Alexandre-Edmond Becquerel in 1839.

In 1954, Bell Labs scientists Daryl Chapin, Calvin Fuller, and Gerald Pearson invented the first practical photovoltaic cell, a significant progress in the development of practical applications for photovoltaic cells. The cell, made from silicon, with an efficiency of 6%, which was a significant improvement over previous design [1]. The Bell Labs team also developed the first practical solar panel, which was used in a satellite launched by the U.S. Navy in 1958 [2].

Figure 1. The inventors of the Bell Solar Battery, from left, Gerald Pearson, Daryl Chapin, and Calvin Fuller, check devices for the amount of solar electricity derived from sunlight, here simulated by a lamp [1].

In the following years, the use of photovoltaic cells expanded beyond space applications and began to be developed for terrestrial applications. One early application was in remote locations, where traditional power sources were not available.

Figure 2. Advertisement photos, such as this one that appeared in the 1956 issue of Look Magazine, showing-off the "Bell Solar Battery" to the American public [1].

More specifically, the need for renewable energy sources became more imperative due to the great energy crisis that broke out in the 1970s. As result, new PV technologies developed, including thin-film cells and improved crystalline silicon cells, which increased the efficiency and reduced the cost of PV systems. Further improvements in PV technology came out with the development of multi-junction cells, which provide increased efficiency by capturing a wider range of the solar spectrum. PV systems also became more widely used in grid-connected applications, such as large-scale solar power plants. In the 2000s, the growth of the photovoltaic technology, driven by declining costs and increasing the maximum output power. This led to the development of new materials and technologies, such as thin-film technologies and new manufacturing techniques, such as spray deposition, spin-coating and roll-to-roll

processing. The best recorded efficiencies of different solar cell technologies from 1975 until now are presented on figure 3.

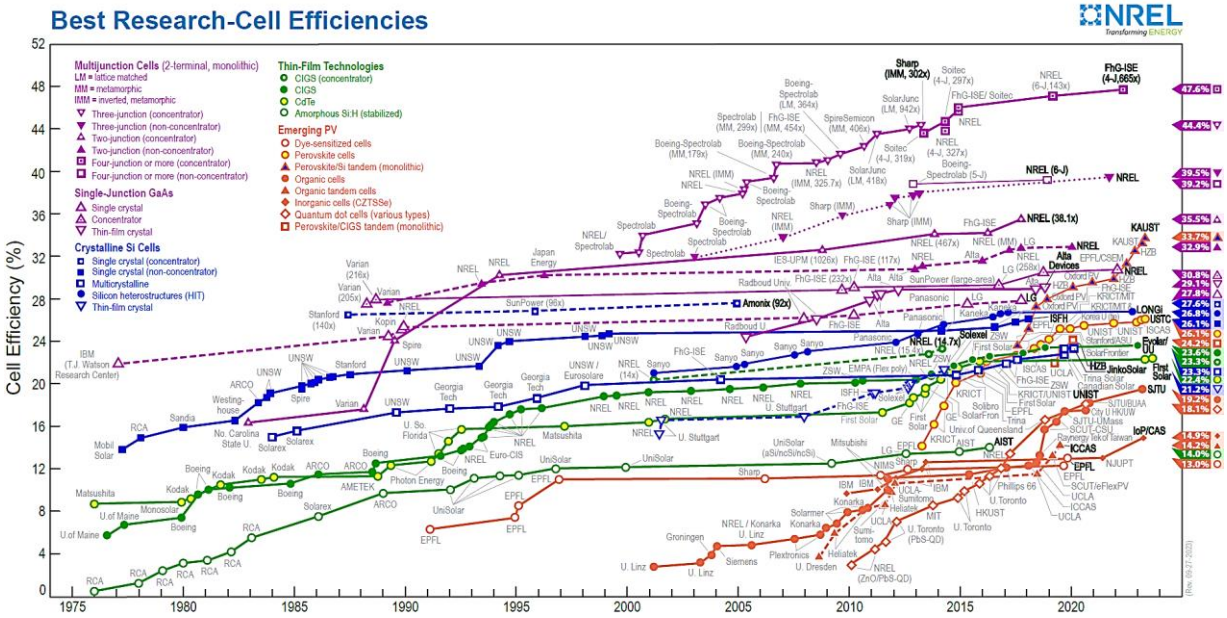

Figure 3. Interactive Best Research-Cell Efficiency Chart from the National Renewable Energy Laboratory (NREL) [3].

Today, PV systems are widely used for residential and commercial rooftop solar systems, large-scale solar power plants, and portable devices such as backpacks and phone chargers. The PV industry continues to evolve and innovate, with new technologies and applications being developed all the time.

Gallium Arsenide Solar Cells

Gallium arsenide (GaAs) is a compound semiconductor material composed of the elements gallium (Ga) and arsenic (As). It has unique properties that make it suitable for various applications in electronics and optoelectronics. More specific, GaAs crystallizes in a zinc-blende crystal structure, similar to diamond. It has a direct bandgap, meaning that electrons can transition between the valence and conduction bands, without assistance by phonon states. The bandgap energy of GaAs is approximately 1.42 electron volts (eV), which corresponds to the near-infrared range of the electromagnetic spectrum. It provides excellent electron mobility (higher than silicon), making it a popular material for high-speed electronic. Due to its high electron mobility, GaAs is well-suited for applications requiring high-frequency operation, such as wireless communication devices and

microwave integrated circuits. Additionally, GaAs is employed in high-efficiency solar cells, while is commonly used also in light-emitting diodes (LEDs) and laser diodes. When GaAs forms alloys with phosphorus or aluminum, can emit light across a wide range of wavelengths, including the visible and near-infrared regions. It has a higher absorption coefficient for sunlight in visible range of spectrum compared to silicon, allowing for a thinner absorbing layer and potentially reducing manufacturing costs. The good thermal conductivity enables it to dissipate heat effectively. This property is beneficial in high-power electronic devices where heat management is crucial. Also, GaAs can be integrated with other semiconductor materials, such as silicon and indium phosphide, to form hybrid structures that leverage the unique properties of each material for specific applications. Gallium arsenide has found widespread use in the telecommunications, aerospace, defense, and photovoltaic industries. Its superior performance in high-frequency and optoelectronic applications has made it a valuable material for advanced electronic devices.

For the history, Gallium arsenide (GaAs) solar cells were first developed in the 1960s, as researchers were exploring alternatives to silicon for solar cell technology, as silicon solar cells had limitations in terms of efficiency, especially for high-temperature applications. In the early 1970s, scientists at RCA Laboratories, including Zhores Alferov and Herbert Kroemer, began working with GaAs for solar cell technology. In 1973, Alferov and Kroemer proposed a new type of solar cell, called a tandem cell, which combined two layers of different semiconductors to achieve even higher efficiency. They received the Nobel Prize in Physics in 2000 for their work on semiconductor heterostructures [4].

Today, GaAs solar cells are widely used in space applications, where their high efficiency and radiation resistance are important. They are also used in terrestrial applications for specialized purposes, such as in concentrator photovoltaics, which use lenses or mirrors to focus sunlight onto small, highly efficient solar cells. It's important to note that gallium arsenide solar cells are not as commonly used for residential or commercial rooftop installations due to their higher cost. However, ongoing research and technological advancements may lead to cost reductions in the future, making them more accessible for a wider range of applications.

Perovskite Solar Cells

Perovskite materials refer to a class of materials that have a specific crystal structure known as the perovskite structure (the first perovskite mineral discovered in the Ural Mountains in Russia in 1839). The name "perovskite" comes from the mineral perovskite, which was named after Russian mineralogist Lev Perovski. Perovskite materials have gained significant attention in recent years, particularly in the field of solar cell technology, due to their exceptional optoelectronic properties. They have demonstrated high power conversion efficiencies, low-cost fabrication processes, and the potential for scalability. Perovskite materials can be solution processed, which means they can be deposited onto various substrates using techniques like spin coating, inkjet printing, or vapor deposition. This makes them attractive for large-scale manufacturing and integration into flexible and lightweight solar cells. Apart from solar cells, perovskite materials have shown potential in other areas such as light-emitting diodes (LEDs), photodetectors, lasers, and various optoelectronic devices. They have also been investigated for applications in catalysis, sensors, batteries, and memory devices. It's worth noting that while perovskite materials offer great promise, there are still challenges that need to be addressed, such as stability issues, moisture sensitivity, and toxicity concerns related to lead-containing perovskites[5]. Researchers are actively working to overcome these challenges and develop more stable and environmentally friendly perovskite materials. Overall, perovskite materials have emerged as a highly promising class of materials with a wide range of applications in the field of energy and optoelectronics, and ongoing research continues to uncover new possibilities for their use.

In terms of solar cells, perovskite-based solar cells have gained significant attention in recent years due to their potential for high efficiency and low cost. The history of perovskite solar cells dates back to 2006, when researchers at the Tokyo Institute of Technology first demonstrated the use of perovskite materials in a solar cell. The first perovskite solar cell was made using a dye-sensitized solar cell (DSSC) architecture, with a perovskite material serving as the light-absorbing layer. However, the efficiency of these early perovskite solar cells was relatively low, with a maximum efficiency of around 3.8% [6]. In 2012, researchers made a breakthrough in the development of perovskite solar cells, achieving an efficiency ~ 10% [7].

This was achieved by using a solid-state perovskite material, rather than a liquid material used in previous designs. Since then, the efficiency of perovskite solar cells has continued to improve rapidly, with record-breaking efficiencies of over 25% reported in 2020 from UNIST and EPFL researchers, while in 2023 reported an efficiency of 26.08% [8]. This has made perovskite solar cells a promising candidate for low-cost, high-efficiency solar energy generation.

Tandem Solar Cells

Tandem solar cells are a promising technology that has the potential to significantly improve the efficiency of solar energy conversion. These devices are designed to combine two or more different types of solar cells on top of each other, with each cell absorbing a different portion of the solar spectrum. The idea behind tandem solar cells is to capture more of the available sunlight by utilizing efficiently a broader range of wavelengths. By stacking multiple cells, each optimized for a different portion of the spectrum, the overall efficiency of the device can be greatly increased. The concept of tandem solar cells has been around for many years, but there is no work reported until the 1980s. In the 1990s, researchers began to explore the use of different materials for the top and bottom cells in tandem cells. This led to the development of heterojunction tandem cells, where the top and bottom cells are made of different materials. One of the primary works of multijunction solar cells, published in 1978 from S. M. Bedair et al. with a GaAs/AlGaAs tandem solar cell with an open circuit voltage of 2Volts, the highest value until then. Although the maximum calculated efficiency for a GaAs/AlGaAs was ~25%, due to non-optimized parameters, the efficiency on this work was ~9% [9]. In 1990, J.M. Olson et al. developed a GaAs/InGaP tandem solar cell with an efficiency of 27.3% [10] while in 1994, researchers at the National Renewable Energy Laboratory (NREL) reported a tandem cell based on the same GaAs/InGaP heterostructure with an optimized efficiency of 29.5% [11]. As soon as after the perovskite break through, hybrid tandem structures reported. In 2015, P. Mailoa et al. published a Si/Perovskite tandem solar cell device, with an efficiency of 13.7% [12] , while, 2 years later published a Si/Perovskite tandem solar cell device with a significant increased efficiency of 23.6% [13]. A little bit later, published and the first

work based on GaAs/Perovskite solar cell from Z. Li et all with an efficiency of 25.19% [14].

Chapter 2

Introduction

The increasing demand for renewable energy has led to significant advancements in solar cell technology. Gallium arsenide (GaAs) is a widely used material in the field of photovoltaics due to its excellent optoelectronic properties. However, GaAs solar cells have limitations in terms of cost-effectiveness and efficiency, which has prompted researchers to explore new architectures and/or the combination with other materials in terms of a relatively high efficiency and low-cost device, with the optimum utilization of the solar energy. On this point, perovskite solar cells, a relatively new class of ''solar cell material'', provides low cost, ease of fabrication and high efficiency either as a single solar cell or as a combination with other materials.

The main goal of this thesis is the development of GaAs-Perovskite tandem solar Cell, the design and optimization of the parameters that will offer the proper combination and interconnection of these two materials and will lead to high efficiency tandem solar cell. Additionally, this work includes electrical and optical characteristics analysis of the cells, optimized bandgap of the perovskite cell for efficient tandem operation, and investigating the effect of various parameters on the overall performance of the tandem cells.

GaAs Solar Cells

Growth Process

Gallium Arsenide growth requires multiple and well control steps for reproducible and high-quality results. Epitaxy of Gallium Arsenide refers to the process of depositing thin layers of gallium arsenide (GaAs) semiconductor material on a suitable substrate to fabricate GaAs solar cells. Epitaxy is a crucial step in the manufacturing of GaAs solar cells, as it determines the structural and electrical properties of the material, which directly impact the cell's efficiency and performance. The most well-known epitaxy techniques are molecular beam epitaxy (MBE) and metalorganic vapor phase epitaxy (MOVPE), also known as metalorganic chemical vapor deposition (MOCVD). The process begins with preparing a suitable

substrate, typically a single-crystal substrate like gallium arsenide itself or other materials such as germanium (Ge) or silicon (Si). The substrate should have a lattice structure and a matching crystal orientation to facilitate the growth of high-quality GaAs layers. The substrate is carefully cleaned thoroughly to remove any contaminants or oxide layers. Various cleaning techniques, such as chemical etching or thermal treatments, are employed to ensure a clean and smooth surface for epitaxial growth. In MBE or MOVPE, the GaAs layers are grown atom by atom on the prepared substrate. The process involves introducing controlled amounts of gallium (Ga) and arsenic (As) precursors into a reaction chamber, where they react and deposit onto the substrate. The growth conditions, such as temperature, pressure, and precursor flow rates, are precisely controlled to achieve the desired layer thickness and quality.

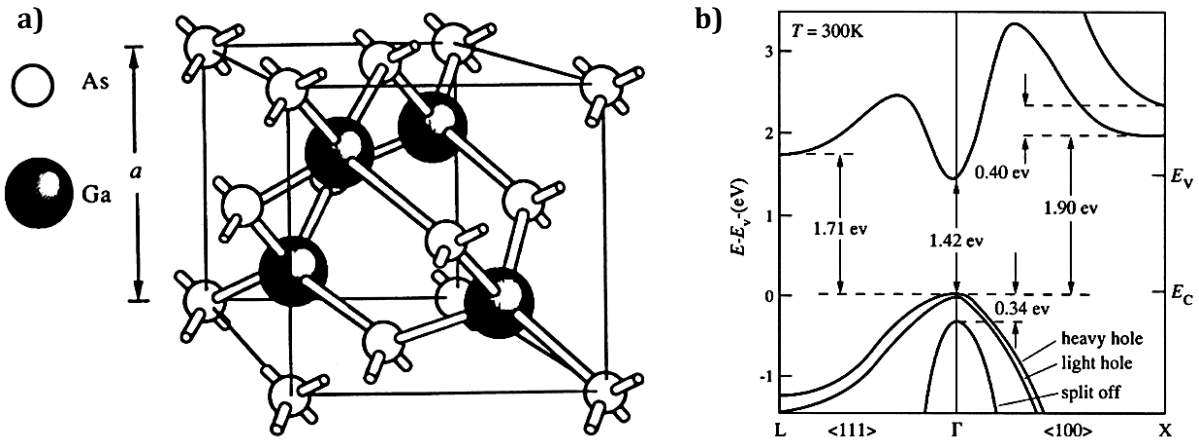

Figure 4. a) Zincblende structure of GaAs showing the relative positions of arsenic and gallium atoms and b) Conduction and valence band energies of GaAs as a function of wave vector. Pictured are the conduction and valence band edges. The values noted on the diagram are those appropriate for room temperature [15].

In terms of solar cells, multiple layers are grown for a GaAs solar cell structure. These layers include n-type and p-type doping and contain light-absorbing layers, and various other functional layers, depending on the specific design of the solar cell. After the epitaxial growth, the solar cell structure undergoes additional processing steps such as annealing, surface passivation, and metallization. These steps optimize the electrical and optical properties of the device and facilitate efficient charge extraction and collection. The epitaxy of GaAs solar cells requires excellent control at each step, for a high quality, uniformity, and with the suitable doping profiles for

the energy band alignment device. The goal is to create a high-performance solar cell with optimal light absorption and efficient carrier transport. Continuous research and development in epitaxial growth techniques are focused on enhancing the efficiency and reliability of GaAs solar cells for a wide range of applications, including space exploration, terrestrial power generation, and portable electronics.

Solar Cell Architecture

A typical architecture of a GaAs solar cell typically contains several layers, with each layer playing its specific major role. A simplified description for a GaAs solar cell growth with an n-p or an n-i-p structure start with a heavily n-doped substrate which could ensure the efficient collection of electrons to the bottom contact of the solar cell. Then, an n-type material with the suitable energy levels will be deposited as a back surface field layer. Above the substrate, there is a thin layer of n-type GaAs. This layer is doped with elements such as silicon or tellurium to introduce free electrons, creating an excess of negatively charged carriers. On top of the n-type layer, there is a thin layer of p-type GaAs. This layer is doped with elements such as zinc, beryllium or carbon to create an excess of positively charged carriers known as "holes." The interface between the n-type and p-type layers forms a region, called depletion region. This region is crucial for the solar cell as it creates an internal electric field that separates photo-generated electron-hole pairs. In a p-i-n approximation, an intrinsic layer of GaAs is deposited between n-region and p-region for a larger depletion area. On top of the p-region is deposited an extra p-type layer, called window layer, respectively to the back surface field. To improve light absorption, an anti-reflection coating is applied to the top surface of the solar cell. This coating reduces the reflection of incident light, allowing more photons to enter the cell. Electrical contacts made of metals, such as silver, gold or aluminum, are placed on the top and bottom surfaces of the solar cell. These contacts enable the extraction of electric current generated by the absorbed photons.

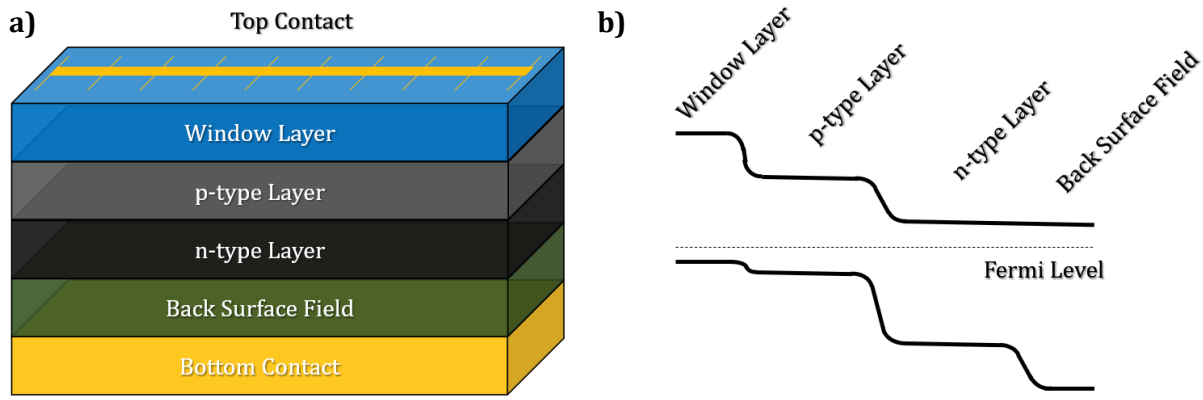

Figure 5. a) Schematical representation of a typical Solar cell Architecture and b) the energy band diagram for a p-n Solar Cell.

P-N and P-I-N Diode

A p-n junction is a boundary or interface between two regions of a semiconductor material, one doped with p-type impurities and the other with n-type impurities. This junction plays a fundamental role in the operation of various electronic devices, including diodes, transistors, and solar cells. In a p-n junction, the p-type region contains an excess of positively charged carriers, known as "holes," due to the introduction of impurities (acceptors) that have fewer valence electrons than the host material. The n-type region, on the other hand, has an excess of negatively charged carriers, typically electrons, introduced by impurities with more valence electrons (donors) than the host material. When the two regions are brought into contact to form a p-n junction, a diffusion of carriers occurs across the junction due to the concentration gradient. Holes from the p-region diffuse into the n-region, and electrons from the n-region diffuse into the p-region. This diffusion process continues until an equilibrium is reached, resulting the formation of a depletion region. The depletion region is a thin region near the p-n junction where the free carriers have diffused away, leaving behind immobile ions with opposite charges. In this region, positive and negative charges create an internal electric field that prevents further diffusion of carriers. As a result, an electric potential barrier is formed, known as the built-in potential or junction potential.

The p-i-n diode is a type of diode that incorporates an intrinsic (i) region between the p-type and n-type regions. The "p" stands for the p-type region,

"n" represents the n-type region, and "i" refers to the intrinsic region. The p-i-n diode's intrinsic region enables several important applications. It provides higher breakdown voltage capabilities compared to standard p-n junction diodes, making it suitable for high-power and high-frequency applications. The wide intrinsic region also allows for improved sensitivity in photodetection applications, such as photodiodes, where incident light generates electron-hole pairs in the intrinsic region, resulting in a measurable photocurrent. In contrast, in a p-n diode does not have a native intrinsic region and consists of two heavily doped regions with higher conductivity each one. It's worth noting that while p-i-n diodes have certain advantages over p-n diodes in specific applications, p-n diodes are still widely used in various electronic circuits for rectification, switching, and voltage regulation due to their simplicity and cost-effectiveness.

Window Layer

The window layer in GaAs solar cells is an important component that plays a crucial role in optimizing light absorption and electron extraction. It is usually made of a thin layer of a different semiconductor material with higher bandgap, such as aluminum gallium arsenide (AlGaAs) [16] or gallium indium phosphide (GaInP) [17]. The window layer is placed on top of the GaAs layer to form a heterojunction, which allows for efficient extraction of photo-generated electrons. The primary function of the window layer is to reduce surface recombination losses and improve the collection of photo-generated carriers. It serves as a selective contact, allowing photons with energies above the GaAs bandgap to pass through and reach the active region where they can be absorbed. By using a window layer with a wider bandgap than GaAs, a favorable energy level alignment can be achieved. This alignment promotes efficient charge carrier extraction, minimizing losses due to recombination and enhancing overall cell performance. Additionally, the window layer also helps in passivating the GaAs surface, reducing surface defects and improving the device's stability and reliability.

Overall, the window layer in GaAs solar cells is a critical component that contributes to the high efficiency and excellent performance of these solar cells. It enables efficient light absorption, enhances charge carrier extraction,

and minimizes surface recombination losses, ultimately leading to improved conversion of sunlight into electricity.

Back Surface Field

Back surface field (BSF) is a technique used in solar cell design to minimize recombination losses at the back surface of the cell, thereby improving the overall efficiency of the cell. The BSF layer is commonly used in silicon-based solar cells [18], as and in gallium arsenide (GaAs) solar cells [19]. The main role of this layer is to repeal the minority carriers and helps the majority carriers to pass through, to the electrodes. It's important to note that GaAs solar cells are typically heterojunction devices, consisting of a higher bandgap window layer, a GaAs absorber layer and a thin, high-quality layer of a different material, such as aluminum gallium arsenide (AlGaAs) for a proper energy alignment. This heterojunction design already helps to reduce recombination at the back surface, making the use of a dedicated BSF layer less necessary. In summary, back surface field (BSF) plays a similar role to the window layer an rely to minimize recombination at the back surface, taking advantage of the heterojunction design to achieve high efficiency.

Perovskite Solar Cells

Solar Cell Architecture

Perovskite solar cells are a type of photovoltaic device that utilize perovskite materials as the active layer to convert sunlight into electricity. A typical architecture of a perovskite solar cell includes a lot of sub-layers. The whole device is processed on a substrate with a Transparent Conducting Oxide (TCO) Layer deposited on it. The substrate, which is the bottom layer of the solar cell, provides mechanical support for the full device, usually made of glass, plastic, or a flexible material such as metal foil. The TCO layer, which allows light to pass through to reach the active layer while providing electrical conductivity for one of the two device electrodes, is typically made of a transparent conductive material like indium tin oxide (ITO) or fluorine-doped tin oxide (FTO). Two crucial layers for perovskite solar cells are the Electron Transport Layer (ETL) and Hole Transport Layer (HTL). The ETL is a thin layer that facilitates the efficient extraction of electrons from the

perovskite layer, while it also helps to block holes inside the perovskite layer, thus improving the device's performance. On the other hand, the HTL is a thin layer that facilitates the efficient extraction of holes from the perovskite layer and block the free electrons to pass through and recombine with the holes. These two layers, play a major role for the solar characteristic and the final performance of the perovskite solar cell. Between ETL and HTL is deposited the perovskite/photo-active layer. The perovskite layer is the heart of the solar cell and is responsible for absorbing photons and generating electron-hole pairs. Perovskite materials have a unique crystal structure that enables efficient light absorption and charge transport. Finally, for a complete solar cell circuit, is deposited the metal electrode. The metal electrode serves as the respectively to the TCO electrode, and collects the extracted carriers from the ETL and HTL, according to the structure design (p-i-n or n-i-p). It is important to note that perovskite solar cell architectures can vary depending on the specific device design, as there are numerous research efforts underway to optimize efficiency, stability, and scalability. Therefore, the above architecture represents a general framework for perovskite solar cells, but variations and improvements are continuously being explored by researchers in the field.

Perovskite Compounds

Perovskite materials have gained significant attention in the field of solar cells due to their remarkable photovoltaic properties. Perovskite solar cells (PSCs) offer the potential for high efficiency, low-cost, and easy fabrication, making them an attractive alternative to traditional silicon-based solar cells. Perovskite refers to a specific crystal structure that many materials can adopt. The perovskite structure has the general formula ABX_3, where A and B are cations, and X is an anion. In the case of perovskite solar cells, the most commonly used material is a hybrid organic-inorganic perovskite, where the A-site is occupied by an organic cation, such as methylammonium (MA), formamidinium (FA) and Cesium (Cs), the B-site is occupied by a metal cation, typically lead (Pb) or Tin (Sn), and X is a halide anion, like iodide (I), bromide (Br) or chloride (Cl). A typical perovskite structure is presented on figure 6, where the organic cation is between the tetrahedron, with a metal cation in the center and the halide anions on the corners of each tetrahedron. Perovskite materials have exceptional light absorption properties, allowing

them to efficiently convert a wide range of sunlight wavelengths into electrical energy.

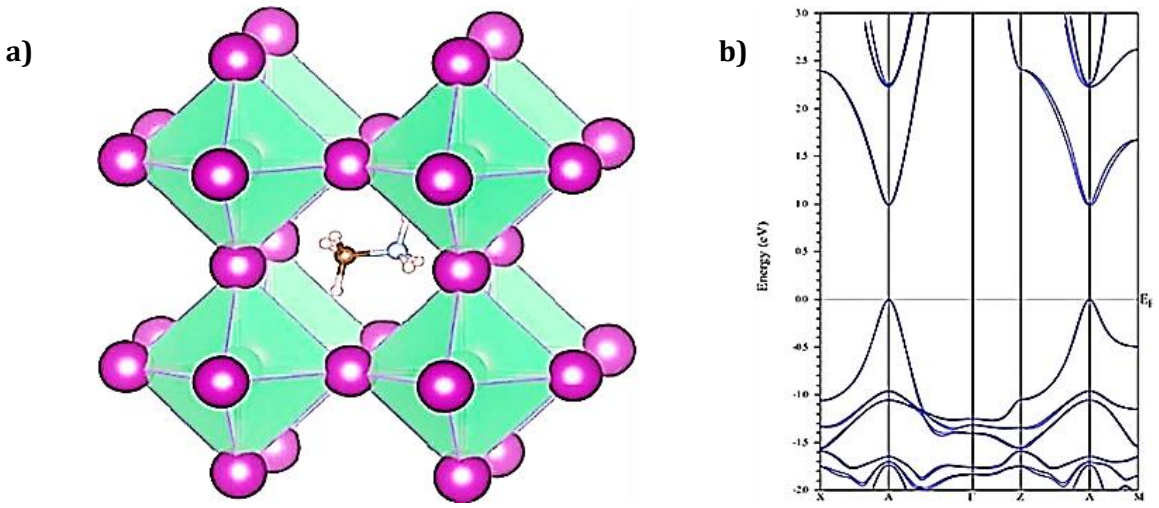

Figure 6. a) $MAPbI_3$ perovskite structure [20] and b) Energy band structure of $MAPbI_3$ as a function of wave vector [21].

The high absorption coefficient and the tunable bandgap, enabling them to absorb a large portion of the solar spectrum. Despite their promising performance, perovskite solar cells face several challenges. One major concern is their stability, as perovskite materials can degrade in the presence of moisture, heat, and light. Researchers are actively working on developing more stable perovskite formulations and encapsulation techniques to enhance their durability. Additionally, the toxicity of lead in some perovskite formulations is a subject of concern, and efforts are being made to develop lead-free perovskite materials. From the other side, perovskite solar cells hold great potential for the future of solar energy. They offer the advantages of low-cost production, easy fabrication on flexible substrates, and high efficiency. Continued research and development are focused on addressing stability and toxicity concerns, improving scalability, and exploring tandem architectures with other solar cell technologies to achieve even higher efficiencies.

Electron Transport Layers

Electron transport layers (ETLs) play a crucial role in perovskite solar cells by facilitating the extraction and transport of electrons from the perovskite layer to the electrode, as well as by minimizing electron-hole recombination.

For the efficient process of an ETL, it is important that the energy level of the Lowest Unoccupied Molecular Orbit (LUMO) and the Highest Occupied Molecular Orbit (HOMO) of the ETL to be lower than the LUMO and HOMO of the perovskite layer, in order to have efficient extraction of free electrons and efficient repulsion of free holes respectively. It is also important to be a transparent material in order to avoid parasitic losses of the incident photons. The most common materials that fulfill these criteria are TiO_2, SnO_2, ZnO and some organic molecules as PCBM.

Hole Transport Layers

HTLs, respectively to ETLs, are responsible for the efficient extraction of free holes and the repulsion of free electrons. Contrary to the ETLs, for the efficient process of an HTL, it is important the energy level of the LUMO and the HOMO layer to be higher than the LUMO and HOMO of the perovskite for the efficient extraction of holes and minimization of recombination effects. High transparency is also required. Well known materials for HTLs are organic small molecules as SPIRO-OMeTAD and P3HT, conducting molecules as PEDOT: PSS and PTAA, transition metals as NiO and MoOx and inorganic materials as CuSCN and CuI.

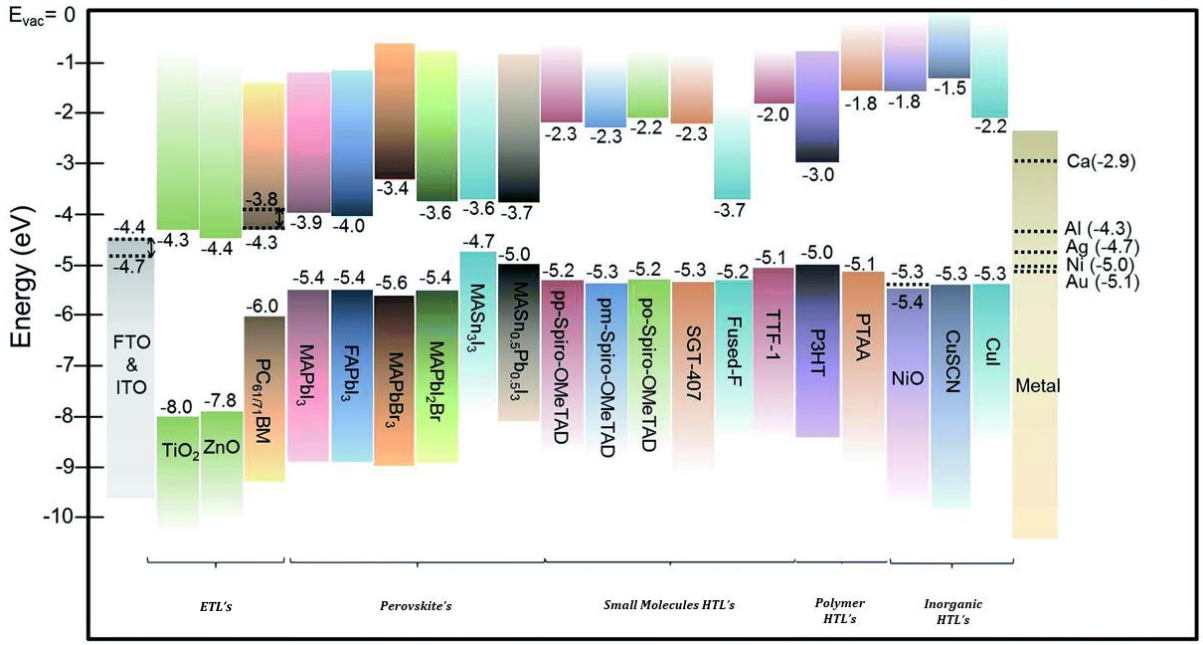

Figure 7. A summarized energy level diagram of representative organometal perovskites and charge-extraction interlayers. The dotted lines represent the work function of the materials [22].

Transparent Conductive Oxides

Transparent conductive oxides (TCOs) are a class of materials that possess both transparency and electrical conductivity. These materials are widely used in various applications where transparent conductors are required, such as touchscreens, solar cells, light-emitting diodes (LEDs), and smart windows. The primary characteristic of TCOs is their ability to allow light to pass through, while simultaneously conducting current. This combination of properties is crucial for applications that require the transmission of light, while maintaining electrical functionality. TCOs typically exhibit high optical transparency in the visible spectrum and low sheet resistance for efficient electrical conduction. The most commonly used TCOs are indium tin oxide (ITO), which consists of a transparent matrix of indium oxide (In_2O_3) with tin oxide (SnO_2) dopants, and Fluorine-doped Tin Oxide (FTO) which is a TCO that consists of tin oxide (SnO_2) doped with fluorine (F) atoms. The fluorine doping enhances the electrical conductivity of tin oxide, making it suitable for applications requiring transparent electrical contacts. FTO and ITO offer relatively high electrical conductivity and good transparency in the visible spectrum. They are commonly employed in photovoltaics, such as thin-film solar cells, as a transparent electrode. Alternative to ITO and FTO, a TCO with promising characteristics is Aluminum-doped Zinc Oxide (AZO), which offers good conductivity and transparency and has shown potential as a replacement for ITO [23]. Some other types of TCO are the transparent conducting polymers (TCPs) [24] which offer flexibility, lightweight properties, and compatibility with low-temperature processing techniques, Copper-based TCOs which have demonstrated good transparency and electrical conductivity, with copper to be more abundant and cost-effective than indium while some other oxide materials such as gallium-doped zinc oxide (GZO) [23] are being investigated as TCOs with main focus of the desired balance between transparency and conductivity. Research in the field of TCOs aims to develop materials that are not only highly transparent and conductive but also cost-effective, environmentally friendly, and suitable for flexible and large-scale applications.

Metal Electrode

The metal contacts on solar cells play a crucial role in extracting electrical current from the photovoltaic device. Some typical specifications and considerations regarding metal contacts on solar cells are that the metal contacts must form a low-resistance ohmic contact with the semiconductor material of the solar cell, typically silicon. This ensures efficient charge carrier extraction without significant energy losses. Various techniques are used to deposit and pattern the metal contacts onto the solar cell surface. These include screen printing, sputtering, thermal evaporation, laser ablation, and inkjet printing. The choice of technique depends on factors such as cost, scalability, and the specific requirements of the solar cell technology. For perovskite solar cells, in terms of research and development, the most common techniques are sputtering and thermal evaporation. The metal contacts are typically made of highly conductive materials, such as gold (Au), silver (Ag), aluminum (Al), or copper (Cu). It's important to note that the specifications and considerations mentioned above can vary depending on the specific type of solar cell technology, such as crystalline silicon, thin-film, or emerging third-generation solar cells. Each technology may have unique requirements and optimizations for the metal contacts.

Tandem Solar Cells

Design and architecture of Tandem solar cells

Tandem solar cells, also known as multi-junction solar cells, are a type of photovoltaic devices that combine multiple solar cells with different bandgaps to achieve higher energy conversion efficiency compared to single-junction solar cells. The design and architecture of tandem solar cells are optimized to enhance the absorption of sunlight and improve overall energy conversion efficiency. Two basic and well-known architectures of tandem solar cells are the 4 terminal/mechanically stacked and the 2 terminal/monolithic tandem solar cells.

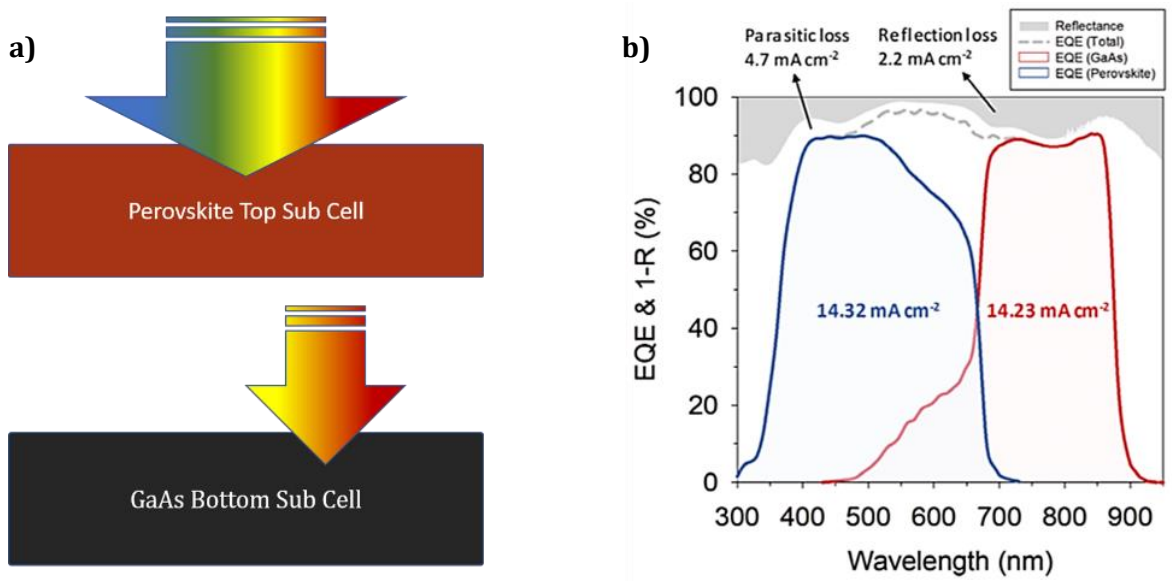

Figure 8. a) Schematical representation of a Perovskite/GaAs Solar Cell and b) External quantum efficiency (EQE) and total absorbance (1-R) of the 2T tandem cell [14].

2-Terminal Monolithic Tandem Solar Cells

Two-terminal tandem solar cells, also known as monolithic tandem solar cells or multi-junction solar cells, are a type of photovoltaic devices that consist of multiple individual sub-cells stacked on top of each other. Unlike traditional single-junction solar cells, which can absorb solar light with a single energy gap, increasing the energy losses for more of the energetic photons, tandem solar cells can harvest efficiently a broader range of wavelengths, resulting in higher overall efficiency.

In a two-terminal tandem solar cell, the individual sub cells are connected electrically in series, allowing the current to flow through them sequentially. Each sub cell is designed to absorb a specific portion of the solar spectrum efficiently. Typically, each sub cell is made of a different semiconductor material with a bandgap that matches the energy range of the targeted wavelengths. The top sub cell in a tandem solar cell is designed to absorb the high-energy photons (shorter wavelengths), while the bottom sub cell absorbs the low-energy photons (longer wavelengths) (figure 8a). This arrangement allows the tandem solar cell to absorb more efficiently the solar spectrum and convert more sunlight into electricity. To connect the sub cells in series, transparent conducting layers or tunnel junctions are used between them. These layers enable the efficient transfer of charge carriers

(electrons and holes) from one sub cell to the next, minimizing losses in the overall energy conversion process.

The advantage of two-terminal tandem solar cells is their higher efficiency compared to single-junction solar cells. By combining multiple sub cells with different bandgaps, tandem solar cells can achieve power conversion efficiencies greater than those of individual sub-cells or single-junction solar cells. This increased efficiency makes tandem solar cells particularly suitable for applications where high-power output is desired, such as space exploration, concentrator photovoltaics, and other specialized applications.

4-Terminal Mechanical Stacked Tandem Solar Cells

The 4-terminal configuration refers to separate electrical contacts for each of the two sub-cells. It enables the independent control and optimization of each sub-cell's current and voltage output. The sub-cells are connected independently and the final output power arises from the summation of each sub-cell power conversion. The design of four-terminal solar cells is complex and requires precise engineering of the sub-cells' bandgaps and material properties to ensure optimal performance. By using different materials with varying bandgaps, each subcell can absorb a specific portion of the solar spectrum more efficiently. This approach helps to overcome the limitations of single-junction solar cells, which are primarily limited by the bandgap of the absorbing material. Four-terminal solar cells have the potential to achieve higher conversion efficiencies compared to single-junction solar cells. The additional sub-cells allow for a higher utilization of the solar spectrum, especially in the case of concentrated sunlight or in environments with varying lighting conditions. These cells are often used in advanced photovoltaic applications, such as space satellites, high-efficiency solar panels, and concentrator photovoltaics systems. It's worth noting that four-terminal solar cells are still an active area of research and development, and their commercialization and widespread adoption are yet to be fully realized. However, their potential to significantly improve solar cell efficiency makes them an exciting prospect for the future of solar energy technology.

Comparing to the two basic architectures of tandem solar cells, in a two-terminal tandem solar cell, the individual sub-cells are connected in series,

which means that current flows through all the sub-cells in the same path. Additionally, the voltage output of a two-terminal tandem solar cell is the sum of the voltages generated by each sub cell. However, if there is a significant difference in the current produced by the sub cells, it can lead to current losses across the sub cell with the lower current output. From the other side, in a 4-terminal tandem solar cell, each sub cell has its own set of front and back contacts, and the sub cells are electrically independent from each other. This configuration allows independent control of each sub cell and eliminates the current-matching constraint. This means that each sub cell can provide its maximum characteristics without being affected by the other sub cells, resulting in higher power conversion comparing to the 2-terminal solar cell. In terms of manufacturing cost and complexity, a two-terminal tandem solar cell is relatively simpler compared to the four-terminal configuration since it requires fewer electrical contacts and interconnections. From the other side, the manufacturing process for 4-terminal tandem solar cell is more complex due to the additional contacts and interconnections required for each sub cell. Also care has to be taken for antireflective (AR) coatings of interfaces to minimize optical losses by internal reflections. This complexity can increase the manufacturing cost.

In summary, a four-terminal tandem solar cell offers advantages in terms of independent control of each sub cell, higher overall efficiency, however, it comes with increased complexity and manufacturing cost compared to a two-terminal tandem solar cell. The choice between the two depends on specific requirements, cost considerations, and technological capabilities.

Chapter 3

Characterization Techniques

X-Ray Photoelectron Spectroscopy

X-ray photoelectron spectroscopy (XPS) is a technique that provides information about the composition and chemical bonds of the surface of a solid material. The basic mechanism of this technique, is the generation of X-Rays by a monochromatic X-Ray source which collide on the material surface. As a result, core-electrons of the surface atoms are ejected. These electrons, which are also called photoelectrons, carry information about the chemical bonding, the oxidation level of the atom, the environment of the atoms they came from, the energy and electronic structure of the surface.

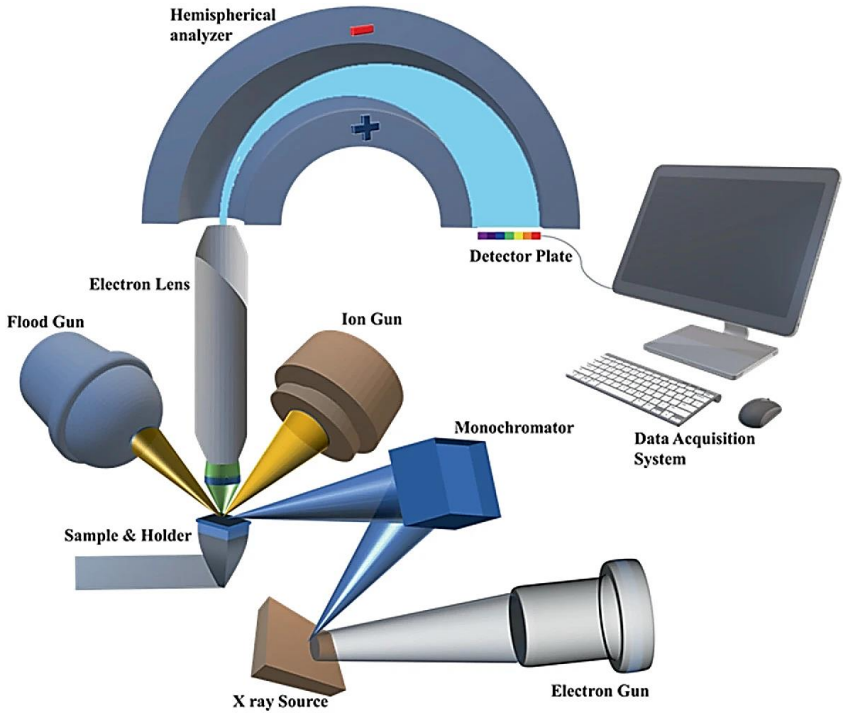

Figure 9. Animation of the instrumentational operation of XPS [25].

The photoelectrons are collected and analyzed by a hemispherical energy analyzer which measures the kinetic energy of the photoelectrons and generates a spectrum that represents the number of electrons at each energy level. The binding energy of the photoelectrons is determined by comparing their kinetic energy with that of electrons in reference materials. XPS is commonly used in various fields, including materials science, surface

chemistry, catalysis, semiconductor research, and nanotechnology. It is important to note that XPS is a surface-sensitive technique, typically probing depths of a few nanometers. Therefore, it provides information primarily about the surface of a material rather than its bulk composition. Sample preparation and handling are crucial to ensure representative and reliable results in XPS measurements [26], [27].

X-Ray Diffraction

X-ray diffraction (XRD) is a technique used to characterize the crystallinity of the materials. It is a commonly used technique in various scientific fields, including solid-state physics, materials science, chemistry, geology, and biology, to determine the crystal structure of a wide range of materials. It can provide valuable information about the atomic space, crystal symmetry, and the presence of impurities or defects in a crystal lattice. XRD is based on the principle that when X-rays pass through a crystalline material, they interact with the atoms in the crystal lattice and are diffracted in specific directions. The Bragg-law can describe the correlation between the source wavelength (λ), the distance between the atomic planes (d) and the specific angle that we expect the signal peak of each material. The basic components of an XRD system include an X-ray source, a sample holder, a detector, and a data analysis software. The X-ray source emits a beam of X-rays that is directed at the sample. The X-rays interact with the sample and produce a diffraction pattern, which is collected by the detector. The detector measures the intensity of the diffracted X-rays as a function of the angle of incidence. The data obtained from the detector is then analyzed to determine the crystal structure of the sample. XRD can be used to identify unknown materials by comparing their diffraction patterns with known patterns in databases. It can also be used to study phase transformations, crystal defects, and the effects of temperature or pressure on the crystal structure of materials.

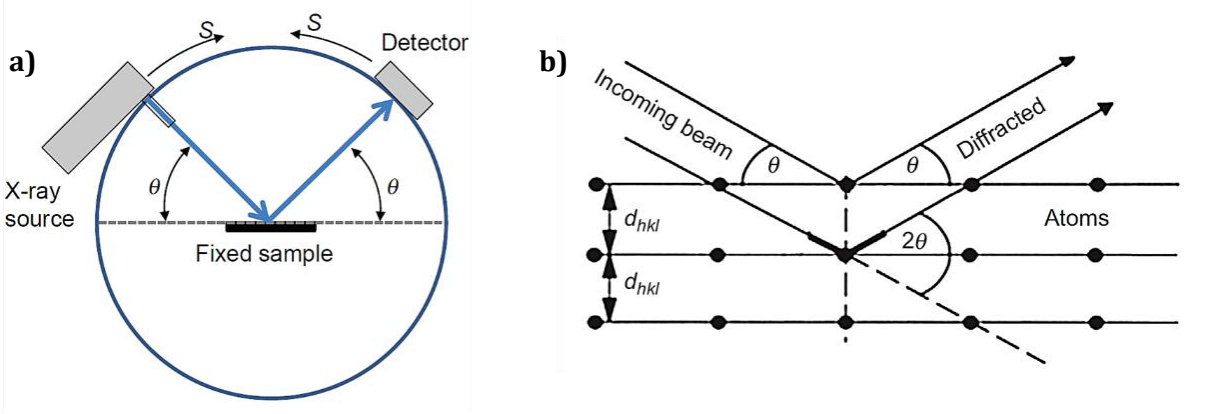

Figure 10. Schematical representation of a) an XRD set-up for a θ-2θ measurement and b) the interaction of the X-rays with the crystalline material and the diffractive spectrum which is collected from the detector [28].

Overall, X-ray diffraction is a powerful tool for studying the atomic and molecular structure of crystalline materials, providing valuable insights into their physical and chemical properties.

UV-Vis Spectroscopy

UV-visible measurement refers to the spectroscopic technique used to analyze the absorption, reflection or transmission of ultraviolet (UV) and visible light by a sample. It is commonly employed in various scientific fields, including chemistry, biology, physics, and materials science, to investigate the interaction of a material (film, powder or solution) with big parts of the solar spectrum. In UV-visible spectroscopy, a spectrophotometer is used to measure the intensity of light passing after the interaction with the sample as a function of wavelength. The instrument consists of a light source, a monochromator to isolate specific wavelengths, a sample holder, and a detector to measure the light intensity. By measuring the absorption, reflectance or transmission of light through a sample at different wavelengths, information about the sample's chemical composition, concentration, energy gap and structure can be obtained. UV-visible spectroscopy has numerous applications. In a general approximation, it provides useful information of the materials such as determining the concentration of a compound in a solution through Beer's law, the electronic transitions and energy levels of molecules, it is utilized to analyze biomolecules like proteins and nucleic acids [29], providing insights into

their structure, conformational changes, and interactions of the materials [30].

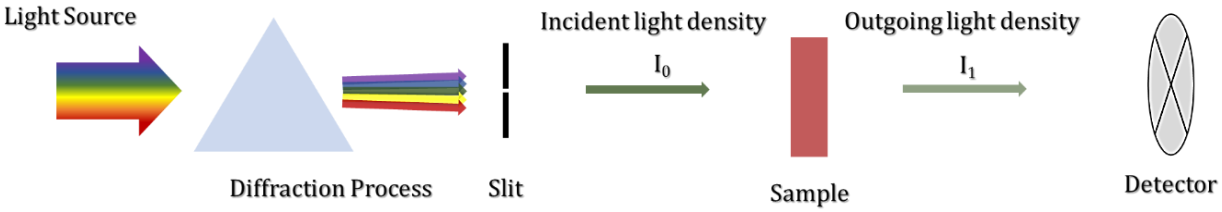

Figure 11. Ultraviolet-Visible measurement, a schematic representation.

UV-visible measurement is a versatile technique that allows scientists to explore the electronic properties of substances and obtain valuable information about their chemical composition, concentration, and structure.

Photoluminescence Spectroscopy

Photoluminescence spectroscopy is a powerful technique to study the optical properties of materials and molecules. The main process of this measurement is based on the absorption of the incident light and the excitation of electrons to higher energy levels. It involves the emission of light by a sample after it has absorbed photons of a higher energy. The excited electrons, relax down to the lowest excited states and they emit photons with energy equal to the energy difference of the lowest excited and ground state. The emitted light is called photoluminescence, and its properties can provide valuable information about the sample's structure, composition, and electronic properties.

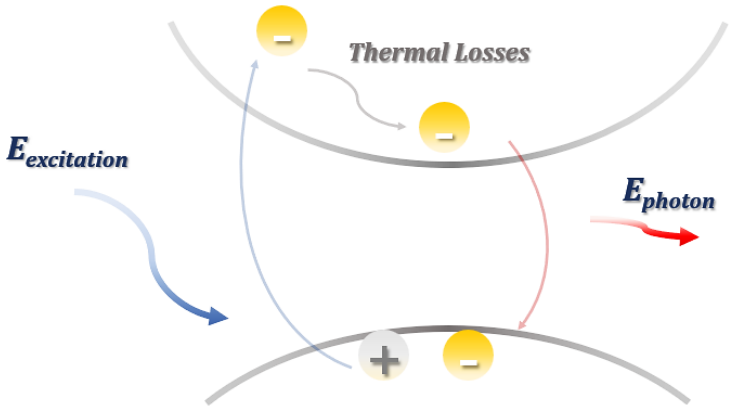

Figure 12. Representation of excitation and emission process of an electron via photoluminescence measurement.

There are different variations of this technique. Some commonly used techniques are the photoluminescence excitation (PLE) where is measured the excitation spectrum by monitoring the intensity of emitted light while varying the excitation energy, photoluminescence emission (PL) which measures the emission spectrum, which provides information about the energy levels involved in the relaxation process and time-resolved photoluminescence (TRPL) which measures the decay of the photoluminescence signal over time. Each technique can provide different information such as details about the band structure, defects, impurities, or other properties of the material (PL) and information about the lifetime of the excited states, carrier dynamics, and other time-dependent phenomena (TRPL) or it helps identify the absorption bands that contribute to the observed photoluminescence (PLE).

Scanning Electron Microscopy

Scanning Electron Microscopy (SEM) is a powerful technique, used to zoom in the materials at high resolution. It provides detailed images and information about the surface morphology and the thickness of the samples. The SEM works by using a focused electron beam that scans across the surface of the sample. It has an electron source, typically a heated tungsten filament (SEM) or a field emission gun (FE-SEM), which emits a beam of high-energy electrons. The emitted electrons are accelerated through an electric field and focused using a set of electromagnetic lens~~es~~. These lenses help to form a narrow, converging electron beam which scan across the sample in a systematic pattern. This interaction generates various signals which are collected from different detectors. The most common signal, detected in SEM, secondary electrons (SE) which are low-energy electrons that are generated when the

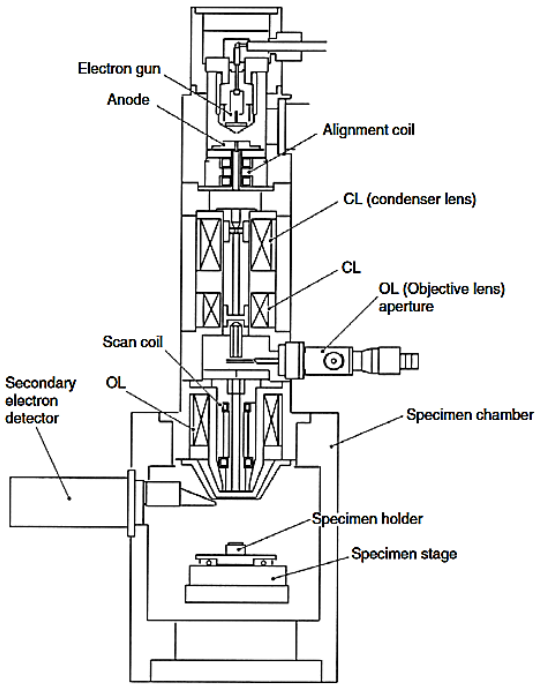

Figure 13. Schematic representation of a scanning electron microscope (JSM—5410, courtesy of JEOL USA) [31].

primary electron beam strikes the sample surface and carries information about the surface topography, providing high-resolution micrographs. Another type of generated signal is the backscattered electrons (BSE) which have higher energy compared to SEs and are generated when the primary electron beam interacts with the atomic nuclei of the sample's atoms. BSE signal–is used to obtain image contrast which is due to compositional differences. An important step for high resolution/noise free images is the sample preparation. If the sample is not conductive, it must be coated with a thin layer of a conductive material like gold or carbon. This coating prevents the accumulation of electric charge on the sample surface and improves the quality of the resulting images. Additionally, SEM can be equipped by Energy-Dispersive X-ray Spectroscopy (EDS) detectors which collect and analyze the X-rays produced also from the interaction between the electron beam and the sample, used for qualitative and quantitative elemental composition analysis. SEM is widely used in various fields, including materials science, biology, geology, nanotechnology, and provides valuable insights into the structure and properties of materials [31].

Hall Measurement

The Hall effect is a phenomenon observed in conductive materials when a current flows through them in the presence of a magnetic field perpendicular to the current direction. It was discovered by Edwin Hall in 1879 [32]. When a current is passed through a material in the presence of a magnetic field, a voltage perpendicular to both the current and the magnetic field is induced. This voltage is known as the Hall voltage (V_H) and depends on the magnetic field strength (B), the current (I), and a material-specific parameter known as the Hall coefficient (R_H).

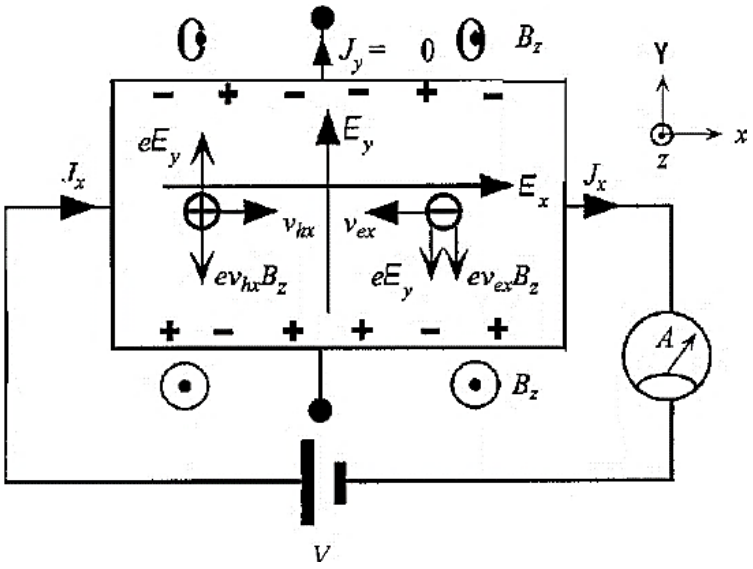

Figure 14. Hall effect for ambipolar conduction as in a semiconductor where there are both electrons and holes which are deflected from the magnetic field toward the bottom surface of the conductor and consequently the Hall voltage depends on the relative mobilities and concentrations [33].

The Hall coefficient (R_H) is a material-specific property that depends on the type of charge carriers (p-type or n-type) and their concentration in the material. By measuring the Hall voltage for a specific magnetic field strength and current, it is possible to determine the Hall coefficient, which provides valuable information about the charge carriers in the material.

External Quantum Efficiency

External Quantum Efficiency (EQE) is a measurement that extracts the ratio of the number of charge carriers (electrons or holes) generated and collected from the electrodes, compare to the number of incident photons. Is a well-known measurement for optoelectronic devices such as solar cells, photodetectors, and light-emitting diodes (LEDs). Experimentally, for the EQE measurement you need a monochromator and a white light-source, a chopper for lock-in detection, a power meter and an electrometer.

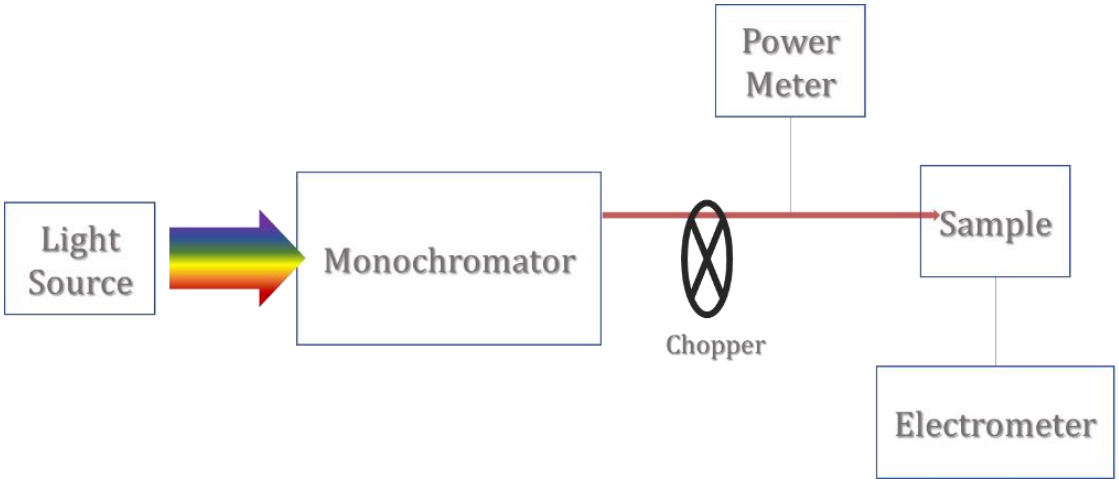

Figure 15. Animation of EQE experimental set-up.

The EQE can then be determined by comparing the extracted photocurrent with the incident optical power. EQE is a very important parameter which pronounces the efficient performance and the responsivity of the device on a wide range of solar spectrum. It provides insight information about the efficiency and overall effectiveness in converting light into electricity or vice versa [34].

Dark I-V

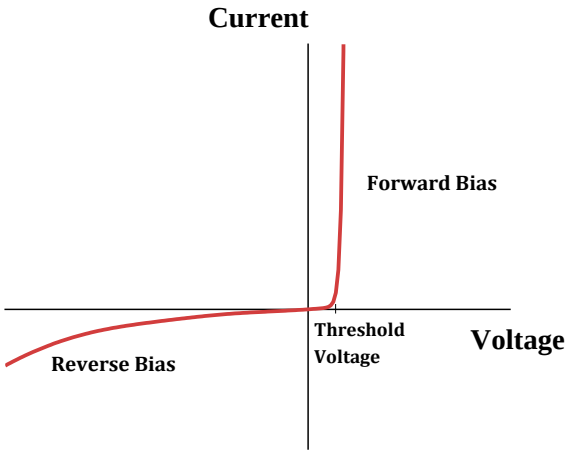

Figure 16. Dark IV of a pn GaAs Solar Cell.

Dark I-V measurement, is a measurement performed by applying a voltage bias across the device and measuring the resulting current. This technique used to characterize the electrical behavior of a semiconductor, a diode or device in the absence of external light illumination. This current is a combination of drift and diffusion currents, and is affected mainly from traps in the bulk material or on the interfaces, and from the resistivity of each material. With that measurement you can determine a lot of parameters such as the leakage current, threshold voltage, breakdown voltage, and the overall quality of the device. There is also a well-known model, the diode model (figure 17) where all the losses are described with a shunt and a series resistance and affect the performance of the device. From this model, except of the resistance values, you can extract also the ideality

factor, which pronounce different recombination losses according to the material that is measured.

Photo I-V

A photo I-V measurement, also known as illuminated I-V measurement, is a process pretty similar with the dark I-V measurement, but it takes place under illumination. It is a specific type of current-voltage (I-V) measurement for solar cells and you can extract important characteristics such as open circuit voltage (V_{oc}), short circuit current (J_{sc}), fill factor (FF) and overall, the power conversion efficiency (PCE) which is the final figure of merit for a good solar cell. The diode model can describe very well a solar cell and from the extracted resistance values we can predict the quality of the photovoltaic parameters described above. More specifically, the R_{sh} describe a parallel path where we can have carrier losses due to defects, while R_s represents the total resistance of the device through the electrodes.

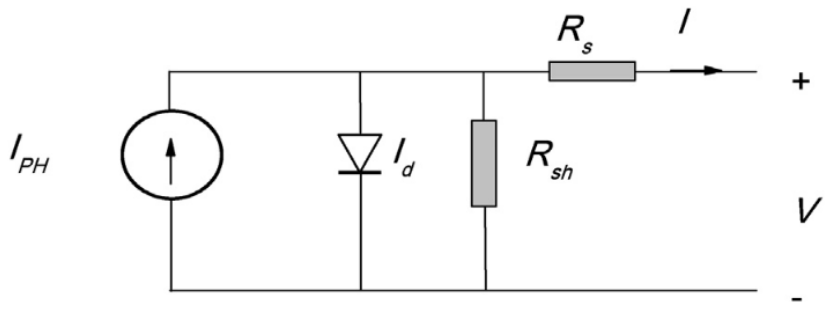

Figure 17. A schematic of a solar cell described as a single diode [35].

For the illumination conditions regarding, to the solar spectrum, two basic irradiation conditions are well known for this type measurements, Air Mass 1 (AM1) and Air Mass 1.5 (AM15). AM1 represents the solar spectrum at sea level when the sun is directly overhead (zenith angle of 0 degrees), and the light passes through a vertical path of the Earth's atmosphere (ideal conditions) while AM1.5 represents the solar spectrum when the sun is at a 41.81-degree angle above the horizon, which corresponds to sunlight passing through approximately 1.5 times the thickness of the Earth's atmosphere. AM1.5 is more usual irradiation condition as is takes account the atmosphere effect [36].

Chapter 4

Gallium Arsenide Solar Cells

Introduction

Gallium Arsenide is a well-studied material due to its excellent optoelectronic properties. One of the applications that GaAs excels in terms of efficiency is the solar cell. GaAs is a III-V material with an ideal direct energy band gap at 1.42eV (at room temperature) for the solar spectrum utilization and thus, for solar cell applications [37]. It has also high absorption coefficient and high electron mobility [38], specifications that make this material promising for ultra-thin solar cells and very competitive in terms of high-end products in Solar Cells industry. A lot of works based on GaAs solar cells have been published with a lot of recorded efficiencies with a range of 22.2% (1977) to 29.1% (2018) according to NREL Best-Research Efficiencies Chart (figure 18) while Si recorded efficiencies in the same period from 13.9% (1977) to 26.8% (2022).

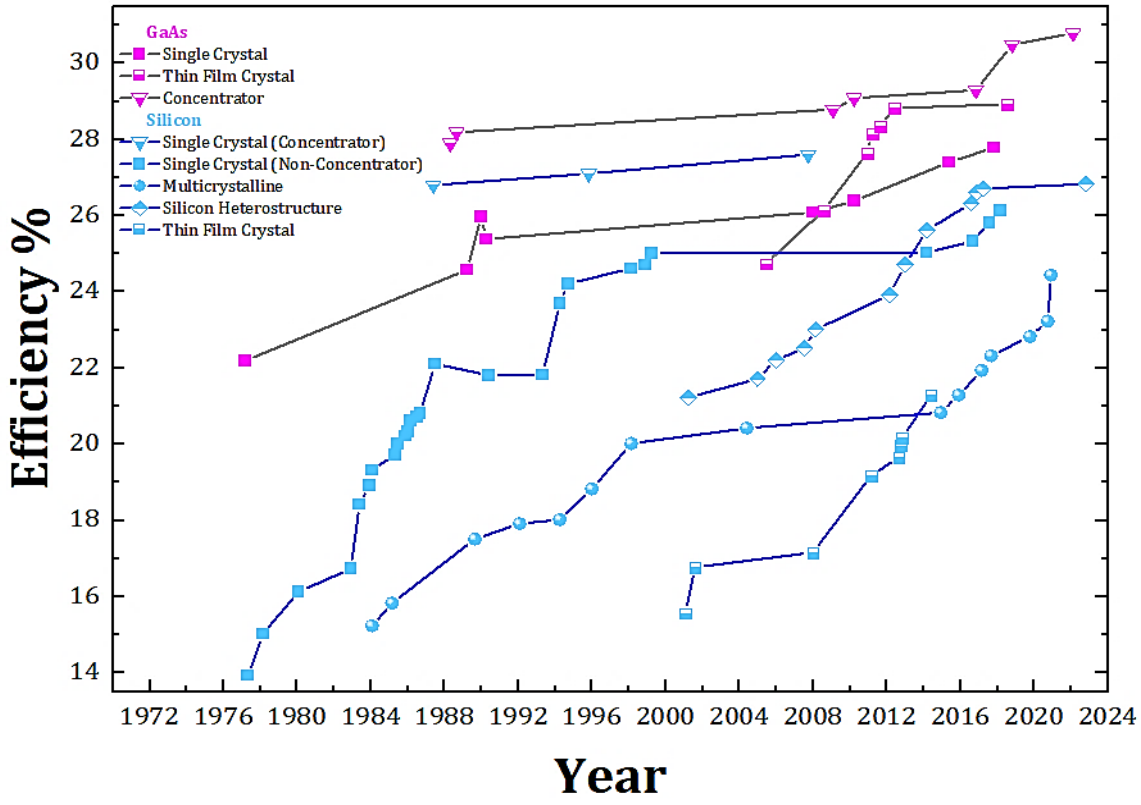

Figure 18. Results exported from interactive Best Research-Cell Efficiency Chart from the National Renewable Energy Laboratory (NREL) focusing on single-junction GaAs-based (magenta points) compared to Si-based (cyan points) solar cells [3].

On the rationale of material-cost reduction and increased efficiency devices, scientists improved techniques and added extra steps on solar cell fabrication. One of the very first steps of improved efficiency was the increased power density via light concentrators. For the history, the first recorded efficiency for GaAs with concentrated light was in 1988 with 205-suns incident power and an efficiency of 27.9% while the first corresponding results on Si were one year earlier, in 1987 with 140-suns and an efficiency of 26.8%. The highest values so far according to the NREL chart, are 30.8% with 61-suns (2022) and 27.6% with 93-suns (2007) for Gallium Arsenide and Silicon respectively. Another trick for increased efficiency is the reduction of reflectance for the incident photons on the solar cell surface. That was obtained with the deposition of an extra layer known as antireflection layer. The first tests of antireflection layer began in 1964, while now days more than 70% of solar cells in the market have adjust this technology [39], [40]. Along the same line, scientists focused on the deposition of back mirror-like layer deposition enhancing the photon-recycling [41], [42] . On the issue of minimization of material used, many structures were designed and characterized with simulator machines dedicated on Solar Cells so that experimental realization of a solar cell is better targeted and thus avoiding unnecessary material losses. One of these well-known simulator machines is Silvaco ATLAS and many works were published based on these simulations [43], [44], [45].

GaAs: Designs and Growth Techniques

As we previously mentioned, a conventional GaAs solar cell contains a combination of layers that targets to the maximum absorption of the incident photons and the generation of free carriers, and subsequently the efficient separation and collection of the free carriers of the electrodes. This presupposes the availability of the materials with the best possible energy level alignment, as well as proper growth techniques for the minimization of defects and thus recombination centers that generate parasitic losses during the photovoltaic process. Two well-known growth techniques are the molecular beam epitaxy (MBE) and the metalorganic chemical-vapor deposition (MOCVD)[46] . Both techniques are well studied and can produce

high efficiency top-quality solar cells. Molecular Beam Epitaxy (MBE) is a technique where films are grown layer by layer with precise control and the process take place under ultra-high vacuum conditions in order to minimize any defects. The deposition process occurs via controlled flux of molecular or elemental beams arriving on the heated substrate surface where they directly incorporate and form high quality crystalline layers [47]. On the other hand, metalorganic chemical-vapor deposition (MOCVD) is a technique which uses metalorganic precursors (metal-containing compounds in gaseous form) and other reactive gases in the growth process. The deposition takes place in a chamber with restrictions of the high-vacuum. The reactive gases are introduced into a heated reactor chamber, and the formation of high-quality films happens with the decomposition of the gases and the incorporation of the desired atoms on the substrate [48].

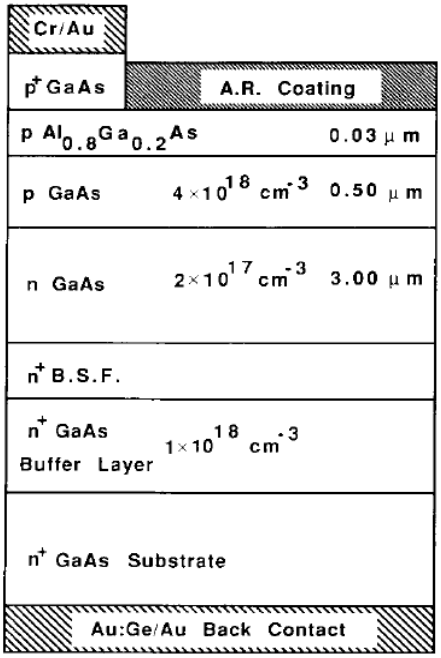

Figure 19. p-n GaAs structure with the nominal values [49].

A work published in 1990 from P. Tobin et al. and compares the effect of these two growth techniques on the final performance of the solar cell [49]. The work focused on GaAs solar cells with two identical structures shown in figure 19, grown via MOCVD and MBE. Both techniques produced high quality solar cells with the efficiency of the MOCVD-grown solar cell reaching 24.8% while the MBE-grown solar cell 23.8%. They mentioned that they observed growth defects with a density to 500-1000 cm^{-2} for MBE-grown devices while they did not observe defects for the MOCVD grown devices. Despite that, the experimental values (thickness and doping) were in good agreement with the nominal values and the uniformity of the efficiency across the cells was excellent for both techniques. It is worth mentioning that in this work, they replaced the conventional thick film of AlGaAs for back surface field with a GaAs-AlGaAs superlattice, as it exhibits better electrical characteristics as reported elsewhere [50], [51].

This structure, received the interest of the researchers, while Melloch et al. re-fabricated via MBE a very similar structure with a $8cm^2$ active area,

focusing on the large area production with an efficiency of 21.7% [52]. Almost 10 years later, this structure design was fabricated again with an extra i-region between the n and p regions and was characterized in terms of electrical performance and carrier transport mechanisms [53]. Here, we present structures based on the same line of thought, designed by Dr. E. Aperathitis, and grown via MBE by Dr. Z. Hatzopoulos, that we subsequently characterized with dark and photo-IV measurements.

Gallium Arsenide Solar Cells Grown via MBE

For our Gallium Arsenide based structures a VG80 III-V MBE system was used. The chamber was loaded with the proper material-sources (K-cells), such as Aluminum, Gallium, Arsenide for the GaAs and AlGaAs alloys, while the doping materials were Beryllium and Silicon for p-type and n-type doping, respectively. As substrate was used a n-type 2 inches GaAs 100 substrate.

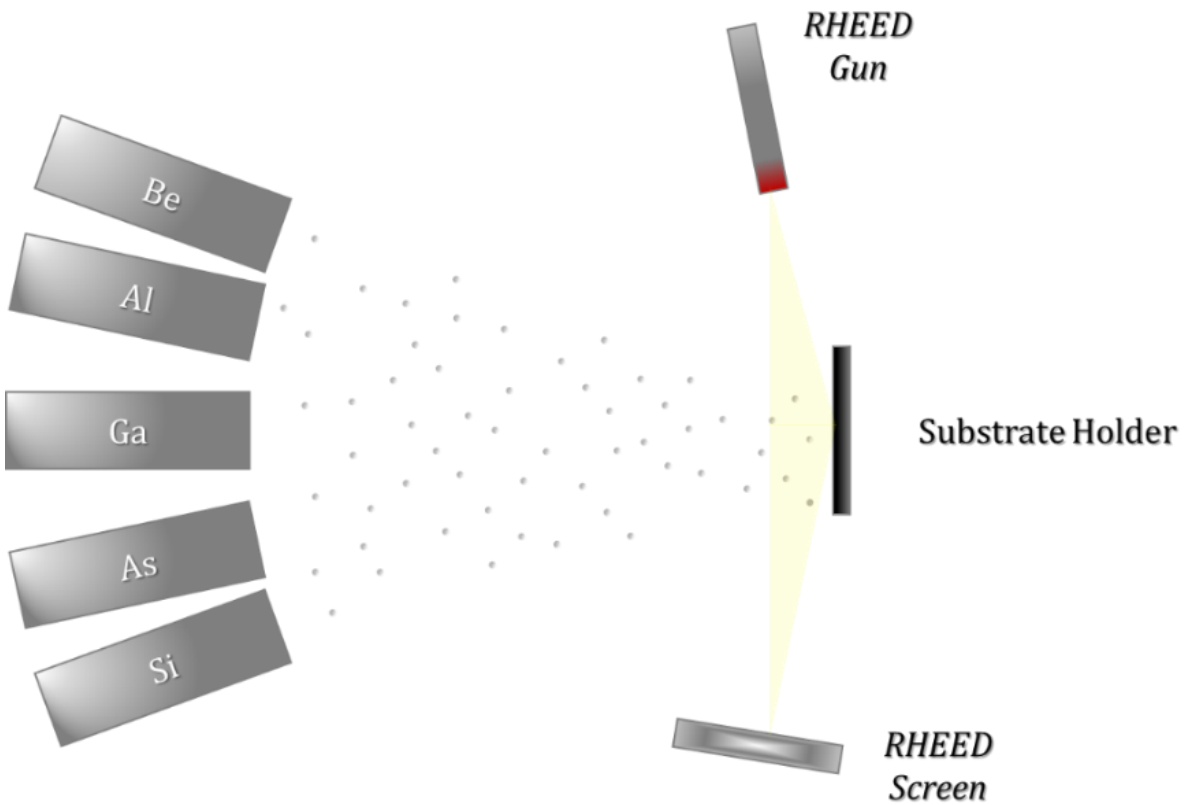

Figure 20. Simple representation of MBE process.

After the growth process, a uniform over 2 inches, heterostructure with suitable band alignment for light harvesting and generation of current was

produced. For this work, 4 similar structures were grown, with the main differences being on the thickness of the i-region and of the top cap-layer.

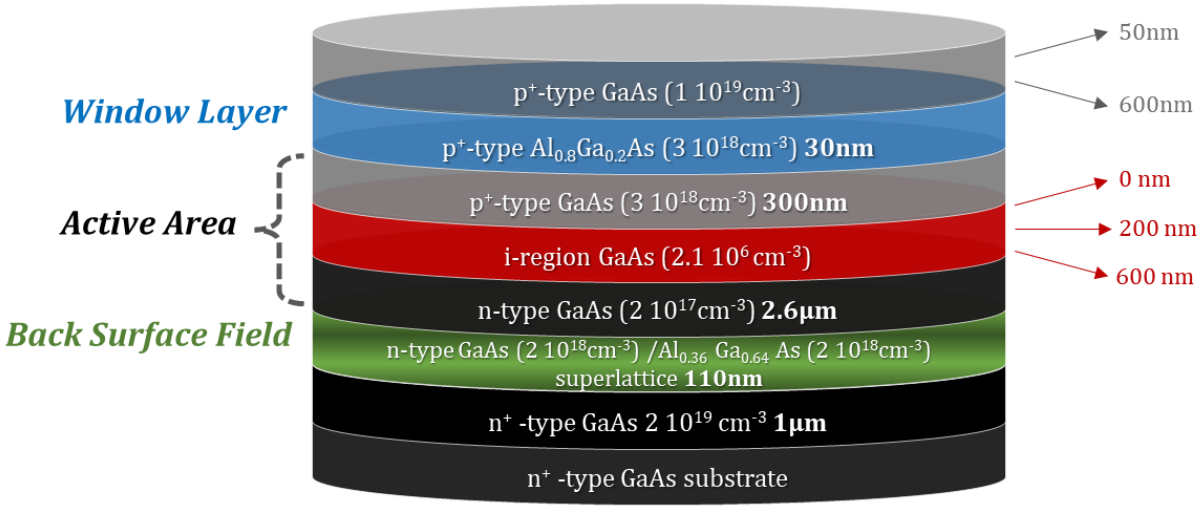

Figure 21. Schematic of the typical GaAs solar cell structure used in this thesis.

As represented in figure 21, the whole device is grown on a n-type (100) GaAs substrate, where an n-type GaAs layer with 1µm thickness deposited as buffer layer, with a donor's concentration of about $2{\cdot}10^{19}$ cm^{-3}. Then, follows the deposition of a n-type GaAs/$Al_{0.36}Ga_{0.64}As$ 20-period superlattice, with thicknesses 2.7nm and 2.8nm respectively, and total thickness of 110nm. The donor concentration was $2{\cdot}10^{18}$ cm^{-3} in both GaAs-AlGaAs. This superlattice plays the role of back surface field (BSF) as described elsewhere [50], [51]. On top of the BSF is deposited the n-region of the active area with a donor concentration of $2{\cdot}10^{17}cm^{-3}$ and a thickness of 2.6µm. In order to examine the effect of the i-region, two samples were fabricated with no i-region, while a sample was fabricated with a 200nm i-region and another with 500nm i-region. The p-region of the active area is 300nm-thick GaAs with an acceptor concentration of $3{\cdot}10^{18}$ cm^{-3}, while as window layer a 30nm thick p-type $Al_{0.8}Ga_{0.2}As$ layer with $3{\cdot}10^{18}cm^{-3}$ was used. Finally, an extra p^+-GaAs layer with $1{\cdot}10^{19}$ cm^{-3} dopant concentration is deposited in order to protect from oxidation the window layer which contains aluminum and to improve the contact with the top electrode. In this work we study 4 different solar cells, the first one with no i-region and a 50nm cap layer (1265), the second one with no i-region and a 600nm cap layer (1663), the third one with a 200nm i-region and a 600nm cap layer (1275) and the fourth one with

a 500nm i-region and a 600nm cap layer (1274). The details of the samples are presented on the table of figure 22.

a/a	Sample No / Layers	MBE 1265 (old)	MBE 1663 (new)	MBE 1275 (old)	MBE 1274 (old)
1	p^+-GaAs ($1x10^{19}$ cm^{-3})	500 Å	0.6 μm	0.6 μm	0.6 μm
2	p^+-$Al_{0.8}Ga_{0.2}As$ ($3x10^{18}$ cm^{-3})	300 Å	300 Å	300 Å	300 Å
3	p^+-GaAs ($3x10^{18}$ cm^{-3})	0.3 μm	0.3 μm	0.3 μm	0.3 μm
4	i-region GaAs	0 μm	0 μm	0.2 μm	0.5 μm
5	n GaAs ($1x10^{17}$ cm^{-3})	2.6 μm	2.6 μm	2.6 μm	2.6 μm
6-25 (BSF)	Nx { $Al_{0.36}Ga_{0.64}As$ ($2x10^{18}$ cm^{-3}); n GaAs ($2x10^{18}$ cm^{-3}) }	20x { 28 Å; 27 Å }	20x { 28 Å; 27 Å }	20x { 28 Å; 27 Å }	20x { 28 Å; 27 Å }
26	n^+-GaAs ($2x10^{18}$ cm^{-3})	1 μm	1 μm	1 μm	1 μm
27	n^+-GaAs substrate	substrate	substrate	substrate	substrate

Figure 22. Samples' code-name and the respective structure.

Following growth of the structures, an extra processing step by A. Kostopoulos (FORTH-IESL staff) produced isolated photovoltaic devices over the substrate in large numbers for statistical measurements. The full process finishes with the deposition of top contacts with a thermal evaporator.

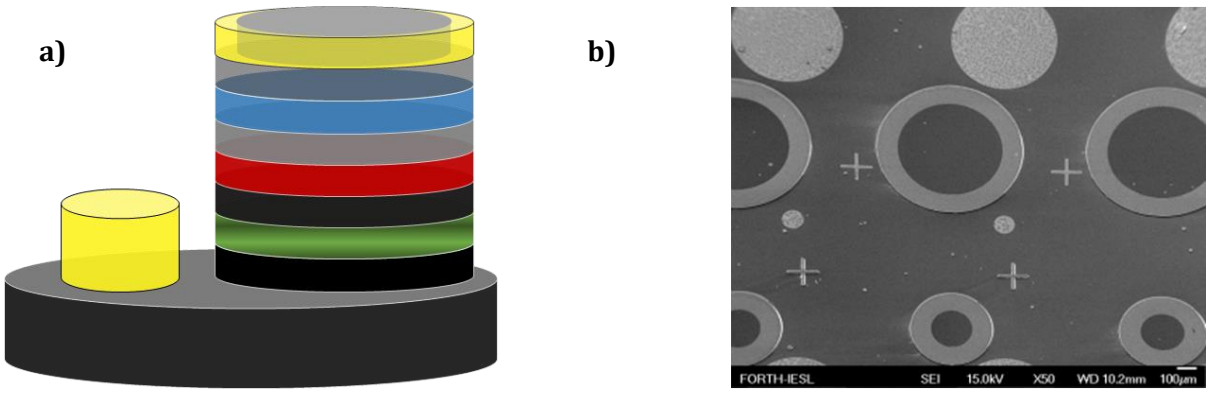

Figure 23. a) After etching mesa of a single devices on the surface and b) SEM image of the surface of a GaAs solar cell with the au top (ring like) and bottom (compact circle) contact.

As presented in figure 23 (a), mesas of GaAs are created and an additional Au contact next to the mesas plays the role of the bottom contact. For better statistics, two different radii of GaAs mesas are created (figure 23-b), a small

and a big one with the inner diameter of 520μm and 210μm respectively. The Au-top contact ring width is 100μm and the height 200nm.

Results, Analysis and Discussion

For the IV measurements of GaAs solar cells, we used a KETHLEY 2000 multimeter while for the illumination we used a Xenon lamp simulating to 1sun (AM1.5). For the analysis, a simple diode model is applied as represented before in figure 17 (chapter 3). This model is described from the Shockley equation:

$$|I_D| = I_{ph} - I_0\left(e^{\frac{q(V_D+I_D R_{series})}{nk_BT}} - 1\right) - \frac{V_D+I_D R_{series}}{R_{shunt}} \quad (\mathbf{eq.\,1})$$

where I_{ph} is the photocurrent, I_0 is the saturation current of the diode, R_{series} is the series resistance, R_{shunt} the shunt resistance, q the electron charge, n the ideality factor of the diode, k_B the Boltzmann constant, and T the temperature [54]. The series resistance represents the resistance that free carriers encounter on the ''road'' to the electrodes and is due to each layer's resistance, the resistance of the layers' interconnection and the contact resistance. A good solar cell presents low series resistance, while high values affect the fill factor of the device and the short circuit current [54]. On the other hand, shunt resistance represents the possibility of free carriers to follow alternative paths and be lost for the device. Shunt resistance, can be due to manufacturing defects, lattice imperfections etc. Ideally, shunt resistance should be as high as possible. Low values of the shunt resistance decrease the fill factor of the device as well as the open circuit voltage [54], [55]. The ideality factor of the device represents the recombination processes in the diode and affects its overall quality [56]. In dark conditions (I_{ph}=0), the deviation of equation (1) at short circuit conditions (V=0) and assuming that R_{shunt}>>R_{series}, gives the equation:

$$\frac{dV}{dI}(I \approx I_{sc}) = R_{shunt} \quad (\mathbf{eq.\,2})$$

while in higher voltage values, where the series resistance dominates, and since the shunt resistance is usually much larger than the series resistance, the second term's value is much lower compare to the first one, the equation can be simplified to:

$$I_D = I_0\left(e^{\frac{q(V_D+I_DR_{series})}{nk_BT}} - 1\right) \textbf{(eq. 3)}.$$

By taking the natural logarithm of equation (3) we extract the below equation:

$$\ln I_D = \ln I_0 + \frac{qV_{Measured}}{nk_BT} \quad \textbf{(eq. 4)}$$

where $V_{Measured}=V_D+I_DR_{series}$. Such a plot showing in figure 24 (b), can give you information about the ideality factor from the slope of the dashed line, the saturation current from the intercept with the y-axis, and the series resistance from the deviation of the I-V curve from the dashed linear curve.

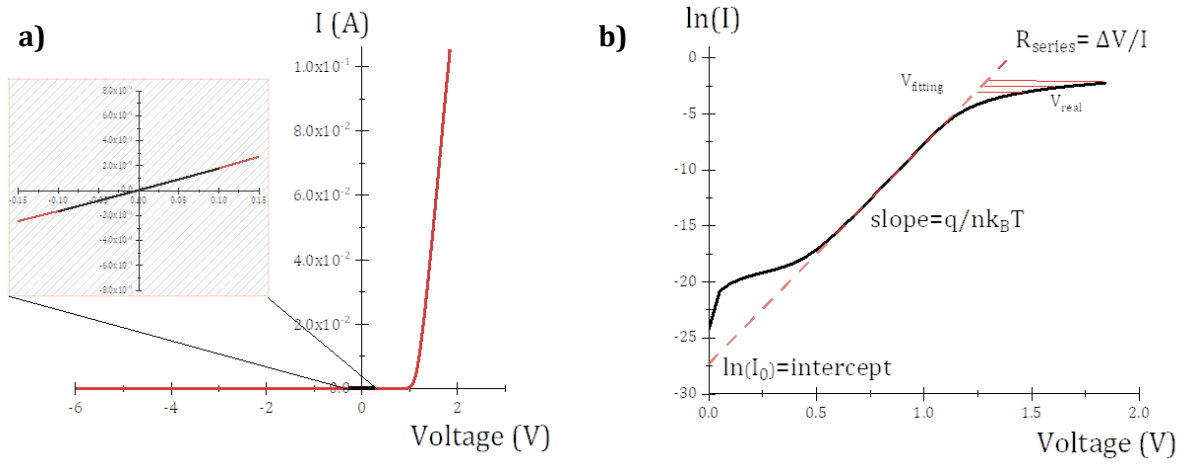

Figure 24. Extraction of diode parameters using a) equation (2) to extract shunt resistance and b) equation (4) for ideality factor, saturation current and series resistance.

The results of the dark analysis are extracted and presented in figure 25.

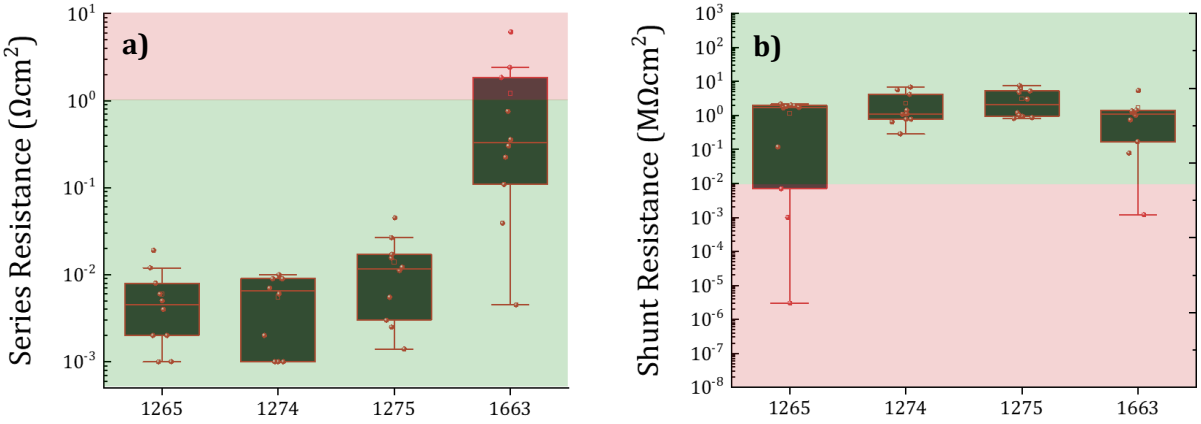

Figure 25. a) Series Resistance and b) Shunt Resistance of the 4 Gallium Arsenide Solar Cells samples multiplied with the active area.

The green areas of figure 25 a) and 25 b) are the areas where there is no important effect in the photo-IV due to the parasitic resistances [57], [58], [59]. For 1265, 1274 and 1275 we observe significantly low values for series resistance, despite the differences in the cap layer and i-region. On the other hand, the sample 1663 presents higher values of series resistance. This cannot be attributed to the increased cap layer thickness compare to 1265 sample, as the other two samples 1274 and 1275 have the same thickness in the cap layer. It is most likely due to variations of the doping profile from its nominal values. It should be mentioned that sample 1663 was fabricated almost 20 years later than the other samples. From the other side, all 4 samples present sufficiently high values of shunt resistance, in good agreement with MBE is a technique which produces high quality samples.

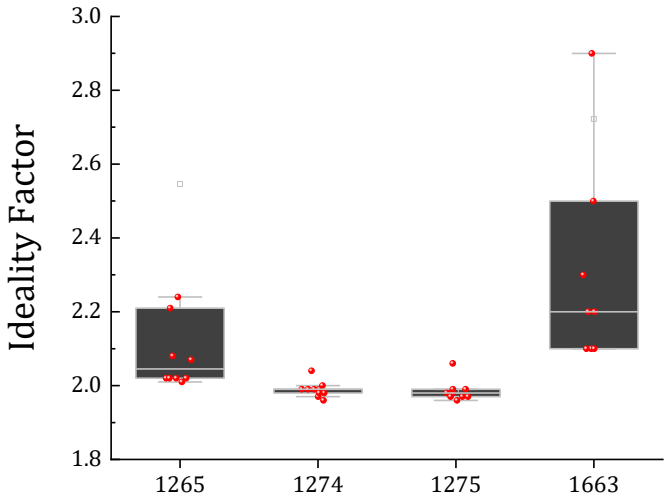

Figure 26. Ideality factor values extracted as described in the text, from dark IV analysis.

For ideality factor values extracted at high injection levels, we observe that 1274 and 1275 have well defined values close to 2, suggesting limited radiative recombination (band to band) in the depletion region [60], [61].

For the samples with no i-region, we observe slightly higher values of ideality factor, whose origin requires further investigation.

The cap-layers seem to have no important effect on the electrical characteristics of the diodes, and a 50nm layer is enough to protect the AlGaAs window layer and to provide a good ohmic contact with the top electrode. The characterization of these devices went on with photo-IV measurements. The extracted parameters from such a measurement are the most important for each solar cell, as they define the power conversion of the incident photons to electrical energy.

As described in the techniques, a photo-IV measurement can give as information about open circuit voltage (V_{OC}), short circuit current (J_{SC}), fill factor (FF%) and the overall efficiency of the solar cell (n%). In general, the open circuit voltage of a diode is the difference in electric potential for zero current between the positive and the negative electrodes[62] , while a model that can describe an equation of the V_{OC} as follows:

$$V_{OC} = \frac{nk_BT}{q} \ln\left(\frac{I_{ph}}{I_0} + 1\right) \quad \textbf{(eq.5)} \text{ [63], [64]}$$

where I_{ph} is the photocurrent, I_0 the saturation current of the diode and n the ideality factor. V_{OC} is critically dependent on the saturation current and the recombination losses. Another approximation for V_{OC} definition can be described as:

$$V_{OC} = \frac{k_BT}{q} \ln\left(\frac{(N_A+\Delta n)\Delta n}{n_i^2}\right) \quad \textbf{(eq.6)} \text{ [63], [65]}$$

where N_A is the dopant density, n_i the intrinsic carrier concentration and Δn the excess carrier concentration. According to eq.6, the open circuit voltage of a solar cell can be controlled with doping with respect to the intrinsic carrier concentration. Calculational measurements show that the saturation current decreases with the bandgap of the photo-active materials and thus the open circuit voltage increases [63], [66]. This fact is also expected according to the first consideration that the open circuit voltage value is the

difference in electric potential between the positive and the negative electrodes.

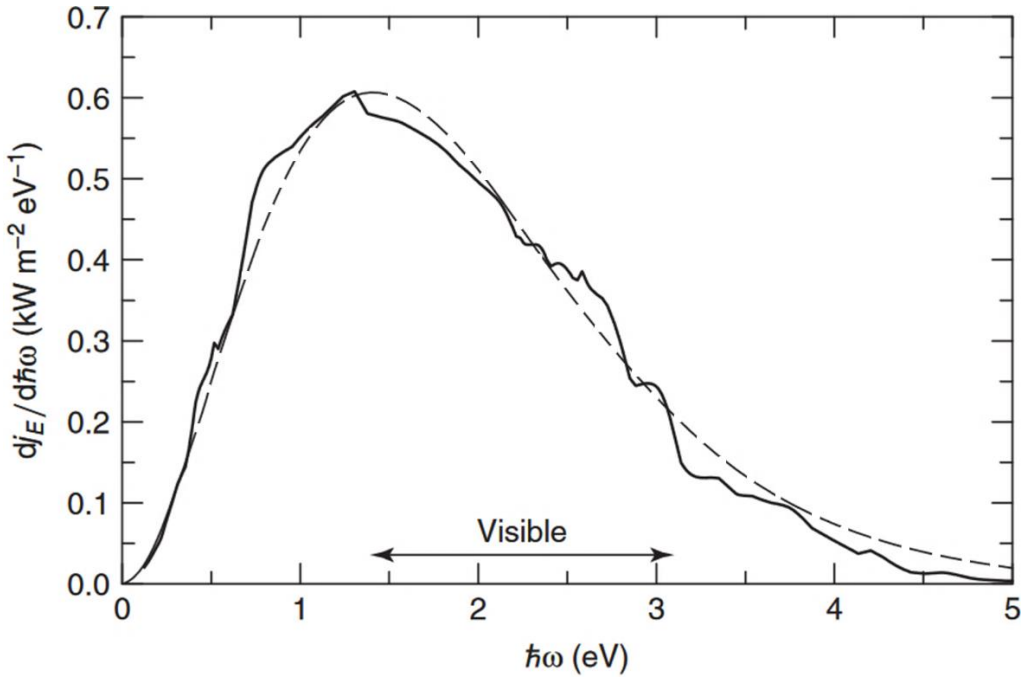

Figure 27. Energy current density per photon energy from the Sun as a function of photon energy just outside the Earth's atmosphere (heavy line) compared with a black-body at a temperature of 5800 K (thin dashed line) [36].

Regarding photocurrent, a relationship between diode characteristics and photocurrent is given in eq.1. Besides that, the photocurrent depends strongly on the energy gap of the active material [36], and the effectiveness of the internal electric field to separate the photo-carriers to the electrodes with minimum recombination losses. Finally, the fill factor is strongly affected by parasitic losses by high series and low shunt resistances.

For our measurements, the irradiation conditions were under 1sun (100mW/cm^2) in AM1.5 and the extracted parameters are presented below:

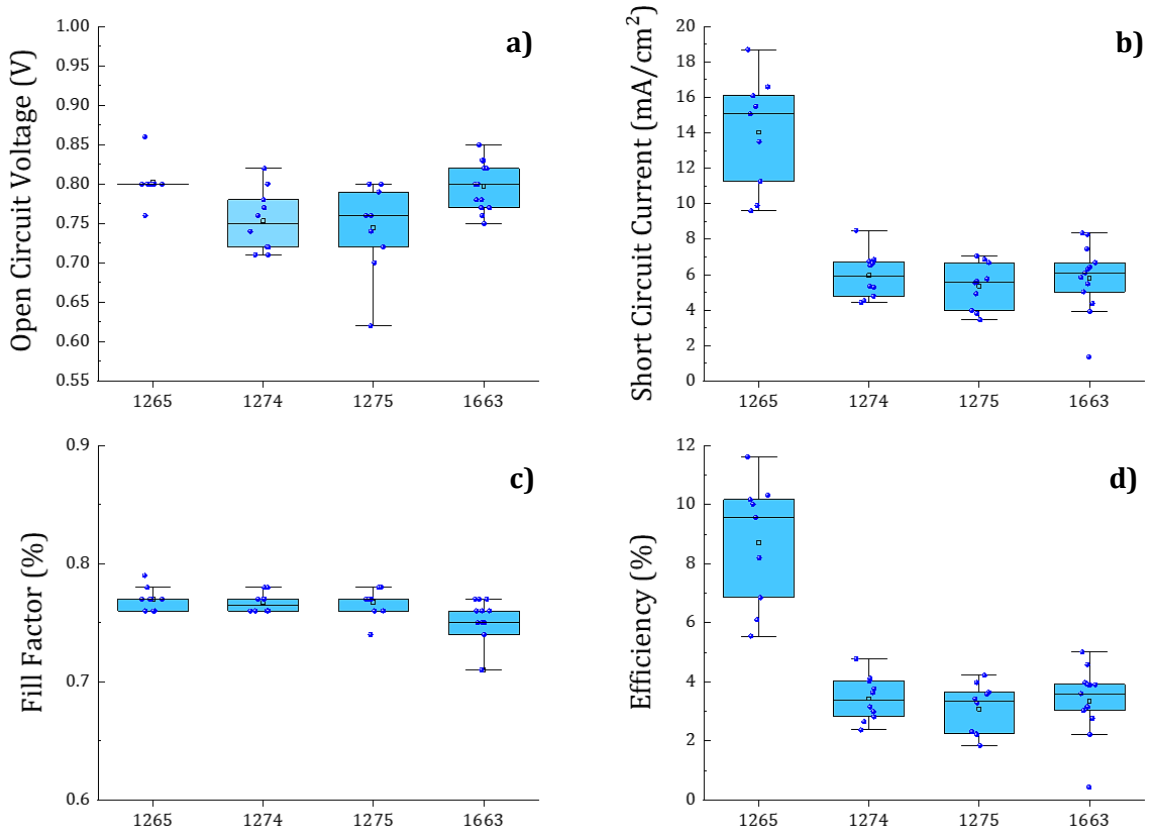

Figure 28. Extracted statistics of photovoltaic parameters of a) Open Circuit Voltage, b) Short Circuit Current, c) Fill Factor and d) Efficiency of different solar cells.

According to the extracted values, the highest performance is observed for the 1265 sample, with no i-region and the thinnest cap layer, with larger difference in the J_{SC}. This diode performs better due to the thin cap layer, as it prevents parasitic absorption in the cap layer. Additionally, the V_{OC} values are statistically a bit higher for the samples with no i-region, while the fill factor does not seem to present any important difference between the samples. The calculated efficiency of the samples is given as:

$$n = \frac{P_{out}}{P_{in}} = \frac{V_{OC} \cdot J_{SC} \cdot FF}{P_{in}} \quad (\mathbf{eq.7})$$

and follows the tendency of the J_{SC} which presents the most important difference. The highest values are presented for the thinnest cap layer with no i-region sample (1265) with a V_{OC}=0.86V, J_{SC}=18.7mA/cm^2, FF=79% and n=11.62% (not all values extracted from the same diode). To sum up, from the photo-IV measurements, the i-region does not affect much to the total photovoltaic performance. On the other hand, using a thin cap layer benefits a lot the pv-efficiency, as it prevents significant absorption losses in the cap layer according to the penetration depth spectrum showing in figure 29 [67].

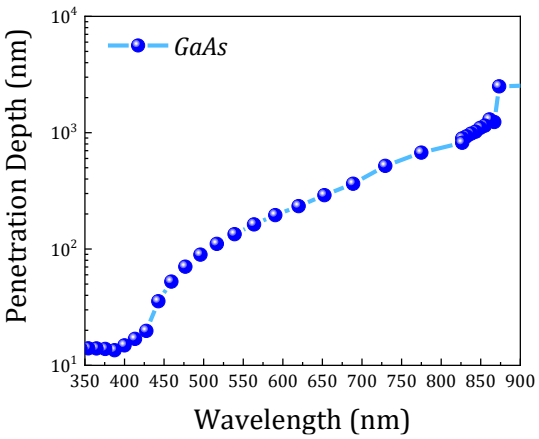

Figure 29 Penetration Depth of Gallium Arsenide [67].

For further investigation of these devices, we focused on samples with no i-region which presented the highest efficiencies. More specific, the cap layer from the active area removed and an additional deposition of an antireflection layer (AR-layer) was applied, in order to minimize the reflections from the surface and increase the efficiency. At the same time, the AR-layer replaces the cap layer in terms of AlGaAs protection (fig. 31). Before the deposition of AR-layers, we proceeded to theoretical calculations using a free-online program, the Filmetrics [68].

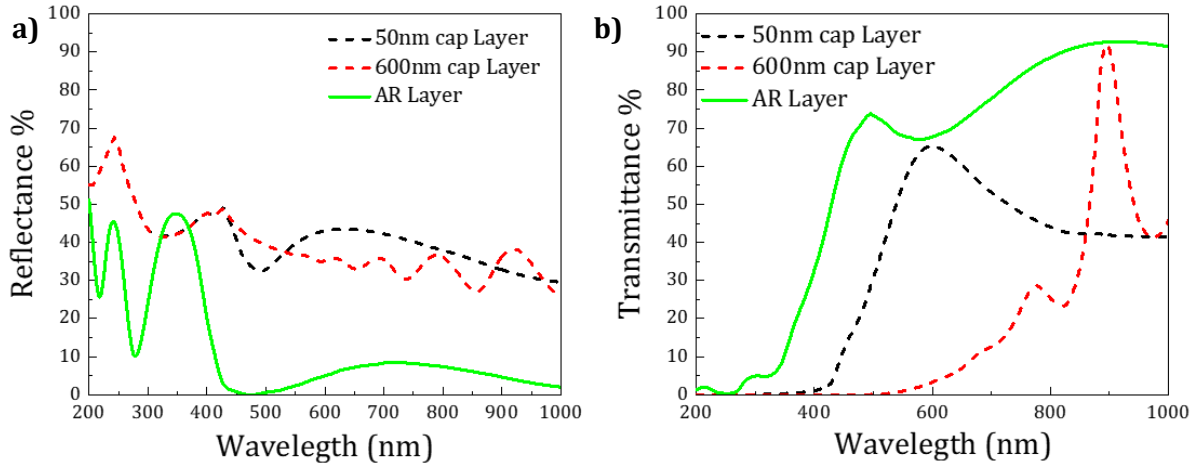

Figure 30. a) Calculated reflectance of the 1265 and 1663 before removal of cap layer (dashed lines) and following removal of the cap layer and deposition of an AR-layer. b) Calculated transmittance curves obtained for three cases of panel (a). For the transmittance calculation we consider a cap-layer/window layer (dashed lines) and AR layer/window layer (solid line) on quartz.

As presented in figure 30 b), the incident photons that finally reach in the active material are well below 30% for a 600nm cap layer, less than 60% for the most of the spectrum for a 50nm layer, while by replacing the cap layer with the AR layer more than 70% of the visible incident photons reach the depletion region. For the calculations, a SiO_2(120nm) /HfO_2(80nm) deposited on the window layer and the reflections minimized from ~40% to less than 10% (figure 30 a).

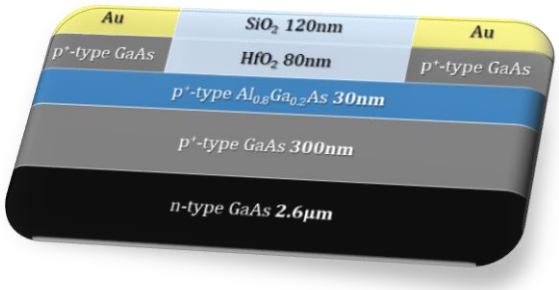

Figure 31. Cap Layer etching and AR layer deposited on Window Layer

By measuring the photovoltaic devices after AR- deposition, we observe an increase of both V_{OC} and J_{SC}, while the FF stayed constant. It should be mentioned that the rest of parameters determined by dark-IV measurements after AR-coating were also identical to the diodes before AR-deposition.

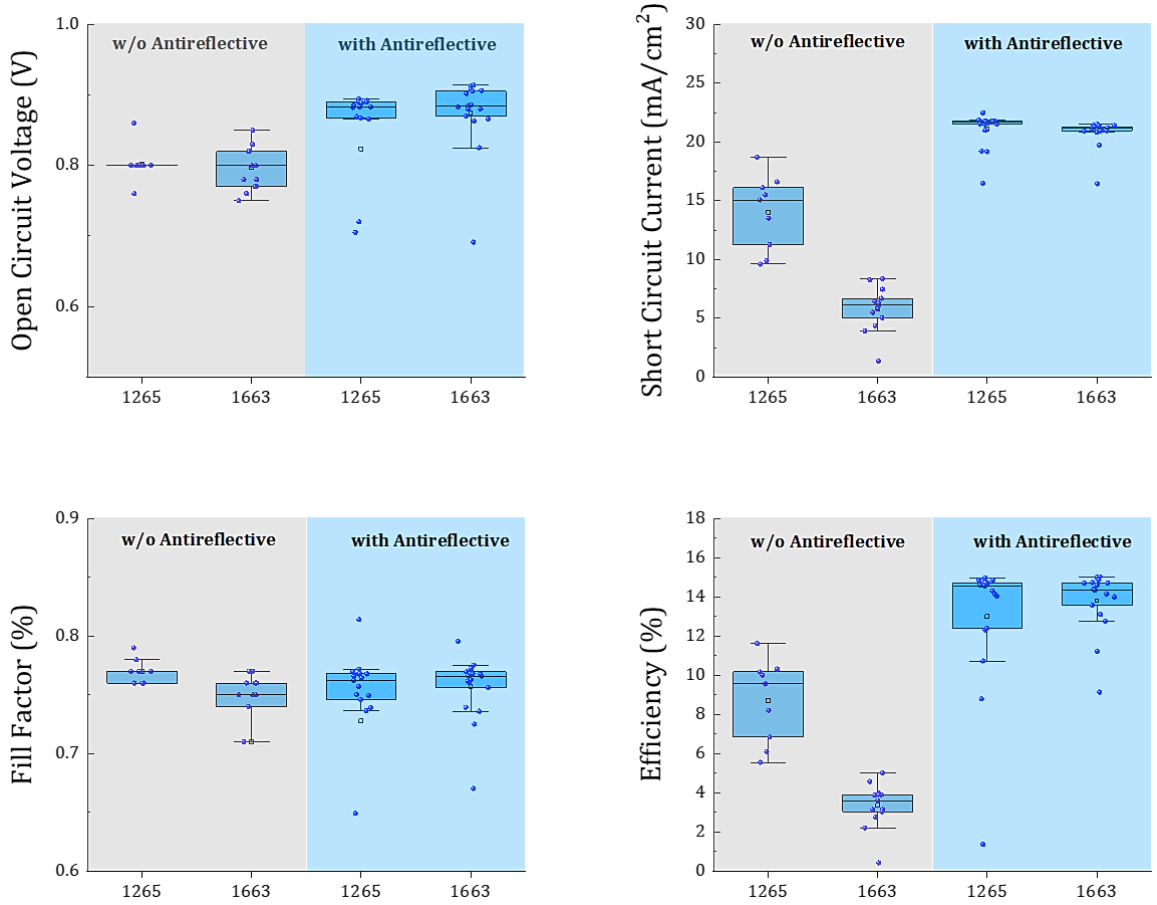

Figure 32. Compared Photovoltaic Results with and without antireflective layer for 1265 and 1663 devices.

The behavior of these two samples 1265 and 1663 after AR processing became almost identical, something expected considering that the top-layer is now removed in both samples.

Overall, we fabricated 4 GaAs solar cells with different structures in order to examine the effect of the i-region and of the cap layer. All 4 samples present excellent electrical characteristics as verified from dark IV measurements. Also photo IV measurements took place under 1 sun illumination (AM1.5). These measurements show that the i-region has a minor effect to the overall performance of the photovoltaic device. On the other hand, the cap layer thickness seems to have an important effect. Calculations show that there are important photon losses due to the cap layer, while after replacing the cap-layer with an AR layer, the pv-efficiency of the tested samples without i-region reaches ~15% values which compare reasonably well with previously reposted values for GaAs solar cells, with similar design. Furthermore, these PV efficiencies are more than enough for the purpose of this work, which is to demonstrate the benefits of tandem devices.

Chapter 5

Perovskite Solar Cells

Introduction

Perovskite Solar Cells is a new type of solar cells that have attracted the interest of the research community all over the world [69]. They present PV efficiencies comparable to the alternative technologies of Silicon but with possibility of low fabrication costs, which explain the vast interest in this technology.

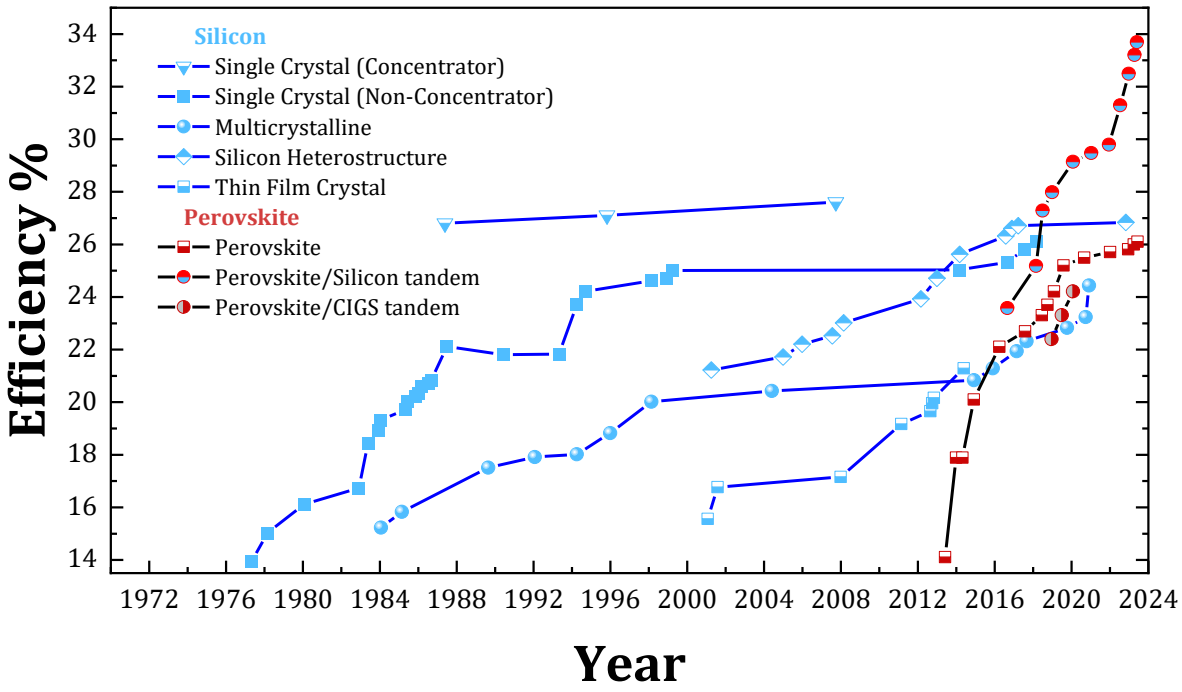

Figure 33 . Interactive Best Research-Cell Efficiency Chart from the National Renewable Energy Laboratory (NREL) focused on perovskite-based (red lines) compared to Si-based (blue lines) solar cells [3].

Coming back to the discussion of efficiencies, the first certified perovskite solar cell efficiency was 14.1% in 2013 (EPFL group), while after exactly 10 years the efficiency has reached 26.1% (University of Science and Technology of China) under 1 sun illumination as recorded by NREL. This extraordinary development explains further the researchers' interest in this technology. This becomes clear if we take a look in figure 33, where the ''slope'' of the efficiency is much steeper for the perovskite SCs compared to Si. Some well-known drawbacks of perovskite SCs are the sensitivity to moisture and to photodegradation mechanisms occurring under solar

illumination. However, great progress has been accomplished on this aspect over years. While the first measured devices lasted a few minutes of exposure in ambient conditions, chemical and mechanical strategies have led to a ~one year stability [70].

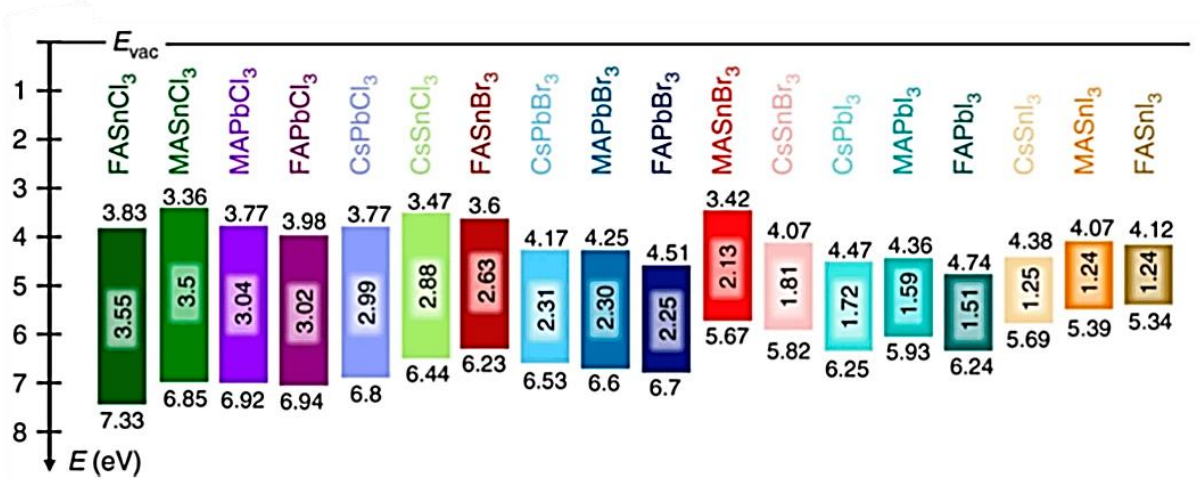

Figure 34. Energy map of various perovskite compounds and the respective HOMO and LUMO levels [71].

Another great advantage of this technology is the bandgap tunability of these materials, making them attractive in terms of tandem solar cell applications, either in combination with other semiconductors or in all-perovskite configuration. A general energy level map for perovskite compounds is presented in figure 34, while intermediate gaps can be obtained with the combination of anions or cations in the limits allowed by the tolerance factor [72].

Except of the energy gap of the perovskite, an efficient perovskite solar cell, pre-supposes the deposition of multi layers, with a proper band alignment. The role of the window and the back surface field in a GaAs heterostructure, is played by the electron transport layer (ETL) and the hole transport layer (HTL) respectively. In our case, we used TiO_2 as ETL and SPIRO-OMeTAD and CuSCN as HTL.

With respect to theoretical expectations, if we want to study the effectiveness of our transport layers first, we should check the uniformity of our layers. Non-uniformity issues can lead to immediate contact of the perovskite with the metal, inducing losses and short circuit effects. Second, we need to optimize their thickness. The ETLs' or HTLs' thickness has to be small enough to minimize photon losses and the layers' resistance, but thick

enough to provide the necessary density of states for the efficient separation of free carriers. This phenomenon, can be characterized with photoluminescence measurements.

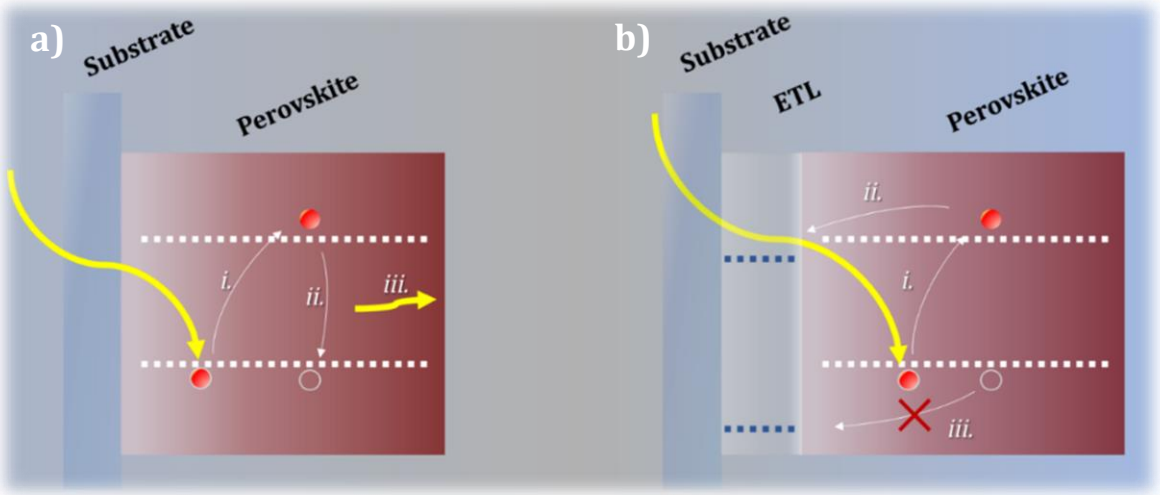

Figure 35. Illustration of photoluminescence measurement in a a) a Glass/Perovskite and, b) Glass/ETL/Perovskite structure.

More specific, a good photo-active layer for solar cells, generates free carriers when it interacts with incident photons, as presented in the first step (i.) of fig. 35 (a) and (b). If there are no-favored escape paths for the generated carriers, they recombine (fig.35 a)-ii) and give what we call photoluminescence (fig.35 a)-iii). The more counts of photoluminescence, the more efficient generation of free carriers occurs. From the other side, if free carriers find favored paths, they separate and in ideal conditions, no recombination process occurs, as represented in fig.35 (b). It is important for a transport layer to provide an efficient escape path for one type of carriers, while at the same time to provide a repulsive potential for the other type of carriers (fig.35 b)-iii) contributing thus to efficient separation.

Figure 35, represents this separation process with an ETL, while a similar process occurs for the holes using an HTL.

Often, we call the ETL and HTL as quenching layers in the sense that their presence leads to a photoluminescence quenching due to carrier separation.

Preparation, Deposition and Characterization of Transport Layers

Figure 36. Spin150 spin coater machine

Many techniques are used in the literature for transport layers deposition, such as sputtering, evaporation, spray pyrolysis and solution processed techniques. The main aspect for each technique is to produce a uniform film, with a good thickness control and with no damage of the underlayers. In our case, we used solutions deposited on the substrate with spin coating technique for both electron and hole transport layer. This technique provides a good control of deposited films with reproducible results. The spin coater was a spin150 model which is a programmable spin coater with multiple steps of velocity and acceleration.

Titanium Dioxide (ETL)

Titanium dioxide, is a n-type material, with a good transmittance in the ultraviolet and visible spectrum, with a bandgap ~3-3.2eV, which provides an excellent energy band alignment with most of perovskite compounds for an efficient transport of electrons and blocking of holes, minimizing with that way parasitic recombination which can affect the total efficiency of a perovskite solar cell. In our case, we used 3 different recipes, a good combination of which give the expected results in our solar cells. The first recipe, is based on a solution of Titanium Isopropoxide, Hydroiodic acid and ethanol. More specific, we mix 50μL of HCL (37%) in 2.3mL of Ethanol and stir for several minutes. After that, we add 150μL Titanium Isopropoxide and stir for ~2hours. The chemical reaction of such a solution can be described from a general formula of Titanium alkoxides with aqueous solutions such as:

$$Ti(OEt)_4 + 2\ H_2O \rightarrow TiO_2 + 4\ EtOH\ [73]$$

where the ethanol is used as a solvent and the HCl as a catalyst [74]. The deposition of such a solution produces produce a uniform amorphous film.

In terms of improving the electrical and optical characteristics, after deposition of TiO_2 film, an extra thermal treatment at high temperature should follow. There are three well known crystal phases for TiO_2, anatase, rutile and brookite[75]. The first two phases present a tetragonal structure while brookite presents an orthorhombic. Rutile seems to be a more stable phase, but for solution-processed films anatase seems to be a favorable phase.

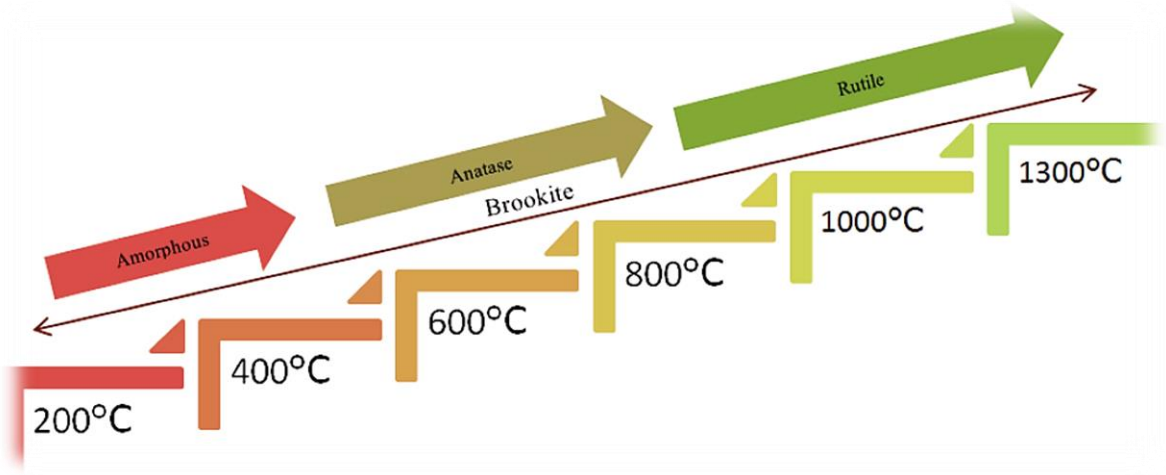

Figure 37. Phase Transition of TiO_2 with the temperature [74].

In our case, although the electrical characteristics of the TiO_2 are improved with the temperature [74], the annealing treatment of TiO_2 is set at 500°C for 15minutes in an air furnace. This is because the FTO's maximum operating temperature according to the manufacturer seems to be ~500-550°C. If we overpass this temperature, even if we obtain a better operation from the ETL, we will have degradation of the bottom electrode.

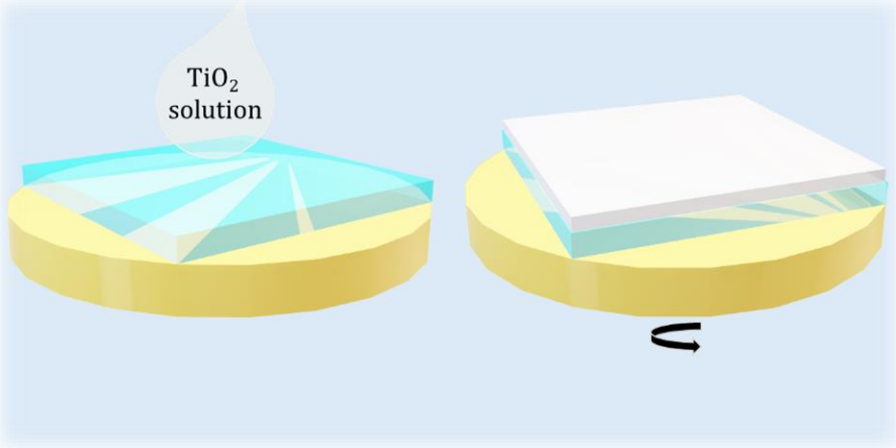

Figure 38. Deposition Process of Titanium Dioxide on glass substrate.

For the deposition conditions, we used an ultra-clean substrate, treated with oxygen plasma for enhanced hydrophilic character. As presented in figure 38, we drop the TiO_2 solution on the substrate, and spin-coat at 2000rpm with 1000rpm/sec for 30sec, producing a uniform film. In figure 39, is presented a SEM image of a 75nm thick TiO_2 film on Silicon substrate. The thermal treatment took place after the deposition.

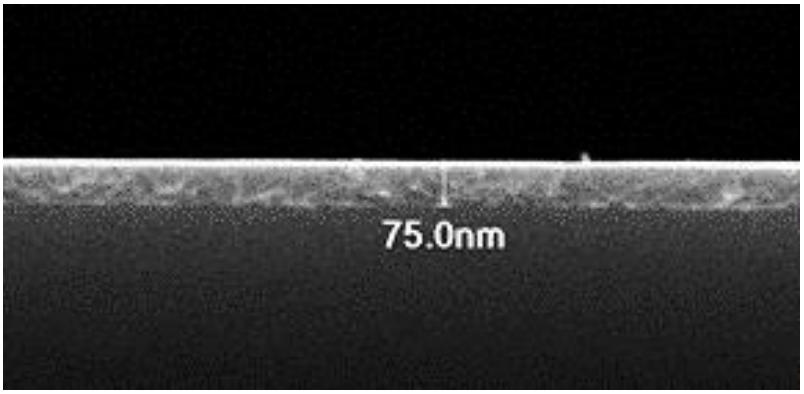

Figure 39. SEM Image of 75nm TiO_2 on Silicon substrate.

In order to avoid undesired pin holes or cracks that will lead to recombination centers and shunt paths, we proceed with an extra step of $TiCl_4$ treatment. More specific, the annealed TiO_2 films, are dipped in a 0.05M of $TiCl_4$ in aqua solution at 70°C for 30minutes, and are then rinsed with de-ionized water and subjected to an extra annealing treatment at the same temperature conditions. The reaction of this process can be described as:

$$TiCl_4 + 2H_2O \rightarrow TiO_2 + 4HCl.$$

The effect of TiO_2 film post-treatment with an extra step of $TiCl_4$ hydrolysis is described elsewhere[75] and contributes to the photovoltaic behavior of perovskite solar cells with a slight increase of V_{OC}, Jsc and FF and an important decrease of series resistance.

Although extra layers add to the total series resistance of a solar cell, the increase of the active interface area between perovskite and transport layers seems to provide significant improvement on the overall efficiency. Thus, the last step for TiO_2-ETL deposition finishes with an extra mesoporous TiO_2 layer. For that purpose, a commercial paste with ~50nm TiO_2 nanoparticles

is diluted in ethanol and stirred for several hours, until we have a completely homogeneous solution. Then we use again spin-coating technique to deposit on the substrate with an extra thermal annealing again at 500°C for 15minutes for enhanced optoelectronic properties. The density of the paste in ethanol and the rpms during the spin coating determine the final thickness of the film. In our case, an optimized thickness for ~50nm TiO_2 nanoparticles seems to be ~ 200nm [76].

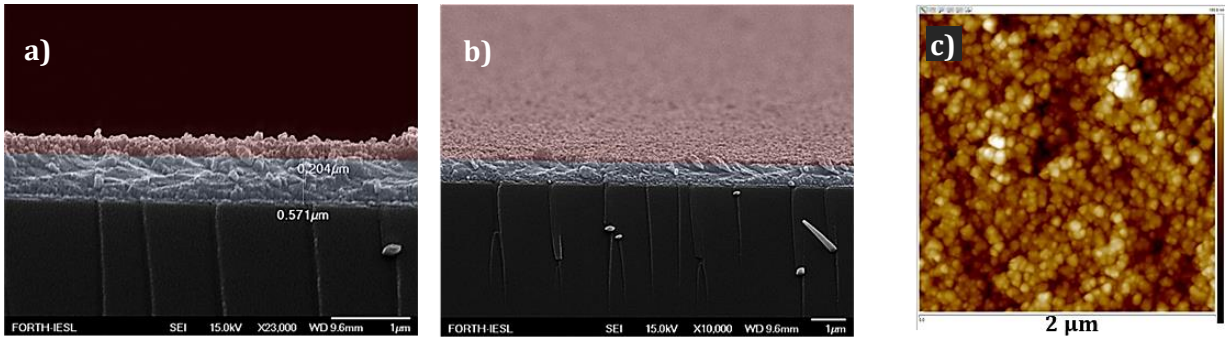

Figure 40. a) Cross Section and b) Tilted SEM image of FTO/$TiO_{2\text{-compact}}$/$TiO_{2\text{-mesoporous}}$ and c) the respective AFM image of the surface.

The conditions for a 200nm-thick mesoporous layer were 6000rpm for 30sec of a 1:7 (weight ratio) TiO_2-paste: Ethanol with a prior oxygen plasma treatment of the FTO/$TiO_{2\text{-compact}}$ substrate, while after deposition follows a final annealing step at 500°C. The RMS value of the mesoporous surface is ~ 20nm.

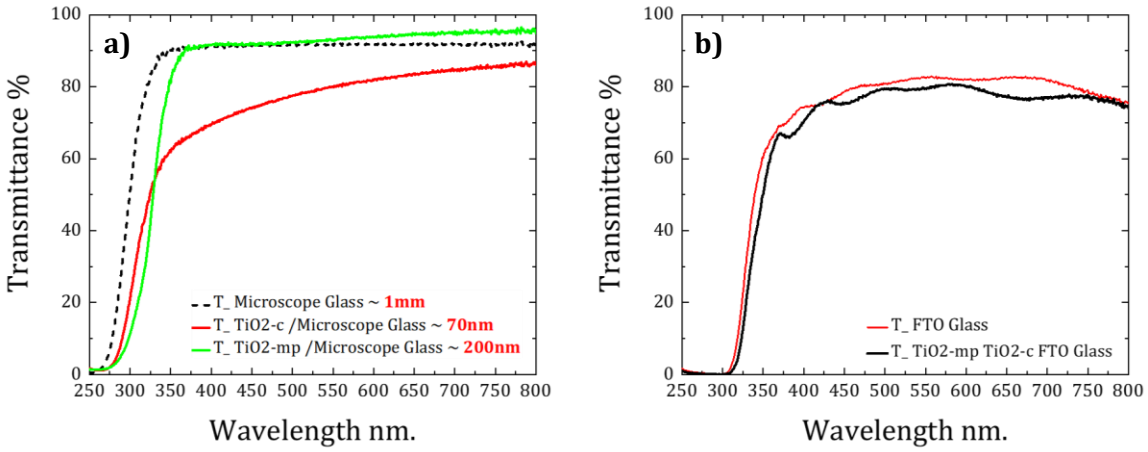

Figure 41. Transmittance measurements of a) Glass/$TiO_{2\text{-com}}$ and Glass/$TiO_{2\text{-mesop}}$ and b) FTO/$TiO_{2\text{-com}}$ /$TiO_{2\text{-mesop}}$. All TiO_2 layers are thermal treated at 500°C for 15min. The transmittance of substrates also presented in both diagrams.

According to transmittance results in figure 41 a), a 70nm compact TiO_2 seems to result to more parasitic photon losses than a 200nm mesoporous layer which, due to its structure seem to contribute to less transmittance. Both layers' bandgap is more than 3.8eV, while in figure 41 b) is shown the transmittance of an FTO/$TiO_{2\text{-com}}$ /$TiO_{2\text{-mesop}}$ which are the first 3 layers of our perovskite solar cell. From this figure, we conclude that the combination of the two layers TiO_2 does not significantly reduce the transmittance and the parasitic optical losses are caused almost entirely by the FTO substrate.

After the optical characterization, we try to extract the resistance that free electrons encounter when they pass through the $TiO_{2\text{-c}}$. For that reason, we deposit a 75nm-thick compact annealed layer of TiO_2 on an FTO substrate and then we deposit via RF-sputtering an extra Au layer.

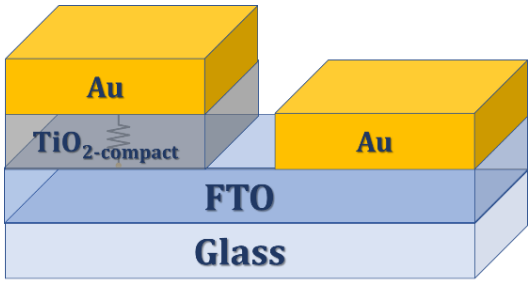

Figure 42. Illustration of $TiO_{2\text{-comp}}$ structure for IV measurement.

Using the structure of figure 42 and assuming that the whole measured resistance is due to $TiO_{2\text{-com}}$, we measured a 2kΩ vertical resistance for a 0.04cm^2 Au area and a 75nm thick TiO_2 film. Assuming that we have a well-defined structure and using the resistance equation

$$\rho = R\frac{A}{l} \quad \textbf{(eq.8)}$$

We extract a ~1 10^7 Ωcm specific resistance, which is very high compared to reported values [74],[77]. This difference probably arises from the differences in the solution procedure or/and the measurement process.

Additionally, we characterized the quenching effect in perovskites/TiO_2 heterostructure under photo excitation. More specific, we used 2 different excitation lasers, one at 325nm excitation and another at 650nm. By using

absorption results of reference [78], we found that the penetration depth for a 330nm thick $MAPbI_3$ film is ~ 18nm for a 325nm excitation and ~ 610nm for a 650nm excitation.

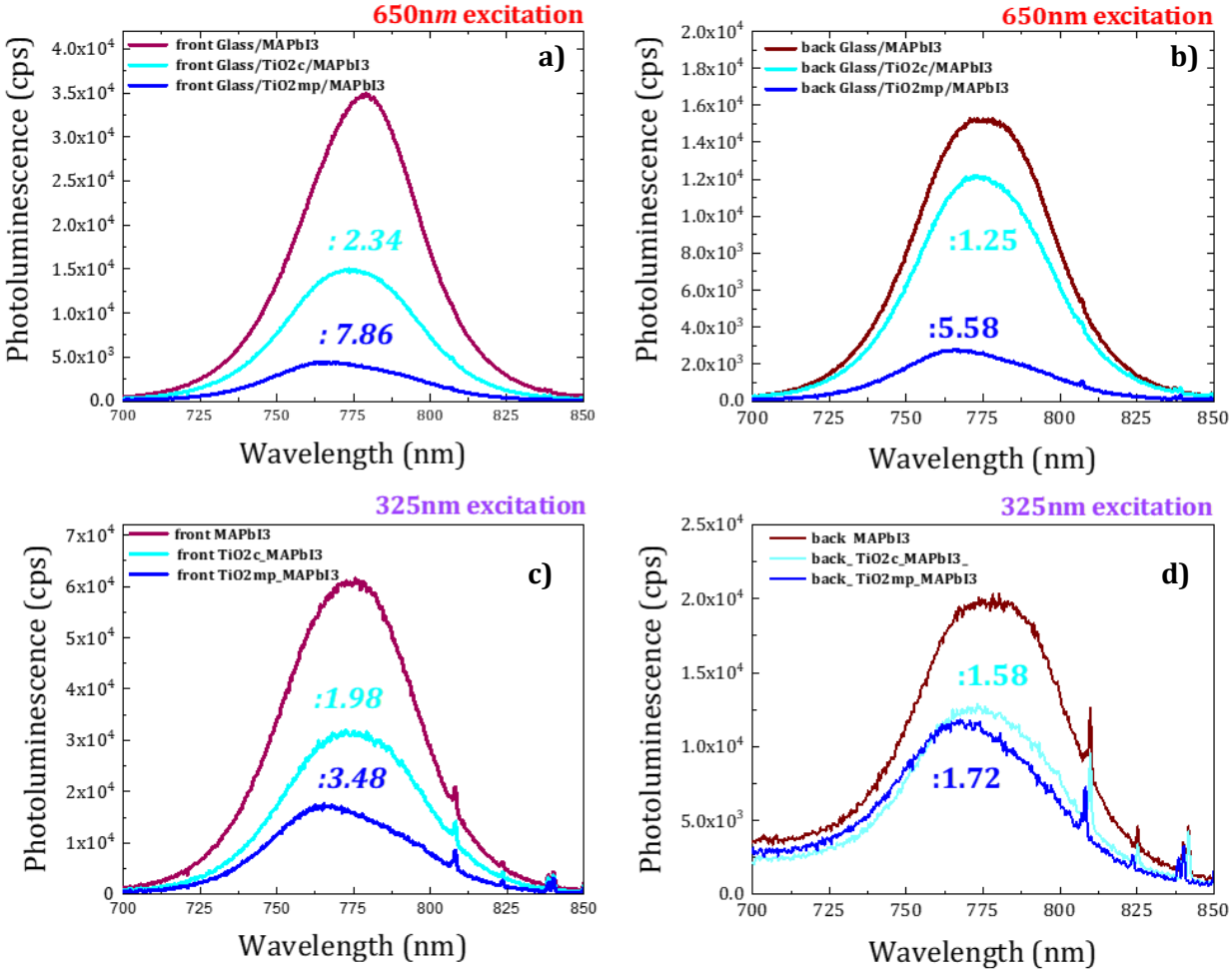

Figure 43. Photoluminescence measurements at room temperature for $MAPbI_3$-TiO_2 heterostructures excited from a), c) Perovskite side and from b), d) TiO2-side with a), b) 650nm and c), d) 325nm laser

From fig. 43 we observe that the quenching-effect is more obvious for mesoporous TiO_2 suggesting a better ETL effect. In addition, although we would expect a stronger quenching effect when we excite from the back close to the interface, the effect appears more pronounced when we excite from the front perovskite side. The explanation of these results needs further investigation. Finally, electrons seem to travel through the perovskite with no ''issues''. The lower PL intensity from the back side (glass side) is justified by parasitic optical losses due to glass and ETLs'.

In terms of light harvesting, in co-operation with E. Aperathitis' team, we used these structures ($FTO/TiO_{2\text{-com}}/TiO_{2\text{-mesop}}$) for all metal-oxide based

junctions using NiO [79], [80] or Niobium Doped NiO heterostructures [81], showing promising characteristics for further investigation in terms of ultra-violet radiation harvesting.

SPIRO-OMeTAD (HTL)

2,2',7,7'-Tetrakis [N, N-di(4-methoxyphenyl) amino]-9,9'-spirobifluorene or better SPIRO-OMeTAD, is a small organic molecule which is well-studied in the context of perovskite solar cells. The role of this molecule is the effective transport of holes from the perovskite layer to the electrode with the simultaneous repulsion of the electrons, minimizing thus the recombination losses. Its HOMO/LUMO levels provide an excellent alignment with most of perovskite compounds, and make it one of the most efficient HTLs, to the point that in many works the scientists use it as reference for other HTLs. It is a p-type material, with low hole mobility ($\sim 10^{-4} cm^2/V$) [82] and conductivity (10^{-5} S/cm) [83]. The p-type character of SPIRO-OMeTAD is based on the efficient oxidation of this molecule, and thus many additives and strategies are used for the efficient oxidation process. The most common additives are *Lithium bis(trifluoromethanesulfonyl)imide* (Lithium-TFSI) which acts as a catalyst for the efficient oxidation of SPIRO-OMeTAD when it is exposed to the air, while another additive, *4-tert-Butylpyridine* (TBP), is used to offer to the solubility of Li-TFSI for its uniform distribution in SPIRO-OMeTAD, and thus, its uniform oxidation [84] [85]. Further investigations of SPIRO-OMeTAD discovered a new additive as dopant of SPIRO-OMeTAD, the *tris(2-(1H-pyrazol-1-yl)-4-tert-butylpyridine)cobalt(III)tri[bis(trifluoromethane) sulfonamide] or FK209* [86]. SPIRO-OMeTAD film is a little tricky in terms of uniformity, as Li-TFSI which is a basic additive for the p-character of SPIRO, is a very hydroscopic material. The uniformity of this HTL film is based on the evaporation-rate of the TBP and the ''crystallization'' of the film, so if there are water molecules, they will produce uniformities, cracks and in-holes which act as recombination centers for the device. For this reason, it is very important that all the materials that will be used for SPIRO-OMeTAD synthesis to be super-dry, both for obtaining a uniform HTL, but also for protecting the perovskite material, during the deposition of SPIRO-OMeTAD, as the water molecules can dissolve the perovskite film.

Many works have focused on the improvement of SPIRO-uniformity, for which Guoxin Li et al. [85] provide a good representation of this

phenomenon in figure 44 (a), while they suggest the addition of a small amount of CsI in order to further enhance the uniformity.

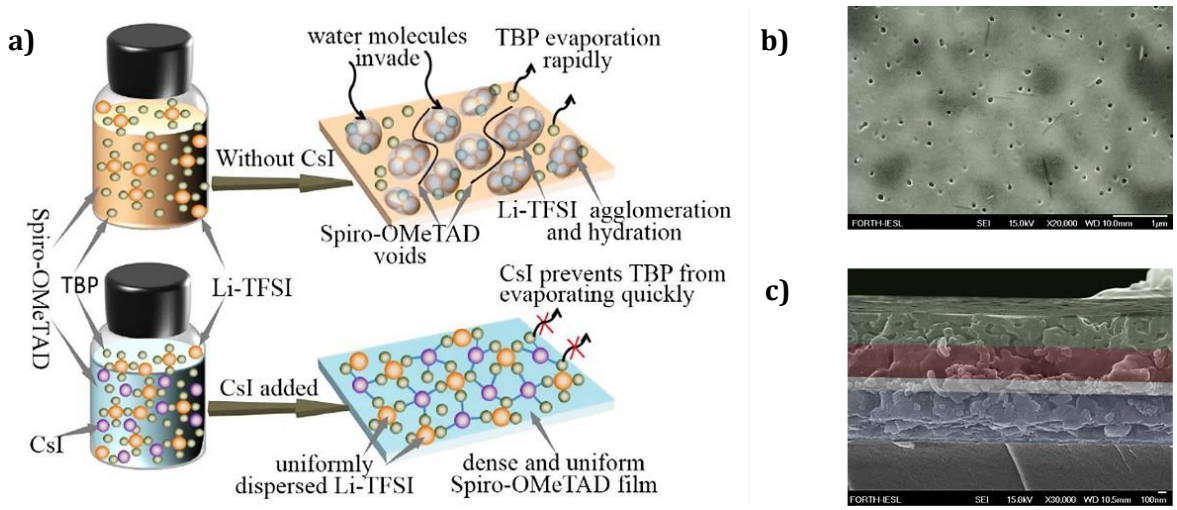

Figure 44. a) Effect of water molecules on SPIRO-OMeTAD uniformity and the improvement by CsI additives [85], b) Top and b)Cross Section SEM image of a FTO(blue)/ TiO_2(gray)/ Perovskite(red)/ SPIRO-OMeTAD(green) where undesired cracks and holes are observed on SPIRO-OMeTAD layer.

After all, there are many recipes in the literature with different but similar ratios of the additives which are used for the final SPIRO-OMeTAD solution. In our work, the optimized recipe that we used contains 144,6mg Spiro-OMeTAD, 57.6μL TBP, 35μL Li-TFSI (520mg/mL in acetonitrile), 58μL FK-209 (320mg/ mL in acetonitrile) and 1mL Chlorobenzene. It is important that all the solvents of SPIRO-OMeTAD cannot dissolve the perovskite layer. The deposition process is via spin coating at 3000rpm, with 1000rpm/s for 40 sec with no extra annealing treatment. After deposition, the layer is exposed to ambient conditions for further oxidation. The time of this exposure depends on the humidity and the temperature.

Copper Thiocyanate (HTL)

Copper Thiocyanate (CuSCN) is another solution-processed HTL layer that can effectively replace the SPIRO-OMeTAD layer. It seems that the HOMO levels of these two materials are almost the same, with the CuSCN having a higher barrier for electrons [22], thus we expect less recombination losses compared to the SPIRO-OMeTAD while the recipe is much simpler with no extra additives and thus, less expensive. In terms of stability, as a simple layer CuSCN is very stable, but there are issues when it interacts immediately

with the perovskite layer [87]. The interaction between CuSCN and MAPbI3 described as:

$$CuSCN + CH_3NH_3PbI_3 \rightarrow CuI + PbI_2 + CH_3NH_3SCN$$ [88]

To avoid this, intermediate layers such as 2D passivation layers, seem to protect the device [89] and provide stable and comparable devices with the respective SPIRO-OMeTAD devices. E. Madhavan et al. [90] present a comparative work of these two HTLs on a n-i-p structure with efficiencies that exceed the 18%.

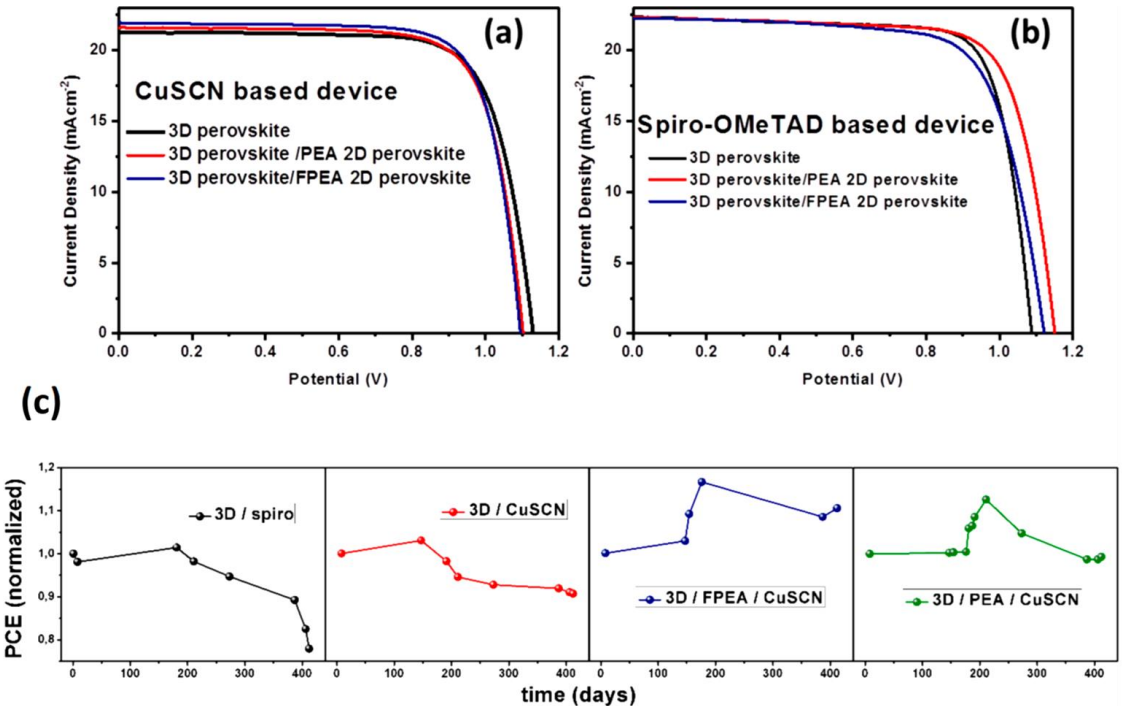

Figure 45. J–V measurements of a) CuSCN based and b) SPIRO-OMeTAD-based perovskite solar cells using different 2D cation-based perovskite additives, and c) Ambient laboratory stability data [90].

In this work, the *CuSCN* was dissolved in diethyl sulfide (30mg/mL) and deposited via spin coating with no extra thermal treatment. Comparing these two HTL's, we could say that CuSCN is a promising alternative to SPIRO-OMeTAD layer, in terms of high efficiency, low cost and long stability perovskite solar cells.

As we did with the TiO_2 layers, we examined the quenching mechanism of the CuSCN layer on $MAPbI_3$ using PL. In this study, we used the same

excitation conditions as with the TiO_2 layers. The penetration depth of CuSCN is 250nm for 325nm excitation and 920nm for 650nm excitation [91].

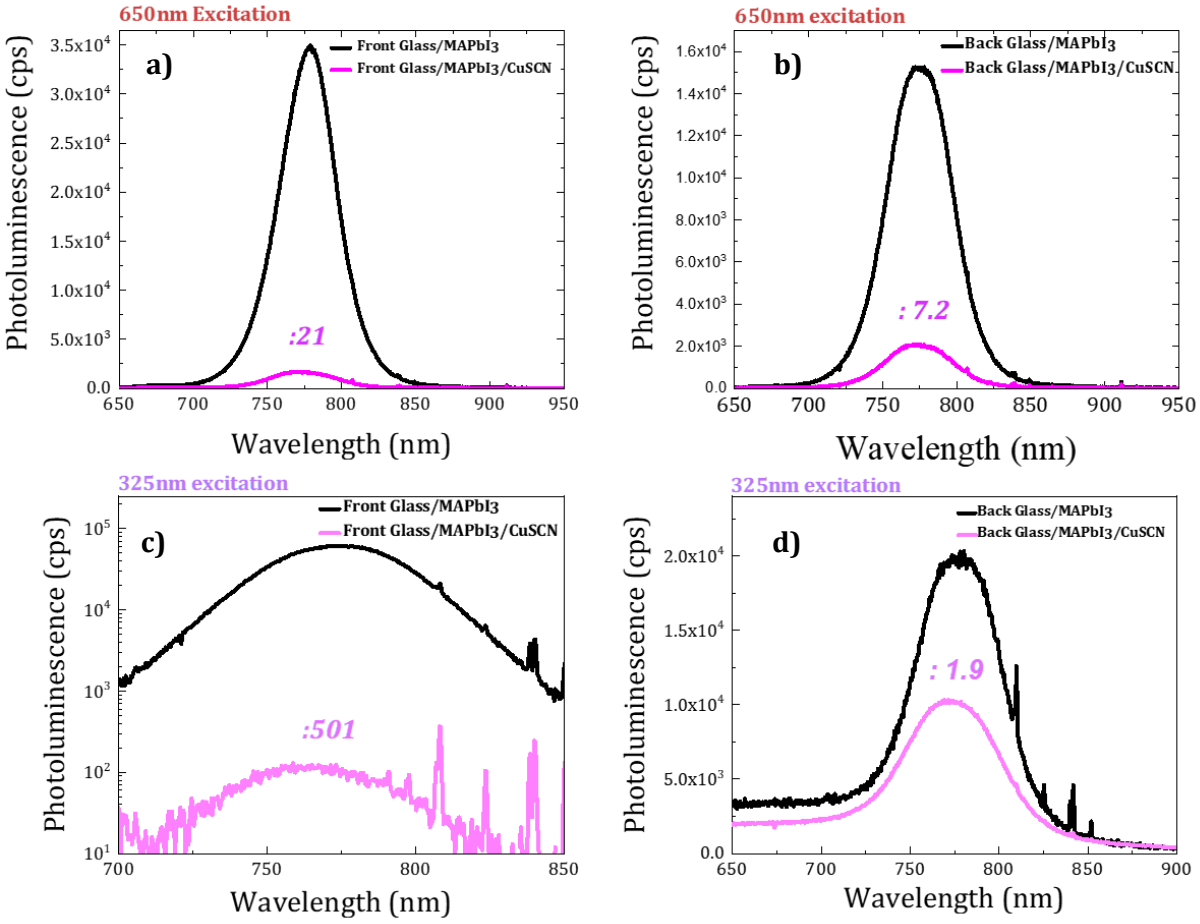

Figure 46. Photoluminescence measurements for $MAPbI_3$-CuSCN heterostructures excited from a), c) Perovskite and CuSCN side and from b), d) glass side with a), b) 650nm and c), d) 325nm laser

When we excite from the CuSCN side we see an important PL decrease, especially with 325nm excitation, which could be interpreted by the small penetration depth of $MAPbI_3$ in this wavelength. Most of the excited carriers are close to the interface of perovskite-CuSCN and the quenching process is more obvious and effective. A smaller decrease of the PL intensity is observed when the illumination occurs from the glass side. There, the free carriers have to travel through a part of $MAPbI_3$ to reach the HTL layer, so the phenomenon is weakened, especially for a 325nm laser where the distance to the HTL is increased.

In order to compare our HTL layers, firstly we deposit SPIRO-OMeTAD and CuSCN on a glass substrate for transmittance measurements. The measured

thickness for SPIRO-OMeTAD on glass was ~65nm while CuSCN is estimated to be less than 10nm-15nm and could not be measured.

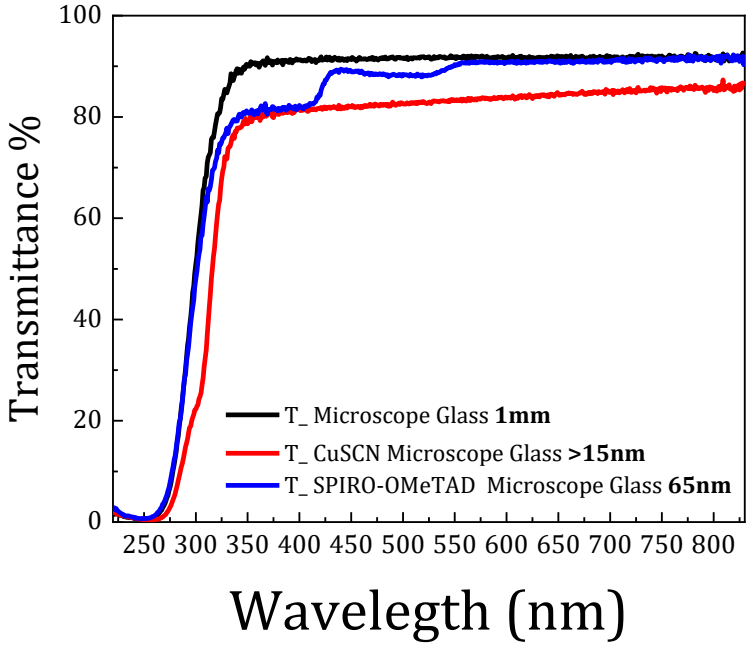

Figure 47. Transmittance of CuSCN and SPIRO-OMeTAD on glass substrate.

Although the HTL transmittance is not important for a single n-i-p solar cell, for more complex systems such as tandem solar cells, it is a parameter that we should take into account.

Perovskite Solar Cells

Preparation of perovskite films, is one of the most crucial steps for perovskite solar cells. The proper choice of the cations-anion for the $A^{1+}B^{2+}(X^{1-})_3$ in order to form the desired structure can be well defined from the radius of ions with the empirical tolerance factor relationship.

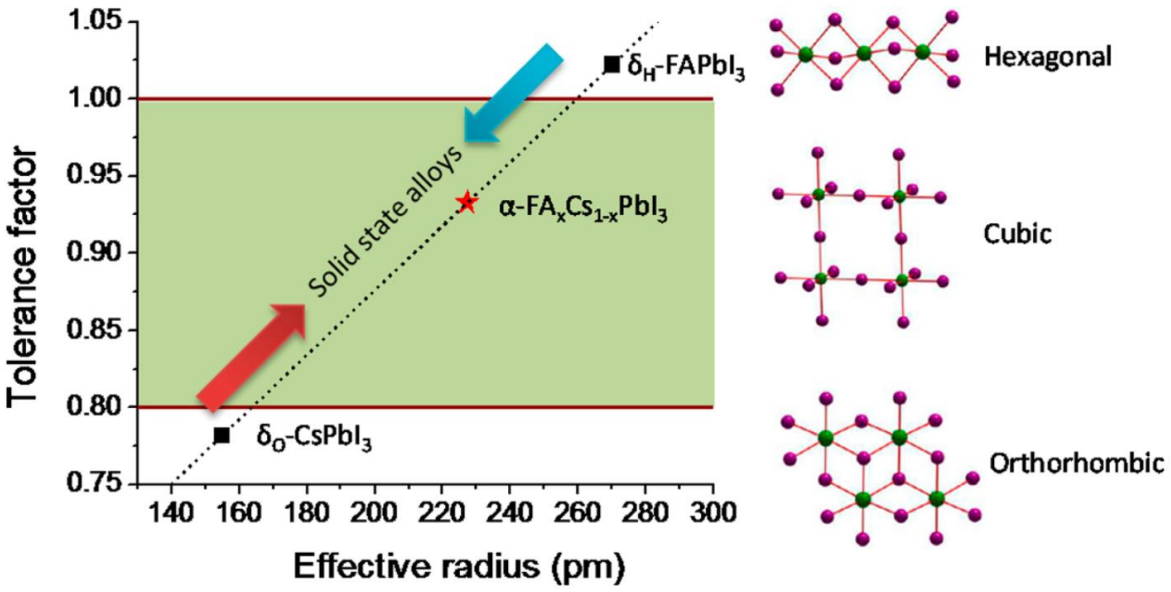

Figure 48. Goldsmith Tolerance factor values versus perovskite structure [72].

The Goldsmith tolerance factor equation can be described as:

$$t = \frac{r_A + r_X}{\sqrt{2}(r_B + r_X)} \quad \textbf{(eq.9)}$$

where r_A, r_B and r_X are the radii of the anions. According to the fig.48, for values smaller than 0.8 the perovskite compounds form an orthorhombic structure, for 0.8<t<1 a cubic structure and for values >1 a hexagonal structure. Orthorhombic and hexagonal are non-perovskite structures and are not desired for photovoltaic systems. Additionally, perovskites are well known to be sensitive in high humidity conditions. More specifically, moisture produces degradation of the perovskite structure, so when perovskite is exposed to a humid environment, we may have instability issues for the perovskite device. These issues are well controlled by using all-anhydrous reactants under controllable conditions (glovebox) for the perovskite fabrication. Additionally, encapsulation techniques protect the device for out of the glovebox measurements[92]. Another issue for perovskite devices is the light-induced degradation. More specifically, the incident irradiation produces ions displacement and finally the gradual decomposition of the structure. This interaction can be described as:

$$CH_3NH_3PbI_3 + hv \xrightarrow{HUV} CH_3I_{(s)} + NH_{3(g)} + HI_{(g)} + PbI_{2(s)} + CH_3NH_{2(g)}$$ [93]

with some interesting results having been published elsewhere.

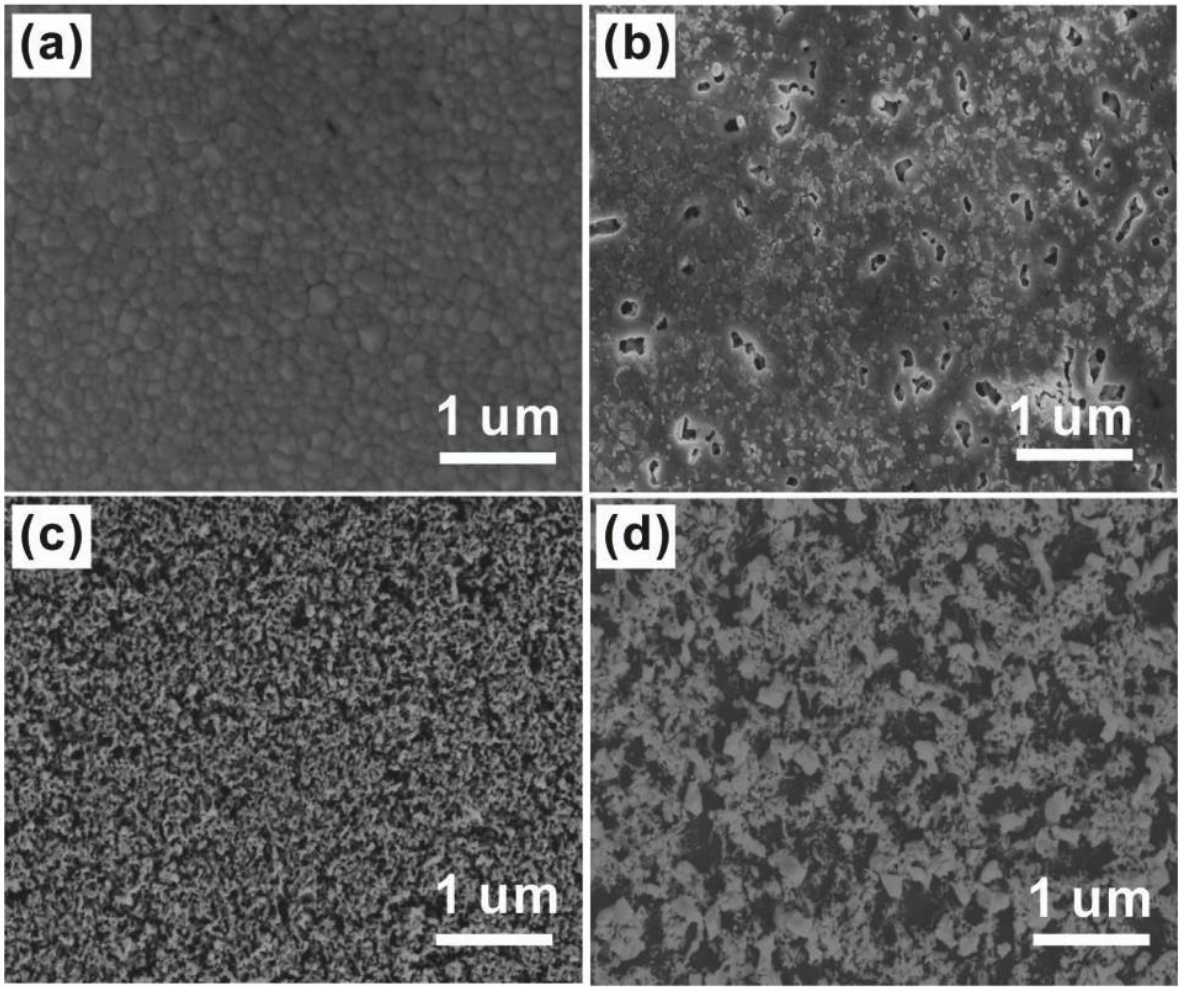

Figure 49. SEM images of $MAPbI_3$ perovskite surface under continuous white light illumination of (a) 0 h, (b) 6 h, (c) 24 h, and (d) 48 h with incident light density of ~434W/m² (0.43suns) [93].

This photo-degradation phenomenon is more intense for mixed-halide perovskites $AB(I_xBr_{1-x})_3$ and increases as the ratio between I^- /Br^- becomes close to 1.

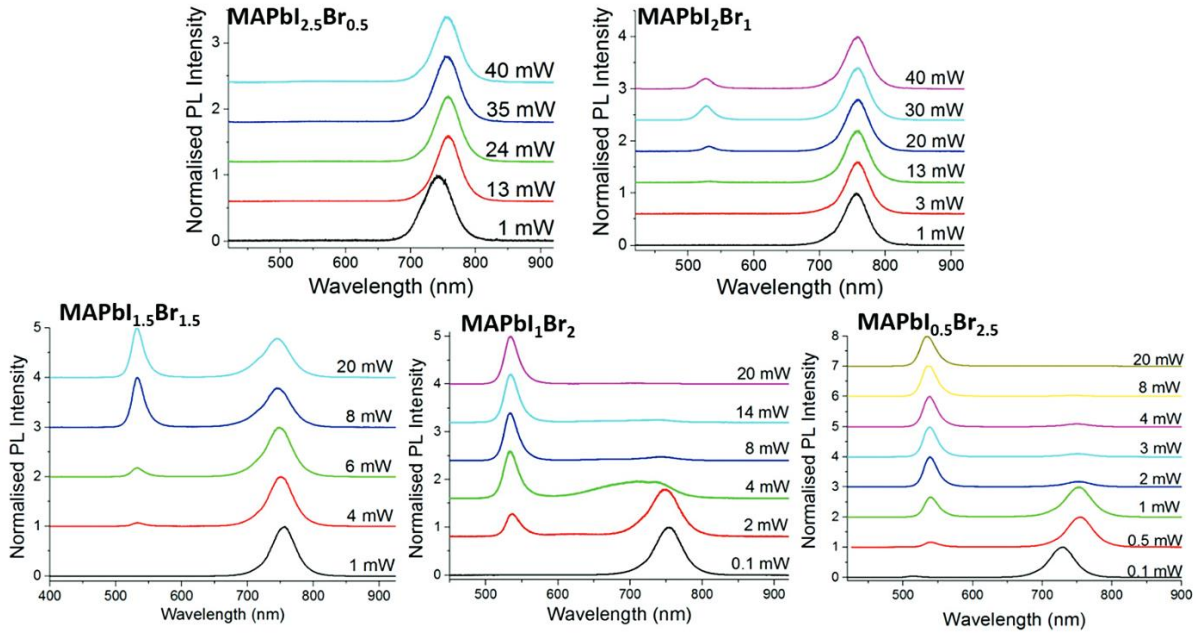

Figure 50. Normalized PL spectra as a function of power at different ratios of $MAPb(I_xBr_{1-x})_3$ mixed-halide perovskites after illumination for 900 s with a 407nm laser in ambient conditions [94].

These light-induced decomposition issues have been answered with composition-tuning strategies, generating stronger bonds between the atoms, as this is a very strong disadvantage for perovskite solar cells. For instance, M. Saliba et al. presented a work where they used a triple-cation scheme for more stable perovskite solar cells [95].

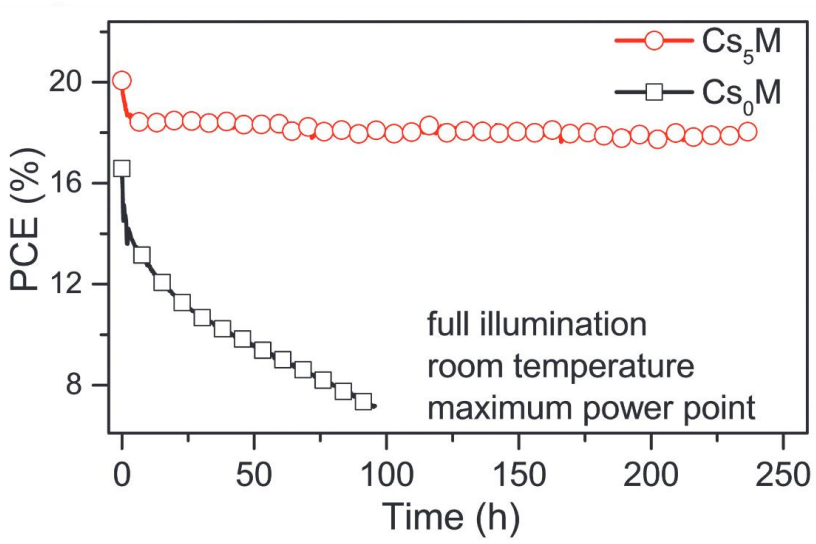

Figure 51. Aging for 250 h of a high performance a FA/MA (black line) and a Cs/FA/MA (red line) perovskite solar cell where even a small amount of Cs is crucial for the device stability. The measurement of these devices took place in a nitrogen atmosphere at room temperature under constant illumination [95].

According to figure 51, a small amount of Cs (5%) in a Cs_x $(MA_{0.17}FA_{0.83})_{(100-x)}$ Pb $(I_{0.83}Br_{0.17})_3$ seems to offer significant enhancement in terms of stability and efficiency of the perovskite solar cell.

Summarizing, for the deposition of a high-quality perovskite layer, there is need of a low humidity and controllable environment, with anhydrous reactants. Additionally, the correct choice of the ions in perovskite compounds is very important for a stable and highly efficient solar cell.

In this work, all the results that will be presented, are in absence of environmental control and at relatively high humidity ambient conditions. For this reason, we focused on techniques and procedures that provide the opportunity of a good control in an all-out-of the glovebox process. The main precaution that we follow in all processes was to use anhydrous solvents, even if they were exposed to humidity conditions for a while, and completely dry compounds. All the solutions used were prepared in the same day, to avoid humidity issues. Additionally, it is very important for the FTO/TiO_2 substrates to be fresh, and stored in a 100°C (or higher) oven, otherwise an extra annealing step is required in order to avoid any OH^- or other undesired bonds on the surface that may act negatively on the device performance. After each sample preparation, the samples were routinely stored in a nitrogen box while for each sample transfer, we used a mini vacuum system where the samples were protected from ambient conditions.

Perovskite Solar Cells- Optimization in Ambient Conditions

MACl: PbI_2 Hot-Casting Technique

Hot casting is a technique that produces large perovskite grains [96]. Large grains mean less interfaces through a perovskite film and thus reduced density of trap centers. Additionally, larger grains have fewer bulk defects and provide higher carrier mobility.

The basic concept on that technique is that substrate is annealed at high temperatures and the casted perovskite solution is crystalized during the spin coating. More specific, the perovskite nucleation starts immediately after the drop of the solution on the hot substrate and continues to crystallize as long as the solvent has not been evaporated. This process, leads to large perovskite grains that with the conventional deposition process

cannot be obtained as the most of the solvent has already been evaporated when we put the sample on the hot plate.

A schematic illustration of this process is presented below.

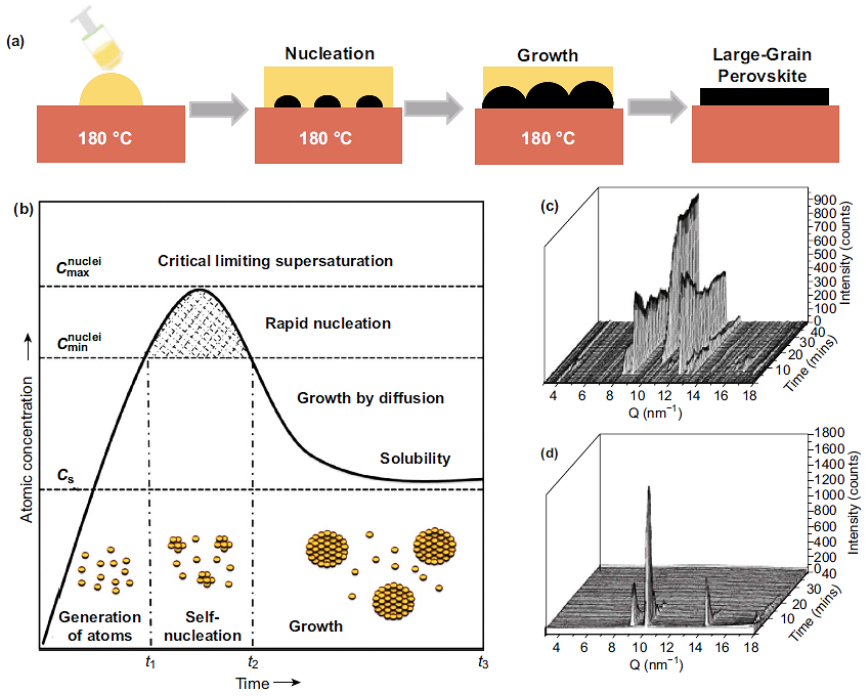

Figure 52. a) Hot-casting process, b) LaMer diagram for crystallite formation stages in a solution, c) Time-dependent grazing-incidence wide-angle X-ray scattering (GIWAXS) profiles of the perovskite film drop cast on the 70 °C substrate and d 180 °C substrate from a solution to a solid state (0–40 min) [96].

W. Nie et al. demonstrated this technique with grain size up to 200μm and showed increase of the current density in SCs for the larger grain sizes [97].

In addition, the hot casting technique provides the opportunity of minimizing the humidity factor in the solution and the substrate.

The recipe that we used was *MACl: PbI_2* in *DMF* solution targeting to a $MAPbI_3$ film. Due to its small size, Cl^{1-} cannot incorporate in the perovskite lattice, but moves inside as a free cation. That operation seems to offer to free carriers' diffusion lengths and lead to higher J_{sc} currents, as shown in the table below (fig. 53).

Perovskite	Species	D ($cm^2\ s^{-1}$)	L_D (nm)
$CH_3NH_3PbI_{3-x}Cl_x$	Electrons	0.042 ± 0.016	1069 ± 204
	Holes	0.054 ± 0.022	1213 ± 243
$CH_3NH_3PbI_3$	Electrons	0.017 ± 0.011	129 ± 41
	Holes	0.011 ± 0.007	105 ± 32

Figure 53. Values for diffusion constants (D) and diffusion lengths (LD) [98].

Another issue is that the excess of MA^+ ensures that we will not have residual PbI_2. Although a PbI_2 film contributes to the band alignment when it is on the interface of ETL and Perovskite [99] , in the hot-casting technique the crystallization starts from the Interface of ETL/Perovskite and thus, this extra barrier of PbI_2 film will appear on the surface of perovskite film, acting negatively for the device performance. Therefore, as a first step, we tried to repeat the recipe of Nie et al. but soon we understood that working in ambient conditions (high values of humidity 60-85%) change everything, when we talk about perovskite materials.

During numerous optimizations that we tried for this material, we found one really interesting in terms of white-light emission. More specific, we used 290mg PbI_2 and 130mg of MACl in 3 mL DMF. The temperatures of the substrate and the solution were at 135°C and 75 °C respectively in ambient conditions, while after deposition, the samples were not annealed further, forming a white-like film on the glass substrate. SEM image of this perovskite shows a cross-like structure, while by exciting with a 325nm cw laser at room temperature we observe a really broad emission covering most of the visible spectrum (fig.54).

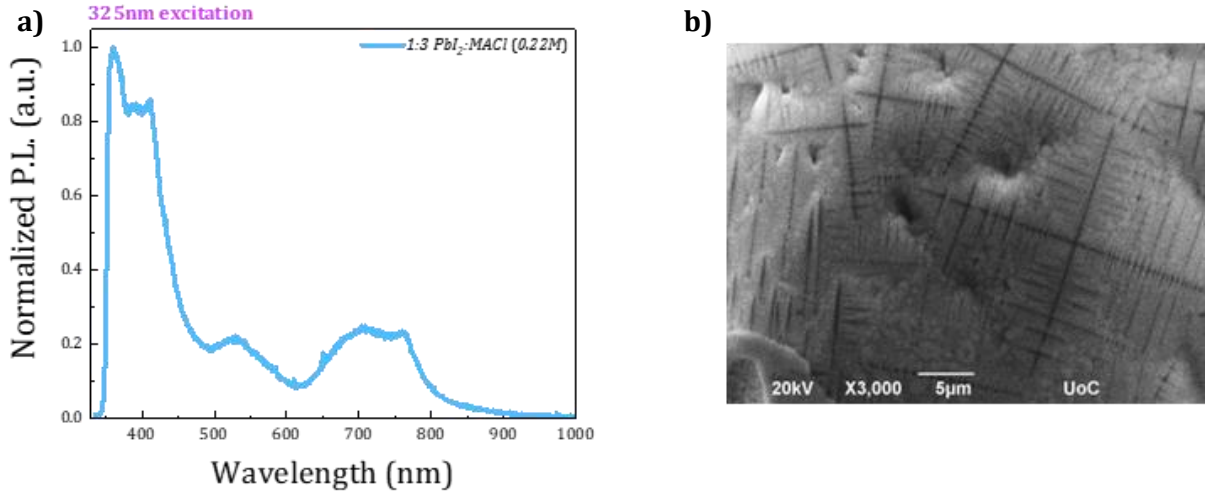

Figure 54. a) Photoluminescence and b) SEM image of MACl: PbI_2 film on glass substrate.

This observation is not very useful in terms of perovskite solar cells, but is quite interesting in terms of white light emitting perovskite, an area that many scientists are currently focusing [100] [101].

Further investigation of substrate and solution annealing's in ambient conditions showed us that humidity set limits on crystallization at high

temperature values. More specifically, after 150°C of the substrate temperature, the films are completely degraded and a yellow film form on the substrate. After numerous experiments in different conditions of temperature and humidity every time, we found some optimum conditions with a temperature for the solution at 70°C and for the substrate at 130°C.

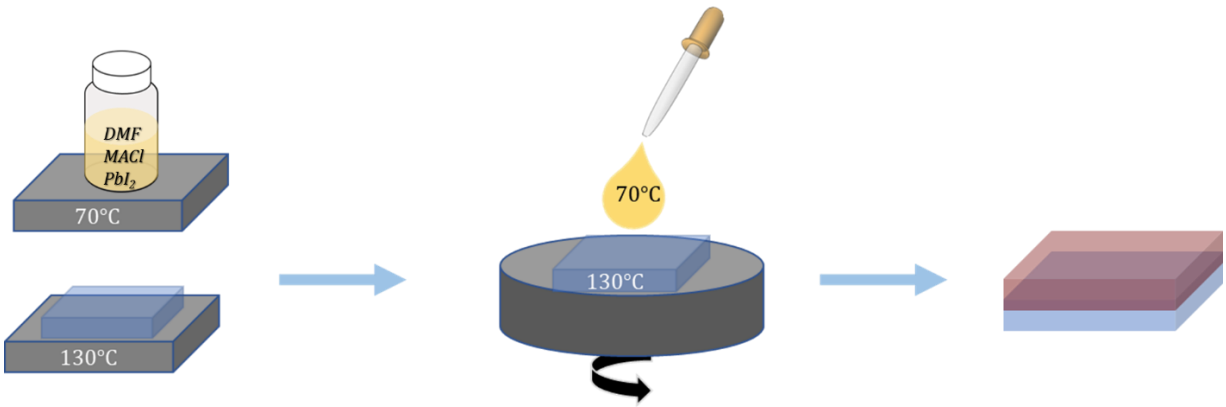

Figure 55. Illustration of optimized hot casting conditions where the crystallization finishes during the spin coating process.

In these conditions, perovskite grains larger than 10μm formed in a pinhole-free perovskite film. The optimum thickness of these films, for a perovskite-based solar, is ~450nm as described elsewhere [94]. For the SC device preparation, prior to the perovskite deposition, we treated the FTO/TiO2-c/TiO2-mp substrates with oxygen plasma for at least 10minutes to obtain a uniform film deposition. After perovskite deposition, the perovskite heterostructure was completed with the CuSCN deposition. For the optimum temperature conditions of MACl: PbI2, the film was spin-coated at 4000rpm with 1000rpm/sec for 30sec, while the CuSCN spin-coating conditions were at 2000rpm with 1000rpm/sec for 30sec.

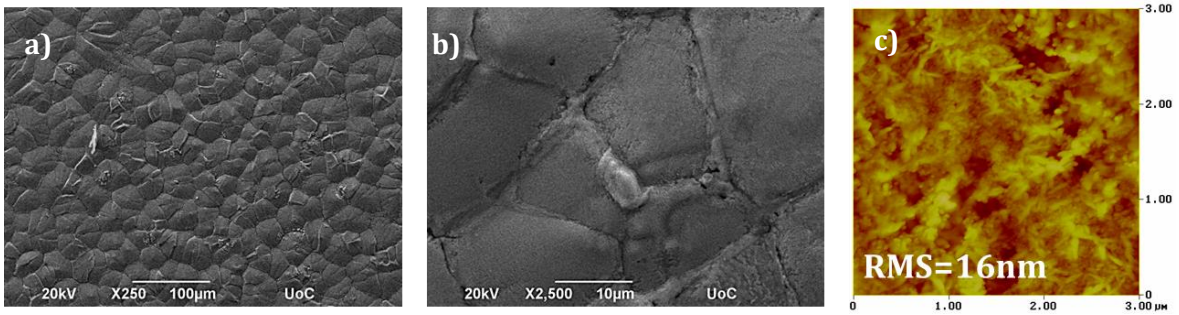

Figure 56. SEM Image of a MACl: PbI_2 hot-casted film on a FTO/$TiO_{2\text{-}c}$/$TiO_{2\text{-}mp}$ substrate a) x250 and b) x2500 zoom in and c) AFM of CuSCN deposited on FTO/$TiO_{2\text{-}c}$/$TiO_{2\text{-}mp}$/Perovskite substrate.

For the top electrode we deposited via RF-Sputtering a ~100nm thick Au layer. These devices exhibited a big non-uniformity from diode to diode,

while for one of the best devices' characteristics were V_{OC}= 0.91V, J_{SC}=9mA/cm^2, FF=48% and efficiency 3.93%. Diode analysis of this device showed an ideality factor ~2.2 with a R_{shunt}= 80 kΩcm^2 and a R_{series}= 10kΩcm^2. This high value of series resistance is probably resistance at the interfaces of different layers rather than resistance from the bulk perovskite layer which nucleates with the hot-casting technique which protects from humidity.

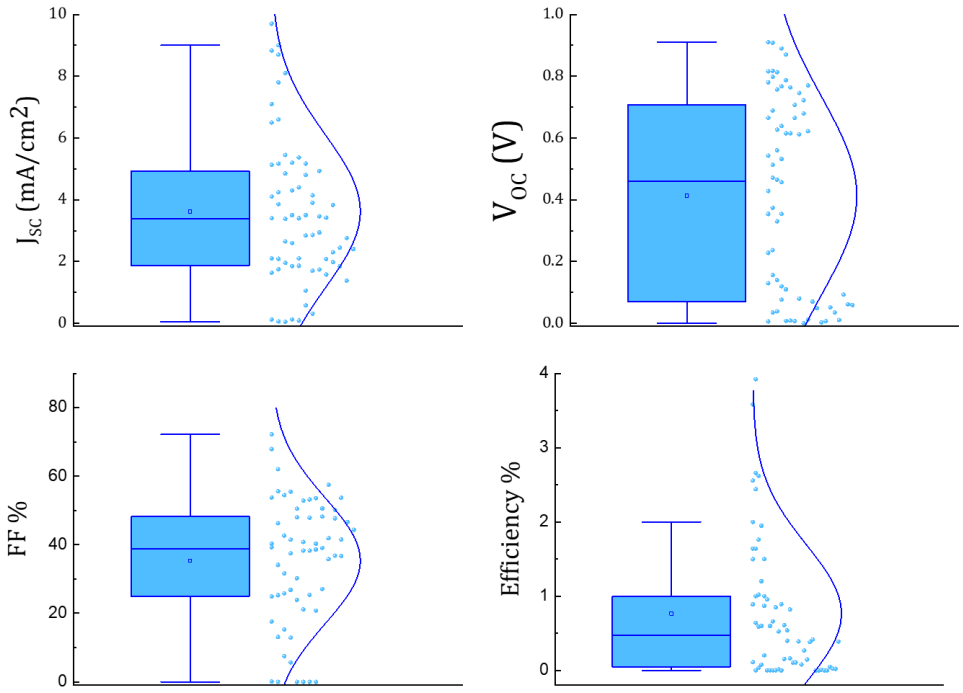

Figure 57. Extracted photovoltaic results of hot casted perovskite solar cells.

Big deviations and low extracted photovoltaic parameters compared to other works, especially for J_{SC} and FF lead to low efficiencies, most likely to the uncontrollable deposition conditions and the high-humidity values. At this point, we should mention that the hot-casting technique requires good control of the deposition process with very quick and repeatable actions during the transport of the substrate and solution from the hotplates to the spin coater, risking to have significant variations of their final temperature by the time uncertainty in this manual operation.

$MA_xFA_{1-x}PbI_3$ Films with antisolvent method

In order to provide a better control of the deposition process and achieve higher efficiencies, we addressed the well-studied antisolvent technique [102] in ambient conditions. This technique introduces more degrees of freedom, which can be controlled for a more efficient, controllable and reproducible procedure. The main steps of this method are represented in figure 58. For this technique, we need an extra solvent, where the perovskite cannot be dissolved (anti-solvent). As a first step, we deposit the perovskite precursor solution, and we spread it to the substrate via spinning. After a few seconds, we drop an amount of the antisolvent, which accelerates the crystallization during the spin-coating process. Finally, we anneal the substrate in order to evaporate the residual solvents.

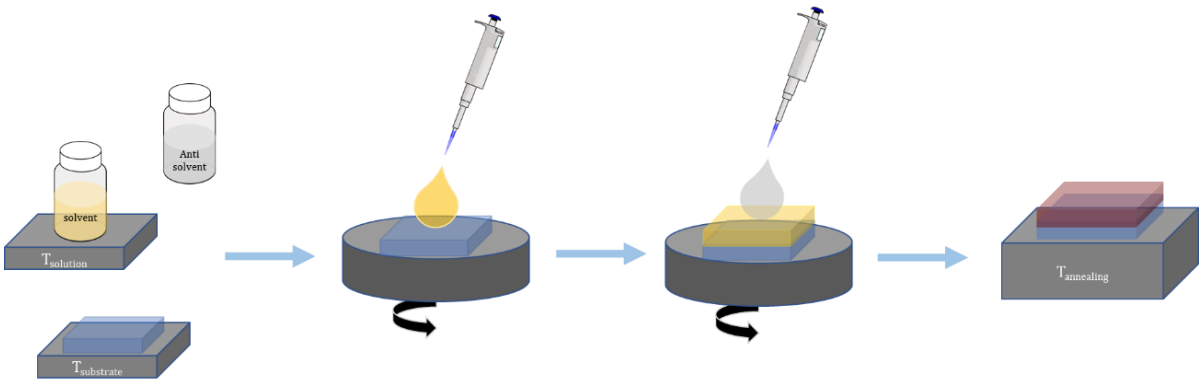

Figure 58. Schematic Representation of Antisolvent Process.

In order to find our optimum conditions, we tried several spin coating routines with different post annealing temperatures up to above 100°C and different durations (5min, 10 min, 15min and 20min). For these experiments we used a $MAPbI_3$ powder in a DMF: DMSO (4:1) mixed solvent for increased solubility, while as antisolvent we used Chlorobenzene. These experiments allowed us to study the post annealing effect on the final structure of the perovskite. According to our observations the crystallization quality of the perovskite was strongly dependent on the annealing time in ambient conditions, where for times longer than 10min the films were degraded and formed a yellow phase on the hot plate. Keeping the annealing time less than 10minutes, we focused on the annealing temperature effect, so we tried to crystallize the perovskite at lower annealing temperatures according to the literature for ~5min.

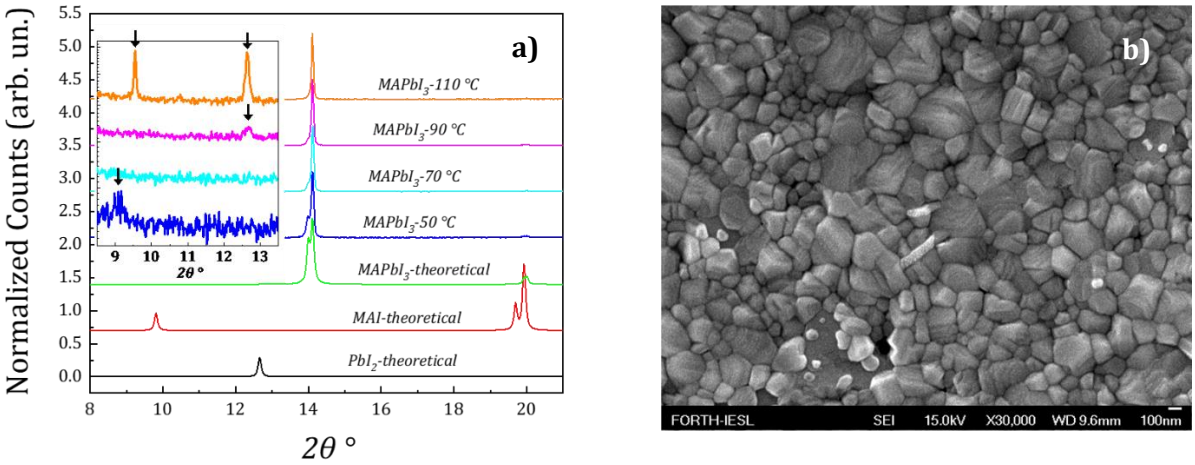

Figure 59. a) XRD patterns for $MAPbI_3$ film crystallization at different temperatures for 5minutes in ambient condition, with a log-scale inset graph focusing on low angles, and b) SEM image of optimum annealing at 65°C for 6minutes.

As shown in figure 59, XRD patterns at various annealing temperatures show a non-degradation of the main perovskite peak, but at 50°C we observe in the inset an extra peak at 9.08°, that we assume it is a phase between the perovskite and the solvent, where the low annealing temperature was not enough to dissolve it. As we increase the annealing temperature from 50°C to 90°C, we observe that the film obtains a preferred orientation at 14.1° for the pure perovskite phase, while for temperatures ~90°C we observe the beginning of degradation of the perovskite as presented in the inset of figure 59 (a). Further experiments showed us that a very important factor for a uniform, well crystallized and pinhole-free film out of a glove-box is that the drop of antisolvent should fall before the solvent of perovskite starts to evaporate. Otherwise, non-uniformities and wire-like structures are formed. After further experiments, we found our optimum annealing conditions at 65°C for 5minutes. A top view SEM image of such a film is presented in figure 59 (b) with well-defined crystallites and pinhole-free film.

In terms of humidity protection during the deposition process, we try to deposit the perovskite on hot substrates in an attempt to imitate the hot-casting technique. For that purpose, we used a 1M $MAPbI_3$ in DMF: DMSO solution at different substrate temperatures, while the solution temperature was fixed at 65°C. The spinning conditions were the same while we used an FTO/$TiO_{2\text{-com}}$/$TiO_{2\text{-mp}}$ substrate.

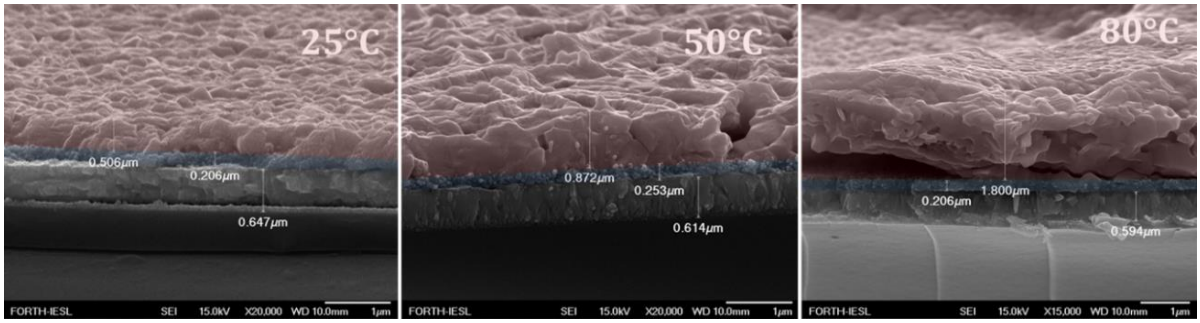

Figure 60. MAPbI3 films at different substrate temperatures.

According to figure 60, we see that by increasing the substrate temperature, the thickness of the film also increased significantly with an extra increase of the surface roughness. Moreover, for a better control in our experiments, we tried to optimize further the uniformity and thickness of perovskite film varying the spin-coating conditions and the molarity of the solution, while we kept the substrate and the solution temperature at 65°C, which is also the optimum annealing temperature based on the experiments described above.

Additionally, an extra 2D passivation layer was deposited on $MAPbI_3$ [90]. This layer seems to protect/decrease surface and grain defects and provides more efficient and stable solar cells.

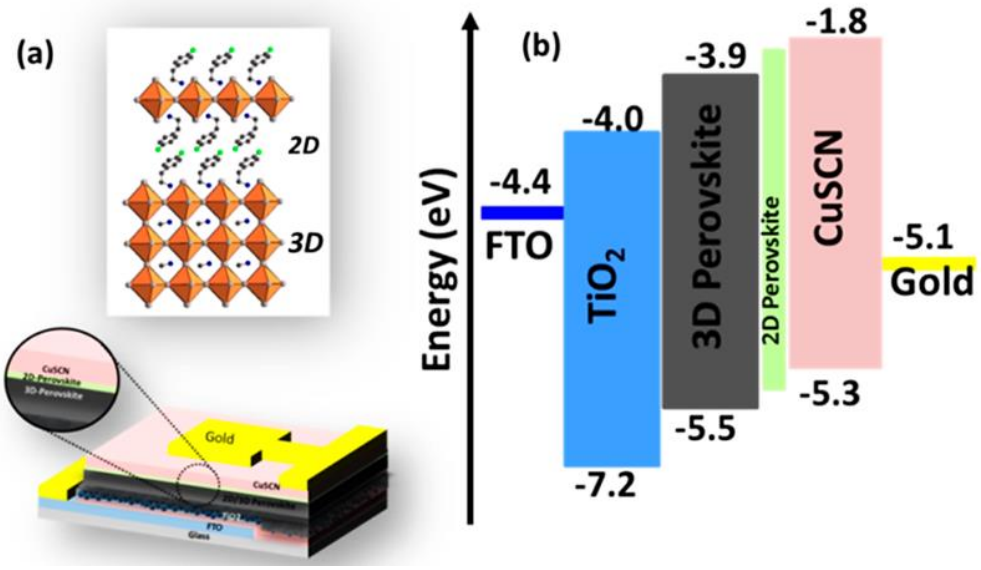

Figure 61. (a) Device architecture with a 2D passivation Layer and (b) the respective energy band alignment of this structure [90].

For our purpose, a 15mM of PEA-Cl in IPA was deposited on the perovskite layer at 2000rpm, 1000rpm/sec for 30sec.

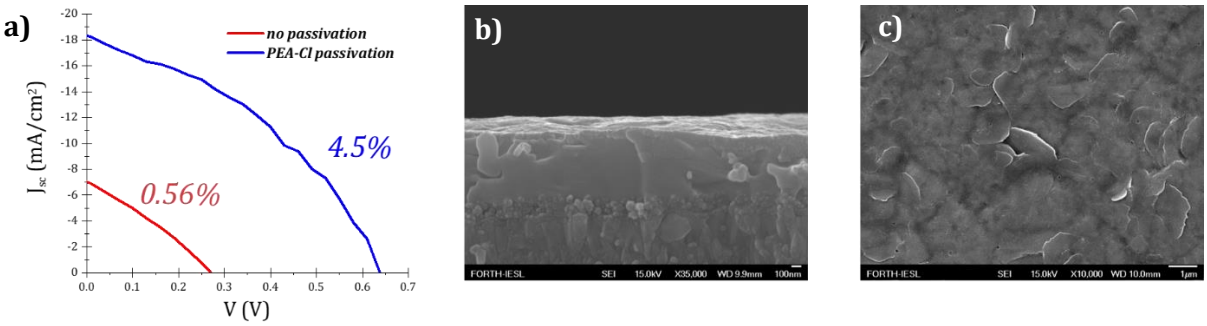

Figure 62. a) J-V measurements under 1sun illumination for a passivated and an un-passivated film, b) cross section SEM image and c) passivated surface with PEA-Cl flakes.

In order to examine the passivation effect, two identical devices were fabricated using the antisolvent technique with a ~600nm thick $MAPbI_3$ layer and a 100nm thick CuSCN HTL layer (figure 62). The only difference between these two devices was the extra 2D passivation layer. According to the J-V results, we observe a giant increase of efficiency, from 0.56% to 4.5% with significant increase of J_{sc} and V_{oc} as a result of passivation of surface and grain defects but also protection of moisture damage. Therefore, it is clear that we have a serious effect of the ambient conditions in our device's behavior, while this 2D passivation layer seems to be necessary for any further optimizations we may perform.

Another extra step in terms of increased stability and enhanced efficiency in ambient conditions was the addition of an extra cation. For that purpose, we used the less hygroscopic FA^+ in a 50:50 ratio with MA^+ and we tried the same optimization procedure with the $MAPbI_3$ films. Much to our surprise, the optimized conditions were the same as for the MA-based films, which suggest a general out-of-the-glovebox procedure for high quality perovskite films.

Another optimization we tried was varying the solvent of the precursor solution. Specifically, we replaced the DMF solvent with GBL, using a 7:3 GBL: DMSO solvent for a $MAPbI_3$ perovskite [102], keeping all the other parameters constant for comparison. From our experiments, we saw that the GBL: DMSO based films produced more uniform but thinner films compared to the DMF: DMSO. Additionally, the GBL-based perovskite surface, due to the lower overall roughness, enhanced the uniformity of the SPIRO-OMeTAD HTL layer.

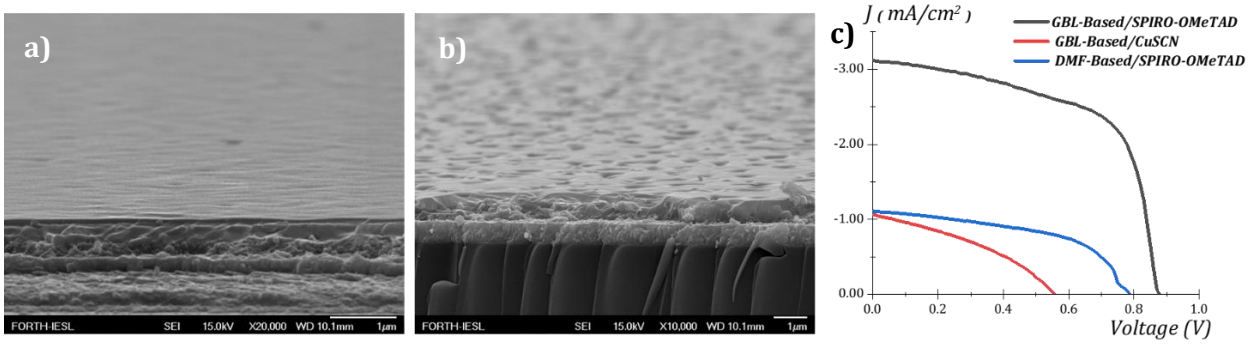

Figure 63. SEM image of FTO/$TiO_{2\text{-}com}$/$TiO_{2\text{-}mp}$/Perovskite/SPIRO-OMeTAD device with a a) GBL: DMSO and b) DMF: DMSO precursor solvent with c) the respective J-V curves.

For that batch, we used 0.2M $MA_{0.5}FA_{0.5}PbI_3$ perovskite compound with instant acceleration at 6000rpm with a 500μL Chlorobenzene antisolvent drop at the 15th second of the spin-coating process, leading to a ~200nm GBL-based and a ~400nm DMF-based thick film as presented in figure 63 (a) and (b) respectively. Additionally, we compare the effect of SPIRO-OMeTAD and CuSCN as HTLs', so an identical to GBL-based device with CuSCN instead of SPIRO-OMeTAD was also measured. The extracted resistances from dark IV analysis for Perovskite (GBL -based)/SPIRO-OMeTAD were R_{series}= *1.6 Ωcm² and* R_{shunt}= *27.2 Ωcm²*, for Perovskite (DMF -based)/SPIRO-OMeTAD were R_{series}= *68 Ωcm² and* R_{shunt}= *3.1 MΩcm²* and for Perovskite (GBL -based)/CuSCN were R_{series}= *2.2 Ωcm² and* R_{shunt}= *1 KΩcm²*. As we see, the GBL-based devices provide low series resistance, while it seems that we have shunt paths especially for SPIRO-OMeTAD-based devices. For DMF-based device we have serious series resistance issues, while the shunt resistance is much higher compared to the GBL-based devices.

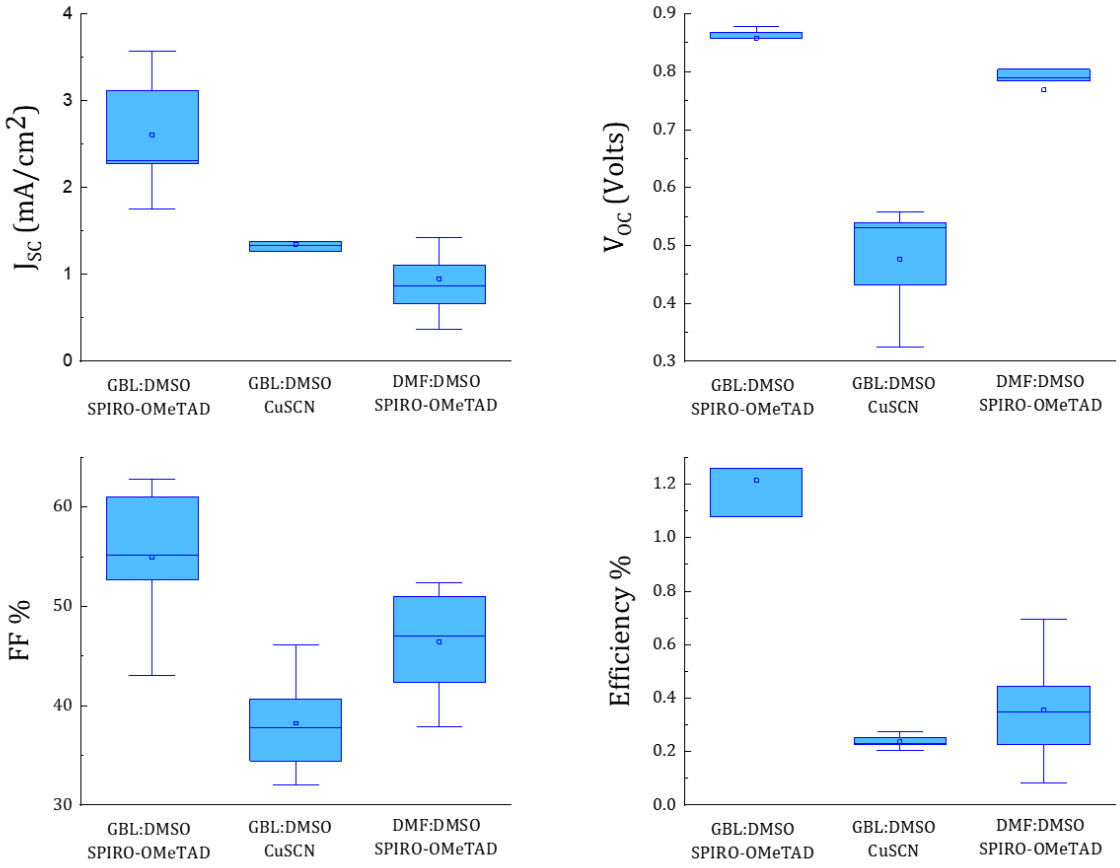

Figure 64. Statistical extracted photovoltaic characteristics for GBL-based and DMF-based devices with SPIRO-OMeTAD and CuSCN HTLs'.

According to the extracted photovoltaic parameters, we can understand that SPIRO-OMeTAD provides a better band alignment compared to CuSCN and this becomes clear from the extracted open circuit voltage values. The resistance effect provides low fill factor values for all three devices, while highest current density is measured for the Perovskite (GBL -based)/SPIRO-OMeTAD device having the best performance.

$MA_xFA_{1-x}PbI_3$ Films with gas-quenching technique

Further investigations in terms of perovskite uniformity led us to an alternative, antisolvent–free technique which provides more uniform and well-defined films. This technique is well known as gas-quenching technique [103], where we replace the chlorobenzene drop with continuous nitrogen flow.

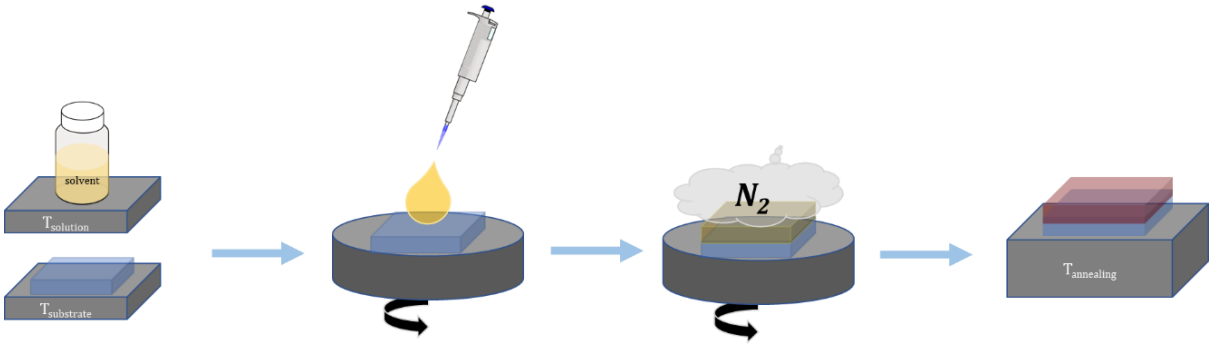

Figure 65. Gas Quenching Technique step by step.

This technique is more friendly for out-of-glovebox deposition and provides more uniform films, even in the macroscopic scale with naked eye. The produced films are uniform over a large area of the film, while antisolvent technique produces non-uniformities as we move from the center to the edges of the film. In order to compare these two techniques, we deposited two identical films with the same conditions, where in one we used antisolvent (chlorobenzene) crystallization technique and for the other gas-quenching technique. For the gas-quenching technique, we follow a pretty similar deposition process with that of antisolvent, where we first drop the perovskite solution and we spread via spin-coating. After a few seconds of the deposition, we apply the nitrogen flow until the end of the spinning, where the color of the perovskite film turns to darker, as evidence of crystallization of the film, as shown in figure 65. As final step, we anneal the sample on a hot plate in order to remove the residual solvents.

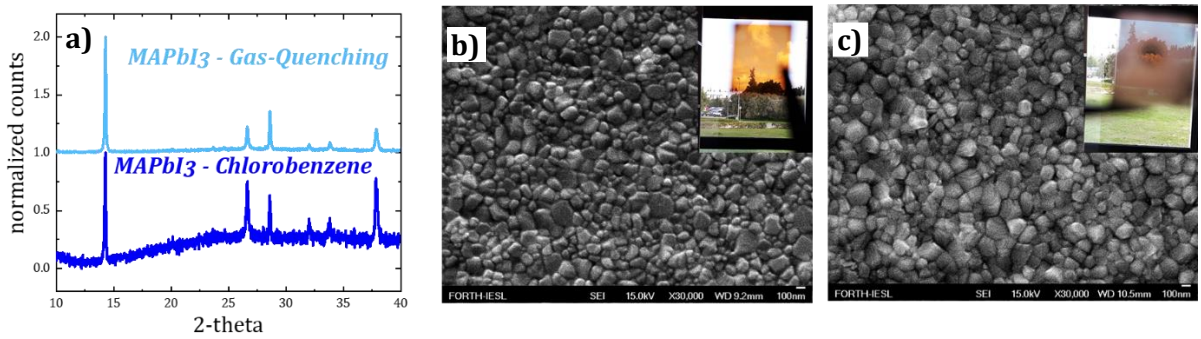

Figure 66. a) XRD pattern SEM images and a macroscopic picture (inset) of b) gas-quenching and c) antisolvent crystallization technique.

Although chlorobenzene-based grains seem a little bigger than gas-quenching grains in figure 66 b,c, the total film provides more uniformity and a less noisy XRD pattern as shown in figure 66 a, which is a sign of higher crystal quality of the film. In terms of further comparison of these two

techniques, we fabricated two FTO/TiO2-com/TiO2-mp/MAPbI3/SPIRO-OMeTAD/Au devices with the GBL: DMSO solvent mixture, where the only difference was in the crystallization process during the spin coating.

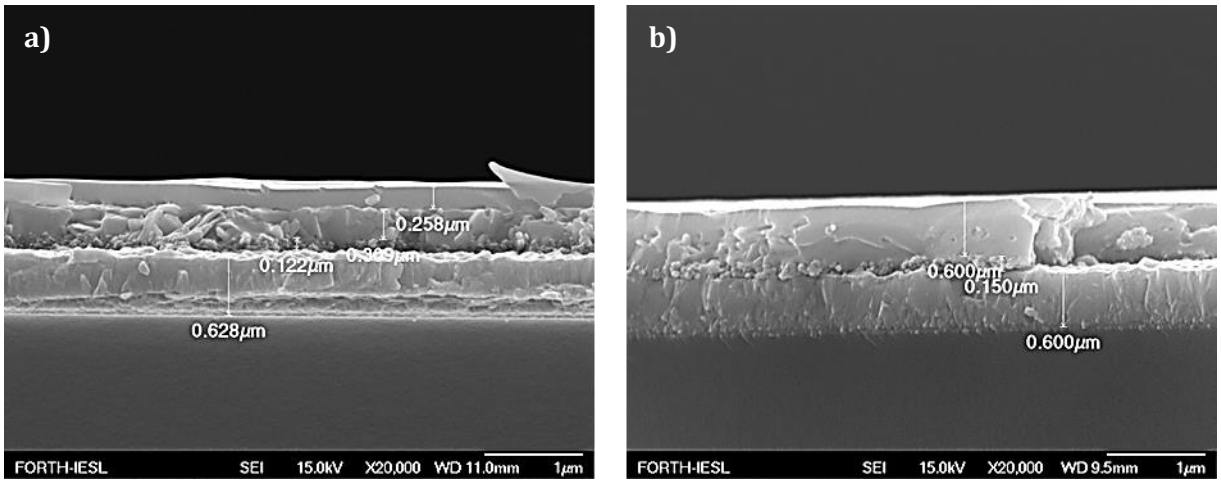

Figure 67. FTO/TiO2-com/TiO2-mp/MAPbI3 /SPIRO-OMeTAD a) Antisolvent assisted and b) Gas-Quenching assisted.

Both techniques provide a uniform ~300nm thick perovskite film with a 250nm thick SPIRO-OMeTAD as HTL on top, giving pv efficiencies ~1% for antisolvent and 1.15% for gas-quenching technique.

According to all our observations until this point, we could say that we can efficiently produce each layer of a perovskite Solar cell. We used as ETL a combination of a 60-75nm TiO_2 compact layer and a 200nm mesoporous, which were both annealed at 500°C for enhanced crystallinity and electrical properties. Although the compact TiO_2 layer is necessary for efficient isolation of the perovskite from the bottom electrode, mesoporous TiO_2 seems to be more efficient in terms of electron quenching. For HTL, we compare the CuSCN and SPIRO-OMeTAD layers and conclude that, in our system, SPIRO-OMeTAD seems to work much better. Investigations of a reproducible high quality perovskite layer showed that the key-parameter in ambient conditions is the relatively low annealing temperature after perovskite layer deposition. In terms of protection from humidity, we tried to keep the substrates ''hot'' before the perovskite deposition. We observe that by increasing the temperature of the substrate, the perovskite thickness increases with a concomitant increase of the surface roughness. In order to reduce this roughness, but keeping the pre-heated substrates, we controlled the perovskite thickness with molarity changes of the precursor solution,

while for increased surface uniformity we introduced a solvent engineering process with meaningful results. Additionally, we provided an alternative deposition process, the gas-quenching assisted process, which is environmentally friendlier, with less cost and much easier in terms of reproducibility of large deposition areas compared to the antisolvent process. Besides the above traits, both gas quenching and antisolvent process give comparable results in terms of pv efficiency.

In spite of the optimization of each individual layer with comparable results to the literature, the final solar cell devices seem to have serious resistivity issues with significantly low short-circuit currents and fill-factor values, results that reduce significantly the power conversion energy of the device. These issues probably arise from recombination centers, present either on the surface or at the grain boundaries within the layer, due to the out-of-the-glove-box fabrication process.

High Bandgap Perovskite Solar Cells for Tandem Applications

The acquired knowledge of an out-of-the-glovebox process, with main issue the humidity manipulation, allowed us to go ahead on a high-bandgap perovskite solar cell in order to combine it with the GaAs solar cells. According to other works based on GaAs-Perovskite 2-junction solar cells, the optimum bandgap of perovskite as top sub-cell is ~1.9eV. As a first step, we tried to fabricate high bandgap perovskite films, by adding Br halogens in a mixed halide MA^+-based perovskite. Toward this end, we found that a 50:50 ratio of I^-: Br^- can produce such a high bandgap $MAPb(I_{0.5}Br_{0.5})_3$ film. The mixed solvent for the precursor solution was a GBL: DMSO with a 4:1 ratio while the substrates ($T_{substrate}$) and solution ($T_{solution}$) were preheated at different temperatures prior deposition, as presented in figure 68. while we used the gas quenching technique with nitrogen pressure at 1.5mBar with 1.5cm distance from the substrate. In terms of post annealing optimization, we followed a similar routine as with the low gap perovskite films.

a)

Sample ID	$T_{solution}$	$T_{substrate}$	T_{anneal} / Δt
pv789	65°C	RT	65°C/6min
pv790	65°C	65°C	65°C/6min
Pv791	65°C	RT	65°C/6min *
Pv792	75°C	RT	75°C/6min
Pv793	75°C	RT	75°C/6min*
Pv794	100°C	RT	100°C/6min
pv795	75°C	75°C	75°C/6min

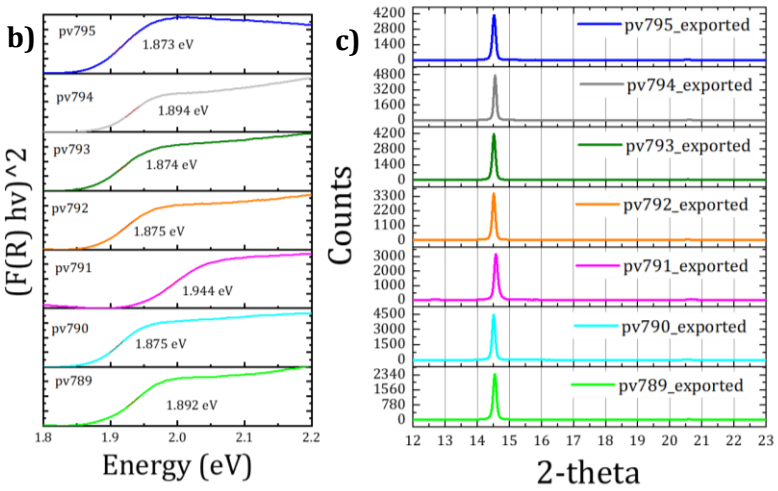

Figure 68. a) Sample's ID and respective deposition conditions, b) Kubelka-Munk Transmittance spectra and c) XRD curves of various $MAPb(I_{0.5}Br_{0.5})_3$ high bandgap films.

We see that for different annealings at low temperatures, all films are well crystallized. Additionally, Kubelka-Munk Transformation[104] spectra show a bandgap ~1.9eV for all deposition conditions. Note that pv793 is identical to pv792 with the only difference that we used 1mBar nitrogen pressure, while pv791 sample has identical deposition conditions with pv789 but for the annealing it was covered with a petri dish with a drop of isopropanol, creating an ''isopropanol-rich atmosphere'' instead of ambient conditions.

From the XRD curve and the equation:

$$2\theta_{exp} = x \cdot 2\theta_{MAPbI_3} + (1-x) \cdot 2\theta_{MAPbBr_3}$$

we extracted the composition of each film, using the theoretical position of $MAPbI_3$ and $MAPbBr_3$ XRD peaks.

	789	790	791	792	793	794	795
$MAPbI_3$ %	46	51	43	51	51	46	51
$MAPbBr_3$ %	54	49	57	49	49	54	49

Table 1. Compositional analysis of $MAPb(I_xBr_{1-x})_3$ films from a $MAPb(I_{0.5}\ Br_{0.5})_3$ precursor solution.

According to the extracted results, we see that we only get small deviations from the 50:50 composition of the precursor solution, while the XRD

patterns and the Kubelka-Munk transformation seems to be in a good agreement.

For further investigation of the perovskite film quality, we performed photoluminescence lifetime measurements. We used a 375nm pulsed laser in an Edinburg Photoluminescence Spectrometer.

For the lifetime extraction we used a two-exponential-decay fitting where, according to the literature, the fast decay was ascribed to Shockley–Read–Hall (SRH) recombination and the slow decay lifetime to radiative recombination [105], [106].

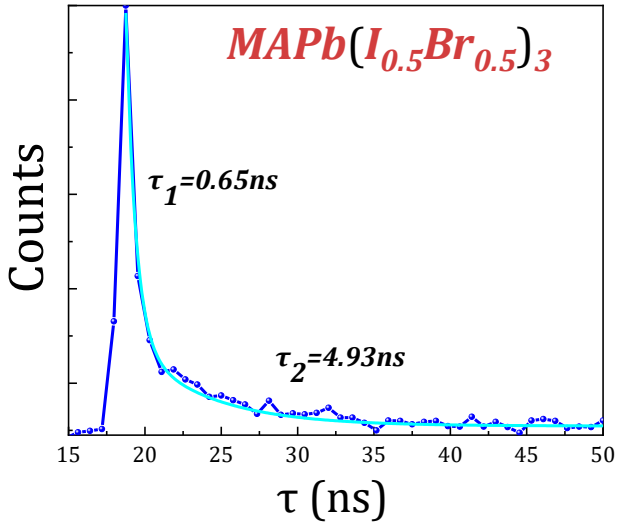

Figure 69. Lifetime-Photoluminescence for $MAPb(I_{0.5}Br_{0.5})_3$ film at 650nm on Glass Substrate.

Compared to the literature, these lifetimes are low which has impact on the extracted current and the overall performance of the solar cell[107]. Additionally, we examined the light-induced degradation of these films. For that purpose, we used a 325nm cw laser, under different illumination times and powers.

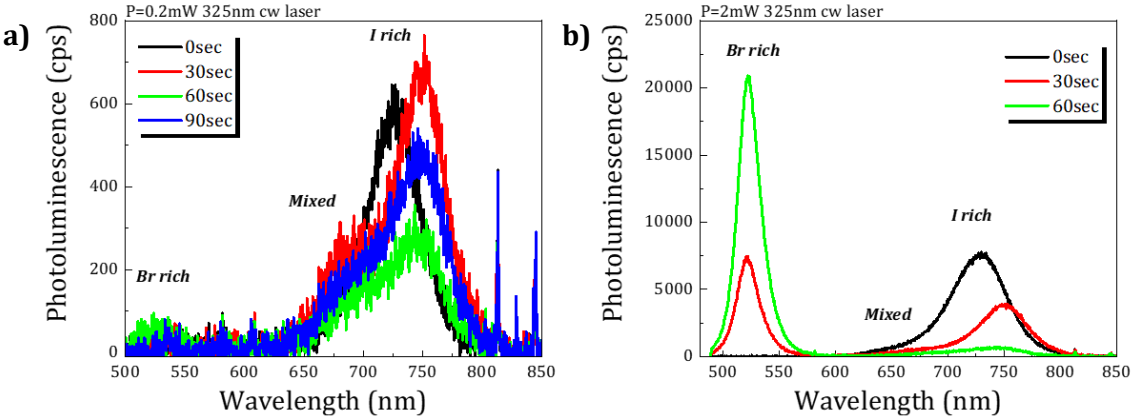

Figure 70. $MAPb(I_{0.5}Br_{0.5})_3$ film excited with a 325nm cw laser with a) 0.2mW and b) 2mW at different excitation time exposures.

The presented results show the decomposition of the perovskite film and its structural instability under illumination. More specifically, when the sample is illuminated even with a 0.2mW power, giving a low cps peak at ~675nm for the mixed compound, soon-after the photo-degradation of the film becomes obvious with a stronger peak at ~730nm as presented in figure 70(a). This decomposition gets stronger with time, with a further red-shift of the I-rich region after 30sec (fig. 70-a) and a simultaneous appearance of a Br-rich region at 520nm accompanied by a decrease of the mixed-region emission. When we increase by one-decade the power, the effect becomes more obvious with a pronounced Br-rich emission (fig. 70-b). It should be noted that these excitation powers are much higher than the 1 Sun illumination. If we think that the spot size of the incident beam was 15μm in diameter, we estimate for 1mW power a power density of ~ $3W/cm^2$ or ~ 30 Suns. To obtain a more stable high-band-gap film, we tried different approaches.

One of the compounds we tried, was the $FAPb(I_{0.5}Br_{0.5})_3$ in GBL:DMSO solvent. To our surprise, the film displayed an amorphous character according to the XRD pattern, despite any optimization that we tried.

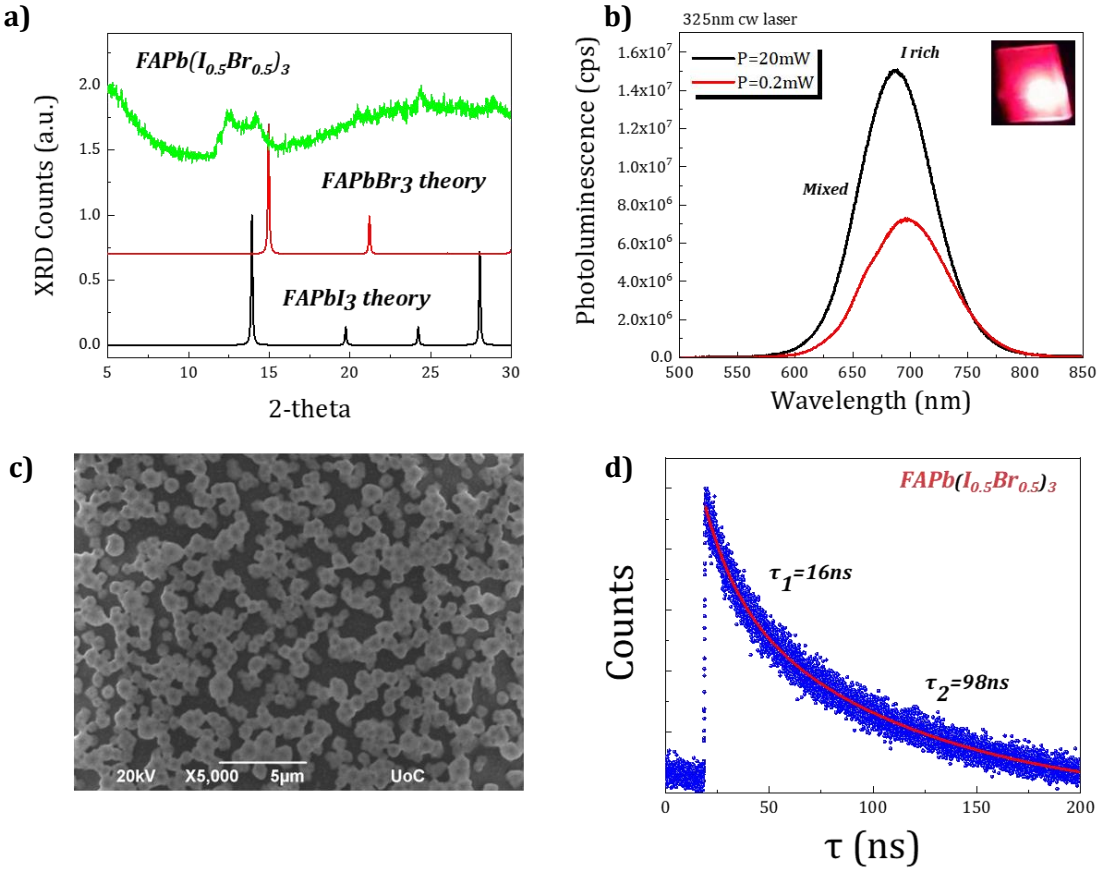

Figure 71. Characterization of a $FAPb(I_{0.5}Br_{0.5})_3$ film: a) XRD pattern, b) Photoluminescence measurement with the samples' photo shown under excitation (inset) and c) SEM image of the sample's surface and d) Time – Resolved Photoluminescence measurement at 660nm.

The main feature of this film was its photoluminescence behavior. Even a 150μm-spot was enough to spread the PL emission throughout the sample. Measuring lifetime for this sample showed increased values for both SRH and radiative recombination processes by more than one order of magnitude compared to $MAPb(I_{0.5}Br_{0.5})_3$, while its low crystallinity was observed from XRD and SEM images. For further investigation, we tried different compositions such as those presented below.

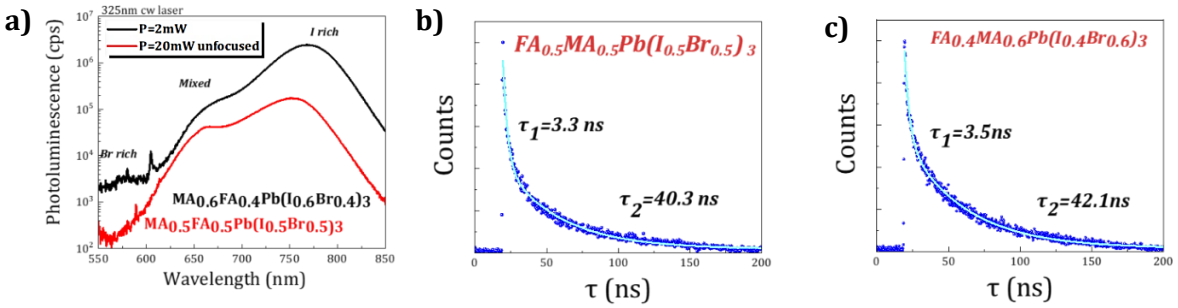

Figure 72. a) Photoluminescence measurement and lifetime photoluminescence measurement for b) $FA_{0.5}MA_{0.5}Pb(I_{0.5}Br_{0.5})_3$ and c) $FA_{0.4}MA_{0.6}Pb(I_{0.4}Br_{0.6})_3$ films.

Two films prepared as the MA-based and FA-based conditions, but with a mixed cation composition were also fabricated and characterized. The first one was $FA_{0.5}MA_{0.5}Pb(I_{0.5}Br_{0.5})_3$ and the second one was $FA_{0.4}MA_{0.6}Pb(I_{0.4}Br_{0.6})_3$ with an increased amount of MA^+ and Br^+. Both films had a pretty similar behavior, while the increased amount of Br^+ did not restrict the domination of the I-rich region. From lifetime measurements at 660nm, we could confirm that the two films were very similar. Also, the extracted lifetimes seem to be something like an average of $MAPb(I_{0.5}Br_{0.5})_3$ and $FAPb(I_{0.5}Br_{0.5})_3$ film lifetimes.

In summary, $MAPb\ (I_{0.5}Br_{0.5})_3$ films, provide the desired bandgap but they are very sensitive under illumination, with short lifetimes which make these materials inappropriate for solar cells. An interesting behavior in terms of photoluminescence measurements was shown by $FAPb\ (I_{0.5}Br_{0.5})_3$, but the low crystallinity and non-uniformity of the film sets limits for photovoltaic applications. For this reason, we moved to a mixed cation solution based on the work of P. McMeekin et al. for wide bandgap perovskites [108]. More specific, we focused on the $FA_{0.8}MA_{0.04}Cs_{0.16}Pb(I_{0.5}Br_{0.5})_3$ + 5% $PbCl_2$ in a DMF: DMSO (4:1) solvent, while as crystallization technique, we used antisolvent technique with ethyl acetate as antisolvent. This combination showed the best morphology of the deposited films, so we focused on the optimization of the deposition parameters of this triple-cation, high-bandgap perovskite. The optimal conditions for these films in our system were 3000rpm with 1000rpm/sec for 40sec, with 1mL of antisolvent at the 10^{th} second of spin coating. The substrate and the solution were at 65°C while after deposition the films were annealed for 6min at the same temperature. The crystallization occurred with the drop of the antisolvent and the film turned into a dark red color.

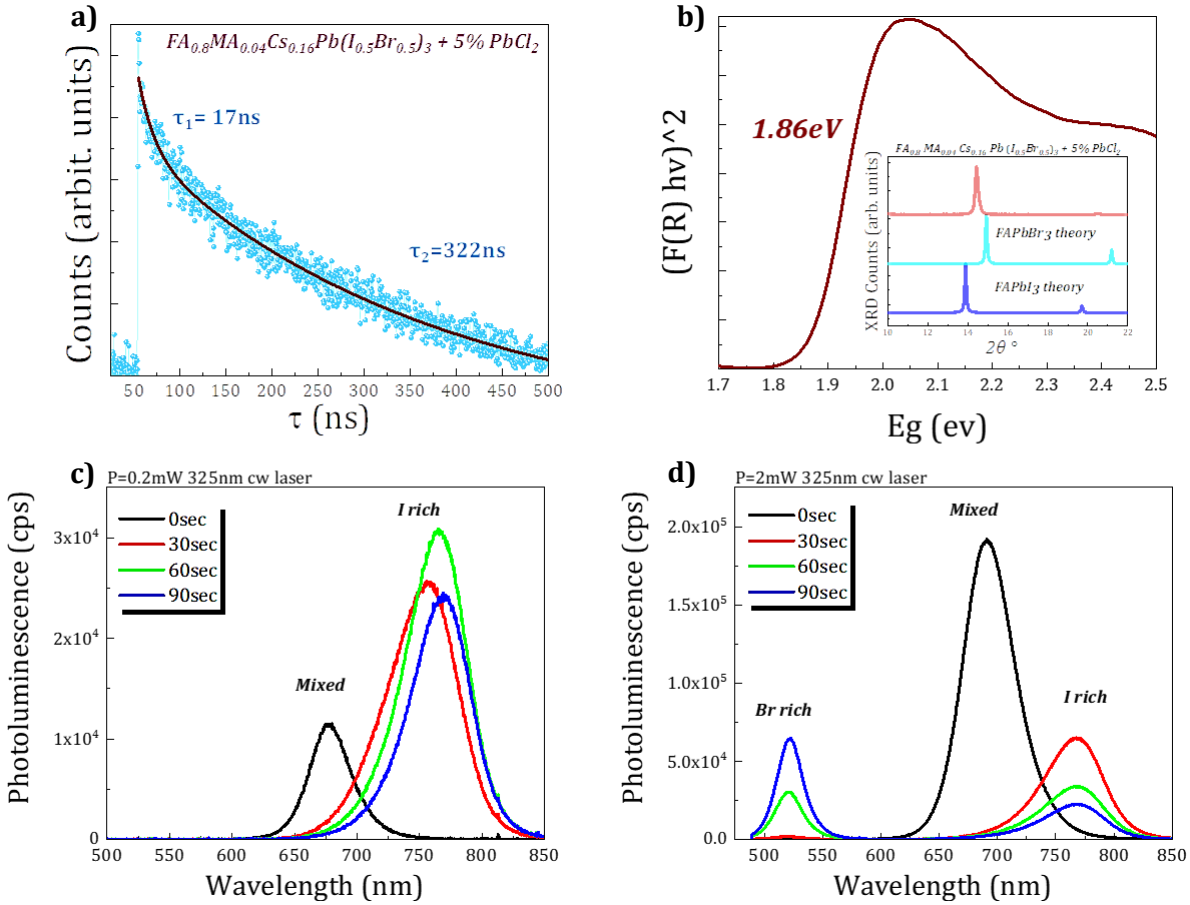

Figure 73. a) Lifetime-Photoluminescence at 660nm with a 375nm pulsed laser, b) Kubelka-Munk Transformation and XRD pattern (inset), photoluminescence using a 325nm cw laser with c) ~0.6W/cm² and d) 6W/cm² at different exposure times for a $FA_{0.8}MA_{0.04}Cs_{0.16}Pb(I_{0.5}Br_{0.5})_3$ + 5% $PbCl_2$ film on Glass Substrate.

This triple-cation film, showed a better behavior in terms of crystallinity and free carrier life time compared to all previously studied films. On other hand, the phase separation phenomena persist. As shown in figure 73c, when exciting with a power density of ~6suns we observe a rapid evolution with exposure time to an I-rich dominated spectrum. The effect is accentuated when using an illumination equivalent to ~60 Suns. In this case, not only do we observe the I-rich formations, but we obtain PL emission from Br-rich inclusions as well.

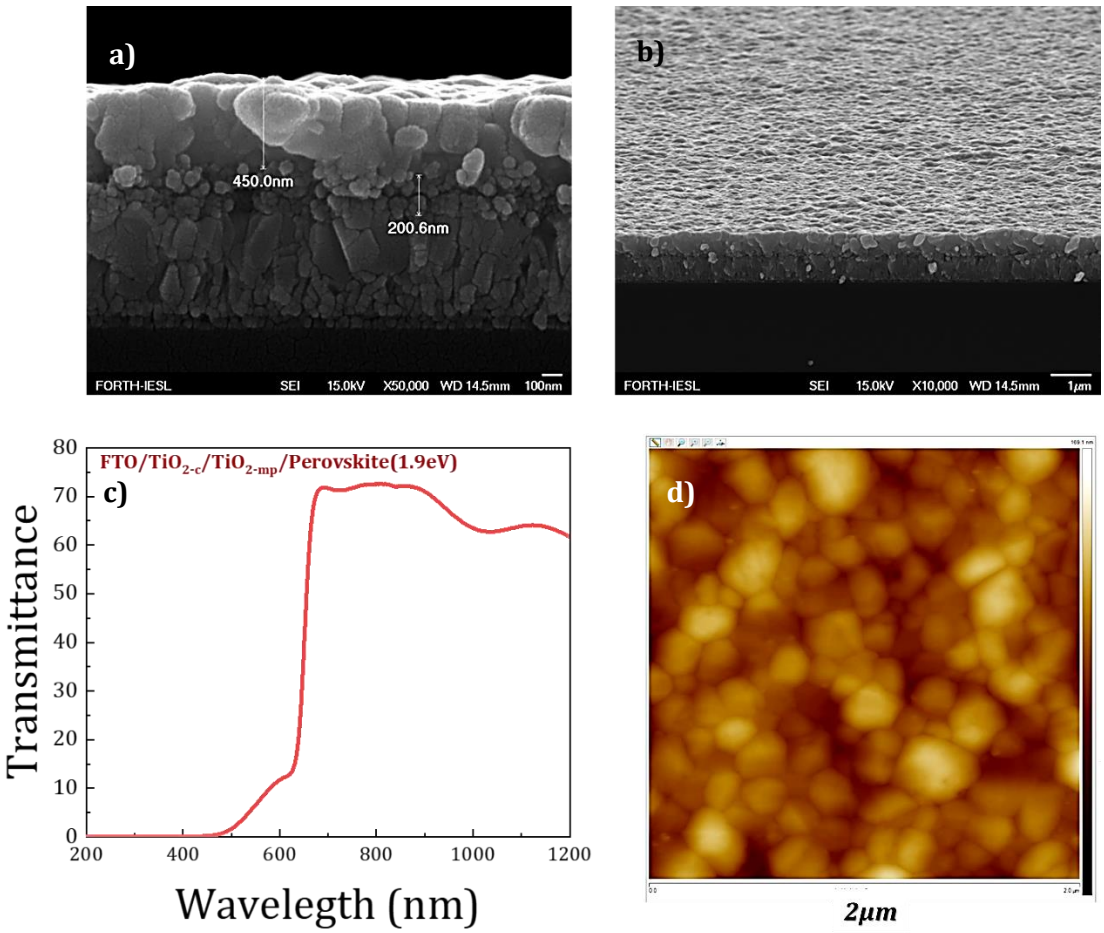

Figure 74. a) Cross section and b) Tilted SEM image of triple-cation deposited on FTO/$TiO_{2\text{-}compact}$/$TiO_{2\text{-}mesoporous}$, c) Transmittance and d) AFM image of the same sample.

As a next step, we fabricated an FTO/$TiO_{2\text{-com}}$/$TiO_{2\text{-mesop}}$/Perovskite/SPIRO-OMeTAD/Au high band-gap perovskite device using our optimum conditions. Transmittance measurements on the device showed an abrupt absorption at ~650nm which is our desired bandgap (fig. 74c).

The SEM images of the device structure show a uniform film with about 450nm thickness, having relatively large grains with an average value of ~200nm, while its surface roughness measured by AFM was low, ~15nm.

We fabricated devices with and without various passivations, while we also introduced the extra $TiCl_4$ treatment between compact and mesoporous TiO_2 layer. Thus, 4 different devices were fabricated, the first one was the regular structure (no passivation, no $TiCl_4$ treatment), the next one was with an extra PEA-Cl passivation layer, the third one with PEA-I instead of PEA-Cl, and the last one with no passivation but with a $TiCl_4$ treatment. As HTL for all 4 samples we used a SPIRO-OMeTAD film with identical deposition

conditions while the extracted device results under 1 sun illumination are presented in figure 75.

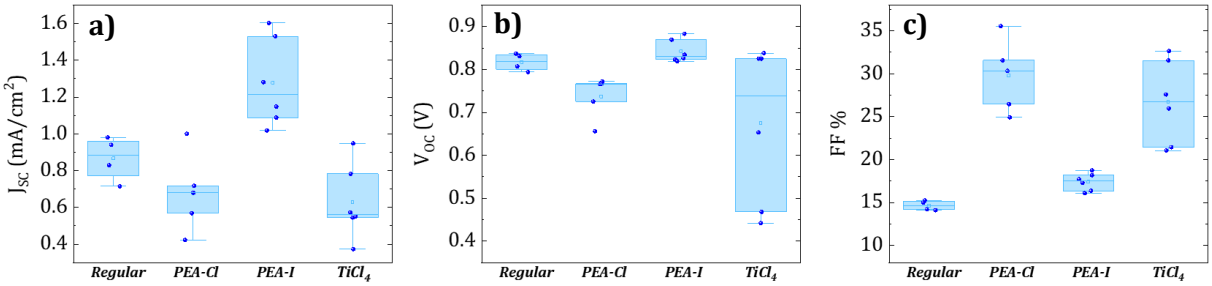

Figure 75. a) Short Circuit Current, b) Open Circuit Voltage and c) Fill Factor of all the triple-cation "red" devices under 1sun illumination.

According to the extracted results, besides their particular low values, we could say that $TiCl_4$ treatment, PEA-Cl and PEA-I seem to increase the Fill Factor parameter, while PEA-Cl and $TiCl_4$ treatment seem to affect the J_{SC} and V_{OC} values. From the other side, PEA-I seems to increase them, especially the J_{SC} values. The extracted efficiencies were between 0.1-0.2%. Further optimization came through the study of SPIRO-OMeTAD.

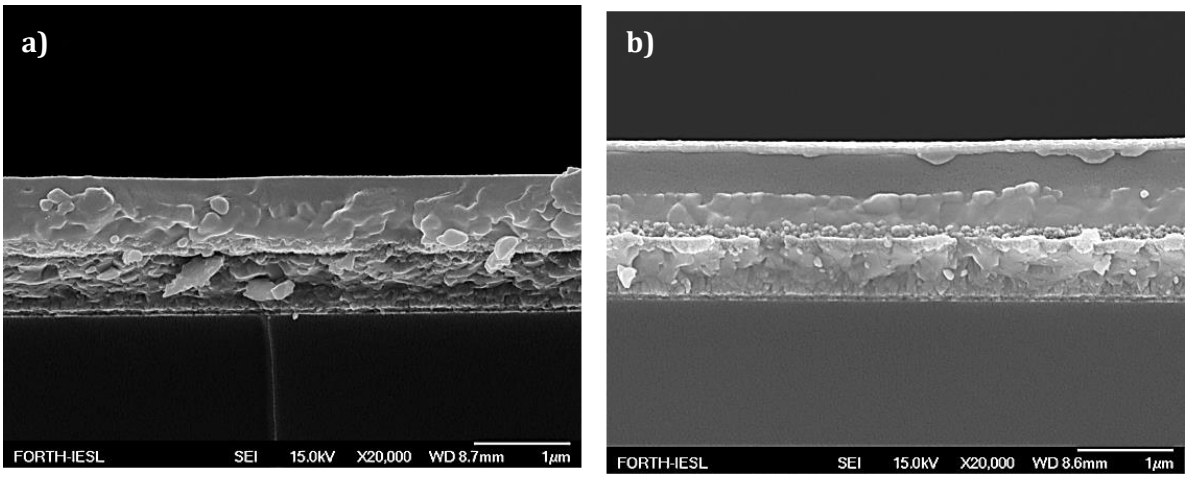

Figure 76. a) FTO/$TiO_{2\text{-}com}$/$TiO_{2\text{-}mesop}$/Perovskite/ Low Molarity (LM) SPIRO-OMeTAD and b) FTO/$TiO_{2\text{-}com}$/$TiO_{2\text{-}mesop}$/Perovskite/High molarity (hM) SPIRO-OMeTAD/Au

On that purpose, we fabricated 2 identical, passivation-free devices. The conventional recipe of SPIRO-OMeTAD gave us a 250nm thick film. In order to increase its thickness, we tried to decreased the spin coating rpms but this step gave us increased non-uniformities. Thus, we increase the molarity of the solution and this process gave us a 400nm uniform HTL film.

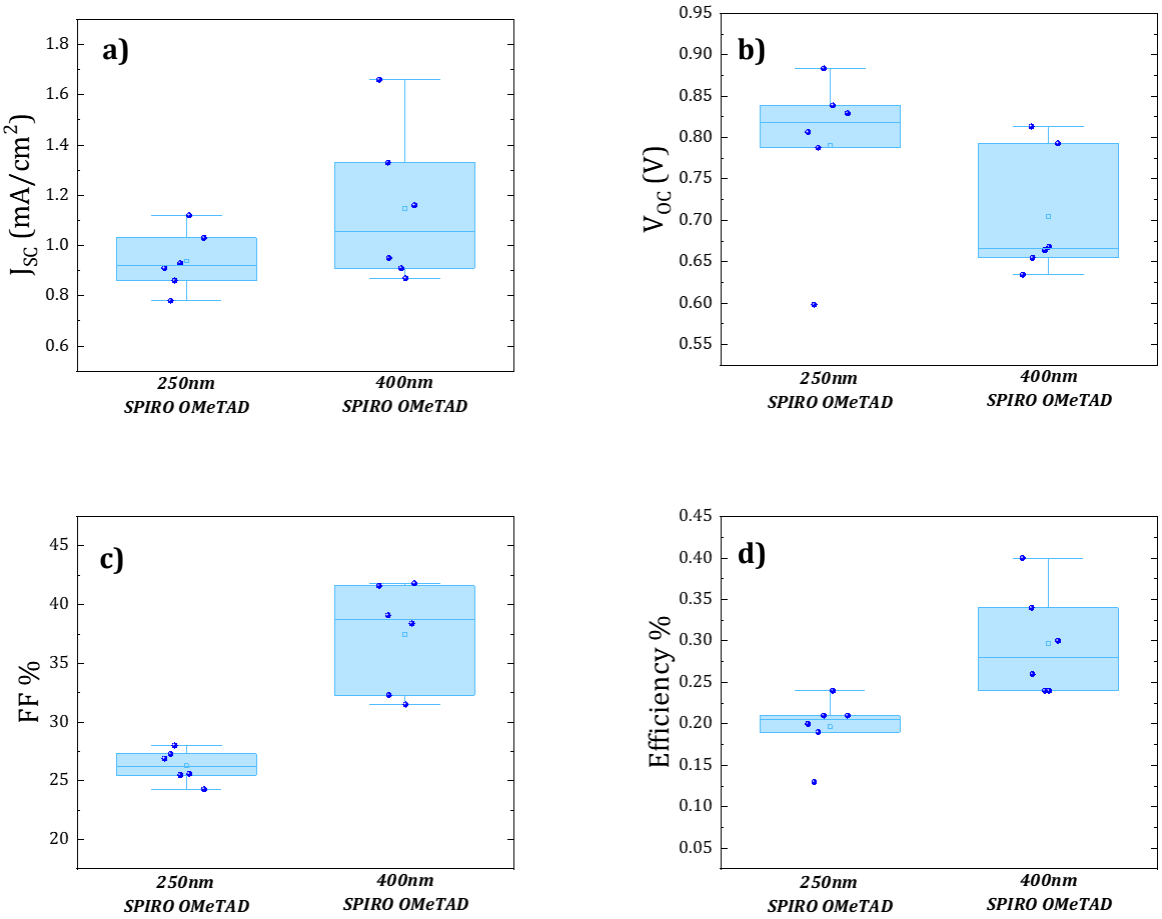

Figure 77. Extracted a) $J_{SC,}$ b) $V_{OC,}$ c) FF, and d) efficiency of the 250nm and the 400nm thick SPIRO-OMeTAD.

The extracted results in figure 77 showed improvement for $J_{SC,}$ FF and efficiency values with a slight decreased for V_{OC}. Besides the low extracted values of the red perovskite solar cells, there is a lot of room for improvements. More specifically, by perovskite powder re-drying before each solution preparation we observed an important increase of the extracted parameters compared to the previous results. This is shown in figure 78, with a PV efficiency reaching on one device 1.6%.

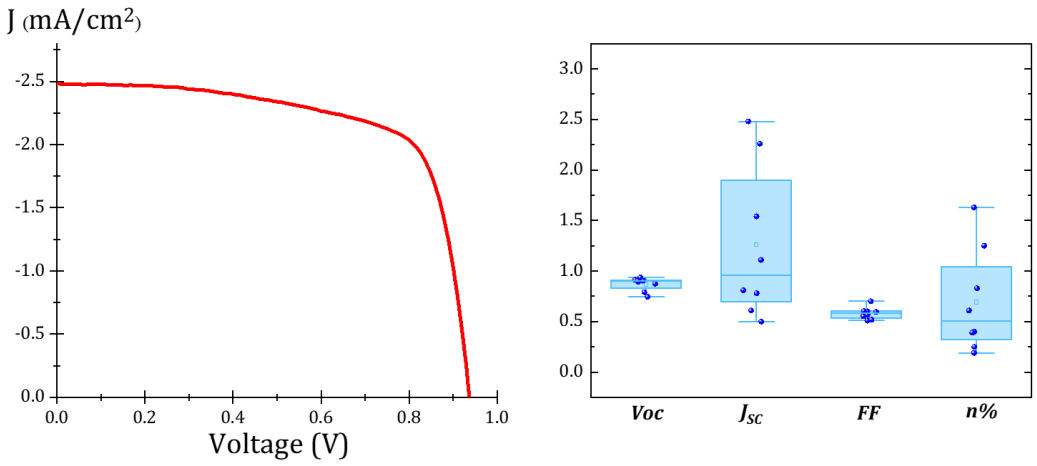

Figure 78. The effect of re-drying the perovskite powder before the solution preparation on statistics of J-V curve under 1sun illumination (forward scan) and the extracted parameters of other diodes of this device.

Clearly, the humidity factor seems to have a serious effect on the overall efficiency. Based on that, we tried to re-dry additionally the SPIRO-OMeTAD powder before HTL preparation, a process that boosted more the extracted efficiency.

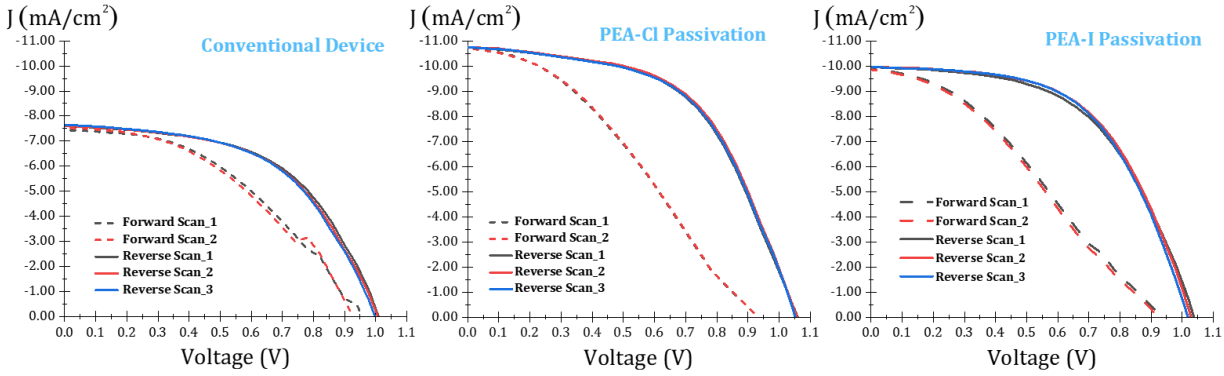

Figure 79. J-V curves of conventional, PEA-Cl passivated and PEA-I passivated device.

This extra dry-step revealed the effect of moisture even on the preparation of SPIRO-OMeTAD, which can produce significant losses on the perovskite device. According to the measurements showing in figure 79, we see that we have a significant increase of current values with a small increase of the V_{OC} as well. Additionally, the device presents stability under repetitive scans in the same direction, while we observe hysteresis between forward and reverse scans. The extra 2D passivation layer also improved the device characteristics with more beneficial the PEA-Cl passivation compared to the PEA-I passivation layer. More specifically, the extracted values for the conventional FTO/ $TiO_{2\text{-com}}$/ $TiCl_4$/ $TiO_{2\text{-mesop}}$/ Red-Perovskite/ (hM)SPIRO-

OMeTAD/ Au device in reverse scan were 4.14% efficiency, with a 54% FF, 7.67mA/cm² short circuit current and ~1V open circuit voltage. For PEA-I and PEA-Cl passivated devices, the extracted values were respectively 5.64% and 6.23% efficiency, 54.8% FF for both, 10.1mA/cm² and 10.76 mA/cm² short circuit current and ~1.02V and 1.05V open circuit voltage. Besides that, PEA-I provided more uniform behavior through the different diodes of the same device, a fact that led us to focus on the PEA-I passivation.

An additional dry-step came by drying the other compounds of SPIRO-OMeTAD (Chlorobenzene, Li-TFSI and FK-209 powders). After this step we immediately made the solution and deposited on the perovskite surface. The results of the pv devices under 1Sun illumination are shown in figure 80.

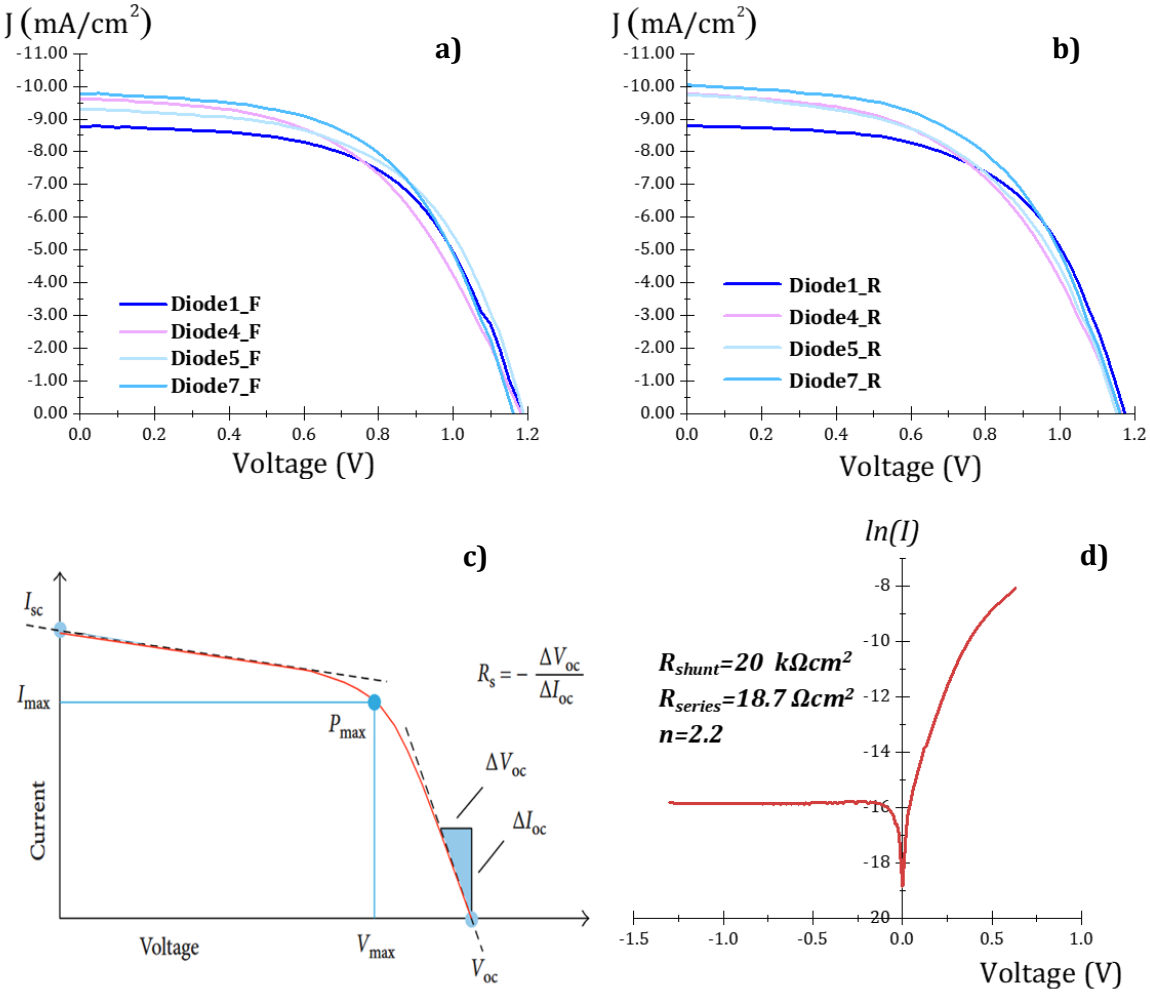

Figure 80. a) Forward and b) Reverse Scans for PEA-I passivated red perovskite solar cell produced after re-drying the other compounds of the SPIRO-OMeTAD, c) a theoretical photo I-V diagram which illustrates the effect of shunt and series resistance on the I-V curve [54] , and d) Dark analysis of diode7.

For the optimized conditions, we get a uniform distribution of the extracted photovoltaic characteristics through the whole device. The I-V curves are obviously enhanced, with almost no hysteresis between forward and reverse scans. The highest achieved efficiency was 6.37% for reverse scan, with 1.16V open circuit voltage, 10.05mA/cm^2 short circuit current and 54.6% FF. The relatively reduced FF can be justified from dark IV analysis. According to the extracted diode characteristics, we have no important shunt-resistance issues, as R_{shunt} is larger than 10 KΩcm^2 but we have series-resistance effect according to the criterion that R_{series} should be smaller than 1Ωcm^2 as per the discussion in chapter 4. This resistance effect can be also justified immediately from the photo JV curve, which provide an obvious slope with the y'y axes at the V_{OC} area (fig. 80c).

Regarding the out-of-the-glovebox perovskite solar cell fabrication, we could say that it is a much more complex procedure which needs continuous optimization in order to approach efficiency values comparable to those obtained inside the glovebox. The fabrication conditions change a lot for out-of-the-glovebox fabrication with significant issues more on the materials' hetero-interfaces than in the bulk. This conclusion arises from the detailed characterization of each layer which gives a behavior that is pretty similar to the bibliography. On the other hand, when we combine all these materials in a full perovskite device, we end-up with significantly reduced currents and with series-resistance issues. These issues reduce additionally the FF of the device and the overall power conversion efficiency.

For our optimized solar cells in ambient conditions, with humidity values between 60-75%, we show that an important step for optimization was to dry each powder. This drying process occurred in vacuum oven at 65°C, for at least 2hours. The crystallization temperature of perovskite was fixed at 65°C for 6 minutes with preheated solution and substrate at the same temperature. Moisture issues were observed also for SPIRO-OMeTAD, with the deposition on the perovskite surface immediately after the solution preparation seem to be a necessary step for improving the device. Finally, passivation layers seem to improve significantly the photovoltaic characteristics.

TiO_2 Nanorods as Transport Layer

In terms of exploring alternative perovskite solar cell architectures, we compared our FTO/TiO_{2comp}/$TiO_{2\text{-}mesop}$ layer with a respective FTO/TiO_{2comp}/TiO_2-Nanorods structure. For that purpose, two different-height Nanorods were examined. The Nanorods where fabricated by I. Syngelakis [109] on the same FTO/$TiO_{2\text{-}compact}$ template prepared by us, and the SEM images are presented below in figure 81.

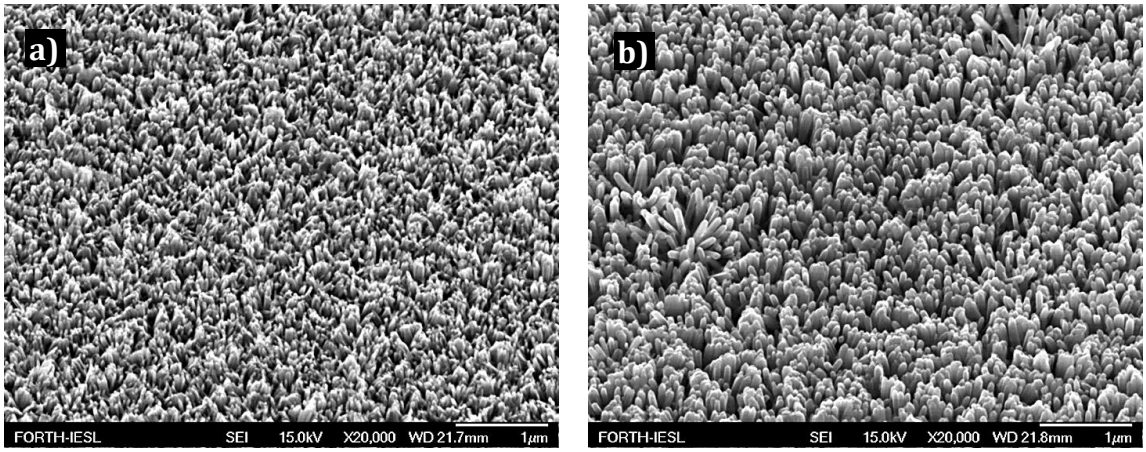

Figure 81. a) 300nm and b) 600nm Nanorods of FTO/$TiO_{2\text{-}c}$ substrate as ETLs.

UV-Visible measurements of these structures compared to the conventional FTO/TiO_{2comp}/$TiO_{2\text{-}mesop}$ sequence are also presented in figure 82.

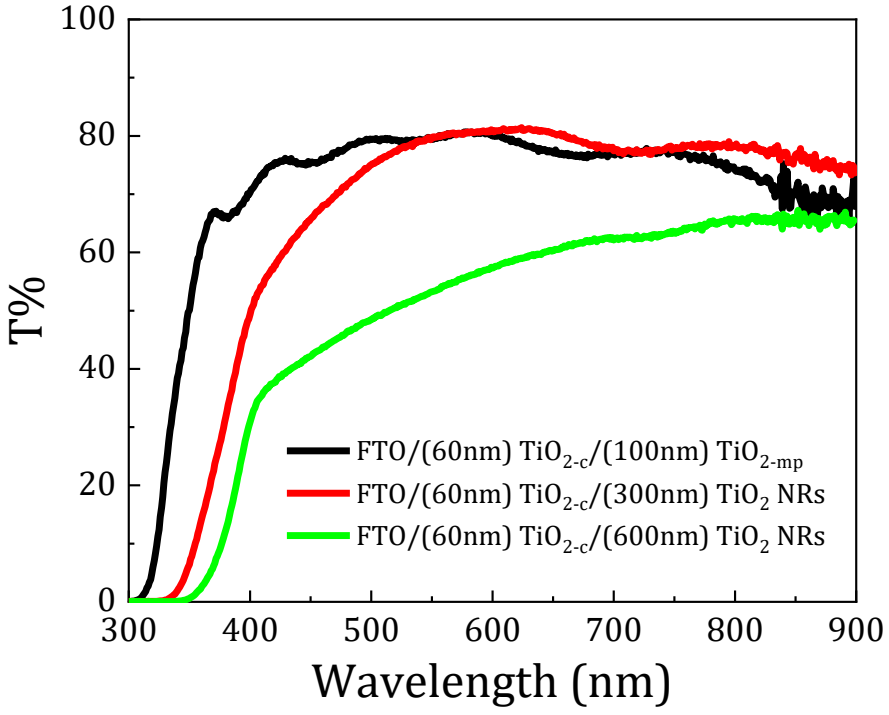

Figure 82. Transmittance measurement of the different TiO_2 based ETL structures

As we observe, the transmittance decreased by using the nanorod layer and increasing the nanorod height. Targeting at an enhanced interface of perovskite-TiO_2 interface, we deposited a $FA_{0.8}MA_{0.04}Cs_{0.16}Pb(I_{0.5}Br_{0.5})_3$ + 5% $PbCl_2$ perovskite film via gas-quenching technique, aiming at an enhanced uniformity of the deposited film on these rough substrates.

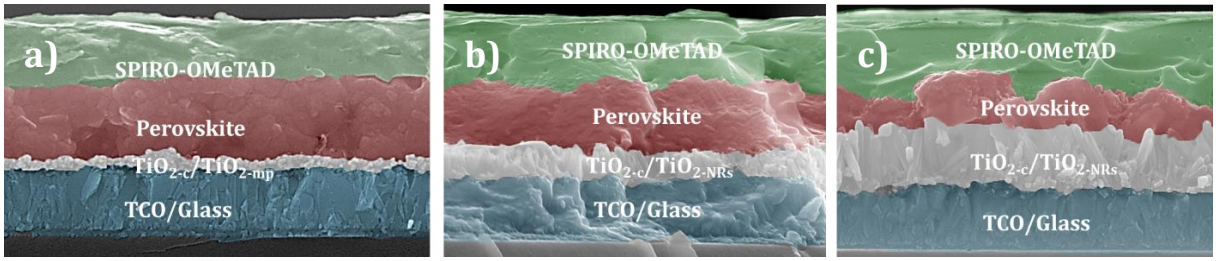

Figure 83. Cross section SEM images of a) mesoporous structure with a ~100nm mesoporous TiO_2 ETL, a ~650nm perovskite film and a ~500nm SPIRO-OMeTAD film, b) Nanorod-based structure with b) ~300nm-high TiO_2 Nanorods and a 500-600nm perovskite film with a 500-600nm SPIRO-OMeTAD film and c) Nanorod-based structure with ~600nm-high TiO_2 Nanorods, 450-650nm perovskite film and 500-650nm SPIRO-OMeTAD film.

Although the deposition process was identical for all the structures, the substrate roughness seems to affects on the final perovskite and SPIRO OMeTAD characteristics.

Photo IV measurements of these devices also took place in order to extract the photovoltaic characteristics, while further dark IV analysis helped for a better understanding of their behavior.

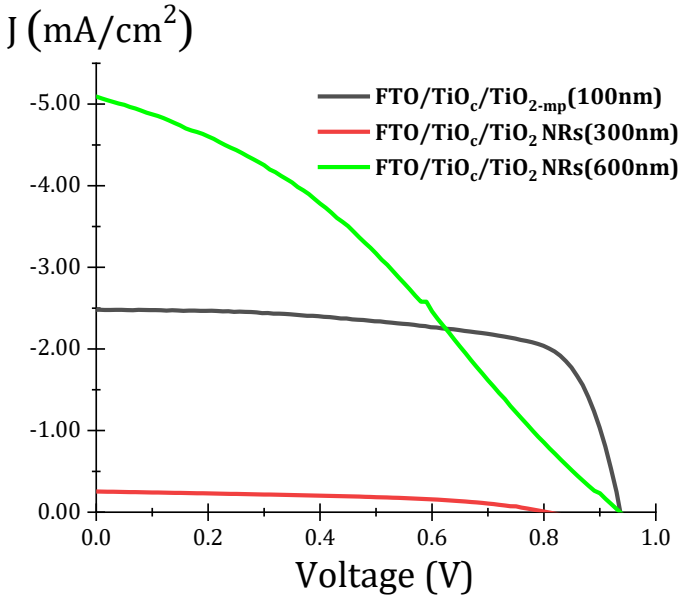

Figure 84. JV curves under 1sun illumination for three different TiO_2-based ETLs

As we see in figure 84, the device with TiO_2 Nanorods present reduced FF values compared to the standard mesoporous device. The 300nm NR extracted values are significantly worse compared to the other two ETLs, while the 600nm-NRs present higher short-circuit current. For a better comparison, we present all the extracted parameters in the table below.

ETL	Ideality Factor	R_{shunt} ($k\Omega\ cm^2$)	R_{series} ($\Omega\ cm^2$)	V_{oc} (mV)	J_{sc} (mA/cm^2)	FF %	Efficiency %
$TiO_{2\text{-mp}}$ (100nm)	2.30	82	6.4	936	2.47	70.50	1.63
TiO_2 NRs (300nm)	11.60	60	1806	805	0.26	45.40	0.09
TiO_2 NRs (600nm)	4.60	57.2	130	936	5.10	33.10	1.58

Table 2. Dark and Photo IV extracted characteristics of the three different ETLs.

Comparing the morphology of these devices, we see that due to the inherent roughness of the TiO_2 nanorod layer, the perovskite film also reproduces similar roughness, while the HTL seems to reduce the final roughness of the Perovskite Solar Cell as presented on figure 83. Additionally, the dark IV measurements indicate inferior diode characteristics for the TiO_2-NRs-based solar cells, with increased series-resistance and lower shunt-resistance compared to the mesoporous diodes. Significant differences on series resistance are also observed between the 300nm-NRs' device and the 600nm-NRs' device, with the ~1 order of magnitude difference on the extracted series-resistance values to be attributed on the lower thickness of the 300nm heigh nanorods as we observe on figure 81. Focusing on the nanorod-based devices, we observe that despite the decreased transmittance of 600nm-NRs' device, and thus the reduced number of photons that will be absorbed by the perovskite, we extracted better solar cell characteristics, than the 300nm-TiO2-NR. We suggest that this is due to increased interface of 600nm-NRs with the perovskite and the better electrical characteristics. Additionally, in terms of efficient extraction of carriers, we see that the increased interface seems to offer even better for the 600nm-NR compare to the conventional mesoporous TiO_2 structure, with almost 2 times higher current densities despite the poor transmittance and electrical characteristics of NR-based structure.

A better control and further optimization of TiO_2-NRs, could significantly improve the diode characteristics of such a solar cell device. Such an

improvement, would be very promising for an alternative ETL instead of mesoporous structure.

Summarizing the results of this chapter, we have fabricated and optimized various perovskite films in ambient conditions, while we employed a post-annealing technique for high-quality perovskite films in an “out-of-the-glovebox” process, under relatively high humidity conditions. The low-temperature annealing was the key factor in this process. In addition, we tried 3 different perovskite deposition techniques, the hot-casting, the gas-quenching and the antisolvent technique. The hot-casting technique was the most promising in terms of being functional in ambient conditions. Despite the large perovskite grains we obtained, and the relatively high carrier lifetimes we observed, the technique had issues with the reproducibility and uniformity of the perovskite films. Thus, we experimented with a modified antisolvent technique, where we used hot substrates as an extra step to eliminate the humidity from the substrate surface, which gave us better control on the perovskite morphology and reproducibility. An alternative technique for perovskite-film deposition was the gas-quenching one, where we replaced the anti-solvent solution with a continuous flux of nitrogen. The advantage of this technique compared to the antisolvent one, was the ease of reproducibility and the increased uniformity of the perovskite film in larger areas. Additionally, we optimized high-bandgap perovskite films for our tandem device. More specifically, we developed a triple-cation mixed-halide 1.9 eV "red" perovskite, which showed increased stability under illumination and higher lifetimes compared to single or double cations.

Finally, we optimized our transport layers. As ETL, we used a TiO2-compact/ TiO2-mesoporous heterostructure, where an extra TiCl4 treatment between compact and mesoporous layer improves the transport process and the overall device characteristics. Additionally, we examined the effect of different TiO2 architectures, which showed promising results and the need for further optimizations. As HTL, we examined both CuSCN and SPIRO-OMeTAD, putting the emphasis on the SPIRO-OMeTAD optimization, as it gave us better results compared to CuSCN. The synthesis of the SPIRO-OMeTAD solution proved to be a little tricky, with moisture issues and the re-drying of all the reagents as a prerequisite for increased efficiency.

Overall, the perovskite solar cells we have fabricated and tested showed inferior characteristics compared to the literature, most likely due to

humidity issues during the “out-of-the-glovebox” fabrication. Focusing on the ''red'' perovskite devices, using the optimized conditions for TiO2-ETL's and SPIRO-OMeTAD, we have observed a PV efficiency of ~6.5 % with limited hysteresis phenomena.

Chapter 6

Perovskite-Gallium Arsenide Tandem Solar Cells

The combination in a tandem configuration of a GaAs and a Perovskite solar cell was our final target. For that purpose, both sub-cells should be as much optimized as possible for optimum efficiency under this combination. This optimization strongly depends on the architecture of the Tandem structure. There are 4 different well-known configurations that we could study.

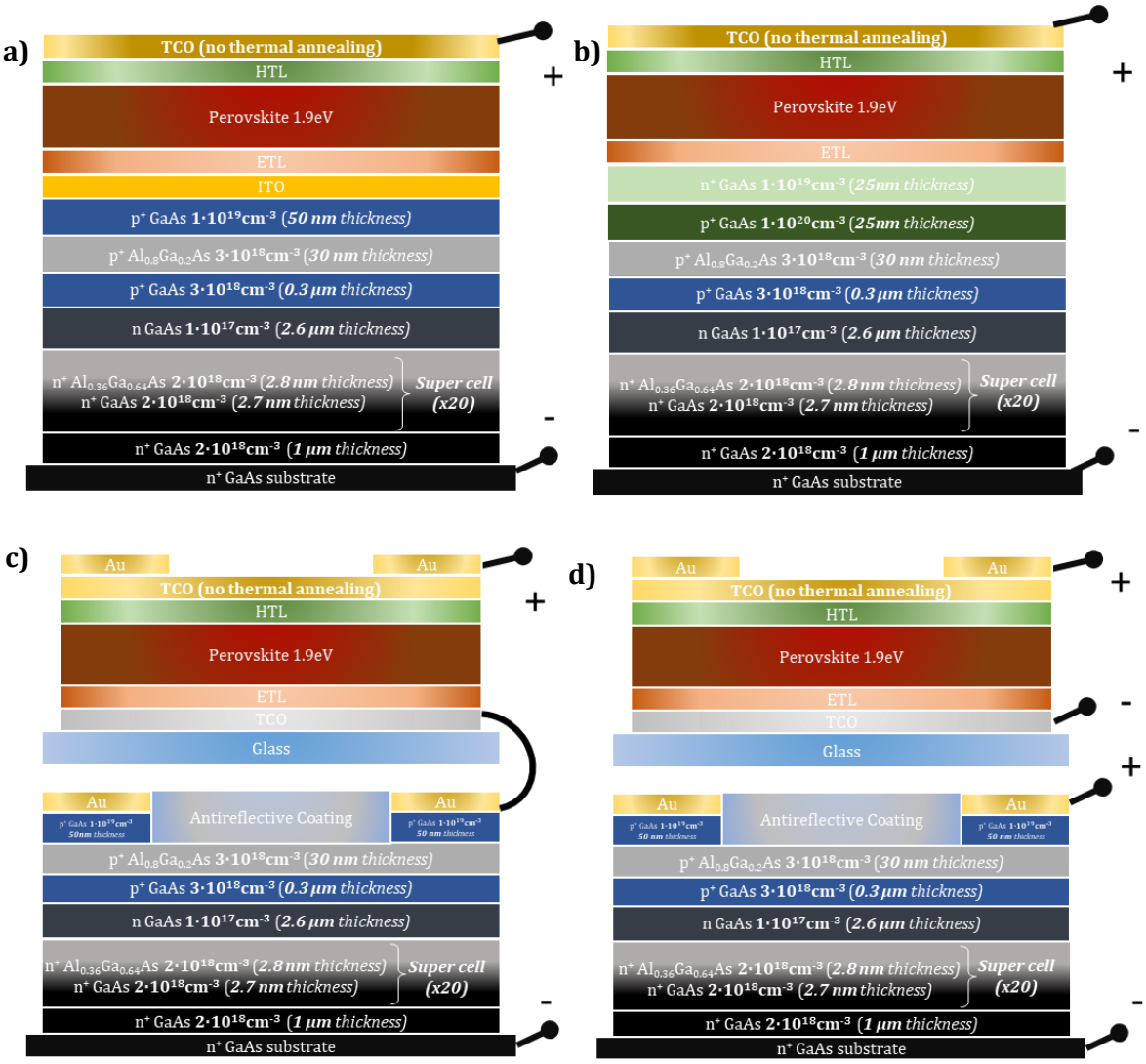

Figure 85. Monolithic Tandem Solar cell with a) recombination layer and b) tunnel diode, c) 2-Terminal Mechanically Stacked Tandem Solar Cell connected in series and d) 4-Terminal Mechanically-Stacked Tandem Solar Cell.

Monolithic Tandem Solar cells a) and b) require current-matching for the two sub-cells, while this current-matching condition for the serially-

connected tandem solar cell c) is less stringent in the sense that we can adjust the different areas of the sub-cells. The 4-Terminal mechanically Stacked Tandem Solar Cell d) allows you to develop two separate Solar cells and leads to the optimum performance with no current-matching requirements.

One very important point in terms of tandem configuration is that the top sub-cell should have both electrodes transparent to minimize the absorption losses. Additionally, for monolithic configurations, an extra recombination layer or an ultra-thin tunnel-junction should be brought to optimum conditions in terms of minimizing the electrical resistance and optical losses, providing at the same time an effective interconnection of the two sub cells.

Oxides for Tandem Solar Cells

In terms of transparent electrodes, one of the best-known electrodes is the Indium Tin Oxide (ITO). In terms of depositing ITO on the HTL of the perovskite device, one should try to optimize the as-deposited ITO at appropriate conditions for a low resistance electrode utilizing an rf-power low enough such as not to destroy the HTL. Additionally, ITO can be also used as recombination layer in between the two sub-cells of a monolithic structure. In this work, as first step we tried to examine the optimum conditions in the rf-sputtering chamber during the ITO deposition. We tried 3 different conditions at 300-Watt deposition power. After each deposition the samples were characterized with HALL measurements.

In the first deposition, the chamber was 100% Ar-environment under 5mTorr pressure.

No annealing	300°C (30min)	300°C (2h)	350°C (30min)
R= 300 Ω/□	R= 130 Ω/□	R= 116 Ω/□	R= 97.8Ω/□
ρ= $40.41 \cdot 10^{-4}$ Ω·cm	ρ= $17.48 \cdot 10^{-4}$ Ω·cm	ρ= $15.63 \cdot 10^{-4}$ Ω·cm	ρ= $13.2 \cdot 10^{-4}$ Ω·cm
ns= $1.2 \cdot 10^{15}$ cm^{-2} (n-type)	ns= $3.175 \cdot 10^{15}$ cm^{-2} (n-type)	ns= $3.16 \cdot 10^{15}$ cm^{-2} (n-type)	ns= $3.36 \cdot 10^{15}$ cm^{-2} (n-type)
nd= $8.9 \cdot 10^{19}$ cm^{-3}	nd= $2.36 \cdot 10^{20}$ cm^{-3}	nd=$2.35 \cdot 10^{20} cm^{-3}$	nd=$2.5 \cdot 10^{20} cm^{-3}$
μ= 17.4 $cm^2/V \cdot s$	μ= 15.1 $cm^2/V \cdot s$	μ= 17.1 $cm^2/V \cdot s$	μ= 19.05 $cm^2/V \cdot s$

Table 3. Electrical characteristics of a 135nm thick ITO under 100% Ar conditions at different annealing temperatures/duration.

As shown in table 3, this film presents really good electrical characteristics, which are improved with subsequent annealings. The surface resistance of the as-deposited film was ~300 Ω/square with a significant low specific resistance in the magnitude of $\sim 40 \cdot 10^{-4}$ Ωcm with a high mobility $\sim 17 cm^2/Vs$. Reasonable values are obtained also for the surface carrier density $\sim 1 \cdot 10^{15} cm^{-2}$ and the additional carrier density $\sim 9 \cdot 10^{19} cm^{-3}$. After subsequent annealing treatments, the corresponding values improved to ~100Ω/square, $\sim 13 \cdot 10^{-4}$ Ωcm, $\sim 19 cm^2/Vs$, $\sim 3.3 \cdot 10^{15} cm^{-2}$ and $\sim 19 \cdot 10^{20} cm^{-2}$ for the surface and the specific resistance, mobility, surface carrier density and carrier density respectively. In the second deposition, we deposited a 120nm-thick ITO at 5%O_2- 95% Ar environment under 5mTorr pressure.

No annealing	300°C (30min)	300°C (2h)	350°C (30min)
R= 5450 Ω/□	R=403 Ω/□	R= 307.5 Ω/□	R=283 Ω/□
ρ= $68.4 \cdot 10^{-3}$ Ω·cm	ρ= $50.57 \cdot 10^{-4}$ Ω·cm	ρ= $38,58 \cdot 10^{-4}$ Ω·cm	ρ= $35.5 \cdot 10^{-4}$ Ω·cm
ns= $2.6 \cdot 10^{14}$ cm^{-2} (n-type)	ns= $1.36 \cdot 10^{15}$ cm^{-2} (n-type)	ns= $1.47 \cdot 10^{15}$ cm^{-2} (n-type)	ns= $1.46 \cdot 10^{15}$ cm^{-2} (n-type)
nd= $2.1 \cdot 10^{19}$ cm^{-3}	nd= $1.08 \cdot 10^{20}$ cm^{-3}	nd= $1,17 \cdot 10^{20}$ cm^{-3}	nd= $1,16 \cdot 10^{20}$ cm^{-3}
μ= 4.5 $cm^2/V \cdot s$	μ= 11.4 $cm^2/V \cdot s$	μ= 13.8 $cm^2/V \cdot s$	μ= 15.1 $cm^2/V \cdot s$

Table 4. Electrical characteristics of a 120nm thick ITO under 5%O- 95% Ar conditions at different annealing temperatures/duration.

As shown in table 4, we observe that 5% oxygen degrade the electrical characteristics of the as-grown film compared to the 100%Ar while by annealing, these characteristics are significantly improved.

In the third deposition, we increased the oxygen content at 10%, for a 10%O_2-90%Ar environment at the same power.

No annealing	300°C (30min)	300°C (2h)	350°C (30min)
R= 6250 Ω/□	R= 400 Ω/□	R= 335 Ω/□	R= 293 Ω/□
ρ= 91.3·10^{-3} Ω·cm	ρ= 58.4·10^{-4} Ω·cm	ρ= 48,9·10^{-4} Ω·cm	ρ= 42.8·10^{-4} Ω·cm
ns= 2.8·10^{14} cm^{-2} (n-type)	ns= 1.59·10^{15} cm^{-2} (n-type)	ns= 1.56·10^{15} cm^{-2} (n-type)	ns= 1.36·10^{15} cm^{-2} (n-type)
nd= 1.9·10^{19} cm^{-3}	nd= 1.08·10^{20} cm^{-3}	nd= 1.07·10^{20} cm^{-3}	nd= 0.93·10^{20} cm^{-3}
μ= 3.6 cm^2/V·s	μ= 9.84 cm^2/V·s	μ= 12cm^2/V·s	μ= 15.7cm^2/V·s

Table 5. Electrical characteristics of a 145nm thick ITO under 10%O_2 - 90% Ar conditions at different annealing temperatures/duration.

Clearly as shown in table 5, the increased oxygen contents affects the electrical properties of ITO, and the best conditions in our system was the 100% Ar environment.

Although we observe that annealing improves the ITO properties, we should find the optimum conditions of the as-deposited films, considering that the perovskite layers cannot sustain annealing at high temperatures. For this purpose, we repeated the deposition in a 100% Ar-environment, at different RF-Powers.

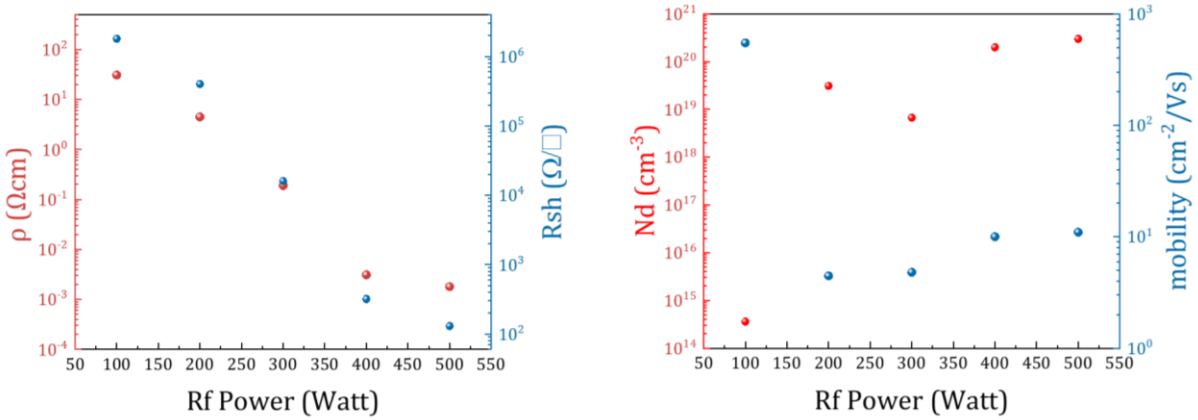

Figure 86. Electrical characteristics of as deposited ITO at different RF powers.

The extracted results in figure 86 show a gradual improvement of all properties with the power. Summarizing the above results, we could say that the best ITO properties are presented for the highest RF-Power deposition in 100% Ar-environment. Extra annealing steps further provide improvement of the ITO film characteristics.

To examine the effect of optimizations of the RF-Power during the deposition of ITO, avoiding any damage-effect on the underneath HTL or perovskite layers, we made a series of ITO depositions directly on the perovskite film. In fact, we should optimize the conditions on SPIRO-OMeTAD layer, but as we could not examine the damage on this layer with our available techniques we proceeded on the direct deposition on perovskite. For that purpose, we prepared 300nm $MAPbI_3$ films deposited on a glass substrate via gas-quenching technique. We tried ITO depositions at different combinations of RF-power as presented in Table 6 below. For each deposition, we used a glass/$MAPbI_3$ film for XRD and PL measurements and a plain glass substrate for transmittance measurements.

			I13 - S175		**I14** - S176		**I15** - S177			**I16** - S178		**I17** - S179			**I18** - S180	
Power	Depo. Rate (nm/ min)		t (min)	d (nm)	t (min)	d (nm)	t (min)	d (nm)		t (min)	d (nm)	t (min)	d (nm)		t (min)	d (nm)
100 W	1.43						12.6	18		21.0	30	7.0	10		21.0	30
150 W	2.2						7.2	18				4.5	10			
200 W	2.82						6.3	18				3.5	10			
250 W	3.8						4.7	18				2.6	10			
300 W	4.80		18.75	90			3.7	18		12.5	60	2.1	10			
350 W	6.0											1.7	10			
400 W	6.8											1.5	10			
450 W	8.0											1.2	10			
500 W	9.13				9.86	90						1.1	10		6.6	60
TOTAL targeted Time & Thickness			18.75	90	9.86	90	34.5	90		33.5	90	25.2	90		27.6	90
Measured total thickness (nm)				**99.8**		**50**		**86**			**67.7**		**81**			**29**

Table 6. RF-Sputtering powers of different deposition of ITO on perovskite films and on glass substrates.

Our idea was to compare two conditions with fixed RF-Power, where the electrical characteristics for as-deposited films were reasonable, with films with gradual increase of rf-power, where the low-power deposited ITO layer is supposed to protect the HTL, while the final high-power layer should enhance the current spreading and the collection of carriers, based on their improved electrical characteristics.

The deposition conditions are presented on Table 6, for 6 different layers, where the estimated thickness (d/nm) was controlled with the deposition-time (t/min), and the total thickness was measured after each deposition.

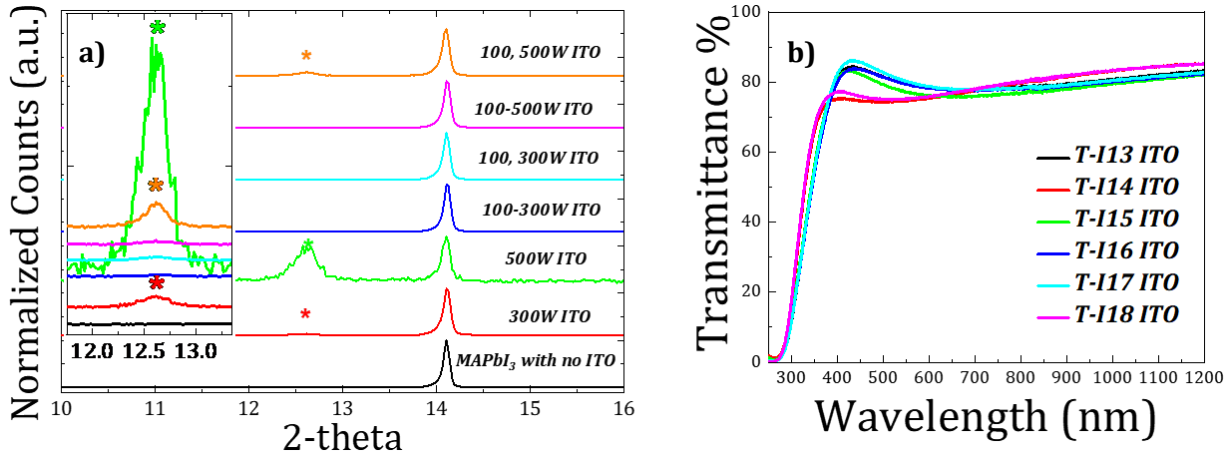

Figure 87. a) XRD of glass/ $MAPbI_3$/ ITO focused on the PbI_2 peak as a decomposition issue (inset) and a) Transmittance ITO respective layers deposited on glass substrates.

From the XRD measurements, we conclude that even 300W produce a decomposition effect on the perovskite, based on the appearance of a secondary peak at lower diffraction angles (~12.6°, denoted with a star). Besides that, depositing a ~30nm layer of 100W seems to be sufficient for protecting from an extra 300W deposition. On the other hand, an extra 500W deposited layer produces damage, which disappears when we deposit intermediate ITO layers with intermediate rf-powers. From transmittance measurements, for all depositions we have values ~80% in most of the spectral range, while if we take into account of the glass transmittance which is ~90%, the ITO transmittance also reaches a ~90% value.

The optimum ITO conditions found above were tested in a full perovskite device, directly on the HTL, as transparent top electrode, but the results were not very encouraging, which led us to believe that SPIRO-OMeTAD is much more sensitive under the rf-deposition powers used, and thus we need to address alternative hole-transport layers which are more stable and resistant under high rf-powers. Towards this end, we deposited NiO and NiAlO on different chamber conditions as HTLs, while we also tested an alternative ZnO ETL.

SAMPLES	Rsheet	ρc
NiAlO 2.8% O_2-97.2% Ar	*448 Ω/□*	*0.010 Ωcm²*
NiAlO 50%O_2 -50% Ar	*119.6 kΩ/□*	*0.145 Ωcm²*
NiO 2.8%O_2 -97.2% Ar	*133.8 MΩ/□*	*69.953 Ωcm²*
NiO 50%O_2 -50% Ar	*5.8 MΩ/□*	*2.465 Ωcm²*
ZnO 50%O_2-50% Ar	*41.5 MΩ/□*	*0.0002 Ωcm²*

Table 7. NiO, NiAlO and ZnO electrical characteristics at different chamber conditions

The electrical characteristics of these as-deposited layers were extracted via TLM measurements, where the TLM pattern was prepared via lithography with square pads with 5, 10, 20, 30, 40 50 and 100μm distance between each square pad. In addition, these layers were also used in a full perovskite device with no satisfactory results. Despite this, we think that these layers are promising and merit further investigation for alternative transport layers in more stable perovskite solar cells.

As a last step in the study of oxide layers, we tried to optimize a thin ITO layer on a p-type GaAs in view of a monolithic structure where the ITO would be in contact with the p-GaAs. The ITO-recombination layer should offer ohmic contact with both top layer of the bottom sub-cell and with the bottom layer of the top sub-cell. It is well-known that ITO provides an ohmic contact with many of the ETLs of a perovskite cell, thus we focused on the top layer of our GaAs structure.

For this purpose, we deposited a 10nm film with 500Watt RF-Power on p-GaAs and performed I-V measurements, where the top contact was an extra 0.25x0.25cm square Au contact on the ITO surface.

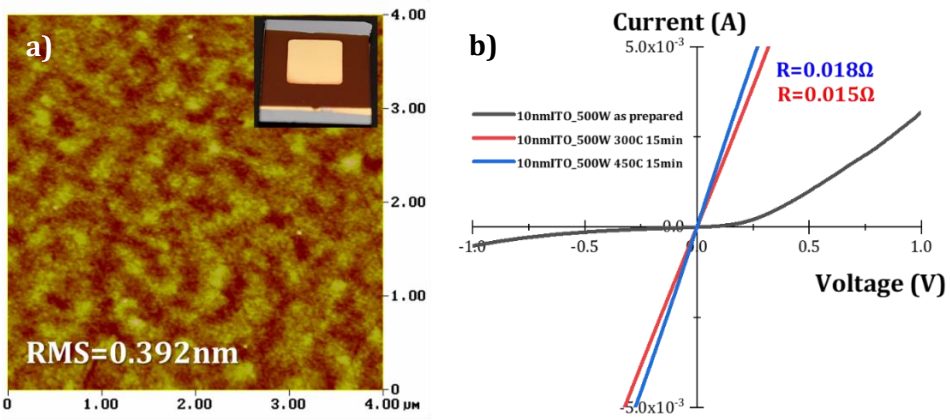

Figure 88. a) AFM image of 10nm ITO surface deposited on GaAs with an extra picture of the measured pGaAs/ ITO/ Au sample (inset) and b) IV results of the as prepared and annealed at 300C and 450C for 15min

According to the extracted results, the 10nm-thick ITO on GaAs substrate forms a low roughness film with good electrical ohmic properties after annealing, while the as-deposited IV results present a Schottky behavior. More specifically, the optimum behavior is for the 300°C annealed sample with a ~0.0009Ωcm^2 resistance, while the annealing at 450°C presents a slightly higher resistance at ~0.0011Ωcm^2.

We should mention that all these ITO depositions were made by Dr. E. Aperathitis with an RF-Sputtering system.

Modeling of a Tunnel Junction

An alternative way for a monolithic tandem solar cell is the introduction of a tunnel diode. This diode can replace the recombination layer based on the tunneling effect. The deposition of such a diode demands a good control of thickness and doping profile, thus requires expensive deposition techniques such as an MBE process. Nevertheless, we examined using the Silvaco TCAD simulator machine, the optimum thickness and doping profile for an efficient tunnel diode in a monolithic perovskite/GaAs tandem configuration. For this purpose, we used as ETL on the tunnel junction a ZnO layer which is available in our lab as we showed earlier. More specifically, we used in the simulation a 30nm thick ZnO with N_D=3 10^{18}cm^{-3}, while we take into account the MBE limitations in this optimization.

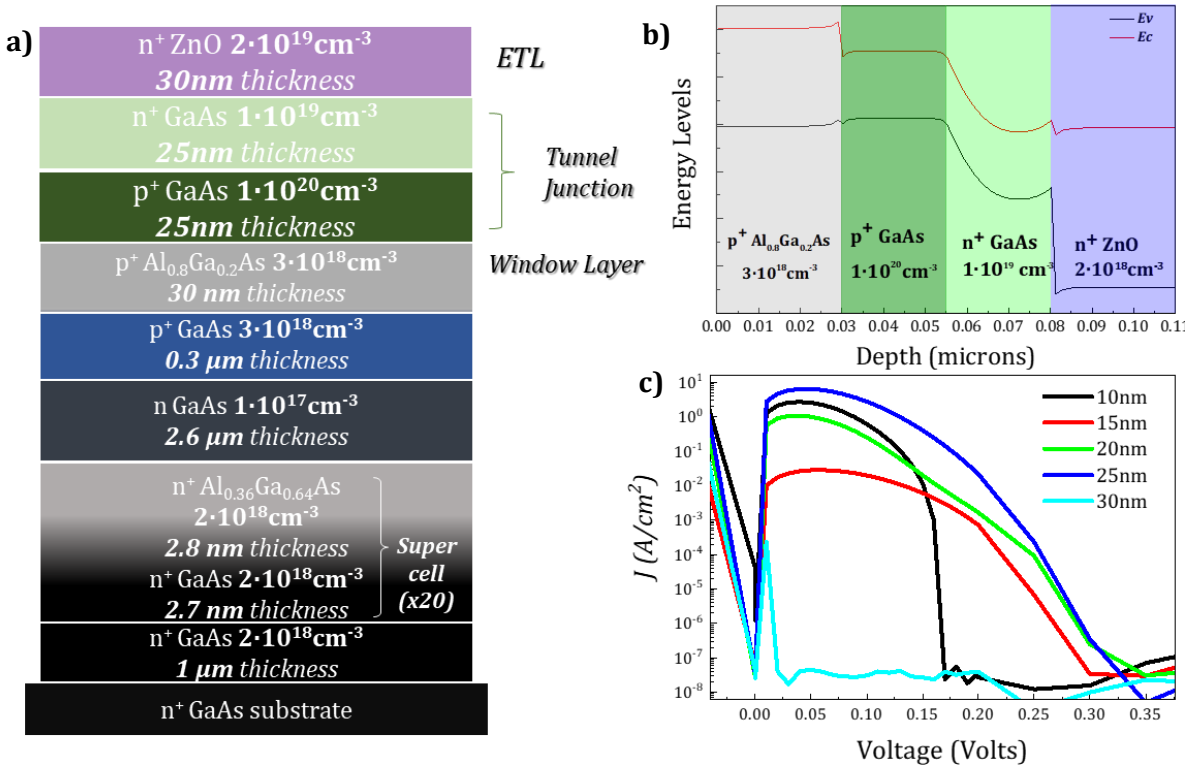

Figure 89. a) GaAs bottom sub-cell with a tunnel diode and a ZnO ETL from the top perovskite based subcell with b) the respective energy band alignment and c) J-V curves which present the tunneling effect for different thicknesses of the tunnel junction.

According to our optimization, we found that a 25nm-25nm p^+-n^+ tunnel diode seems to present the optimum characteristics in terms of tunneling effect with a very good energy band alignment for a monolithic GaAs-Perovskite tandem solar cell.

4-Terminal Configurations

In terms of a tandem configuration, it is clear that we should optimize a lot of layers for an optimum band gap alignment, with minimization of parasitic electrical and optical losses. A very important step is the optimization of the transparent electrodes. In particular, we should optimize the deposition of ITO on SPIRO-OMeTAD for minimization of HTL damage. This process requires plenty of dedicated experiments in order to obtain sufficient know-how. In our laboratory, this process was new and in the preliminary experiments during the course of this thesis, we realized that we are still facing problems that affect significantly the HTL and the final efficiency. An alternative way to evaluate the benefit of a tandem structure, was to fabricate two identical devices at 1.9 eV. The first one should be used to evaluate the top sub-cell, where we deposited opaque Au top contacts, while

the second device did not have top contacts and was be used as a spectral filter for the bottom subcell.

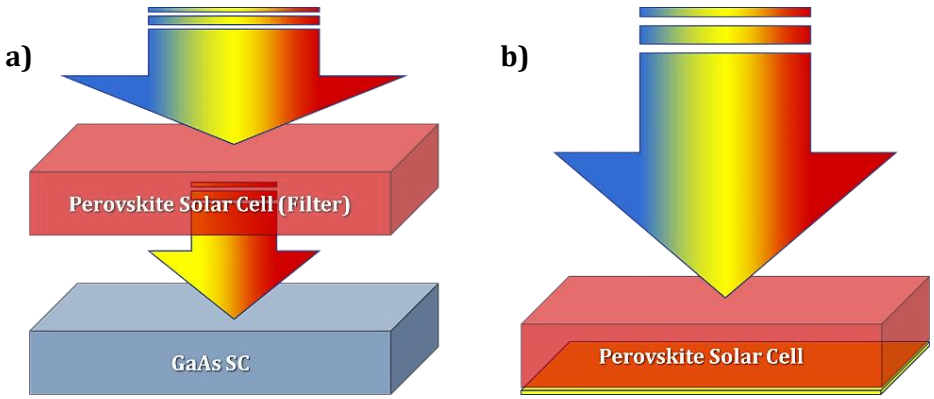

Figure 90. Illustration of 4-terminal characterization of the a) bottom subcell with a perovskite solar cell as a spectral filter and b) the top perovskite subcell.

In this direction, we used our optimized high bandgap perovskite solar cell as top subcell and we compared the efficiency benefit with the 1663 GaAs sample with and without A/R coating as described in chapter 4.

For the 1663 sample without A/R coating, we had a 3.62% efficiency for the bottom subcell without perovskite filter, while with the perovskite filter the efficiency decreased to 1.68% (53.6% decrease), with the main affected value to be the current density, showing a drop of 6.2mA/cm^2 to 2.95mA/cm^2 (~52.4% decreased). Adding to 1.68%, the 6.37% efficiency of the top sub-cell, the total efficiency of such a tandem solar cell is ~8%, which is 1.27 times more than the top subcell and 2.22 times more than the bottom subcell.

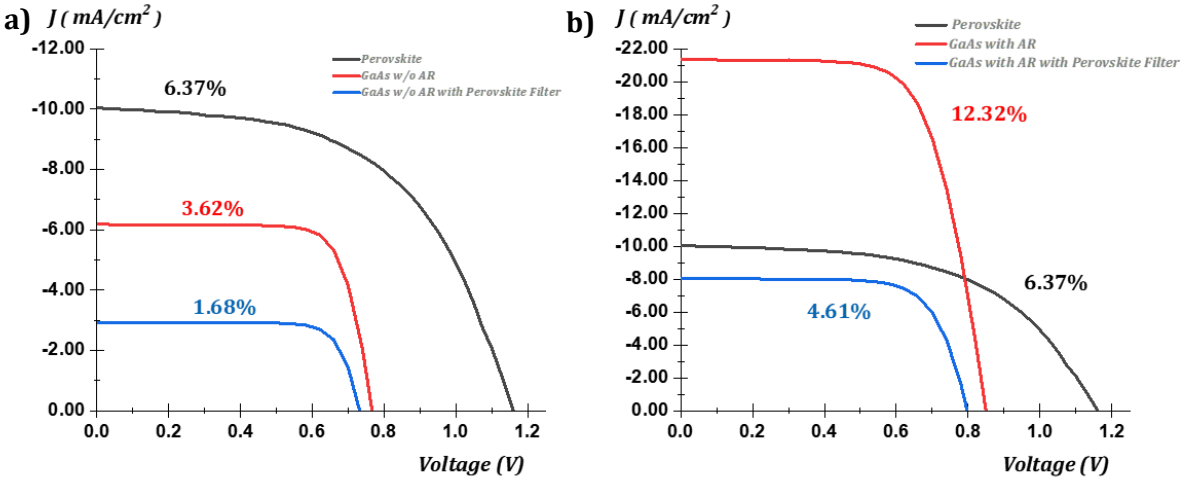

Figure 91. 4-terminal approximation using a GaAs solar cell a) without and b) with antireflective coating.

On the other side, using a 1663 diode with antireflective coating and an increased efficiency at 12.32%, we can see that we do not have benefit from such a 4-T combination. More specifically, following spectral filtering by the top sub-cell, the efficiency of GaAs decreased to 4.61% (62.66% decrease), with again a significant current density decrease from 21.39 mA/cm^2 to 8mA/cm^2 (62.59% decrease). The total efficiency of the 4T combination is 10.98%, which is 1.7 times more than the perovskite solar cell and 1.12 times less than the GaAs solar cell, so such a combination is not worth in this case.

For further investigation, we combined our best efficiency GaAs solar cell with an optimized perovskite solar cell at 1.77eV. Although this bandgap is ~0.1eV lower from the optimum value for tandem combination with the GaAs sub-cell, lower perovskite bandgaps can provide higher efficiencies and allow us to minimize the perovskite thickness for minimizing the absorption losses. For this purpose, Professor Weijun Ke and his student Fu Shiqiang from Wuhan University, provided us with such a perovskite solar cell for a 4T combination with the GaAs solar cell. This perovskite cell has both ITO transparent electrodes with an inverted structure compared to our perovskite devices.

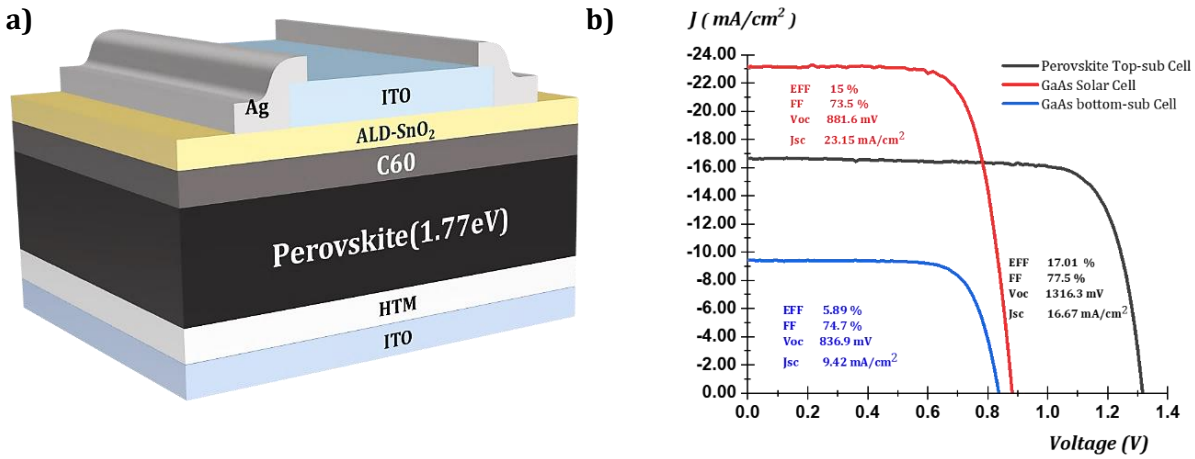

Figure 92. a) 1.77eV perovskite structure for top subcell and b) 4-T results under 1sun illumination.

According to the extracted results, the top subcell showed a 17.01% efficiency while the bottom subcell a 15%. In the 4-T combination, the efficiency of the bottom subcell decreased at 5.89% (60.7% decreased) with again the main decrease being in the current density, from 23.15 to 9.42 mA/cm^2 (59.3% decrease). The total 4-T efficiency is ~22.9% which is 1.35 times more than the top subcell and 1.5 times than the bottom subcell.

In conclusion, we have studied, fabricated, and optimized materials that will be used either for monolithic, or for 4-terminal tandem solar cell devices. More specifically, for monolithic tandem solar cells, we addressed the interconnection layer in our heterostructure using two different approaches, the recombination layer and the tunnel junction. As recombination layer, we optimized an ultra-thin ITO layer on a p-GaAs substrate, while we additionally used Silvaco simulator and designed a GaAs p-n tunnel junction as an alternative interconnection layer. As another prerequisite of the tandem approach, we examined the effect of as-deposited ITO as a transparent top contact. The results of such a deposition showed significant reduction of the perovskite solar cell performance, which is attributed to SPIRO-OMeTAD damage under the high rf-power depositions of ITO. For that purpose, we examined NiO-based layers as alternative HTLs in the tandem configuration. Additionally, we studied different combinations of 4T structures, one with the optimum perovskite sub-cell gap of 1.9eV and one with a gap of 1.77eV. We can say that except of the perfect bandgap alignment of the two sub-cells, other limitations such as optimum thickness, stability, maximum efficiency under the Shockley limit, etc. are important for maximizing the total efficiency. We demonstrated the benefit of the tandem geometry with both types of perovskite cells. Our best efficiency for a 4T-structure approaches the 23%. Further optimizations are certainly possible and based on theoretical estimations, we can hope for 4T-efficiencies higher than 30%.

Chapter 7

$MAPbI_3$ on GaAs: a washable hetero-interface with giant passivation effect

It is well-known that one of the most important disadvantages of GaAs, is the high non-radiative surface recombination velocity [110]. Many works in the past have focused on the passivation of the GaAs surface, employing various methods such as plasma treatment [111], chemical passivation [112], [113] or deposition of another material on the surface as protection layer [114]–[116]. A common characteristic of all these approaches is that prior to any passivation scheme, the native oxide of GaAs is removed either chemically or by desorption and other *in situ* processes inside a high-vacuum epitaxial chamber.

On this chapter, we demonstrate that the deposition of Methylammonium Lead Iodide ($MAPbI_3$) on native nominally-undoped (100) GaAs substrates, generates an enhancement in the GaAs photoluminescence (PL) intensity by more than three orders of magnitude. We attribute this giant PL enhancement to some very efficient $MAPbI_3$-induced passivation scheme of the GaAs surface. Time-resolved PL experiments reveal greatly enhanced carrier lifetimes next to the GaAs surface, in agreement with a passivation process. X-ray photoelectron spectroscopy measurements on ultrathin $MAPbI_3$/GaAs and PbI_2/GaAs samples suggest some Pb-related de-oxygenation of the GaAs surface, as an atomistic mechanism possibly related to the passivation effect. Impressively, the whole process is fully reversible, as it suffices to immerse the $MAPbI_3$/GaAs sample in salt-water and the $MAPbI_3$ layer is completely removed, while the PL intensity and spectral features of the GaAs substrate return to their pristine condition

For this experiment, $CH_3NH_3PbI_3$ powder is synthesized by adding PbO (10 mmol), 57% HI solution (76 mmol) and 50 % aqueous H_3PO_2 (15.5 mmol) and stirring the solution on a hot plate until a bright yellow colour to be formed. Then, CH_3NH_3Cl (10 mmol) powder is added in the solution and a black powder precipitated. The black powder is collected from the solution via a filtering procedure and is dried in a vacuum oven for 5 hours for the final $CH_3NH_3PbI_3$ powder. For the perovskite solution,

$CH_3NH_3PbI_3$ ($MAPbI_3$) powder is dissolved in a DMF: DMSO (4:1) mixed solvent and stirred for 1 h. For GaAs substrate, we use a nominally undoped GaAs (100) substrate by Wafer Technology Ltd. According to the specifications, these GaAs substrates are practically semi-insulating with a resistivity higher than 10^7 Ω·cm. For the perovskite deposition on the GaAs substrate, we use the spin-coating technique under ambient conditions. Prior to deposition, the GaAs substrates are merely oxygen plasma-treated for enhanced adsorption of the perovskite and no native oxide is removed. Next, we drop the precursor solution on the substrate and spread on the substrate via spin-coating for 40 seconds. On the 10^{th} second, we apply a continuous N_2 flow (gas-quenching technique) to enhance the uniformity and crystallization of the perovskite, as described in chapter 5. Finally, we anneal the sample on a hot plate at 65°C for 6 min. The molarity of the perovskite solution and the rpm value can be adjusted according to the wanted thickness. Perovskite films with thicknesses between 10 nm and 520 nm have been produced in this study. For each $MAPbI_3$/GaAs sample, a twin $MAPbI_3$/glass sample is deposited under the same conditions. To examine the reversibility of the deposition process, we remove the $MAPbI_3$ film by immersing the $MAPbI_3$/GaAs sample in a beaker with salt-water and sonicate for 5 min to dissolve the perovskite film. Next, we rinse the substrate with de-ionized water to remove any residual salt or perovskite and sonicate again in de-ionized water for another 5 min to improve cleaning. Finally, we rinse the substrate with acetone and isopropanol, and dry with nitrogen flux.

The morphology of the perovskite film is assessed with Field-Emission Scanning Electron Microscopy (FE-SEM) images, while the crystal quality of the film is characterized by X-Ray diffraction (XRD) measurements. For the temperature-dependent PL experiments, the sample is fixed on the cold finger of a variable-temperature closed-cycle helium cryostat and several continuous-wave (CW) lasers are employed for excitation with a spot size of ~100 μm, such as a He-Cd laser at 325 nm, a laser diode at 650 nm or a Ti:Sapphire laser tuned at 720 nm or 780 nm. The PL signal is analysed using a 0.5 m spectrograph with a 150 g/mm grating and is recorded by a liquid nitrogen-cooled charge-coupled device camera (CCD).

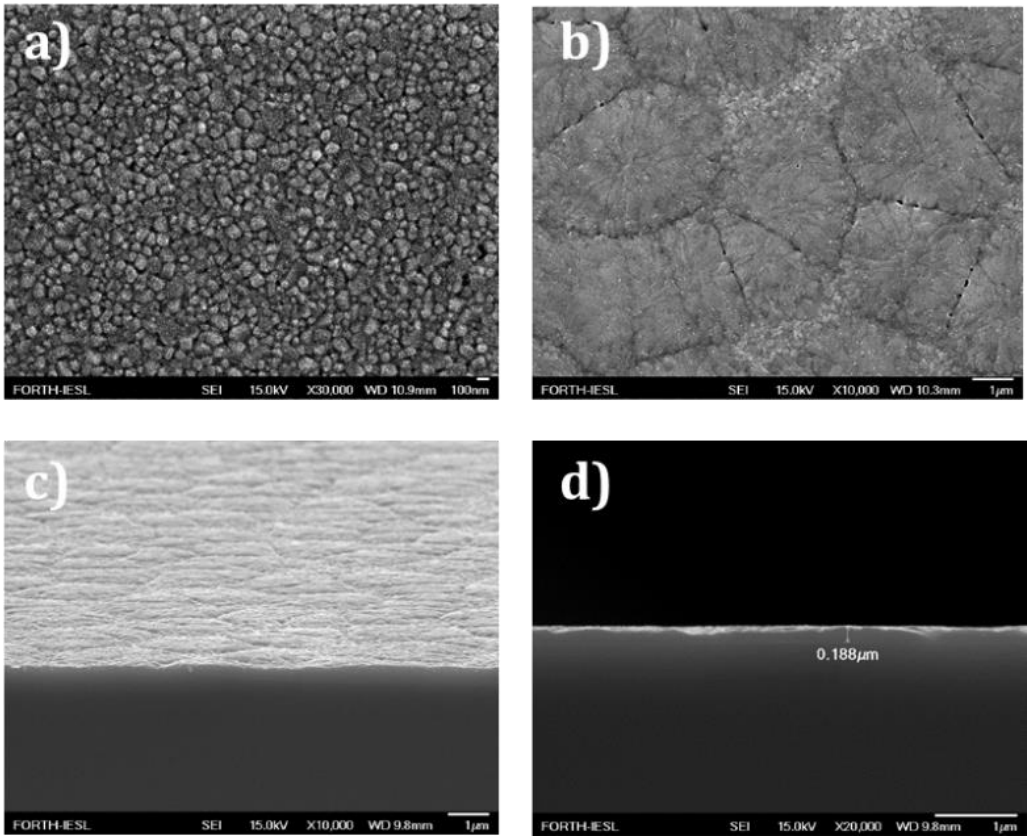

Figure 93. (a) Top-view FE-SEM image from the 67.5nm-thick $MAPbI_3$/GaAs heterostructure. (b) Top-view, (c) Tilted and (d) Cross-section FE-SEM images from another 188nm-thick $MAPbI_3$/GaAs heterostructure confirming the deposition of uniform, dense and pinhole-free perovskite films on GaAs.

As observed in the FE-SEM images of Figure 94(a) and Figure 93(a) for the same sample, a uniform, dense and pinhole-free perovskite film is obtained with a thickness in this case of 67 nm. Similar observations apply to thicker films as well, as shown for instance in Figures 93(b)-(d), for a 188 nm-thick $MAPbI_3$/GaAs sample. In Figure 94(b), the XRD θ-2θ scan obtained on an 80 nm-thick $MAPbI_3$/GaAs sample illustrates the formation of pure $MAPbI_3$.

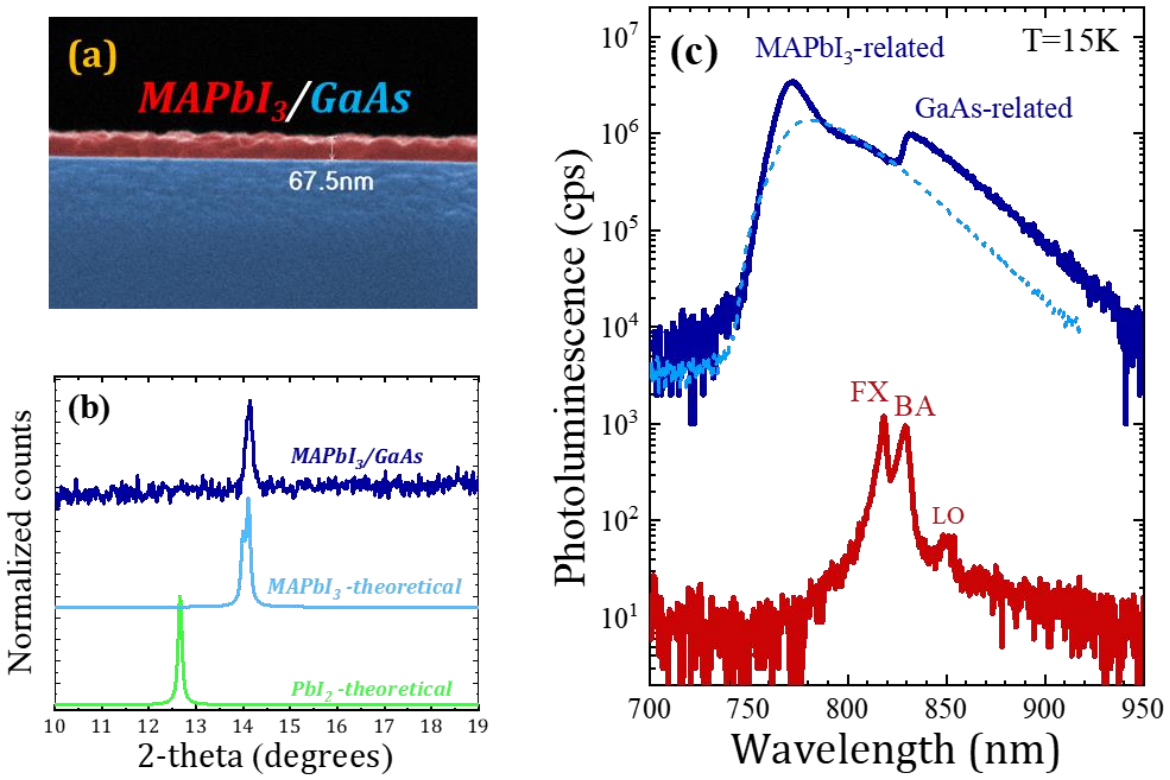

Figure 94. (a) Cross-section FE-SEM image of a 67 nm-thick $MAPbI_3$ on GaAs heterostructure. (b) XRD θ-2θ scan on a similar 80 nm-thick $MAPbI_3$/GaAs sample and comparison with theoretical curves showing the formation of pure $MAPbI_3$. (c) Comparison of low-temperature PL spectra from the 80 nm-thick $MAPbI_3$/GaAs heterostructure (blue solid curve) and a bare GaAs substrate (red solid curve), obtained under same excitation conditions by a 325 nm CW laser. The dashed line corresponds to the PL spectrum of a reference $MAPbI_3$ thin film on glass, spin-cast under the same conditions as in the $MAPbI_3$/GaAs case. The PL intensity of the reference sample has been adjusted in order to highlight the GaAs-related emission peak of the $MAPbI_3$/GaAs sample.

In Figure 94(c), we compare the low temperature PL spectra of the $MAPbI_3$/GaAs heterostructure (upper blue solid curve) and the bare GaAs substrate (lower red solid curve), obtained with a 325 nm CW laser. The PL spectrum of the semi-insulating GaAs substrate contains two main peaks at 15 K. The high energy peak at 1.515 eV corresponds to free-exciton (FX) emission, as confirmed by its spectral overlap with the FX feature in reflectivity. The low energy peak at 1.495 eV is attributed based on the spectral position, to a band to neutral acceptor (BA) recombination line, likely due to carbon atoms occupying arsenic sites [117]. This assignment is further supported by its power and temperature dependence. Specifically, the BA line quenches fast with temperature, at ~40-60 K, a standard behavior for BA transitions in bulk semiconductors due to a combination of electron diffusion and acceptor ionization effects [118] in this temperature range. In addition, with increasing excitation power, the BA line blueshifts

appreciably by several meV, which can be explained by an increased electronic temperature of conduction band electrons participating in the recombination. The possibility of a donor-to acceptor recombination contributing additionally to the BA line cannot be fully excluded, although the spectral position of the peak clearly corroborates in favor of a BA line. A weaker peak at about 850 nm is a longitudinal optical (LO) phonon replica of the BA peak. Importantly, the overall PL emission rate of the semi-insulating GaAs substrate is particularly weak, a consequence of the pronounced nonradiative recombination on surface defects of the GaAs substrate [119]. The situation is drastically altered in the case of the $MAPbI_3$/GaAs sample. Aside from the intense and broad PL emission associated with the perovskite layer, extending in the 760-820 nm range, we can also distinguish a relatively broad "GaAs-related" peak at ~832 nm, which is absent in the PL emission of the reference sample on glass, shown by the dashed line. The assignment of this peak as being "GaAs-related" is further confirmed by the temperature-dependent PL spectra and corresponding peak positions presented in Figure 95 (a),(b), where we observe that the perovskite and GaAs-related peaks shift in opposite directions with temperature, according to the temperature-induced shifts of the respective energy gaps [120], [121].

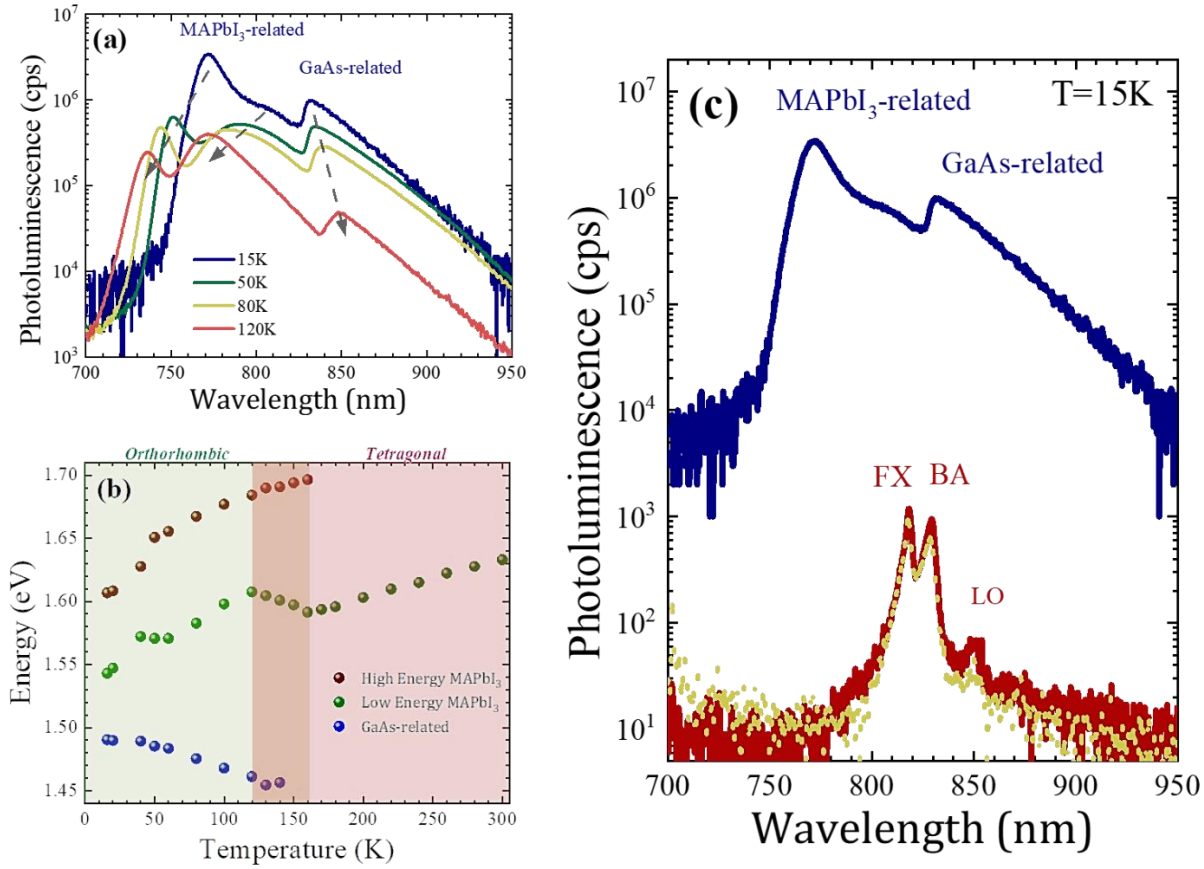

Figure 95. (a) Temperature-dependent PL spectra from the 80 nm-thick $MAPbI_3$/GaAs heterostructure, showing the opposite movement of the $MAPbI_3$-related and GaAs-related peaks with temperature. (b) Energy positions with temperature of the main PL peaks of the same $MAPbI_3$/GaAs sample (c) Reversibility of the passivation process, demonstrated by comparing the low-temperature PL spectra obtained under same excitation conditions by a 325 nm CW laser, from a bare semi-insulating GaAs substrate prior to any deposition (red solid curve), a 80 nm-thick $MAPbI_3$/GaAs sample (blue solid curve), and the same GaAs substrate recovered after washing-away the deposited perovskite film following the cleaning process described in the manuscript (yellow dotted curve).

Coming back to Fig. 94 (c), what is particularly striking is that the PL intensity at the GaAs-related peak, after subtraction of an extrapolated perovskite background, is more than 500 times higher compared to that of the bare GaAs substrate. This giant enhancement can only be attributed to some very efficient passivation of the GaAs surface induced by the presence of $MAPbI_3$. The enhancement process is even more impressive considering that with the 325 nm excitation wavelength, the penetration depth in $MAPbI_3$ is barely ~20 nm[78] while that in GaAs ~13 nm[38]. In other words, even in the 80 nm-thick $MAPbI_3$/GaAs sample of Fig. 94(c), the vast majority (> 98%) of the incident photons is absorbed in the perovskite layer, implying that the GaAs-related emission derives from recombination of carriers, which have diffused first in the perovskite layer and subsequently

transferred to the GaAs region through the $MAPbI_3$/GaAs hetero-interface. Given the efficiency of the whole process, the carrier transfer from the $MAPbI_3$ layer to GaAs appears to be unobstructed, suggesting favorable band-alignments for both electrons and holes in accordance with expectations based on the literature [122], [123]. It is important to note here, that somewhat unexpectedly for the amplitude of the effect, the whole passivation process is fully reversible. As demonstrated in Figure 95 (c), we can fully recover the PL spectrum of the unpassivated GaAs substrate by following a relatively straightforward room-temperature washing procedure described in methods.

This strongly suggests that the passivation process is a surface effect that does not involve any covalent chemical bonding nor any infiltration of atoms inside GaAs, in line with previous studies on oxide-free Pb/GaAs (100) films prepared by molecular beam epitaxy, which showed little chemical interaction between Pb and GaAs and no exchange reaction between Pb and Ga atoms [124], [125].

Interestingly, the "visibility" of the GaAs-related peak with respect to that of $MAPbI_3$ improves significantly with decreasing power of excitation. This can be readily observed in the power-dependent spectra of Figure 96 (a), where at low powers the two peaks seem comparable.

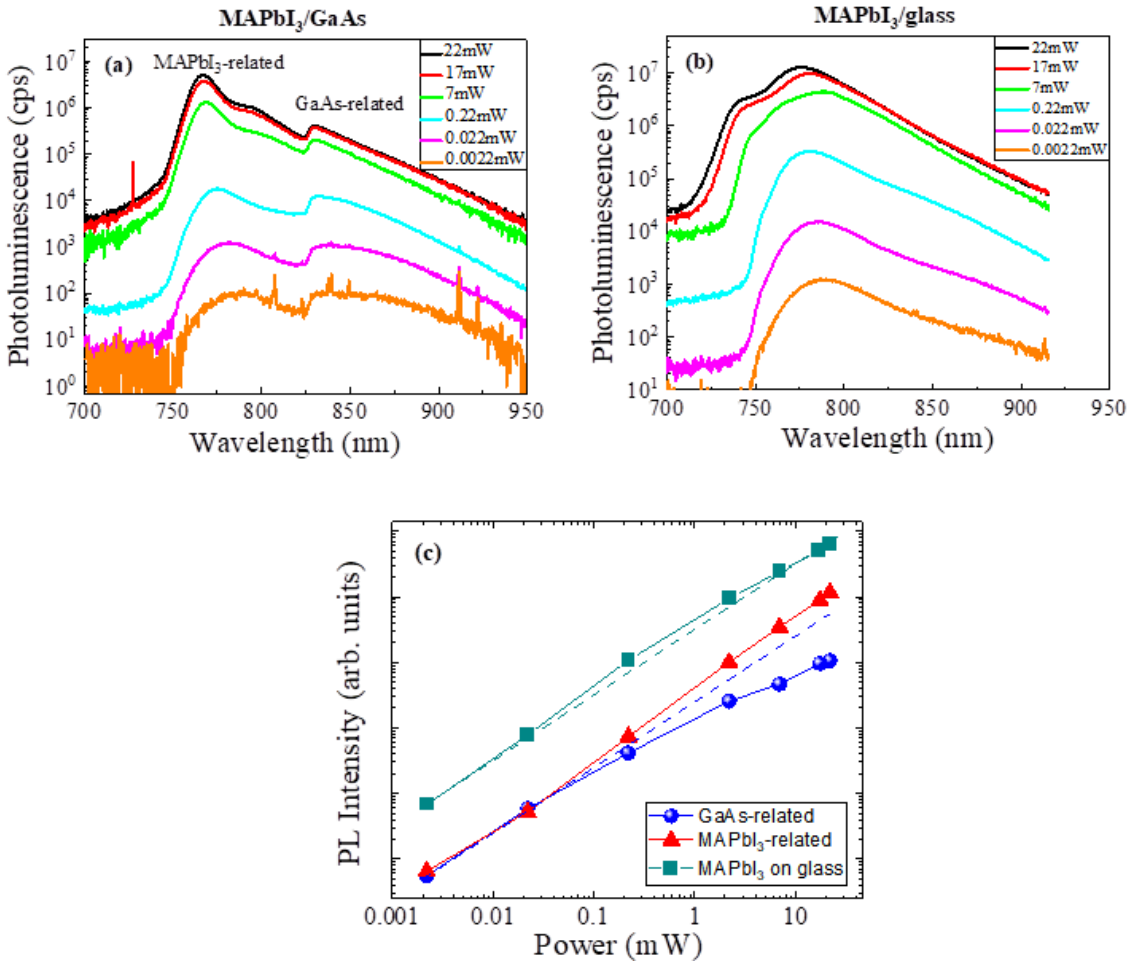

Figure 96. Power-dependent PL spectra at T=20 K obtained with a 325 nm cw laser from (a) an 80 nm-thick $MAPbI_3$/GaAs sample and (b) its twin $MAPbI_3$/glass sample spin-cast under the same conditions. (c) Spectrally-integrated PL intensities as a function of power, for the GaAs-related (spheres) and $MAPbI_3$-related (triangles) peaks of panel (a), as well as the $MAPbI_3$ emission of panel (b). The dashed lines indicate the linear curves in each case. By inspection, it is clear that there exists some saturation mechanism for the GaAs-related peak at high powers, likely related to the carrier diffusion and transfer process from the perovskite layer to the GaAs region, which is also supported by the concomitant super linear increase of the $MAPbI_3$ emission.

On the other hand, at high powers the perovskite peak surpasses that of GaAs by about one order of magnitude. In Figure 96(c), we plot the spectrally integrated PL intensities of the perovskite- and GaAs-related peaks in that experiment, as a function of power. For the spectral integration, we followed a fitting/deconvolution procedure that will be described next. By inspection of Fig. 96(c), it is clear that the GaAs-related peak exhibits a saturation mechanism at high powers, which is likely related to some inhibition of the carrier diffusion and transfer process from the perovskite layer to the GaAs region, an assertion that is supported by the concomitant super-linear increase of the $MAPbI_3$ emission.

Next, we turn our attention to the nature of the GaAs-related emission in the $MAPbI_3$/GaAs heterostructure. First of all, the GaAs-related peak originates from the GaAs region right next to the $MAPbI_3$/GaAs heterointerface. This is particularly true with the 325 nm excitation wavelength, for which the GaAs is necessarily pumped via the perovskite layer.

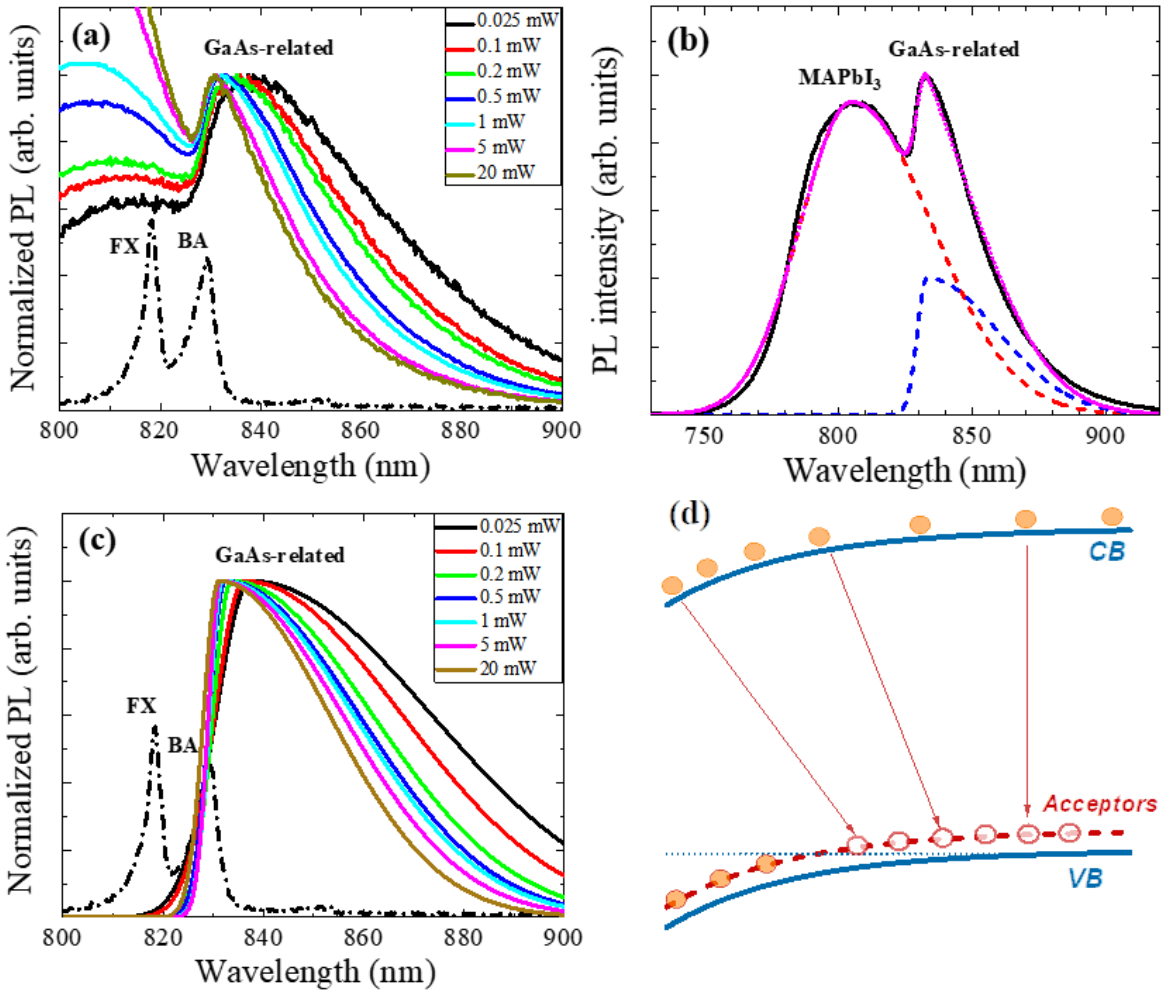

Figure 97. (a) Normalized PL spectra as a function of power, obtained at T=20 K with a 325 nm excitation wavelength from a 300 nm-thick $MAPbI_3$/GaAs sample. The spectra are normalized to the maximum of the GaAs-related peak. The dot-dashed line depicts the PL spectrum of the bare GaAs substrate. (b) Fitting curve (dotted line) of a typical PL spectrum (solid line) of the same $MAPbI_3$/GaAs sample, using two bi-gaussian functions for the perovskite and GaAs-related peaks (dashed lines), as discussed in the text. (c) Deconvoluted GaAs-related peaks versus power, obtained by fitting of the PL spectra of panel (a) and comparison with PL spectrum of GaAs substrate (dot-dashed line). (d) Schematic of the GaAs-related emission mechanism, consistent with experimental findings. The tilted arrows indicate recombination events between conduction band electrons (full circles) and neutral acceptor levels (empty circles) in the valence band. The acceptors near the passivated GaAs surface do not participate in the recombination process as they are ionized by band-bending.

Second, as shown in Figure 97(a), the GaAs-related peak is much broader and significantly redshifted with respect to the BA line of the GaAs substrate.

Notably however, with increasing power of excitation, the GaAs-related peak becomes sharper and its energy position tends asymptotically to that of the BA line. In other words, the GaAs-related peak appears somehow "connected" to the BA line of the GaAs substrate. Third, the GaAs-related peak is distinctly asymmetric, extending significantly toward lower energies, while presenting a high-energy cutoff at about the BA transition energy. To further illustrate this, we fit in Figure 97(b) the perovskite and GaAs-related peaks of a typical PL spectrum, using two bi-gaussian functions whose main adjustable parameters are in this case the amplitude and linewidths of the GaAs-related peak. The outcome of the fitting procedure for the GaAs-related peaks as a function of power is shown in Figure 97(c), with all curves exhibiting pronounced asymmetry and a high-energy cutoff at the BA transition of the GaAs substrate.

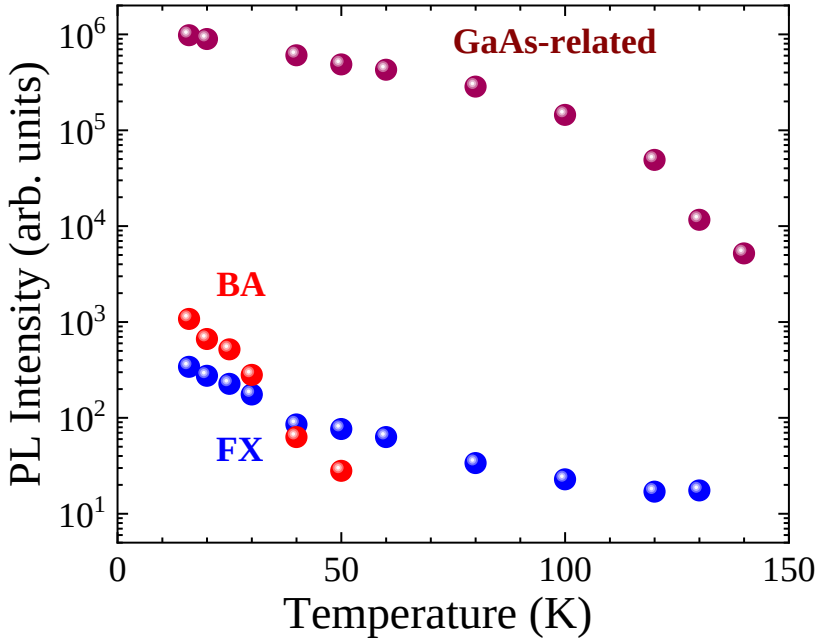

Figure 98. Comparison of the temperature dependence of PL intensity for the GaAs-related peak in a 80 nm-thick $MAPbI_3$/GaAs sample with the band-to acceptor (BA) and free-exciton (FX) peaks of the GaAs substrate.

Fourth, as shown in Figure 98, the GaAs-related peak also collapses abruptly with temperature, at about 120-140 K. All the above observations speak in favor of a "modified" BA transition near the $MAPbI_3$/GaAs hetero-interface. In fact, by assuming slightly tilted BA transitions near the passivated GaAs surface and a small downward band-bending, as schematically depicted in Figure 97(d), we can explain most of the experimental findings regarding the GaAs-related peak, such as the spectral redshift, the asymmetric broadening

toward lower energies, the high-energy cut-off at the BA transition energy of the GaAs substrate, as well as the power-dependent blueshifts and spectral narrowing due to carrier-induced screening of the band-bending. The improved temperature stability of the GaAs-related peak compared to the BA line in the GaAs substrate is not fully clear at the moment, but is probably associated with the enhanced electron lifetimes near the passivated GaAs surface.

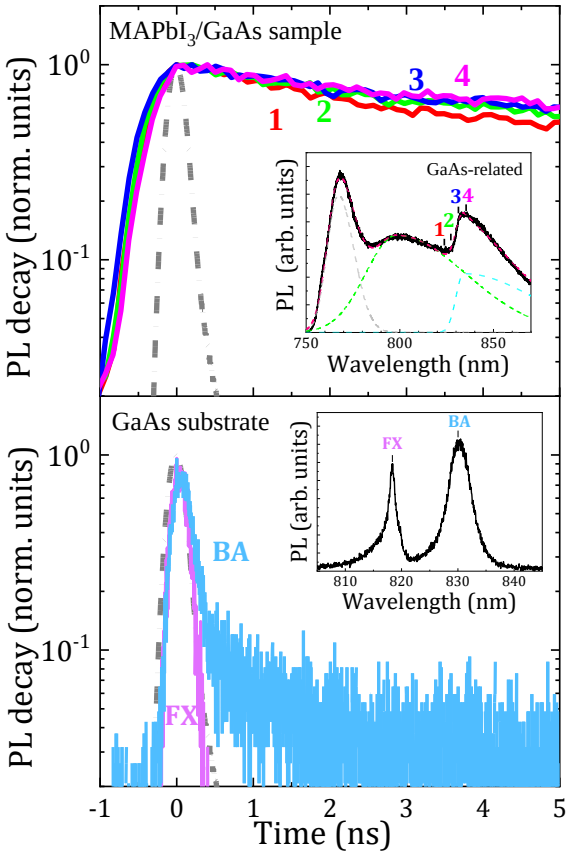

Figure 99. Comparison of time-resolved PL decay curves obtained at T=20 K around the GaAs-related PL peak of a 520 nm-thick $MAPbI_3$/GaAs sample (upper panel) and the FX and BA peaks of the bare GaAs substrate (lower panel). The spectral positions corresponding to the various decay curves are indicated in the PL spectra of the insets, obtained under the same TRPL experimental conditions. In the upper inset, the dashed lines represent the perovskite and GaAs-related contributions leading to the fitting of the PL spectrum. The dot-dashed curve in each panel indicates the instrument response to a sub-picosecond laser pulse in the same spectral range.

Additional evidence on the $MAPbI_3$-induced passivation of GaAs is provided by low temperature TRPL measurements. For the time-resolved PL (TRPL), the samples are excited with a spot size of ~50 μm either by a frequency-doubled Ti:Sapphire laser at 450 nm with 80 MHz repetition rate and 120 fs pulse-width or a picosecond 375 nm laser diode with variable repetition rate 1-100 MHz and 50 ps pulse-width. The TRPL signal is spectrally filtered by a

0.75 m spectrograph with a 1200 g/mm grating blazed at 750 nm and is collected by a fast Silicon fiber-coupled Single-Photon Avalanche Photodiode (SPAD) with time resolution of several hundreds of ps. For the recording of the TRPL curves, the photon incidences in the SPAD are time-correlated in a single-photon counting acquisition card by Becker & Hickl (SPC-130) with a channel width down to 820 fs, using a trigger from a fast photodiode integrated in the pulsed laser.

In Figure 99, we compare the PL decay curves obtained at or near the GaAs-related peak of a 520 nm-thick $MAPbI_3$/GaAs sample (*upper panel*) with those of the FX and BA peaks of a bare GaAs substrate (*lower panel*). In the case of the GaAs substrate the excitation is provided by 80 MHz 120 fs laser pulses at 450 nm, whereas for the $MAPbI_3$/GaAs sample, due to the much longer lifetimes, by 2 MHz 50 ps laser pulses at 375 nm. In both cases, the penetration depth is just a few tens of nm [67], [78], ensuring that the carriers are injected very near the top surface. To maintain the same injection level, the energy density per pulse is adjusted to ~2 μJ/cm^2 in both experiments. The spectral positions corresponding to the various decay curves are indicated in the insets of each panel. The dot-dashed curve in both panels represents the instrument response to a sub-picosecond 800 nm laser pulse, showing a Full-Width at Half-Maximum (FWHM) of ~260 ps and a 1/e-time of ~160 ps, corresponding essentially to the time resolution characteristics of the SPAD detector. Focusing first on the GaAs substrate, the decay curve for the FX line follows closely that of the instrument response, suggesting a FX lifetime that is much shorter than 50 ps. Similarly, the BA decay curve exhibits an initial fast decay with a 1/e-lifetime of ~210 ps, leading after deconvolution of the instrument response to a BA lifetime of about 50-100 ps. At longer times, the BA decay rate progressively slows down, as expected for a BA transition that depends strongly on carrier density [126]. These short lifetimes are commensurate with the particularly weak PL emission of the semi-insulating GaAs substrate. On the other hand, much longer lifetimes are recorded around the GaAs-related peak in the case of the passivated $MAPbI_3$/GaAs sample. As shown in the inset of the upper panel, the GaAs-related peak sits on a perovskite-related background. To disentangle the contributions of the perovskite and the GaAs-related peaks, the selected decay curves correspond to spectral positions 1-4. Position 1 corresponds to almost pure perovskite contribution, while position 4 to the

maximum of the GaAs-related peak. According to the fitting shown in the inset, we estimate that about 50% of the PL intensity in position 4 derives from the GaAs-related peak and 50% from the underneath perovskite contribution. Intermediate positions 2 and 3 progressively increase the contribution of the GaAs-related peak over that of perovskite. Clearly, all decay curves 1-4 exhibit similarly long 1/e-lifetimes of ~20 ns, with the tendency to become slightly longer as the detection wavelength increases. These results allow us to safely conclude that the lifetime of the GaAs-related peak is also of the order of 20 ns or longer. The reason is that if the GaAs-related peak disposed of a lifetime significantly shorter than 20 ns, then at least in the decay curve 4, we would expect to see the coexistence of a fast and a long decay time regime, which is obviously not the case. Hence, to sum up, while in the unpassivated GaAs the BA lifetime is shorter than 100 ps, in the passivated $MAPbI_3$/GaAs case the lifetime of the GaAs-related peak, also of BA origin as discussed in the context of Figure 97, is more than two orders of magnitude longer, in excellent agreement with the giant PL enhancement observed.

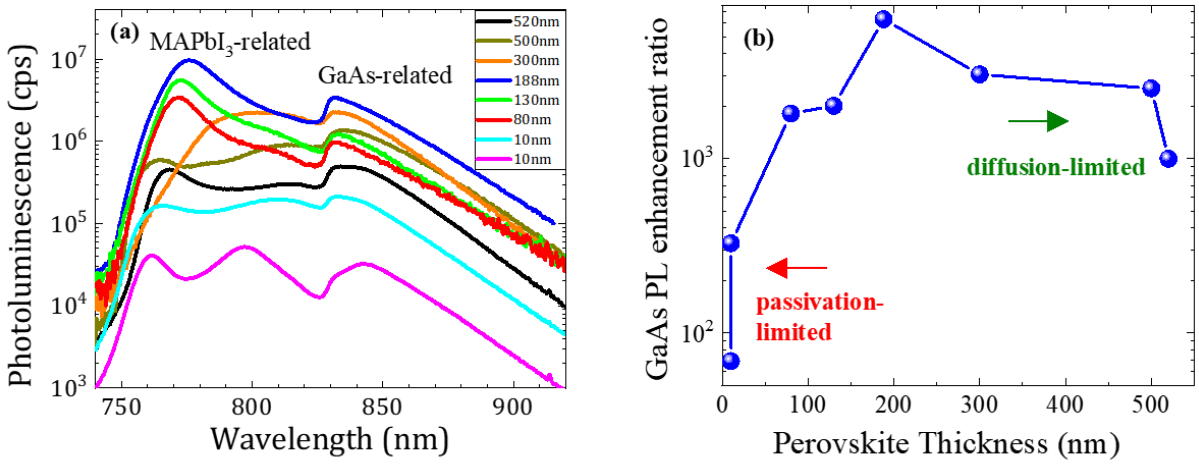

Figure 100. (a) Low-temperature PL spectra obtained with a 325 nm CW laser on several $MAPbI_3$/GaAs thin films of variable thickness. The PL spectra are normalized to the same power of excitation of 22 mW. (b) GaAs PL enhancement ratio as a function perovskite thickness, defined as the ratio of the spectrally-integrated GaAs-related PL intensity in a $MAPbI_3$/GaAs sample (deduced following the fitting/deconvolution procedure described in the text) over that of the unpassivated GaAs substrate.

Another spectacular feature of the passivation process is that even a 10 nm-thick deposition of $MAPbI_3$ on GaAs is sufficient to significantly improve the GaAs surface properties and PL emission. This is emphatically shown in Figure 100(a), where we compare the low-temperature PL spectra of several

$MAPbI_3$/GaAs thin films with varying perovskite thickness between 10 and 520 nm. The PL spectra are obtained with a 325 nm laser and are normalized to the same excitation power. In all samples, we observe the characteristic shape of the GaAs-related peak, sitting on a perovskite background of varying intensity, depending on the film thickness and optical quality. Next, we apply to the PL spectra the fitting procedure described earlier and obtain for each perovskite thickness, the GaAs PL enhancement ratio, defined as the ratio of the spectrally integrated GaAs-related PL intensity in the specific $MAPbI_3$/GaAs sample over that of the unpassivated GaAs substrate. The outcome of this analysis is presented in Figure 100(b), on which we make the following comments: first, for most perovskite thicknesses, enhancement ratios over 1000 are readily observed. These numbers compare favorably to any previously reported value on passivated planar GaAs surfaces. For instance, the sulfide treatment of GaAs [112] leads typically to an enhancement ratio of about 3, while the AlGaAs/GaAs passivation scheme gives a factor of 200 [114],[115]. Second, there seems to be an optimum thickness at ~200 nm, for which an enhancement ratio over 6000 is recorded. Third, for thicknesses larger than 200 nm, there is a systematic decrease in enhancement, most likely associated with limitations of the carrier diffusion process within the perovskite films. Finally, even 10 nm deposition of $MAPbI_3$ leads to enhancements of the order of 100. The lower enhancement values compared to thicker films point at an imperfect passivation of the GaAs surface, possibly due to its incomplete coverage in the ultrathin film limit. This is also discussed in the context of the XPS experiments presented next.

We now attempt to gain insight into the $MAPbI_3$/GaAs hetero-interface by XPS analysis. The X-ray photoelectron spectroscopy (XPS) is carried out in an ultra-high vacuum system (base pressure ≈ $6 \cdot 10^{-10}$ mbar) using non-monochromatic AlKα radiation and a SPECS Phoibos 100 1D-DLD electron analyzer. The pass energy is set at 30 or 10 eV and an electron flood gun is employed for charge compensation during the measurements. The Ga3s peak at 160.1 eV is used as the charge reference, and the electron emission angle is set close to the surface normal. The collection of XPS spectra and the analysis is performed by using the SpecsLab Prodigy software. The peaks are fitted using a mix of Gauss-Lorentzian peak functions, after a Shirley type

background removal. The XPS survey scan of an unpassivated GaAs surface, following treatment with O_2 plasma, is displayed in Figure 101.

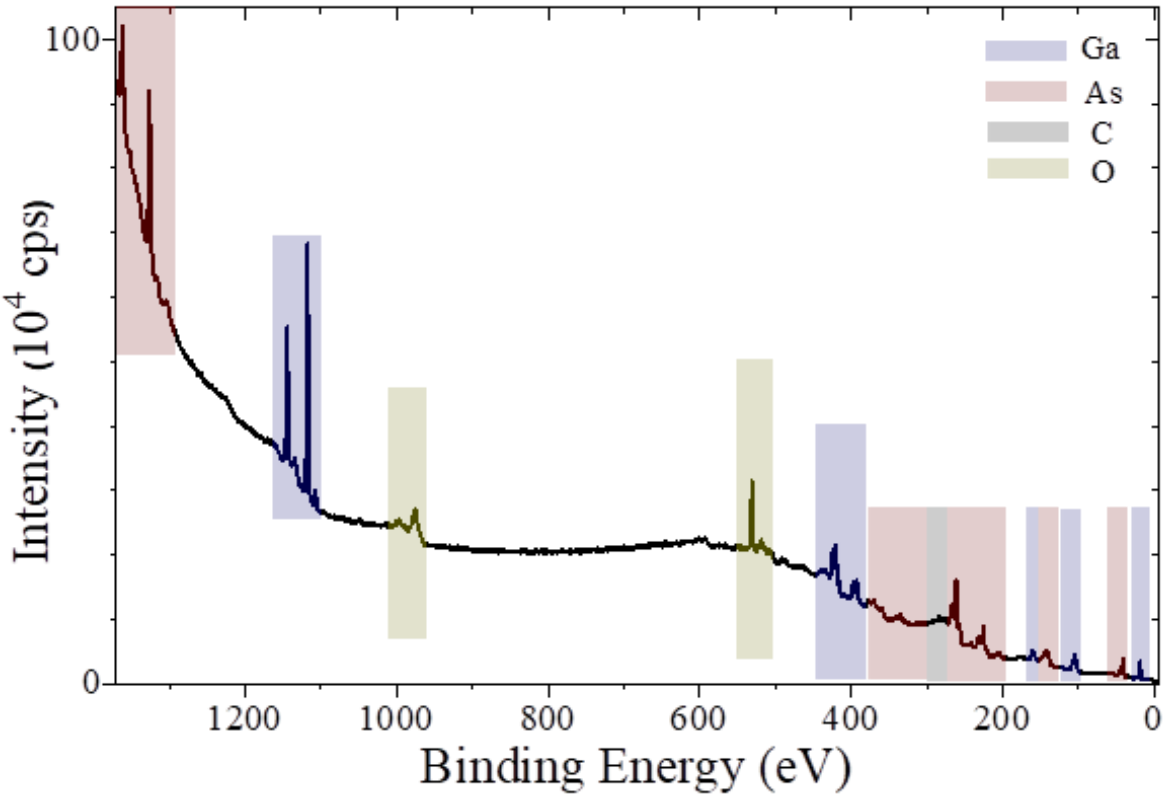

Figure 101. XPS survey scan of the unpassivated (100) GaAs surface treated with O2 plasma.

As expected, the Ga and As peaks dominate the spectrum. Additionally, an O1s peak is observed at 531 eV binding energy. By analyzing the Auger GaLMM and AsLMM peaks, we confirm that the GaAs surface prior to $MAPbI_3$ deposition is oxidized, forming native Ga and As oxides [127].

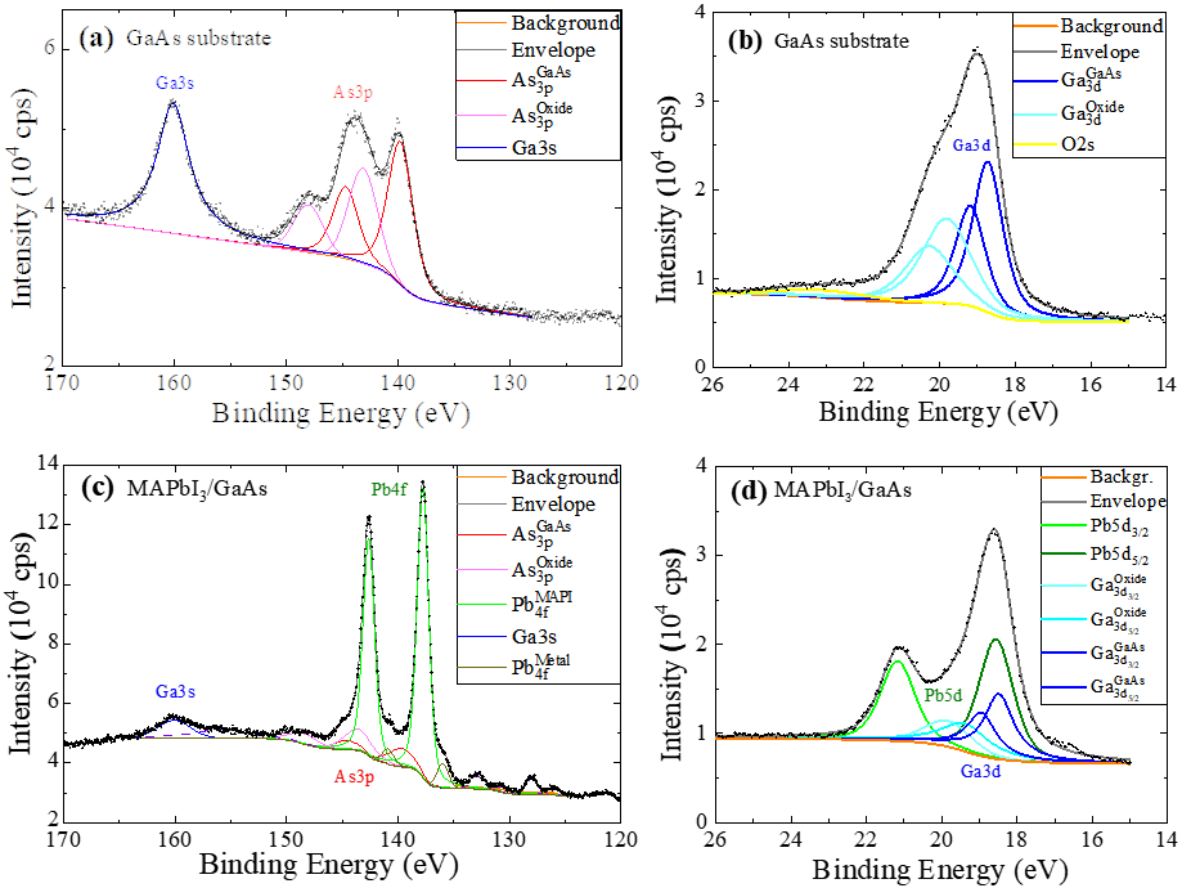

Figure 102. XPS spectra and line fittings for the bare GaAs substrate in the (a) As3p/Ga3s, and (b) Ga3d regions. Respective XPS spectra for a ~20 nm-thick $MAPbI_3$ film on GaAs in the (c) As3p/Ga3s and Pb4f, and (d) Ga3d and Pb5d regions.

This is illustrated for instance in Figure 102(a), where we fit the XPS spectrum of the GaAs substrate in the As3p and Ga3s spectral region, by subtracting a Shirley background and using two doublets for the $As3p_{3/2}$ and $As3p_{1/2}$ lines, corresponding to As atoms in GaAs and As-oxides. The spin-orbit splitting of the As3p doublet peak is set to 4.9 eV [128]. The $As3p_{3/2}$ peak for GaAs is found at 139.8 eV, while that for As oxides at 143.1 eV. Similar observations about the presence of Ga and As oxides on the GaAs surface can be made in other regions of the XPS spectrum, such as the Ga3d peak shown in Figure 102(b), which can be resolved into two doublets corresponding to the GaAs and Ga-oxide species, with a spin-orbit splitting of 0.46 eV, as well as the As3d spectrum of Figure 103, which also very clearly demonstrates the presence of native As-oxide.

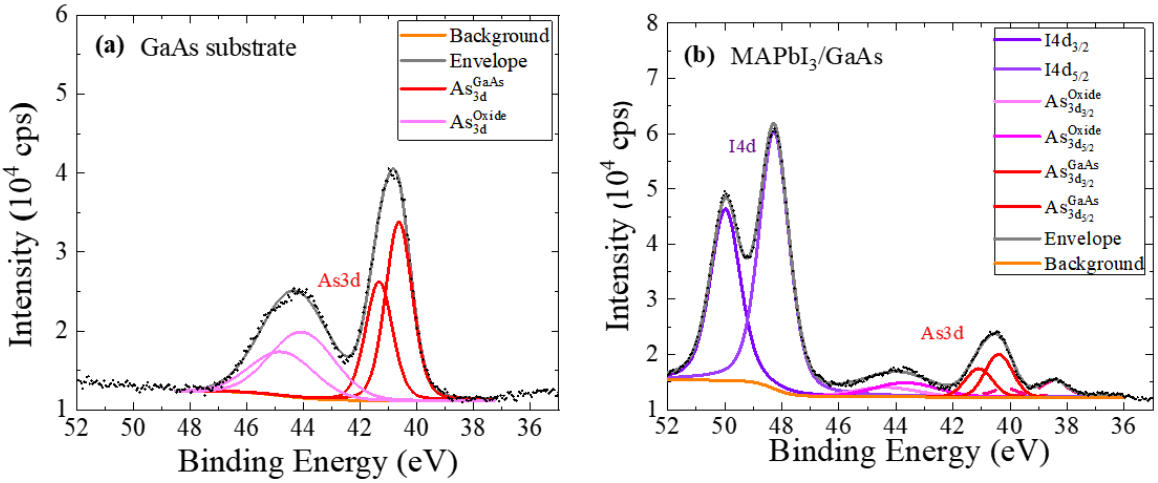

Figure 103. XPS spectrum in the As3d region of (a) an unpassivated GaAs surface and (b) a ~20 nm-thick $MAPbI_3$ film on GaAs.

Passing now to XPS measurements on a 20 nm-thick $MAPbI_3$/GaAs sample, a first general comment is that the GaAs-related XPS peaks are still visible, possibly suggesting that either the GaAs surface is not completely covered or that the perovskite film is not uniformly 20 nm-thick. This picture seems to be supported by atomic force microscopy (AFM) on a twin 20 nm-thick $MAPbI_3$/GaAs sample, presented in Figure 104 (a), showing pronounced granularity and an increased *rms* roughness of about 8 nm, which is comparable to the film's nominal thickness. In Figure 102(c), we present the As3p and Pb4f region of the $MAPbI_3$/GaAs sample. In addition to the GaAs-related peaks seen in Fig. 102(a), we also observe an intense doublet related to the Pb4f lines. In fact, the proximity of the doublets of Pb4f and As3p hinders their analysis. For the fitting process, the binding energies and the FWHM values of the Ga and As peaks are kept the same as in Fig. 102(a). The Pb4f peak is fitted by employing two peaks with a spin-orbit splitting of 4.9 eV. The position of the $Pb4f_{7/2}$ peak at 137.8 eV can be attributed to Pb atoms in perovskite lattice [129]. However, an additional doublet peak is required at lower binding energies, specifically at 136.0 eV ($Pb4f_{7/2}$) and 140.9 eV ($Pb4f_{5/2}$), which can be attributed to metallic Pb. The formation of Pb^0 during the deposition process of the $MAPbI_3$ layer cannot be excluded as a possibility, although it is also possible that the signal deriving from X-ray irradiation damage during the measurement [122],[123]. Figure 102(d) presents the Ga3d spectrum of the $MAPbI_3$/GaAs sample, where the Pb5d peaks overlap with those of Ga3d, complicating the analysis. Nevertheless, the fitting of the data clearly indicates the presence of Ga-oxides in the $MAPbI_3$/GaAs case as well. The possible presence of As-oxides in the

$MAPbI_3$/GaAs interface is further implied by the As3d spectrum of Figure 103(b). However, as noted above, we cannot exclude at this stage the possibility that the detection of the Ga and As oxides in the XPS spectra of the $MAPbI_3$/GaAs sample derives not from the hetero-interface between $MAPbI_3$ and GaAs but rather from areas of the GaAs surface that are not covered by perovskite.

To overcome the difficulty related to achieving a uniform ultrathin $MAPbI_3$ layer on GaAs and to investigate whether the interaction between the GaAs surface and $MAPbI_3$ is compound-specific and not element-specific, a 10 nm-thick layer of PbI_2 was deposited on GaAs and characterized by XPS, using a similar protocol with that of $MAPbI_3$. For compatibility purposes, the fitting of the peaks is based on the binding energies and FWHMs from the previous analyses on $MAPbI_3$/GaAs interfaces.

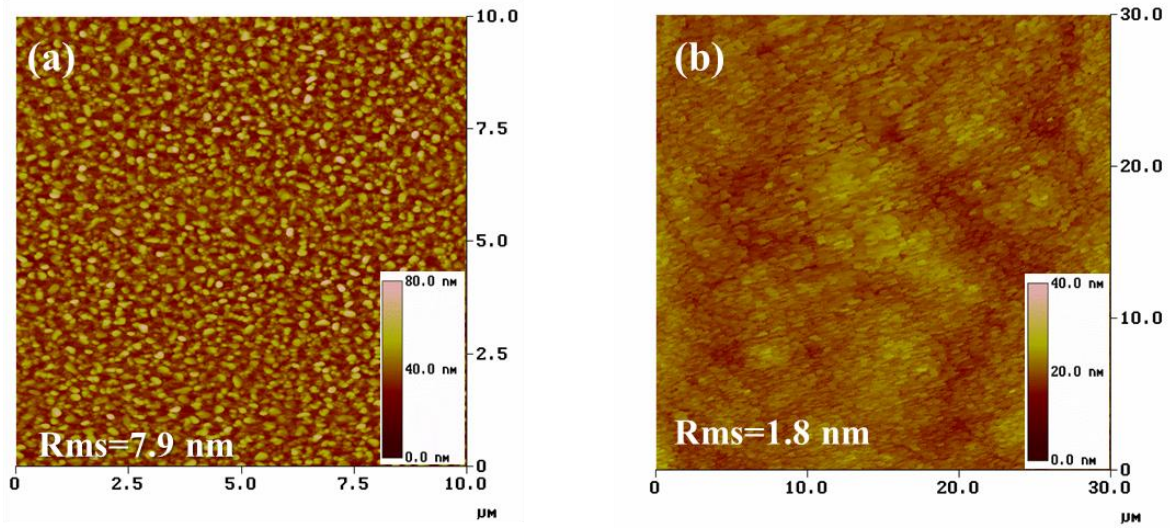

Figure 104. AFM images from (a) a 20 nm-thick MAPbI3/GaAs and (b) a 10 nm-thick PbI2/GaAs sample. Both samples are twins of those studied in XPS, produced in the same run under identical conditions.

The deposition of PbI_2 on GaAs produces uniform and relatively smooth films, even in the ultrathin limit, as displayed in 104(b). Figures 105(a) and (b) present the XPS spectra of Pb4f and I3d, respectively, for the PbI_2/GaAs sample. Remarkably, iodine is completely absent in this hetero-interface as shown in panel (b), despite the clear presence of Pb observed in panel (a).

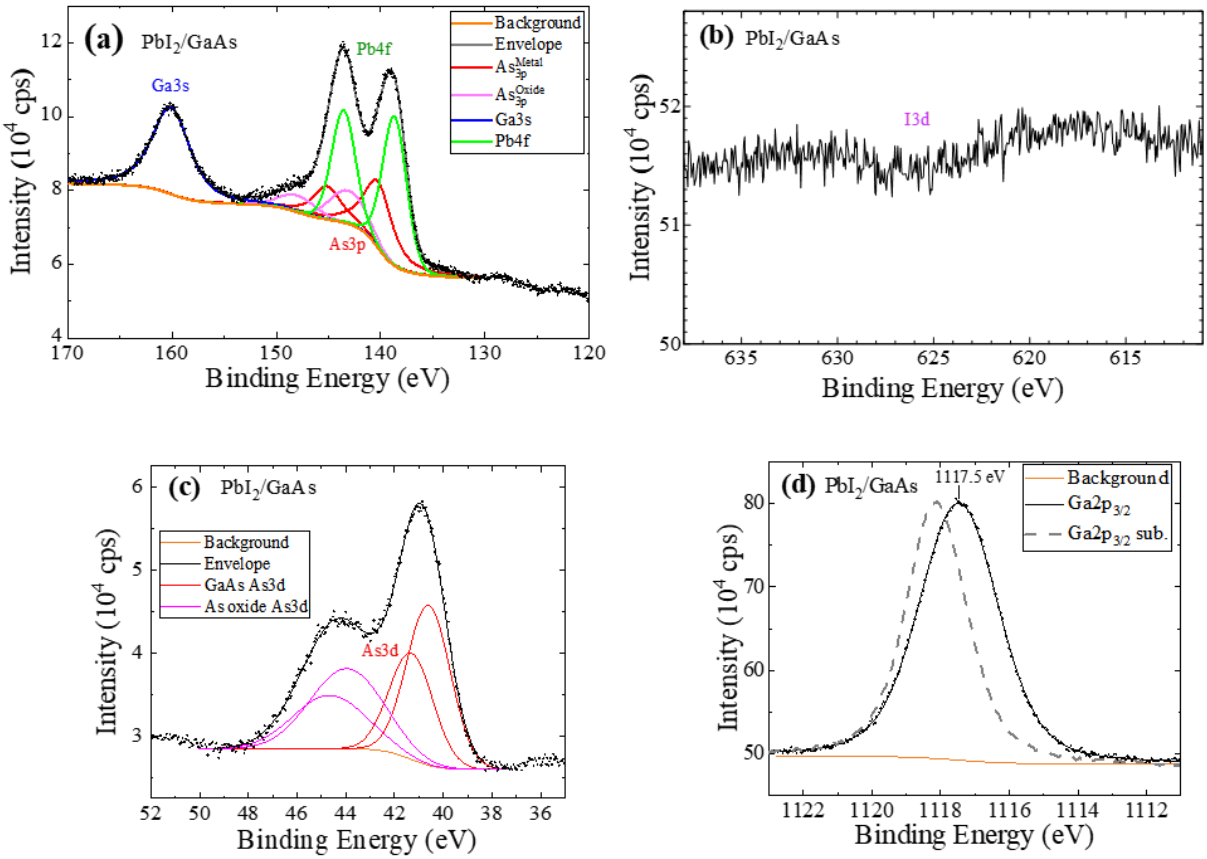

Figure 105. XPS spectra and line fittings for a ~10 nm-thick PbI_2 film on GaAs in the (a) Pb4f and As3p, (b) I3d, (c) As3d, and (d) $Ga2p_{3/2}$ regions. The dashed line in panel (d) shows the adjusted in intensity $Ga2p_{3/2}$ spectrum of the GaAs substrate, for comparison.

According to further analysis, the $Pb4f_{7/2}$ peak is located at 138.7 eV, which is approximately 0.9 eV higher than the Pb^{+2} oxidation state of the $MAPbI_3$ film, pointing towards the formation of intermediate Pb-related species at the interfacial layer, such as PbO, $Pb(OH)_2$ or Pb(OH)I compounds, previously observed in PbI_2-growth studies [132]. Additional information related to the As- and Ga-oxides of the PbI_2/GaAs interface is provided by the XPS spectra of Figures 105(c) and (d). Specifically, a marked signature of As-oxide, as strong as in the GaAs substrate, is obtained in panel (c). On the other hand, the presence of Ga-oxide in the PbI_2/GaAs interface appears significantly reduced. In part, this is already suggested by the Ga3d spectrum of this sample shown in Figure 106, where the spectral fitting is possible without assuming any Ga-oxide peaks.

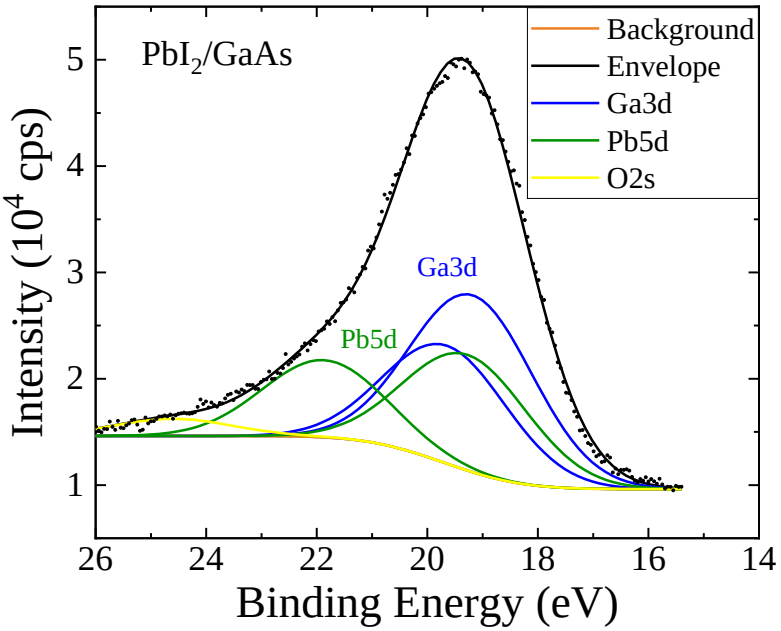

Figure 106. XPS spectrum and fitting lines in the Ga3d and Pd5d region of the ~10 nm-thick PbI_2 film on GaAs.

However, as the analysis of the Ga3d spectrum is obscured by the Pb5d bands, in Figure 105(d) we focus on the $Ga2p_{3/2}$ peak of the PbI_2/GaAs sample, a spectral range without interference by other lines. The $Ga2p_{3/2}$ peak is found significantly shifted by ~0.6 eV toward lower binding energy compared to that of the GaAs substrate (dashed line), strongly suggesting the removal of Ga oxide from the interface.

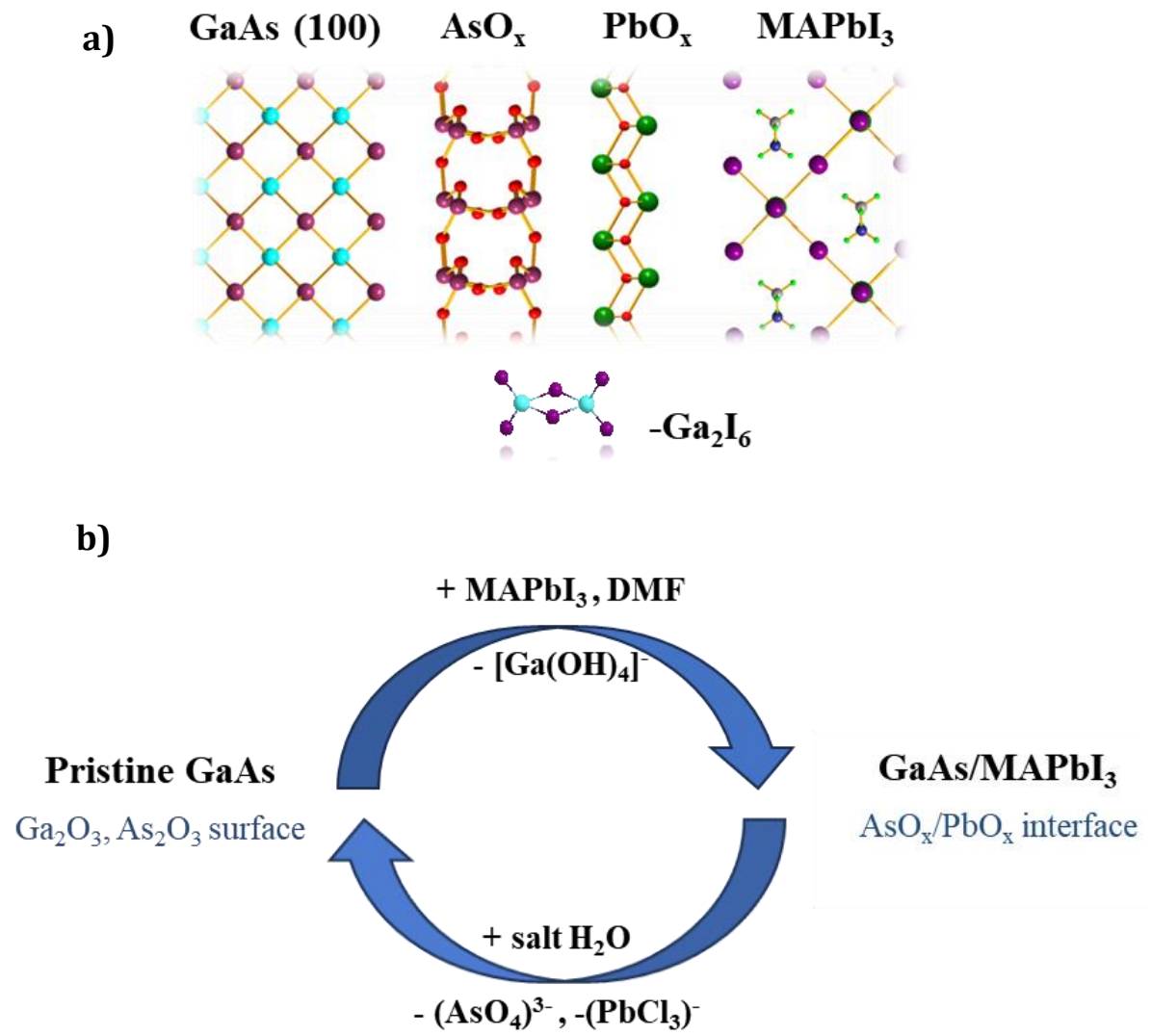

Figure 107. (a) The structural model of the GaAs/MAPbI$_3$ interface. The stacking of oxide layers on the surfaces of GaAs (AsO$_x$) and MAPbI$_3$ (PbO$_x$) is the active interaction layer between the two materials. (b) A proposed mechanism showing the reversibility of the perovskite deposition/removal from the GaAs surface.

Based on the above observations, we hypothesize a GaAs/MAPbI$_3$ interface model shown in Figure 107(a). The model consists of a fully oxidized GaAs surface, which upon deposition of MAPbI$_3$ loses a large fraction of the Ga$_2$O$_3$ component (likely as Ga$_2$I$_6$ or other hydrolysis products), leaving behind an AsO$_x$-rich surface. In parallel, MAPbI$_3$ is deposited on the modified GaAs surface, forming at the contact interface oxide-containing lead species (likely PbO, Pb(OH)$_2$ or Pb(OH)I). An alternative model that could be also considered is the formation at the interface of arseno-apatite, Pb$_5$(AsO$_4$)$_3$I, a stable quaternary compound [133] which offers a common element platform to interface the Pb-based iodide compounds with GaAs. Coming back to the interface model of Figure 107(a), a plausible mechanistic explanation for the

removal of Ga may be sought in the fact that Ga_2O_3 is the most basic of the two oxides of GaAs and is therefore more likely to be attacked by the slightly acidic deposition solution. The acidity of the medium can derive either from complexation of Pb^{2+} or from the presence of weak acids such as CH_3NH_3I or residual dimethylammonium cations from hydrolysis of DMF [134]. Such a hydrolysis path can selectively produce molecular Ga species, which are prone to further hydrolysis under the conditions of the experiment. The hydrolyzed Ga species are subsequently suitable for solvent removal, leaving a more uniform layer of AsO_x oxides to passivate the GaAs surface or form complex interfaces with the residual Pb species. The chemical reaction sequence proposed here, as well as the complex interfacial products that can result from these reactions, are in good agreement with the full recovery of the optical features associated with the unpassivated GaAs surface, by applying the simple perovskite washing procedure described in methods. This is schematically depicted in Figure 108(b), where the solubility of AsO_x in water is the main mechanism for recovering a clean oxide-free GaAs surface upon washing the perovskite layer with salt water.

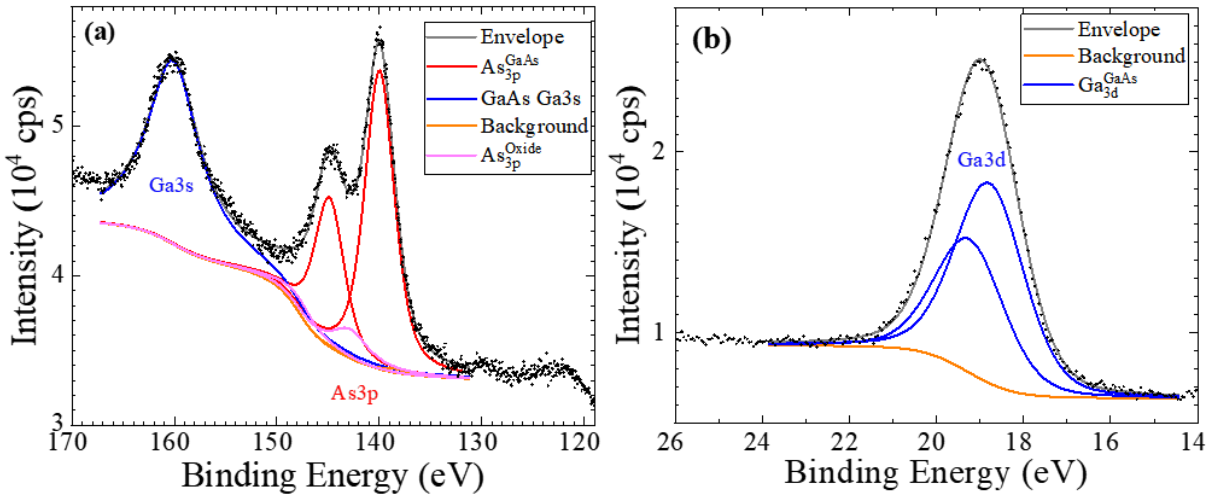

Figure 108. XPS spectra and line fittings in the (a) Pb4f and As3p, and (b) Ga3d regions for the PbI_2/GaAs sample washed with de-ionized water.

Strong hints about the reversibility of the passivation process are also given by XPS spectra, obtained after lightly washing the PbI_2/GaAs specimen with de-ionized water. The spectrum of the Pb4f and As3p region shown in Figure 108(a) indicates the elimination of Pb and the near complete removal of As-oxide from the GaAs surface. This is further illustrated in Figure 108(b), where the shape of the Ga3d peak is distinctly different from that in Figures 102 (b) and (d), confirming the efficient removal of Pb during the washing

step, as well as the absence of any Ga-oxide. The reduced As-oxide peaks in the region around 44 eV of the As3d peak, shown in Figure 109, further support this conclusion.

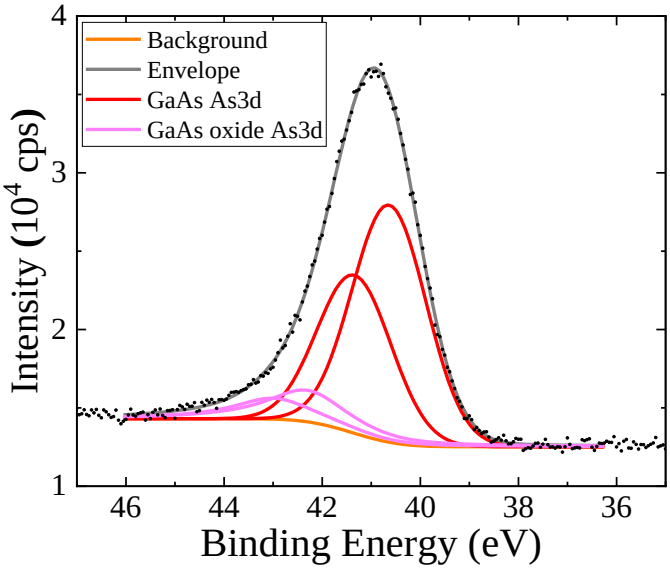

Figure 109. XPS spectrum and fitting lines in the As3d region of the PbI_2/GaAs sample washed with de-ionized water.

Consequently, it is believed that Pb forms complex oxides with O on the GaAs surface, which are subsequently easily removable during H_2O washing, resulting in a clean *re-usable* GaAs surface.

In conclusions, we show that the deposition of a thin film of $MAPbI_3$ on native nominally-undoped (100) GaAs substrates is able to produce a huge passivation effect on the GaAs surface. Specifically, we observe in $MAPbI_3$/GaAs samples, the emergence of a broad and intense "GaAs-related" peak, whose integrated intensity is enhanced by a factor up to 6000, with respect to that of the bare GaAs substrate. We present evidence that the GaAs-related peak derives from "band to acceptor"-type recombination, occurring next to the passivated GaAs surface. The observation in the case of a $MAPbI_3$/GaAs sample of enhanced PL lifetimes, by more than two orders of magnitude, further illustrates the passivating influence of $MaPbI_3$ on the GaAs surface. To the best of our knowledge, the observed PL enhancement factors are the highest ever reported for a passivated two-dimensional GaAs surface. In addition, this should be the first study, reporting *any* passivation effect on a native GaAs surface, *i.e.* without removing first its native oxides. XPS measurements on ultrathin $MAPbI_3$/GaAs and PbI_2/GaAs specimens allow us to delineate a plausible interface model, where a $MAPbI_3$-related

reduction of the native Ga-oxide on the GaAs surface is accompanied by the formation of some oxide-containing lead-species on the $MAPbI_3$ side. Further studies are necessary to elucidate the precise mechanism that leads to the extraordinary passivation factors of GaAs reported here. Finally, we note that the passivation process appears to be fully reversible, in the sense that it is possible with a straightforward cleaning procedure, to completely remove the $MAPbI_3$ overlayer and recover the GaAs substrate is its pristine form.

Conclusions and Future Work

Summarizing the presented results, we have focused on the combination of Perovskite-Gallium Arsenide materials to demonstrate a Tandem Solar Cell with enhanced characteristics. As a first step, we have fabricated and characterized several GaAs-based Solar Cell devices with different structures. Our best structure showed a ~15% PV efficiency with excellent electrical characteristics. Moreover, we have developed a reproducible "out-of-the glovebox" technique, providing high quality, uniform and well controlled perovskite films, either using anti-solvent or gas-quenching technique. Additionally, we have shown that gas-quenching technique is promising for large area films with better control. Focusing on perovskite solar cells with the FTO/$TiO_{2\text{-compact}}$/$TiO_{2\text{-mesoporous}}$/Perovskite/SPIRO-OMeTAD/Au structure, we have characterized several perovskite films of different compositions, exploiting different regions of the solar spectrum. Our final target was a perovskite with an energy gap of 1.9 eV for a GaAs/Perovskite tandem solar cell. Toward this end, we addressed mixed cation perovskite thin films which showed significant photo-induced phase separation effects which should be controlled. Further optimizations led us to a triple-cation perovskite thin film, with an optimized recipe of $FA_{0.8}MA_{0.04}Cs_{0.16}Pb(I_{0.5}Br_{0.5})_3$ + 5% $PbCl_2$ in GBL: DMSO mixed solution. This recipe presented enhanced stability with improved characteristics. Coming back to the perovskite solar cells, we showed that an extra $TiCl_4$ layer between the compact and the mesoporous TiO_2 improves the device performance, while another important step is the surface passivation of the perovskite, using either PEA-I or PEA-Cl 2D perovskite layer. The optimized SPIRO-OMeTAD recipe that presented additional improvements for the perovskite devices was a 144.6 mg Spiro-OMeTAD, 57.6μL TBP, 35μL Li-TFSI (520mg/mL in acetonitrile), 58μL FK-209 (320mg/ mL in acetonitrile) and 1mL Chlorobenzene. A critical step for the "out-of-the-glovebox" depositions proved the re-drying of each material we used. Using all the optimizations, we achieved a "red" perovskite solar cell with a 6.37% PV efficiency, with significantly reduced hysteresis effect under forward and reverse I-V scans. Nevertheless, our "out-of-the-glovebox" "red" solar cells exhibited a significantly lower PV efficiency compared to similar perovskite solar cells reported in the literature, which were fabricated inside a glovebox and showed an efficiency of ~14% [14].

An extra step in terms of Tandem approach, was the fabrication of a transparent top-electrode, which should replace the opaque Au contact. On that term, we addressed the deposition of ITO immediately on the SPIRO-OMeTAD, where we observed significantly lower PV efficiencies. We suggest

that these reduced efficiencies are due to HTL damage during ITO deposition, that we tried to solve by depositing and characterizing alternative oxide-materials, which showed some promising electrical and optical characteristics. Additionally, we took the first steps toward a 2-Terminal monolithic tandem solar cell, using either a recombination layer or a tunnel diode. For the recombination layer, we used an ultra-thin ITO layer which showed promising characteristics while we additionally designed via ATLAS simulator a GaAs tunnel junction.

Finally, we characterized a 4-T GaAs-Perovskite tandem solar cell using our "out-of-the-glovebox" 1.9eV perovskite solar cell, either as a spectral filter or as a top sub-cell, in an effort to address the effect of such a combination even if we do not dispose of a transparent top electrode. This combination showed no gain as we were short of top-sub-cell efficiency. On the other hand, by using an optimized 1.77eV top-sub-cell with transparent electrodes, provided by a collaborating team, even though it did have not the optimum energy gap for a combination with a GaAs bottom sub-cell, such a combination showed a ~1.35 times increased efficiency compared to the top Perovskite solar cell alone, which has the highest efficiency compared to the GaAs bottom-subcell.

To achieve perovskite/GaAs tandem structures, we have experimented with the deposition of a $MAPbI_3$ film on a GaAs substrate, where we realized that this heterostructure exhibits a spectacular enhancement of the GaAs-based emission up to a factor of 6000, that we attributed to some self-deoxidation and passivation process of the GaAs surface. This passivation process is promising for GaAs-Perovskite devices, either in terms of photovoltaics or of other optoelectronic devices.

As future work in terms of tandem solar cells, we would address techniques that can lead to improved efficiencies of an "out-of-the-glove-box" perovskite solar cell. These techniques should contain effective passivation of the interfaces and alternative humidity-insensitive materials in combination with perovskite photo-active layer. These could be oxide-based materials with optimization on the deposition process producing no-damage of the underneath layers. Additionally, we would focus on the optimization of GaAs/Perovskite (1.77eV) tandem solar cell which showed so far, a very competitive tandem PV efficiency. These optimizations could contain deposition of extra antireflective coatings on both sides of the perovskite solar cell, which can effectively increase the overall efficiency. Last but not least, we would further investigate the GaAs/$MAPbI_3$ heterostructure, in view of obtaining a deeper understanding of the passivation mechanism. This investigation could lead to well-designed GaAs-based optoelectronic devices with improved performance.

References

[1] Perlin, J., "Silicon Solar Cell Turns 50," United States, Jan. 08, 2004. [Online]. Available: https://www.osti.gov/biblio/15009471

[2] J. Perlin, *From space to earth: the story of solar electricity*, 1st Havard University Press ed. Cambridge, Mass: Harvard University Press, 2002.

[3] "NREL Interactive Best Research Cell Efficiency Chart." [Online]. Available: https://www.nrel.gov/pv/interactive-cell-efficiency.html

[4] "Advanced information on the Nobel Prize in Physics 2000".

[5] N. F. Atta, A. Galal, and E. H. El-Ads, "Perovskite Nanomaterials – Synthesis, Characterization, and Applications," in *Perovskite Materials - Synthesis, Characterisation, Properties, and Applications*, L. Pan and G. Zhu, Eds., InTech, 2016. doi: 10.5772/61280.

[6] A. Kojima, K. Teshima, Y. Shirai, and T. Miyasaka, "Organometal Halide Perovskites as Visible-Light Sensitizers for Photovoltaic Cells," *J. Am. Chem. Soc.*, vol. 131, no. 17, pp. 6050–6051, May 2009, doi: 10.1021/ja809598r.

[7] H.-S. Kim *et al.*, "Lead Iodide Perovskite Sensitized All-Solid-State Submicron Thin Film Mesoscopic Solar Cell with Efficiency Exceeding 9%," *Sci Rep*, vol. 2, no. 1, p. 591, Aug. 2012, doi: 10.1038/srep00591.

[8] J. Park *et al.*, "Controlled growth of perovskite layers with volatile alkylammonium chlorides," *Nature*, vol. 616, no. 7958, pp. 724–730, Apr. 2023, doi: 10.1038/s41586-023-05825-y.

[9] S. M. Bedair, M. F. Lamorte, and J. R. Hauser, "A two-junction cascade solar-cell structure," *Applied Physics Letters*, vol. 34, no. 1, pp. 38–39, Jan. 1979, doi: 10.1063/1.90576.

[10] J. M. Olson, S. R. Kurtz, A. E. Kibbler, and P. Faine, "A 27.3% efficient Ga0.5In0.5P/GaAs tandem solar cell," *Applied Physics Letters*, vol. 56, no. 7, pp. 623–625, Feb. 1990, doi: 10.1063/1.102717.

[11] K. A. Bertness, S. R. Kurtz, D. J. Friedman, A. E. Kibbler, C. Kramer, and J. M. Olson, "29.5%-efficient GaInP/GaAs tandem solar cells," *Applied Physics Letters*, vol. 65, no. 8, pp. 989–991, Aug. 1994, doi: 10.1063/1.112171.

[12] J. P. Mailoa *et al.*, "A 2-terminal perovskite/silicon multijunction solar cell enabled by a silicon tunnel junction," *Applied Physics Letters*, vol. 106, no. 12, p. 121105, Mar. 2015, doi: 10.1063/1.4914179.

[13] K. A. Bush *et al.*, "23.6%-efficient monolithic perovskite/silicon tandem solar cells with improved stability," *Nat Energy*, vol. 2, no. 4, p. 17009, Feb. 2017, doi: 10.1038/nenergy.2017.9.

[14] Z. Li *et al.*, "Wide-Bandgap Perovskite/Gallium Arsenide Tandem Solar Cells," *Adv. Energy Mater.*, vol. 10, no. 6, p. 1903085, Feb. 2020, doi: 10.1002/aenm.201903085.

[15] T. E. Schlesinger, "Gallium Arsenide," in *Encyclopedia of Materials: Science and Technology*, Elsevier, 2001, pp. 3431–3435. doi: 10.1016/B0-08-043152-6/00612-4.

[16] C. F. Kamdem, A. T. Ngoupo, F. K. Konan, H. J. T. Nkuissi, B. Hartiti, and J.-M. Ndjaka, "Study of the Role of Window Layer Al0.8Ga0.2As on GaAs-based Solar Cells Performance," *ijst*, vol. 12, no. 37, pp. 1–9, Oct. 2019, doi: 10.17485/ijst/2019/v12i37/147207.

[17] D. K.C, "InGaP Window Layer for Gallium Arsenide (GaAs) based Solar Cell Using PC1D Simulation," *JARDCS*, vol. 12, no. SP7, pp. 2878–2885, Jul. 2020, doi: 10.5373/JARDCS/V12SP7/20202430.

[18] J. G. Fossum, "Physical operation of back-surface-field silicon solar cells," *IEEE Trans. Electron Devices*, vol. 24, no. 4, pp. 322–325, Apr. 1977, doi: 10.1109/T-ED.1977.18735.

[19] B. Galiana, I. Rey-Stolle, M. Baudrit, I. García, and C. Algora, "A comparative study of BSF layers for GaAs-based single-junction or multijunction concentrator solar cells," *Semicond. Sci. Technol.*, vol. 21, no. 10, pp. 1387–1392, Oct. 2006, doi: 10.1088/0268-1242/21/10/003.

[20] C. Eames, J. M. Frost, P. R. F. Barnes, B. C. O'Regan, A. Walsh, and M. S. Islam, "Ionic transport in hybrid lead iodide perovskite solar cells," *Nat Commun*, vol. 6, no. 1, p. 7497, Jun. 2015, doi: 10.1038/ncomms8497.

[21] K. P. Ong *et al.*, "Multi Band Gap Electronic Structure in CH3NH3PbI3," *Sci Rep*, vol. 9, no. 1, p. 2144, Feb. 2019, doi: 10.1038/s41598-018-38023-2.

[22] C.-C. Chueh, C.-Z. Li, and A. K.-Y. Jen, "Recent progress and perspective in solution-processed Interfacial materials for efficient and stable polymer and organometal perovskite solar cells," *Energy Environ. Sci.*, vol. 8, no. 4, pp. 1160–1189, 2015, doi: 10.1039/C4EE03824J.

[23] S. Khan and E. Stamate, "Comparative Study of Aluminum-Doped Zinc Oxide, Gallium-Doped Zinc Oxide and Indium-Doped Tin Oxide Thin Films Deposited by Radio Frequency Magnetron Sputtering," *Nanomaterials*, vol. 12, no. 9, p. 1539, May 2022, doi: 10.3390/nano12091539.

[24] J. Abad and J. Padilla, “Transparent Conductive Polymers,” in *Transparent Conductive Materials*, D. Levy and E. CastellÓn, Eds., Weinheim, Germany: Wiley-VCH Verlag GmbH & Co. KGaA, 2018, pp. 193–244. doi: 10.1002/9783527804603.ch3_3.

[25] A. Khan, O. Fayyaz, R. A. Shakoor, and B. Mansoor, “Recent Trends in Applications of X-ray Photoelectron Spectroscopy (XPS) Technique in Coatings for Corrosion Protection,” in *Recent Developments in Analytical Techniques for Corrosion Research*, I. U. Toor, Ed., Cham: Springer International Publishing, 2022, pp. 167–186. doi: 10.1007/978-3-030-89101-5_8.

[26] M. H. Engelhard, T. C. Droubay, and Y. Du, “X-Ray Photoelectron Spectroscopy Applications,” in *Encyclopedia of Spectroscopy and Spectrometry*, Elsevier, 2017, pp. 716–724. doi: 10.1016/B978-0-12-409547-2.12102-X.

[27] C. S. Fadley, “X-ray photoelectron spectroscopy: Progress and perspectives,” *Journal of Electron Spectroscopy and Related Phenomena*, vol. 178–179, pp. 2–32, May 2010, doi: 10.1016/j.elspec.2010.01.006.

[28] J. Epp, “X-ray diffraction (XRD) techniques for materials characterization,” in *Materials Characterization Using Nondestructive Evaluation (NDE) Methods*, Elsevier, 2016, pp. 81–124. doi: 10.1016/B978-0-08-100040-3.00004-3.

[29] G. T. Carroll, R. C. Dowling, D. L. Kirschman, M. B. Masthay, and A. Mammana, “Intrinsic fluorescence of UV-irradiated DNA,” *Journal of Photochemistry and Photobiology A: Chemistry*, vol. 437, p. 114484, Mar. 2023, doi: 10.1016/j.jphotochem.2022.114484.

[30] P. Löper *et al.*, “Complex Refractive Index Spectra of $CH_3NH_3PbI_3$ Perovskite Thin Films Determined by Spectroscopic Ellipsometry and Spectrophotometry,” *J. Phys. Chem. Lett.*, vol. 6, no. 1, pp. 66–71, Jan. 2015, doi: 10.1021/jz502471h.

[31] W. Zhou, R. Apkarian, Z. L. Wang, and D. Joy, “Fundamentals of Scanning Electron Microscopy (SEM),” in *Scanning Microscopy for Nanotechnology*, W. Zhou and Z. L. Wang, Eds., New York, NY: Springer New York, 2006, pp. 1–40. doi: 10.1007/978-0-387-39620-0_1.

[32] E. H. Hall, “On a New Action of the Magnet on Electric Currents,” *American Journal of Mathematics*, vol. 2, no. 3, p. 287, Sep. 1879, doi: 10.2307/2369245.

[33] S. Kasap, “HALL EFFECT IN SEMICONDUCTORS,” *American Journal of Mathematics*, vol. Vol. 2, No. 3, pp. 287–292, Sep. 1879.

[34] W. Ananda, "External quantum efficiency measurement of solar cell," in *2017 15th International Conference on Quality in Research (QiR) : International Symposium on Electrical and Computer Engineering*, Nusa Dua: IEEE, Jul. 2017, pp. 450–456. doi: 10.1109/QIR.2017.8168528.

[35] S. Silvestre, "Strategies for Fault Detection and Diagnosis of PV Systems," in *Advances in Renewable Energies and Power Technologies*, Elsevier, 2018, pp. 231–255. doi: 10.1016/B978-0-12-812959-3.00007-1.

[36] P. Würfel and U. Würfel, *Physics of solar cells: from basic principles to advanced concepts*, 3rd edition. Weinheim: Wiley-VCH Verlag GmbH & Co. KGaA, 2016.

[37] W. Shockley and H. J. Queisser, "Detailed Balance Limit of Efficiency of *p-n* Junction Solar Cells," *Journal of Applied Physics*, vol. 32, no. 3, pp. 510–519, Mar. 1961, doi: 10.1063/1.1736034.

[38] M. R. Brozel, G. E. Stillman, and Institution of Electrical Engineers, Eds., *Properties of gallium arsenide*, 3rd ed. in EMIS datareviews series, no. 16. London: INSPEC - The Institution of Electrical Engineers, 1996.

[39] A. S. Sarkın, N. Ekren, and Ş. Sağlam, "A review of anti-reflection and self-cleaning coatings on photovoltaic panels," *Solar Energy*, vol. 199, pp. 63–73, Mar. 2020, doi: 10.1016/j.solener.2020.01.084.

[40] E. Aperathitis, "RF sputtered indium-tin-oxide as antireflective coating for GaAs solar cells," *Solar Energy Materials and Solar Cells*, vol. 45, no. 2, pp. 161–168, Jan. 1997, doi: 10.1016/S0927-0248(96)00067-0.

[41] Y. Takeda, "Light trapping for photovoltaic cells used for optical power transmission," *Appl. Phys. Express*, vol. 13, no. 5, p. 054001, May 2020, doi: 10.35848/1882-0786/ab8056.

[42] W. Yang *et al.*, "Ultra-thin GaAs single-junction solar cells integrated with a reflective back scattering layer," *Journal of Applied Physics*, vol. 115, no. 20, p. 203105, May 2014, doi: 10.1063/1.4878156.

[43] K. J. Singh and S. K. Sarkar, "Highly efficient ARC less InGaP/GaAs DJ solar cell numerical modeling using optimized InAlGaP BSF layers," *Opt Quant Electron*, vol. 43, no. 1–5, pp. 1–21, Feb. 2012, doi: 10.1007/s11082-011-9499-y.

[44] K. Attari, L. Amhaimar, A. El Yaakoubi, A. Asselman, and M. Bassou, "The Design and Optimization of GaAs Single Solar Cells Using the Genetic Algorithm and Silvaco ATLAS," *International Journal of Photoenergy*, vol. 2017, pp. 1–7, 2017, doi: 10.1155/2017/8269358.

[45] A. Rizk, K. Islam, and A. Nayfeh, “Modeling of InAs/GaAs Quantum Dot Solar Cells,” in *2013 European Modelling Symposium*, Manchester, United Kingdom: IEEE, Nov. 2013, pp. 677–680. doi: 10.1109/EMS.2013.113.

[46] C. Flores, D. Passoni, and G. Timo, “Advanced GaAs space solar cells by MOCVD technique,” vol. 2, pp. 507–510, Aug. 1989.

[47] K. Seshan, Ed., *Handbook of thin-film deposition processes and techniques: principles, methods, equipment, and applications*, 2nd ed. Norwich, N.Y: Noyes Publications, 2002.

[48] G. B. Stringfellow, *Organometallic Vapor-Phase Epitaxy: Theory and Practice*. Saint Louis: Elsevier Science, 2014.

[49] S. P. Tobin *et al.*, “Assessment of MOCVD- and MBE-growth GaAs for high-efficiency solar cell applications,” *IEEE Trans. Electron Devices*, vol. 37, no. 2, pp. 469–477, Feb. 1990, doi: 10.1109/16.46385.

[50] T. J. Drummond *et al.*, “Use of a superlattice to enhance the interface properties between two bulk heterolayers,” *Applied Physics Letters*, vol. 42, no. 7, pp. 615–617, Apr. 1983, doi: 10.1063/1.94021.

[51] K. L. Tan, M. S. Lundstrom, and M. R. Melloch, “Effect of impurity trapping on the capacitance-voltage characteristics of *n* -GaAs/ *N* -AlGaAs heterojunctions,” *Applied Physics Letters*, vol. 48, no. 6, pp. 428–430, Feb. 1986, doi: 10.1063/1.96520.

[52] M. R. Melloch, E. S. Harmon, and K. A. Emergy, “Large-area, 8-cm/sup 2/ GaAs solar cells fabricated from MBE material,” *IEEE Electron Device Lett.*, vol. 12, no. 3, pp. 137–139, Mar. 1991, doi: 10.1109/55.75736.

[53] N. Konofaos, E. K. Evangelou, F. Scholz, K. Zieger, and E. Aperathitis, “Electrical characterization and carrier transport mechanisms of GaAs p/i/n devices for photovoltaic applications,” *Materials Science and Engineering: B*, vol. 80, no. 1–3, pp. 152–155, Mar. 2001, doi: 10.1016/S0921-5107(00)00641-3.

[54] M. Diantoro, T. Suprayogi, A. Hidayat, A. Taufiq, A. Fuad, and R. Suryana, “Shockley’s Equation Fit Analyses for Solar Cell Parameters from I-V Curves,” *International Journal of Photoenergy*, vol. 2018, pp. 1–7, 2018, doi: 10.1155/2018/9214820.

[55] V. d’Alessandro, P. Guerriero, S. Daliento, and M. Gargiulo, “A straightforward method to extract the shunt resistance of photovoltaic cells from current–voltage characteristics of mounted arrays,” *Solid-State Electronics*, vol. 63, no. 1, pp. 130–136, Sep. 2011, doi: 10.1016/j.sse.2011.05.018.

[56] L. Duan *et al.*, "Relationship Between the Diode Ideality Factor and the Carrier Recombination Resistance in Organic Solar Cells," *IEEE J. Photovoltaics*, vol. 8, no. 6, pp. 1701–1709, Nov. 2018, doi: 10.1109/JPHOTOV.2018.2870722.

[57] "Series Resistance Effect_PV Education." [Online]. Available: https://www.pveducation.org/pvcdrom/solar-cell-operation/series-resistance

[58] "Shunt Resistance Effect_PV Education." [Online]. Available: https://www.pveducation.org/pvcdrom/solar-cell-operation/shunt-resistance

[59] M. A. Green, *Solar cells: operating principles, technology and system applications*, Repr. [der Ausg.] Englewood Cliffs, NJ 1982. Kensington, NSW: Univ. of New South Wales, 1998.

[60] "Ideality Factor Effect_PV Education." [Online]. Available: https://www.pveducation.org/pvcdrom/characterisation/measuring-ideality-factor

[61] K. R. McIntosh and Honsberg, C. B., "The Influence of Edge Recombination on a Solar Cell's IV Curve," presented at the 16th European Photovoltaic Solar Energy Conference, 2000.

[62] D. Del Olmo, M. Pavelka, and J. Kosek, "Open-Circuit Voltage Comes from Non-Equilibrium Thermodynamics," *Journal of Non-Equilibrium Thermodynamics*, vol. 46, no. 1, pp. 91–108, Jan. 2021, doi: 10.1515/jnet-2020-0070.

[63] "Open Circuit Voltage_PV Education." [Online]. Available: https://www.pveducation.org/pvcdrom/solar-cell-operation/open-circuit-voltage

[64] F. A. Lindholm, J. G. Fossum, and E. L. Burgess, "Application of the superposition principle to solar-cell analysis," *IEEE Trans. Electron Devices*, vol. 26, no. 3, pp. 165–171, Mar. 1979, doi: 10.1109/T-ED.1979.19400.

[65] R. A. Sinton and A. Cuevas, "Contactless determination of current–voltage characteristics and minority-carrier lifetimes in semiconductors from quasi-steady-state photoconductance data," *Applied Physics Letters*, vol. 69, no. 17, pp. 2510–2512, Oct. 1996, doi: 10.1063/1.117723.

[66] M. Y. Levy and C. Honsberg, "Rapid and precise calculations of energy and particle flux for detailed-balance photovoltaic applications," *Solid-State Electronics*, vol. 50, no. 7–8, pp. 1400–1405, Jul. 2006, doi: 10.1016/j.sse.2006.06.017.

[67] M. R. Brozel, G. E. Stillman, and Institution of Electrical Engineers, Eds., *Properties of gallium arsenide*, 3rd ed. in EMIS datareviews series, no. 16. London: INSPEC - The Institution of Electrical Engineers, 1996.

[68] "Filmetrics Reflectance Calculator." [Online]. Available: https://www.filmetrics.com/reflectance-calculator

[69] C. C. Stoumpos and M. G. Kanatzidis, "The Renaissance of Halide Perovskites and Their Evolution as Emerging Semiconductors," *Acc. Chem. Res.*, vol. 48, no. 10, pp. 2791–2802, Oct. 2015, doi: 10.1021/acs.accounts.5b00229.

[70] G. Grancini *et al.*, "One-Year stable perovskite solar cells by 2D/3D interface engineering," *Nat Commun*, vol. 8, no. 1, p. 15684, Jun. 2017, doi: 10.1038/ncomms15684.

[71] S. Rhee, K. An, and K.-T. Kang, "Recent Advances and Challenges in Halide Perovskite Crystals in Optoelectronic Devices from Solar Cells to Other Applications," *Crystals*, vol. 11, no. 1, p. 39, Dec. 2020, doi: 10.3390/cryst11010039.

[72] Z. Li, M. Yang, J.-S. Park, S.-H. Wei, J. J. Berry, and K. Zhu, "Stabilizing Perovskite Structures by Tuning Tolerance Factor: Formation of Formamidinium and Cesium Lead Iodide Solid-State Alloys," *Chem. Mater.*, vol. 28, no. 1, pp. 284–292, Jan. 2016, doi: 10.1021/acs.chemmater.5b04107.

[73] X. Chen and S. S. Mao, "Titanium Dioxide Nanomaterials: Synthesis, Properties, Modifications, and Applications," *Chem. Rev.*, vol. 107, no. 7, pp. 2891–2959, Jul. 2007, doi: 10.1021/cr0500535.

[74] A. S. Bakri *et al.*, "Effect of annealing temperature of titanium dioxide thin films on structural and electrical properties," presented at the INTERNATIONAL CONFERENCE ON ENGINEERING, SCIENCE AND NANOTECHNOLOGY 2016 (ICESNANO 2016), Solo, Indonesia, 2017, p. 030030. doi: 10.1063/1.4968283.

[75] A. M. Luís, M. C. Neves, M. H. Mendonça, and O. C. Monteiro, "Influence of calcination parameters on the TiO2 photocatalytic properties," *Materials Chemistry and Physics*, vol. 125, no. 1–2, pp. 20–25, Jan. 2011, doi: 10.1016/j.matchemphys.2010.08.019.

[76] D. G. Lee *et al.*, "Effect of TiO2 particle size and layer thickness on mesoscopic perovskite solar cells," *Applied Surface Science*, vol. 477, pp. 131–136, May 2019, doi: 10.1016/j.apsusc.2017.11.124.

[77] Isrihetty Senain, Nafarizal Nayan, and Hashim Saim, "Structural and Electrical Properties of TiO2 Thin Film Derived from Sol-gel Method

using Titanium (IV) Butoxide," vol. International Journal of Integrated Engineering, no. Issue on Electrical and Electronic Engineering, 2011.

[78] X. Ziang *et al.*, "Refractive index and extinction coefficient of CH_3NH_3PbI_3 studied by spectroscopic ellipsometry," *Opt. Mater. Express*, vol. 5, no. 1, p. 29, Jan. 2015, doi: 10.1364/OME.5.000029.

[79] C. Aivalioti *et al.*, "Transparent All-Oxide Hybrid NiO:N/TiO2 Heterostructure for Optoelectronic Applications," *Electronics*, vol. 10, no. 9, p. 988, Apr. 2021, doi: 10.3390/electronics10090988.

[80] C. Aivalioti *et al.*, "An Assessment of Sputtered Nitrogen-Doped Nickel Oxide for all-Oxide Transparent Optoelectronic Applications: The Case of Hybrid NiO:N/TiO2 Heterostructure," in *Recent Trends in Chemical and Material Sciences Vol. 6*, Dr. M. M. El Nady, Ed., Book Publisher International (a part of SCIENCEDOMAIN International), 2022, pp. 86–111. doi: 10.9734/bpi/rtcams/v6/1650A.

[81] C. Aivalioti *et al.*, "Niobium-doped NiO as p-type nanostructured layer for transparent photovoltaics," *Thin Solid Films*, vol. 778, p. 139910, Aug. 2023, doi: 10.1016/j.tsf.2023.139910.

[82] T. Leijtens, J. Lim, J. Teuscher, T. Park, and H. J. Snaith, "Charge Density Dependent Mobility of Organic Hole-Transporters and Mesoporous TiO_2 Determined by Transient Mobility Spectroscopy: Implications to Dye-Sensitized and Organic Solar Cells," *Adv. Mater.*, vol. 25, no. 23, pp. 3227–3233, Jun. 2013, doi: 10.1002/adma.201300947.

[83] J. Burschka *et al.*, "Tris(2-(1 *H* -pyrazol-1-yl)pyridine)cobalt(III) as p-Type Dopant for Organic Semiconductors and Its Application in Highly Efficient Solid-State Dye-Sensitized Solar Cells," *J. Am. Chem. Soc.*, vol. 133, no. 45, pp. 18042–18045, Nov. 2011, doi: 10.1021/ja207367t.

[84] S. Wang *et al.*, "Role of 4- *tert* -Butylpyridine as a Hole Transport Layer Morphological Controller in Perovskite Solar Cells," *Nano Lett.*, vol. 16, no. 9, pp. 5594–5600, Sep. 2016, doi: 10.1021/acs.nanolett.6b02158.

[85] G. Li, Y. Wang, L. Huang, R. Zeng, and W. Sun, "Inhibited Aggregation of Lithium Salt in Spiro-OMeTAD for Perovskite Solar Cells," *Crystals*, vol. 12, no. 2, p. 290, Feb. 2022, doi: 10.3390/cryst12020290.

[86] J. H. Noh, N. J. Jeon, Y. C. Choi, Md. K. Nazeeruddin, M. Grätzel, and S. I. Seok, "Nanostructured TiO2/CH3NH3PbI3 heterojunction solar cells employing spiro-OMeTAD/Co-complex as hole-transporting material," *J. Mater. Chem. A*, vol. 1, no. 38, p. 11842, 2013, doi: 10.1039/c3ta12681a.

[87] B. Lee, A. J. Yun, J. Kim, B. Gil, B. Shin, and B. Park, "Aminosilane-Modified $CuGaO_2$ Nanoparticles Incorporated with CuSCN as a Hole-

Transport Layer for Efficient and Stable Perovskite Solar Cells," *Adv. Mater. Interfaces*, vol. 6, no. 22, p. 1901372, Nov. 2019, doi: 10.1002/admi.201901372.

[88] J. Liu *et al.*, "Identification and Mitigation of a Critical Interfacial Instability in Perovskite Solar Cells Employing Copper Thiocyanate Hole-Transporter," *Adv. Mater. Interfaces*, vol. 3, no. 22, p. 1600571, Nov. 2016, doi: 10.1002/admi.201600571.

[89] G. Wu, R. Liang, M. Ge, G. Sun, Y. Zhang, and G. Xing, "Surface Passivation Using 2D Perovskites toward Efficient and Stable Perovskite Solar Cells," *Advanced Materials*, vol. 34, no. 8, p. 2105635, Feb. 2022, doi: 10.1002/adma.202105635.

[90] V. E. Madhavan *et al.*, "CuSCN as Hole Transport Material with 3D/2D Perovskite Solar Cells," *ACS Appl. Energy Mater.*, vol. 3, no. 1, pp. 114–121, Jan. 2020, doi: 10.1021/acsaem.9b01692.

[91] B. N. Ezealigo *et al.*, "A study on solution deposited CuSCN thin films: Structural, electrochemical, optical properties," *Arabian Journal of Chemistry*, vol. 13, no. 1, pp. 346–356, Jan. 2020, doi: 10.1016/j.arabjc.2017.04.013.

[92] Q. Emery *et al.*, "Encapsulation and Outdoor Testing of Perovskite Solar Cells: Comparing Industrially Relevant Process with a Simplified Lab Procedure," *ACS Appl. Mater. Interfaces*, vol. 14, no. 4, pp. 5159–5167, Feb. 2022, doi: 10.1021/acsami.1c14720.

[93] Q.-M. Hong, R.-P. Xu, T.-Y. Jin, J.-X. Tang, and Y.-Q. Li, "Unraveling the light-induced degradation mechanism of CH3NH3PbI3 perovskite films," *Organic Electronics*, vol. 67, pp. 19–25, Apr. 2019, doi: 10.1016/j.orgel.2019.01.005.

[94] S. Ruan *et al.*, "Light induced degradation in mixed-halide perovskites," *J. Mater. Chem. C*, vol. 7, no. 30, pp. 9326–9334, 2019, doi: 10.1039/C9TC02635E.

[95] M. Saliba *et al.*, "Cesium-containing triple cation perovskite solar cells: improved stability, reproducibility and high efficiency," *Energy Environ. Sci.*, vol. 9, no. 6, pp. 1989–1997, 2016, doi: 10.1039/C5EE03874J.

[96] K. Liao *et al.*, "Hot-Casting Large-Grain Perovskite Film for Efficient Solar Cells: Film Formation and Device Performance," *Nano-Micro Lett.*, vol. 12, no. 1, p. 156, Dec. 2020, doi: 10.1007/s40820-020-00494-2.

[97] W. Nie *et al.*, "High-efficiency solution-processed perovskite solar cells with millimeter-scale grains," *Science*, vol. 347, no. 6221, pp. 522–525, Jan. 2015, doi: 10.1126/science.aaa0472.

[98] S. D. Stranks *et al.*, "Electron-Hole Diffusion Lengths Exceeding 1 Micrometer in an Organometal Trihalide Perovskite Absorber," *Science*, vol. 342, no. 6156, pp. 341–344, Oct. 2013, doi: 10.1126/science.1243982.

[99] D. H. Cao *et al.*, "Remnant PbI2, an unforeseen necessity in high-efficiency hybrid perovskite-based solar cells?," *APL Materials*, vol. 2, no. 9, p. 091101, Sep. 2014, doi: 10.1063/1.4895038.

[100] D. Cortecchia, J. Yin, A. Petrozza, and C. Soci, "White light emission in low-dimensional perovskites," *J. Mater. Chem. C*, vol. 7, no. 17, pp. 4956–4969, 2019, doi: 10.1039/C9TC01036J.

[101] J. Chen *et al.*, "Perovskite White Light Emitting Diodes: Progress, Challenges, and Opportunities," *ACS Nano*, vol. 15, no. 11, pp. 17150–17174, Nov. 2021, doi: 10.1021/acsnano.1c06849.

[102] M. Konstantakou, D. Perganti, P. Falaras, and T. Stergiopoulos, "Anti-Solvent Crystallization Strategies for Highly Efficient Perovskite Solar Cells," *Crystals*, vol. 7, no. 10, p. 291, Sep. 2017, doi: 10.3390/cryst7100291.

[103] A. Babayigit, J. D'Haen, H.-G. Boyen, and B. Conings, "Gas Quenching for Perovskite Thin Film Deposition," *Joule*, vol. 2, no. 7, pp. 1205–1209, Jul. 2018, doi: 10.1016/j.joule.2018.06.009.

[104] A. K. Roy Choudhury, "Instrumental colourant formulation," in *Principles of Colour and Appearance Measurement*, Elsevier, 2015, pp. 117–173. doi: 10.1533/9781782423881.117.

[105] S. Chen *et al.*, "Light Illumination Induced Photoluminescence Enhancement and Quenching in Lead Halide Perovskite," *Sol. RRL*, vol. 1, no. 1, p. 1600001, Jan. 2017, doi: 10.1002/solr.201600001.

[106] D. W. De Quilettes *et al.*, "Impact of microstructure on local carrier lifetime in perovskite solar cells," *Science*, vol. 348, no. 6235, pp. 683–686, May 2015, doi: 10.1126/science.aaa5333.

[107] R. He *et al.*, "Efficient wide-bandgap perovskite solar cells enabled by doping a bromine-rich molecule," *Nanophotonics*, vol. 10, no. 8, pp. 2059–2068, Jun. 2021, doi: 10.1515/nanoph-2020-0634.

[108] D. P. McMeekin *et al.*, "A mixed-cation lead mixed-halide perovskite absorber for tandem solar cells," *Science*, vol. 351, no. 6269, pp. 151–155, Jan. 2016, doi: 10.1126/science.aad5845.

[109] I. Syngelakis, "3D Laser Lithography with Applications in Photocatalysis," Department of Materials Science and Technology, University of Crete, 2022. (Master Thesis)

[110] D. E. Aspnes, “Recombination at semiconductor surfaces and interfaces,” *Surface Science*, vol. 132, no. 1–3, pp. 406–421, Sep. 1983, doi: 10.1016/0039-6028(83)90550-2.

[111] A. Callegari, P. D. Hoh, D. A. Buchanan, and D. Lacey, “Unpinned gallium oxide/GaAs interface by hydrogen and nitrogen surface plasma treatment,” *Applied Physics Letters*, vol. 54, no. 4, pp. 332–334, Jan. 1989, doi: 10.1063/1.100961.

[112] V. N. Bessolov, M. V. Lebedev, N. M. Binh, M. Friedrich, and D. R. T. Zahn, “Sulphide passivation of GaAs: the role of the sulphur chemical activity,” *Semicond. Sci. Technol.*, vol. 13, no. 6, pp. 611–614, Jun. 1998, doi: 10.1088/0268-1242/13/6/012.

[113] G. H. Yang, Y. Zhang, E. T. Kang, K. G. Neoh, W. Huang, and J. H. Teng, “Surface Passivation of (100)-Oriented GaAs via Plasma Deposition of an Ultrathin S-Containing Polymer Film and Its Effect on Photoluminescence,” *J. Phys. Chem. B*, vol. 107, no. 33, pp. 8592–8598, Aug. 2003, doi: 10.1021/jp034597r.

[114] M. Passlack, M. Hong, J. P. Mannaerts, J. R. Kwo, and L. W. Tu, “Recombination velocity at oxide–GaAs interfaces fabricated by *in situ* molecular beam epitaxy,” *Applied Physics Letters*, vol. 68, no. 25, pp. 3605–3607, Jun. 1996, doi: 10.1063/1.116652.

[115] G. Brammertz *et al.*, “Surface recombination velocity in GaAs and In0.15Ga0.85As thin films,” *Applied Physics Letters*, vol. 90, no. 13, p. 134102, Mar. 2007, doi: 10.1063/1.2717533.

[116] M. Hocevar *et al.*, “Residual strain and piezoelectric effects in passivated GaAs/AlGaAs core-shell nanowires,” *Applied Physics Letters*, vol. 102, no. 19, p. 191103, May 2013, doi: 10.1063/1.4803685.

[117] D. J. Ashen, P. J. Dean, D. T. J. Hurle, J. B. Mullin, A. M. White, and P. D. Greene, “The incorporation and characterisation of acceptors in epitaxial GaAs,” *Journal of Physics and Chemistry of Solids*, vol. 36, no. 10, pp. 1041–1053, Oct. 1975, doi: 10.1016/0022-3697(75)90043-8.

[118] E. W. Williams and R. A. Chapman, “Temperature Dependence of Photoluminescence in Cadmium-Doped Epitaxial GaAs,” *Journal of Applied Physics*, vol. 38, no. 6, pp. 2547–2552, May 1967, doi: 10.1063/1.1709947.

[119] L. Calderon *et al.*, “Photoluminescence characterization of nonradiative recombination in carbon-doped GaAs,” *Applied Physics Letters*, vol. 60, no. 13, pp. 1597–1599, Mar. 1992, doi: 10.1063/1.107483.

[120] Y. Liu *et al.*, "Temperature-dependent photoluminescence spectra and decay dynamics of MAPbBr3 and MAPbI3 thin films," *AIP Advances*, vol. 8, no. 9, p. 095108, Sep. 2018, doi: 10.1063/1.5042489.

[121] Y. P. Varshni, "Temperature dependence of the energy gap in semiconductors," *Physica*, vol. 34, no. 1, pp. 149–154, Jan. 1967, doi: 10.1016/0031-8914(67)90062-6.

[122] C. Zhang, W. Luan, and Y. Yin, "High Efficient Planar-heterojunction Perovskite Solar Cell Based on Two-step Deposition Process," *Energy Procedia*, vol. 105, pp. 793–798, May 2017, doi: 10.1016/j.egypro.2017.03.391.

[123] S. M. Sze and M. K. Lee, *Semiconductor devices, physics and technology*, 3rd ed. Hoboken, N.J: Wiley, 2012.

[124] J. F. Van Der Veen, L. Smit, P. K. Larsen, J. H. Neave, and B. A. Joyce, "Interface electronic structure of Pb on GaAs(001)," *Journal of Vacuum Science and Technology*, vol. 21, no. 2, pp. 375–379, Jul. 1982, doi: 10.1116/1.571784.

[125] W. Chen *et al.*, "Schottky barrier formation at nonreactive interfaces: Ga/GaAs(100) and Pb/GaAs(100)," *Journal of Vacuum Science & Technology A: Vacuum, Surfaces, and Films*, vol. 11, no. 4, pp. 854–859, Jul. 1993, doi: 10.1116/1.578317.

[126] R. Dingle, "Radiative Lifetimes of Donor-Acceptor Pairs in p -Type Gallium Arsenide," *Phys. Rev.*, vol. 184, no. 3, pp. 788–796, Aug. 1969, doi: 10.1103/PhysRev.184.788.

[127] R. Toyoshima, S. Murakami, S. Eguchi, K. Amemiya, K. Mase, and H. Kondoh, "Initial oxidation of GaAs(100) under near-realistic environments revealed by *in situ* AP-XPS," *Chem. Commun.*, vol. 56, no. 94, pp. 14905–14908, 2020, doi: 10.1039/D0CC05279E.

[128] M. H. Engelhard, A. Lyubinetsky, and D. R. Baer, "Gallium arsenide (GaAs) (001) after sublimation of arsenic (As) thin-film cap, by XPS," *Surface Science Spectra*, vol. 23, no. 2, pp. 83–92, Dec. 2016, doi: 10.1116/1.4962156.

[129] J. Rodriguez-Pereira, J. Tirado, A. F. Gualdrón-Reyes, F. Jaramillo, and R. Ospina, "XPS of the surface chemical environment of CsMAFAPbBrI trication-mixed halide perovskite film," *Surface Science Spectra*, vol. 27, no. 2, p. 024003, Dec. 2020, doi: 10.1116/6.0000275.

[130] J. D. McGettrick *et al.*, "Sources of Pb(0) artefacts during XPS analysis of lead halide perovskites," *Materials Letters*, vol. 251, pp. 98–101, Sep. 2019, doi: 10.1016/j.matlet.2019.04.081.

[131] C. Das, M. Wussler, T. Hellmann, T. Mayer, and W. Jaegermann, "*In situ* XPS study of the surface chemistry of MAPI solar cells under operating conditions in vacuum," *Phys. Chem. Chem. Phys.*, vol. 20, no. 25, pp. 17180–17187, 2018, doi: 10.1039/C8CP01259H.

[132] T. M. Brenner *et al.*, "Conversion of Single Crystalline PbI_2 to $CH_3NH_3PbI_3$: Structural Relations and Transformation Dynamics," *Chem. Mater.*, vol. 28, no. 18, pp. 6501–6510, Sep. 2016, doi: 10.1021/acs.chemmater.6b01747.

[133] L. Merker and H. Wondratschek, "Bleiverbindungen mit Apatitstruktur, insbesondere Blei-Jod- und Blei-Brom-Apatite," *Z. Anorg. Allg. Chem.*, vol. 300, no. 1–2, pp. 41–50, May 1959, doi: 10.1002/zaac.19593000104.

[134] J. Shamsi *et al.*, "*N* -Methylformamide as a Source of Methylammonium Ions in the Synthesis of Lead Halide Perovskite Nanocrystals and Bulk Crystals," *ACS Energy Lett.*, vol. 1, no. 5, pp. 1042–1048, Nov. 2016, doi: 10.1021/acsenergylett.6b00521.